UNIVERSIDAD NACIONAL AUTÓNOMA DE MÉXICO

PROGRAMA DE MAESTRÍA Y DOCTORADO EN CIENCIAS MATEMÁTICAS Y DE LA ESPECIALIZACIÓN EN ESTADÍSTICA APLICADA

"ESTUDIO DEL TRANSPORTE AUTOCONSISTENTE CAÓTICO A TRAVÉS DE UN SISTEMA DINÁMICO ACOPLADO POR UN CAMPO MEDIO"

TESIS
QUE PARA OPTAR POR EL GRADO DE:
DOCTOR EN CIENCIAS

PRESENTA:
DAVID MARTÍNEZ DEL RÍO

DIRECTORES DE TESIS
ARTURO OLVERA CHAVEZ,
INSTITUTO DE INVESTIGACIONES EN MATEMÁTICAS Y EN SISTEMAS

DIEGO DEL CASTILLO-NEGRETE ROVIRA,
OAK RIDGE NATIONAL LABORATORY, OAK RIDGE, TN, E.U.A.

MIEMBRO DEL COMITÉ TUTOR
PANAYIOTIS PANAYOTAROS,
INSTITUTO DE INVESTIGACIONES EN MATEMÁTICAS Y EN SISTEMAS

CIUDAD UNIVERSITARIA, CD. MX., ABRIL 2019.

Agradecimientos

Deseo agradecer a mis tutores, Arturo Olvera y Diego del Castillo-Negrete por su casi infinita paciencia, apoyo y tutela. Este trabajo no hubiera sido posible sin la colaboración de ambos. Más allá de su considerables conocimientos científicos y facilidad para enseñarlos, su mera calidad humana los hace modelos a seguir.

También quiero agradecer a Renato Calleja cuya colaboración fue crucial para la realización de muchas de las figuras y resultados presentes en este manuscrito, en particular los capítulos 5 y 6. Su conocimiento, habilidad y enorme capacidad de trabajo lo hacen también un ejemplo a seguir.

Extiendo mi agradecimiento al comité revisor que ayudó a mejorar la calidad y claridad de este trabajo.

Estoy en deuda más de lo que puedo decir con palabras con el Dr. Marcos Rosenbaum y el lamentablemente fallecido Dr. Antonmaría Minzoni por convencerme de intentar una vez más con la vida académica.

Agradezco a mis padres, Emilio y Bertha, por su constante apoyo y comprensión. A mis hermanos, Elisa y León, por cuidar de mí y a mis cuñados, Pepe y Amaranta, que cuidan de ellos. Extiendo mis agradecimientos a mi familia extendida que de una forma u otra me han ayudado y compartido sus experiencias para tratar con eso que llamamos vida.

Una mención especial a mis hermanos no consanguineos Román Juárez y Pablo Ruedas, a quienes tuve la suerte de conocer en la Facultad de Ciencias y que tuvieron a bien de quedarse cerca y dejarme ser parte de sus familias.

Quiero dar las gracias a todos los profesores del IIMAS, del posgrado y quienes tuve la buena forturna de conocer en mis viajes, que contribuyeron a

enriquecer mi conocimiento matemático y mi cultura. En particular: Panayiotis Panayotaros, Gustavo Cruz, Nikola Petrov, Rafael de la Llave, James Meiss, Alex Haro, Carles Simó y al también lamentablemente fallecido Gilberto Flores.

Agradezco también a todos aquellos que conocí durante mi tiempo como estudiante de doctorado por ayudarme a crecer en el mundo académico y por compartir conmigo sus historias, mostrándome lo grande y diverso que es el mundo. En especial a: Rosa María Vargas, Iméne Khames, Gerardo Mejía, Mirella Ramírez, Manuel Tejada, Carlos García, Arrigo Coen, Anna Florio, Hongyu Cheng, Dorothy Fremder, Darren Fremder, Zhiqiang Li, Ben Cambon, Ryland Deemer y toda la pandilla del programa de otoño'18 del MSRI.

Y por último, pero no menos importante, agradezco a mi alma mater, la UNAM.

Acknowledgments

I would like to thank my advisors Arturo Olvera and Diego del Castillo-Negrete for their almost infinite patience, support and mentoring. This work would not be possible without the collaboration of both of them. Aside of their considerable scientific knowledge and their ability to communicate it, their human qualities alone make them role models.

Also I would like to thank Renato Calleja, whose collaboration was crucial for many of the figures and results in this manuscript, in particular Chapter 5 and 6. His knowledge, skill and enormous working capacity make him too an example to follow.

I also extended my gratitude to the reviewing committee that helped to improve the quality and clarity of this work.

I am indebted more than I can put in words to Dr. Marcos Rosenbaum and the late Dr. Antonmaria Minzoni for talking me into giving the academic life one more try.

I thank my parents, Emilio and Bertha, for the unfailing support and comprehension. To my brother and sister, Elisa and León, for taking care of me and my brother- and sister in law, Pepe and Amaranta, that take care of them. I must extend my thanks to my extended family that in a way or another lend me help and and shared with me their experiences which helped me to deal with that thing we call life.

A special mention goes to my blood unrelated brothers Roman Juarez and Pablo Ruedas, whom I was lucky to met years ago in the School of Sciences. They have been gracious enough to stay around and let me be part of their families.

I want to thank to all the professors from IIMAS, the graduate program and those who I was lucky to meet in my trips for enriching my mathematical and cultural scope. Specially: Panayotis Panayotaros, Gustavo Cruz, Nikola Petrov, Rafael de la Llave, James Meiss, Alex Haro, Carles Simó and the late Gilberto Flores.

I also would like to thank to all the people I met during my time as a PhD student for helping me to to grow in the academic world and for sharing with me their histories helping me to notice how big and diverse is the world. Specially to: Rosa María Vargas, Iméne Khames, Gerardo Mejía, Mirella Ramírez, Manuel Tejada, Carlos García, Arrigo Coen, Anna Florio, Hongyu Cheng, Dorothy Fremder, Darren Fremder, Zhiqiang Li, Ben Cambon, Ryland Deemer and all the gang at MSRI from the fall'18 program.

And last but not the least,I thank to my Alma Mater, the UNAM.

Introducción

El presente trabajo es un estudio de un modelo de transporte autoconsistente caótico conocido como *modelo discreto de una onda* (*single wave map model*) o *mapeo autoconsistente* (*self-consistent map*), introducido en la Ref. [1]. El objetivo principal de este trabajo fue entender como funciona el fenomeno del transporte caótico desde el punto de vista un sistema dinámico discreto. En particular, se tomó en consideración las similaridades del modelo discreto con el bien conocido y estudiado *mapeo estándar*.

El *mapeo autoconsistente* ha sido estudiado antes en la literatura, donde los trabajos más cercanos al enfoque de este manuscrito pueden encontrarse en las referencias [2, 3] (como mapeo) y en la referencia [4] (como un sistema continuo de EDO's). Una importante diferencia respecto a estas primeras dos referencias radica en que ambas usaron una versión modificada del modelo discreto original, añadiendo un harmónico extra a la perturbación en [2] o cambiando por una perturbación non-twist en [3]. El modelo de EDP's original data de principio de los 70's por O'Neil et.al. (vease Ref. [5]) y originó una amplia variedad de trabajos yendo desde lo experimental hasta lo analítico. En las Refs. [6, 7] este modelo fue generalizado y derivado sistemáticamente del sistema de Vlasov-Poisson usando expansiones asintóticas y teoría no lineal débil.

El cuerpo principal de este trabajo proviene de los recientes trabajos en las Refs. [8, 9] y un manuscrito en proceso, escritos por el autor en colaboración con Diego del-Castillo-Negrete, Arturo Olvera y Renato Calleja. Los resultados empujaron este trabajo hacia el estudio de tipos más generales de mapeos simplécticos y al uso de métodos viejos y nuevos, como el método de superposición de Chirikov (Chirikov's overlap method) [10] y el más reciente *método de la parametrización* (*parameterization method*) [11, 12, 13, 14].

El manuscrito esta organizado de la siguiente manera. El Capítulo 1 introduce el *mapeo autoconsistente* y presenta una derivación corta par-

tiendo de un modelo Hamiltoniano de campo medio $(2N + 2)$-dimensional de EDO's. Este capítulo también introduce conceptos clave como *transporte* y *estructuras coherentes*, presenta simulaciones características del mapeo y presenta un estudio de casos de baja dimensión para luego contrastarlos una solución exacta del modelo continuo original. El Capítulo 2 da una resumen de los resultados matemáticos que serán usados en el resto del trabajo. El Capítulo 3 contiene un estudio de órbitas periódicas del modelo y enfoca su atención en una variedad particular de órbitas periódicas con el uso de formas normales. El Capítulo 4 introduce un modelo reducido de un mapeo no-autónomo (NASM) que intenta imitar el comportamiento oscilatorio observado en el modelo discreto original. En este capítulo, la atención está centrada en el caso dos-periódico del NASM, usando sobre este todas las herramientas disponibles. Para extender los resultados del NASM dos-periódico y caracterizar mejor el comportamiento crítico de mapeos similares, el Capítulo 5 presenta un nuevo método para calcular órbitas periódicas en mapeos *no reversibles* y en el Capítulo 6 se usa este método para estudiar órbitas periódicas en dos ejemplos en un regimen crítico. Las conclusiones se presentan en el Capítulo 7 junto con algunas propuestas de trabajo futuro no mencionadas en capítulos previos.

Introduction

The present work is a study of a discrete model of chaotic self-consistent transport known as *single wave map model* or *self-consistent map*, introduced in Ref. [1]. The main goal of this work was to use it to understand how does the chaotic transport phenomenon work from the discrete dynamical system point of view. In particular, it was taken into account the similarities of the map model with the very well known and studied *standard map*.

The *self-consistent map* has been studied before in the literature, where the closest approaches to the present work can be found in references [2, 3] (as a map) and reference [4] (as continuous ODE system). An important difference in the approaches of the first two references is that both used a modified versions of the original map model, adding one extra harmonic perturbation in Ref. [2] and adding the a non-twist perturbation in Ref. [3]. The original PDE model dates from early 70's by O'Neil et.al. (see Ref. [5]) and it originated a wide variety of works from experimental to analytic. In Refs. [6, 7], this model was generalized and systematically derived from the Vlasov-Poisson system using a weakly nonlinear matched asymptotic expansion.

The main body of this work comes from the recent works Refs. [8, 9] and a manuscript in process, co-written by the author in collaboration with Diego del-Castillo-Negrete, Arturo Olvera and Renato Calleja. The results have pushed the work in the direction to study a more general type of simplectic maps and to use old and new methods, like Chirikov's overlap method [10] and the more recent *parameterization method* [11, 12, 13, 14].

The manuscript is organized in the following manner. Chapter 1 introduces the *self-consistent map* and presents a short derivation of it from a mean-field Hamiltonian $(2N+2)$-dimensional ODE model. The chapter also introduces key concepts like *transport* and *coherent structures*, presents characteristic simulations of the map and studies two low dimensional cases of the

map model to then contrast them with an exact solution of the original continuous model. Chapter 2 reviews the mathematical background that would be used in the rest of the work. Chapter 3 contains a study of periodic orbits of the model and focus the attention on a particular symmetrical kind of periodic orbits with the use of normal forms. Chapter 4 introduces a reduced non-autonomous map model (NASM) that attempts to mimic the oscillatory behavior previously observed in the model. In this chapter, the attention was focused in the period-two case of NASM, using over it all the mathematical tools that were available. To expand the findings on the two-periodic NASM and to better characterize the critical behavior of similar maps, the Chapter 5 presents a new method to compute periodic orbits in *non-reversible* maps and Chapter 6 use this method to characterize the critical behavior of periodic orbits on two examples. Conclusions are presented in Chapter 7 along a few suggestions of future work not mentioned in the previous chapters.

Contents

Chapter 1

The physical model

The model of interest of this work is the so-called *self-consistent map model* or *single wave map model*, for which one of its most popular forms is the following map,

$$x_k^{n+1} = x_k^n + y_k^{n+1}\,, \tag{1.1a}$$
$$y_k^{n+1} = y_k^n + \kappa^{n+1}\,\sin(x_k^n - \theta^n) \tag{1.1b}$$
$$\kappa^{n+1} = \sqrt{(\kappa^n)^2 + (\eta^n)^2} + \eta^n\,, \tag{1.1c}$$
$$\theta^{n+1} = \theta^n - \Omega + \frac{1}{\kappa^{n+1}}\frac{\partial \eta^n}{\partial \theta^n}\,, \tag{1.1d}$$

where $k = 1, 2, ..., N$, Ω is a given real constant and the auxiliar variable η^n is defined as,

$$\eta^n = \sum_{l=1}^{N} \gamma_l\,\sin(x_l^n - \theta^n)\,, \tag{1.2}$$

and γ_k are also given real constants.

This chapter has as its main objective to put in context this map model by giving a short derivation to help understand the physical meaning of its variables. And to complement this, some of the general properties of this model are also presented. A more complete derivation of the model can be found in Refs. [6, 7] for the reduction of the PDE model and in Ref. [1] the successive discretizations that lead to the map (1.1).

1.1 Origin of the model

The map model (1.1) is the result of a symplectic (are preserving) discretization of the evolution equations of this $2N+2$ dimensional hamiltonian system,

$$\frac{dx_k}{dt} = \frac{\partial \mathcal{H}}{\partial p_k}\,, \qquad \frac{dp_k}{dt} = -\frac{\partial \mathcal{H}}{\partial x_k}\,, \tag{1.3a}$$

$$\frac{d\theta}{dt} = \frac{\partial \mathcal{H}}{\partial J}\,, \qquad \frac{dJ}{dt} = -\frac{\partial \mathcal{H}}{\partial \theta}\,, \tag{1.3b}$$

where $k = 1, 2, ..., N$ and the hamiltonian is given by,

$$\mathcal{H} = \sum_{l=1}^{N} \left[\frac{1}{2\Gamma_l} p_l^2 - 2\Gamma_l \sqrt{J} \cos(x_l - \theta) \right] - UJ\,, \tag{1.4}$$

where U and Γ_j are given real constants. More explicitly, the ODE system (1.3) is written,

$$\frac{dx_k}{dt} = \frac{p_k}{\Gamma_k}\,, \tag{1.5a}$$

$$\frac{dp_k}{dt} = -2\Gamma_k \sqrt{J} \sin(x_k - \theta)\,, \tag{1.5b}$$

$$\frac{d\theta}{dt} = -U - \frac{1}{\sqrt{J}} \sum_{l=1}^{N} \Gamma_l \cos(x_l - \theta)\,, \tag{1.5c}$$

$$\frac{dJ}{dt} = 2\sqrt{J} \sum_{l=1}^{N} \Gamma_l \sin(x_l - \theta)\,. \tag{1.5d}$$

The system of Eqs. (1.3)-(1.4) can represent N *non linear oscillators* (x_k, p_k) coupled by a mean field (θ, J). That is, the interaction between the oscillators is given by a field which depends at the same time of a *weighted average* Ξ, of the difference between each x_k and the phase of the mean-field θ, where

$$\Xi = \sum_{l=1}^{N} \Gamma_l \, e^{i(x_l - \theta)}\,. \tag{1.6}$$

It must be clarified that the term "oscillator" is used only in the sense that Eqs. (1.5a)-(1.5b) resemble to the equations of a physical pendulum. The

intermediate step to reduce the system (1.3) to (1.1), is to transform the derivatives to a symplectic (area preserving) discretization by a first order implicit Euler integrator,

$$x_k^{n+1} = x_k^n + \frac{\tau}{\Gamma_k} p_k^{n+1}\,, \tag{1.7a}$$

$$p_k^{n+1} = p_k^n - 2\tau\Gamma_k\sqrt{J^{n+1}}\sin(x_k^n - \theta^n)\,, \tag{1.7b}$$

$$\theta^{n+1} = \theta^n - U\tau - \frac{\tau}{\sqrt{J^{n+1}}}\sum_{l=1}^{N}\Gamma_l\cos(x_l^n - \theta^n)\,, \tag{1.7c}$$

$$J^{n+1} = J^n + 2\tau\sqrt{J^{n+1}}\sum_{l=1}^{N}\Gamma_l\sin(x_l^n - \theta^n)\,. \tag{1.7d}$$

Then the system (1.1) follows from the definitions:

$$y_k^n = \frac{\tau}{\Gamma_k} p_k^n\,, \qquad \gamma_k = 2\tau^3\Gamma_k\,, \qquad \Omega = U\tau \tag{1.8}$$

$$\kappa^n = 2\tau^2\sqrt{J^n}\,, \qquad \eta^n = \sum_{l=1}^{N}\gamma_l\,\sin(x_l^n - \theta^n)\,, \tag{1.9}$$

and the algebraic manipulation of (1.7d) to make the evolution of κ^{n+1} explicit. However, as stated in subsection 1.2.1, this change of variables ($J^n \to \kappa^n$) does not preserve the symplectic structure of the system of equations.

The relevance of this type of hamiltonian system lies in its mean-field coupling, which considerably simplifies the interaction between its main components compared with other cases like the N-body problem or the dynamo problem. Yet, the interaction of the particles exist and is not a given function like in *passive transport* problems, so the system can be considered an intermediate model.

This self-consistent dependency is a trace of the original physical model, a Vlasov-Poisson system, which models a problem of *active transport*.

1.1.1 The transport problem

Transport is the the general term to refer to any phenomena were the spatial distribution of *substance* $\mathcal{A}$ changes in time due the action of an *external field* $\mathcal{F}$. The study of transport is a problem of common interest to fluid dynamics

and plasma physics. A few examples of some of these problems include the dispersion of pollutants in the atmosphere and oceans, the magnetic confinement of fusion plasmas, and more. Broadly speaking it is possible to distinguish two different types of transport: *passive* and *active*. The first refers to the study of *passive scalars* which are transported by the flow without affecting it (like the dispersion of a drop of ink in a glass of water), and the later, the study of *active scalars* that modify the flow while been transported. The prototypical equation to model these type of transport for continuous media is an *advection-diffusion* equation of the form,

$$\partial_t C + \mathbf{v} \cdot \nabla C = D\nabla^2 C, \tag{1.10}$$

where C is the transported scalar, D the diffusivity and $\mathbf{v}$ the velocity field. In the *passive* transport problem $\mathbf{v}$ is assumed independent of C while in the *active*, they are related by a *dynamical self-consistency constraint* of the form $\mathcal{F}(C, \mathbf{v}) = 0$, involving an integral and/or differential operator.

1.1.2 The original physical problem

The original problem from which systems (1.1) and (1.5) are reduced, corresponds to two different physical problems of active transport: the single wave model from plasma physics and a particular case of the vorticity defect problem from fluid mechanics. The active transport problem is the following,

$$\partial_t f + u\partial_x f + (\partial_x \phi)\partial_u f = 0\,, \tag{1.11}$$

with a dynamical self-consistency constraint of a Poisson problem,

$$-\frac{\partial^2}{\partial x^2}\phi(x,t) = \int_{-\infty}^{\infty} f(x,u,t)du\,, \tag{1.12}$$

that can be rewritten in Fourier space as,

$$k^2\tilde{\phi}(k,t) = \int_{-\infty}^{\infty} \tilde{f}(k,u,t)du\,, \tag{1.13}$$

where the tilde correspond to Fourier transform.

The physical model of interest studies the growth of a localized[1] small[2] perturbation of $f_{in} = F_0 + \delta F$ immersed in a $f_{out} = F_0$ constant. For physical reasons and actual experimental observations, the hamiltonian function

[1] For $u \in (u_0 - \varepsilon, u_0 + \varepsilon)$.
[2] $\delta F = O(\varepsilon)$

relevant for this model only considers one (principal) mode,

$$\psi = -\frac{1}{2}u^2 + \phi = -\frac{1}{2}u^2 + a(t)\, e^{ix} + a^*(t)e^{-ix}\,, \tag{1.14}$$

where $\phi = 0$ in the *outer region*. The known relations between the hamiltonian function (streamfunction) and the original variables: $\mathbf{v} = (u, \partial_x\phi) = \hat{\mathbf{z}} \times \nabla\psi$ and $f = \nabla^2\psi$ let a matched asymptotic expansion between a *inner* ($\phi = O(1)$) and *outer* ($\phi = O(\varepsilon^2)$) regions to be computed, leading to a reduced equation for the dynamical constraint,

$$\frac{da}{dt} - iUa = \frac{i}{2\pi}\int_{-\infty}^{\infty}\int_{0}^{2\pi} e^{-ix} f(x,u,t)dxdu\,, \tag{1.15}$$

where U is a given real constant (see Ref. [7]). The system formed by the equations (1.11), (1.14) and (1.15) is often referred as the *single wave model* (SWM).

Although it is not of capital importance to understand mathematical manipulations done over the equations of the SWM for the rest of this work, a more concise of the physical meaning of the quantities (t, x, u, f, ϕ) may help to understand better the results found or at least picture them in a physical frame.

In the original plasma physics problem from which the SWM was proposed in the 70's in Ref. [5], f corresponds to the perturbation δF_* over electron probability distribution F_* of a (one dimensional) beam interacting with a cold plasma, (x, u) corresponded to the relative position and velocity of the electrons and ϕ to the electrostatic potential. The SWM in plasma physics is a phenomenological model to describe the observed behavior of a marginally stable plasma that responds in a *linear*[3] manner away from the linear regimen of the system.

In Refs. [6, 7] using a critical layer approximation (matched asymptotic expansions), it was possible to give a derivation of the SWM from a Vlasov-Possion system (see figure 1.1). For this derivation to work it was critical to assume a scaling between the growth rate λ of the electrical potential ϕ and the distance ε from the localized instability boundary. The *right* scaling, corresponded to the *trapping scaling* $\phi \sim \varepsilon^2$, which is supported by experimental and numerical studies of the beam-plasma instability [15, 16, 17].

[3]For the dispersion relation of f in the plasma interaction, not an ODE *linear* response.

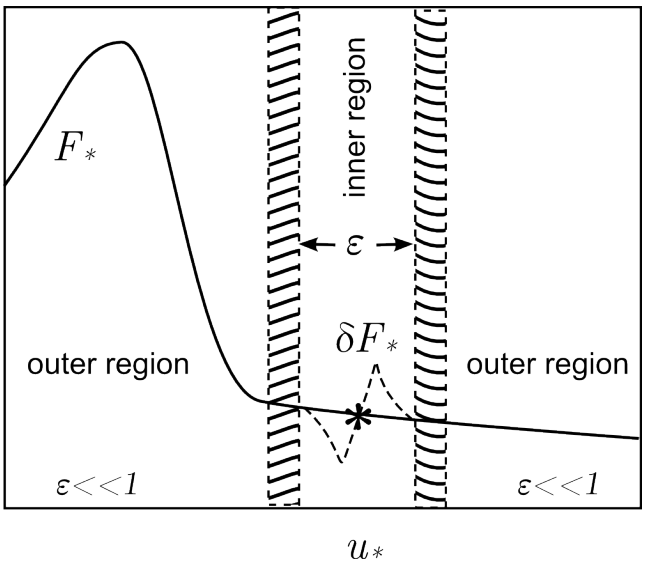

Figure 1.1: Sketch of a localized perturbation δF_* on a marginally stable equilibrium F_*.

The fluid mechanics interpretation of the model was first introduced in Ref. [1], as the *vorticity defect model* (see figure 1.2). In this approach, f is labeled ζ and corresponds to the vorticity of a two-dimensional inviscid, incompressible fluid, (x, u) now correspond to the cartesian coordinates (x, y) of the fluid, and ϕ corresponds to a perturbation in the streamfunction ψ of a plane Couette flow. Also in this scheme, Eq. (1.11) corresponds to taking the curl of the Navier-Stokes equation, while Eq. (1.13) corresponds to the dynamical constraint or self-consistency condition $\zeta = \mathbf{z}\cdot\nabla\times\mathbf{v}$, the definition of the vorticity scalar, rewritten in terms of ψ. In this interpretation, the SWM describes in the weak instability regime the evolution of a localized small perturbation on the constant vorticity field.

1.2 Symmetries and conserved quantities

The system (1.1) inherits several properties from the continuous model (1.3), some of them can be written in a shorter form for the implicit version (1.7) and for that reason they are presented for the later map.

First it is interesting to find that there exist a symplectic structure for

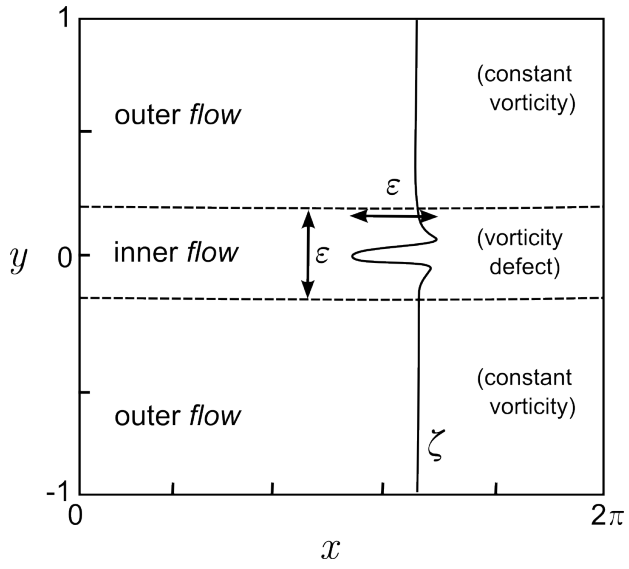

Figure 1.2: Sketch of a localized vorticity perturbation or "defect", ζ, embedded in a constant vorticity shear flow.

the map (1.7) due the discretization procedure that was used, see Ref. [2]. Introducing the canonical conjugated variables: $\mathbf{q} = (x_1, ..., x_N, \theta)$ and $\mathbf{p} = (p_1, ..., p_N, J)$, the map $(\mathbf{q}, \mathbf{p})^n \to (\mathbf{q}, \mathbf{p})^{n+1}$ can be obtained from a generating function, $S = S(\mathbf{q}^n, \mathbf{p}^{n+1})$ according to,

$$\mathbf{q}^{n+1} = \frac{\partial S}{\partial \mathbf{p}^{n+1}}\,, \qquad \mathbf{p}^n = \frac{\partial S}{\partial \mathbf{q}^n}\,, \tag{1.16}$$

where S can be written as,

$$S = S_p + S_f + S_i \tag{1.17}$$

where S_p determines the evolution of the N-oscillators in absence of the mean field,

$$S_p = \sum_{k=1}^{N} \left[x_k^n p_k^{n+1} + \frac{\tau}{2\Gamma_k} (p_k^{n+1})^2 \right]\,, \tag{1.18}$$

S_f determines the uncoupled evolution of the field,

$$S_f = \theta^n J^{n+1} - U\tau J^{n+1}\,, \tag{1.19}$$

S_i determines the interaction of the mean-field with the particles,

$$S_i = -2\tau \sum_{k=1}^{N} \sqrt{J^{n+1}} \Gamma_k \cos(x_k^n - \theta^n) \,. \tag{1.20}$$

The map (1.7) has several symmetries and invariants. A first symmetry corresponds to the fact that for any δ the map is invariant under the transformation,

$$(x_1, x_2, ..., x_N, \theta) \to (x_1 + \delta, x_2 + \delta, ..., x_N + \delta, \theta + \delta) \,. \tag{1.21}$$

Which is a consequence of the definition of ψ in the *single wave model*,

$$\begin{aligned} \psi &= -\frac{y^2}{2} + a(t)e^{ix} + a^*(t)e^{-ix} \\ &= -\frac{y^2}{2} + \sqrt{J(t)} \cos(x - \theta(t)) \,, \end{aligned}$$

where it is always possible to redefine the position of the origin on x and the phase.

Another relevant symmetry of the map (1.7), in the case with $U = 0$ is,

$$(x_k, p_k, \theta, \Gamma_k) \to (-x_k, -p_k, -\theta, -\Gamma_k) \,. \tag{1.22}$$

This symmetry has been used in the continuous system [4] to describe symmetric configurations that represent a dipole, a pair of particles with opposite charge ($\Gamma_2 = -\Gamma_1$), affected by a mean field. Because of this particular interpretation, a configuration of the system will be called *symmetric* if its invariant under the transformation Eq. (1.22). It is straightforward to show that the symmetric states are preserved by the map.

In an analog way to the continuous system's momentum and total energy, it is possible to define two quantities,

$$\mathcal{P}^n = \sum_{k=1}^{N} p_k^n + J^n \,, \tag{1.23}$$

$$\mathcal{H}^n = \sum_{k=1}^{N} \left[\frac{(p_k^n)^2}{2\Gamma_k} - 2\Gamma_k \sqrt{J^n} \cos(x_k^n - \theta^n) \right] - UJ^n \,, \tag{1.24}$$

and show that,

$$\mathcal{P}^{n+1} = \mathcal{P}^n \,, \tag{1.25}$$

$$\mathcal{H}^{n+1} = \mathcal{H}^n + O(\Gamma\tau^2) + O(\tau^3) \,. \tag{1.26}$$

As it is usually the case, the energy conservation breaks down even if the discretization is symplectic. However, the conservation of linear momentum holds.

1.2.1 An explicit symplectic standard mean-field map

The map (1.1) is not symplectic and the simplest way of showing this is by computing the determinant of the Jacobian,

$$\Delta = |D\mathcal{T}| = \frac{\kappa^n}{\kappa^{n+1}} \neq 1 \,. \tag{1.27}$$

On each iteration, the volume of the phase space will vary.

A way to fix this, at the expense of having a more cumbersome expression, is to solve (1.7d) for $\sqrt{J^{n+1}}$, finding,

$$\sqrt{J^{n+1}} = A + \sqrt{A^2 + J^n} \tag{1.28}$$

and,

$$J^{n+1} = J^n + 2A^2 + 2A\sqrt{A^2 + J^n} \,, \tag{1.29}$$

where $A = \tau \mathrm{Im}(\Xi^n)$ and Ξ^n is defined as,

$$\Xi^n = \sum_{l=1}^{N} \Gamma_l \, e^{i(x_l^n - \theta^n)} \,. \tag{1.30}$$

A sympliectic version of the single wave map model is,

$$x_k^{n+1} = x_k^n + \frac{\tau}{\Gamma_k} p_k^{n+1} \,, \tag{1.31a}$$

$$p_k^{n+1} = p_k^n - 2\tau\Gamma_k (A + \sqrt{A^2 + J^n}) \sin(x_k^n - \theta^n) \,, \tag{1.31b}$$

$$\theta^{n+1} = \theta^n - U\tau - \frac{\tau \mathrm{Re}(\Xi^n)}{A + \sqrt{A^2 + J^n}} \,, \tag{1.31c}$$

$$J^{n+1} = J^n + 2A^2 + 2A\sqrt{A^2 + J^n} \,. \tag{1.31d}$$

The Jacobian matrix of this map is,

$$(D\mathsf{T})^{-1}\,\mathbb{J}\,D\mathsf{T} = \mathbb{J}\,, \tag{1.32}$$

where T is the map in (1.31) written (ordered) in Darboux coordinates: $(x_1, .., , x_N, \theta,\, p_1, ..., p_n, J)$, and $\mathbb{J}$ is the usual symplectic matrix,

$$\mathbb{J} = \begin{pmatrix} 0 & \mathbb{I} \\ -\mathbb{I} & 0 \end{pmatrix}. \tag{1.33}$$

However, for actual computation of the map, (1.1) and (1.31) are equivalent. Constants aside, the evolution equation for J^{n+1} in (1.31) is just the square of the evolution of equation of κ^{n+1} from (1.1).

1.3 Coherent structures and transport

Despite its relative mathematical simplicity, the SWM is able to capture important dynamics of the full Navier-Stokes equation. In particular, as Fig. 1.4 from Ref. [1] shows, the SWM exhibit the standard Kelvin-Helmholtz instability leading to the formation of the familiar cats' eyes vorticity structure found in unstable shear flows. The result in Fig. 1.4 was obtained from the direct numerical integration of Eqs. (1.11) and (1.15) with $D = 0.001$, $U = -1$, and initial condition:

$$\zeta(x, y, t = 0) = e^{-y^2/2}\,[1 - 0.2\,y\,\cos(x)]. \tag{1.34}$$

The evolution of the self-consistent map in Eqs. (1.1) has been studied for different initial conditions. Figures 1.4 and 1.5 show the results of a simulation of $N = 13,440$ coupled maps with initial conditions $\{(x_k^0, y_k^0)\}$ uniformly distributed on the region $[0, 2\pi] \times [-0.3, 0.3]$ in the (x, y) plane and $\gamma_k = 3 \times 10^{-6}$ for $k = 1, \ldots N$. The initial condition of the mean-field was $\kappa^0 = 10^{-4}$ and $\theta^0 = 0$, and we assumed $\Omega = 0$.

The simulations show that the self-consistent map reproduces the coherent structures observed in the single wave model (Figure 1.3). In particular for this kind of initial conditions with the particles (x_k, y_k) originally clumped together around $y = 0$, it was observed a big portion of particles would stay trapped, clustered in the center of the cat's eye while particles closer to the instantaneous separatrix present a *strong* dispersion.

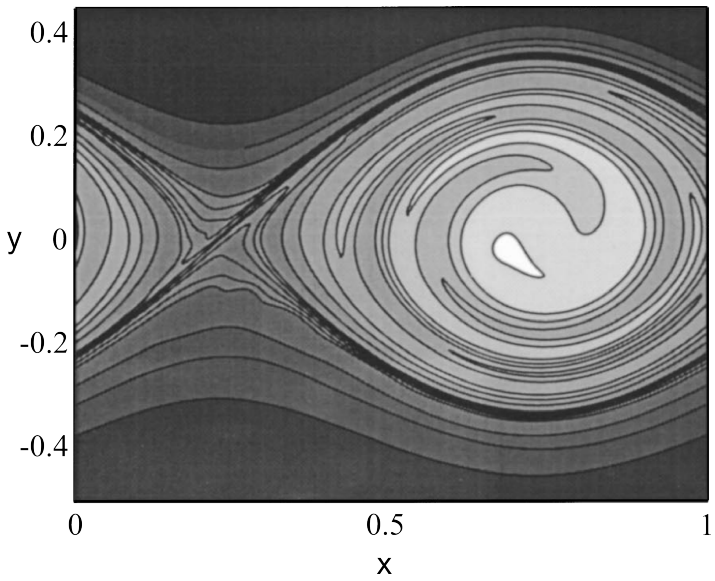

Figure 1.3: Cat's eye formation and vorticity mixing in the single wave model, Eqs. (1.11), (1.14) and (1.15), with initial conditions in Eq. (1.34). The gray scale denotes the vorticity values with white corresponding to $\zeta = 1$ and dark gray corresponding to $\zeta = 0$ [After Ref. [1]].

The evolution of the mean field is represented by the variables (κ^n, θ^n), which are shown in Fig. 1.5. The behavior of κ^n starts with a fast growth until it achieves a maximum value, after that, the κ^n oscillates around a mean value $\bar{\kappa}$ and the amplitude of oscillation is bounded by $\Delta\,\kappa$. A similar situation is observed with the behavior of $\vartheta^{n+1} = \theta^{n+1} - \theta^n$.

Different types of dynamics, including cases in which the magnitude κ^n of mean field decays to zero or saturates at a constant fixed value can be found in Refs. [2, 3] for similar self-consistent maps.

A particular observation from Fig. 1.5, is that κ^n does not reach $\kappa_G = 0.971635406$, the critical value for the *standard map*. Although it is reviewed in the next chapter, the main implication of this remark is that if κ^n were constant, then for any $\kappa < \kappa_G$ there can not be global diffusion (i.e. unbounded evolution on y_k of any initial condition) because of the existence of invariant circles, topological barriers in the phase space, see Ref. [18].

The existence or non-existence of global diffusion in the self-consistent map depends in a nontrivial way on the dynamics of κ^n. On a more fundamental level, the observed rapid growth of κ^n for a given initial condition

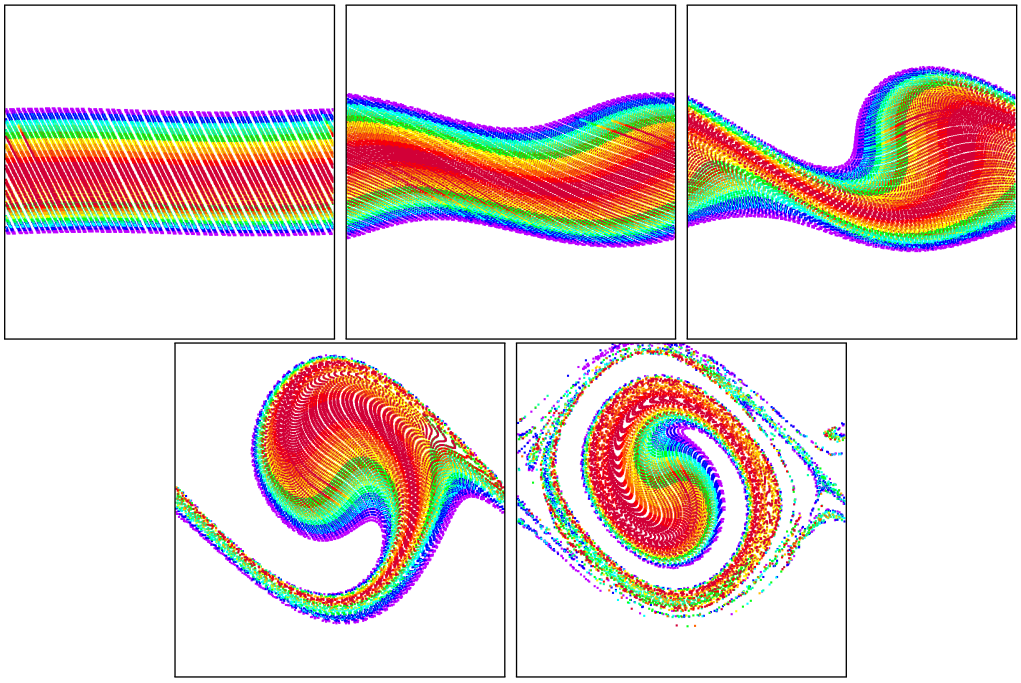

Figure 1.4: Time evolution of the self-consistent map in Eq. (1.1) with $N = 13440$ initial conditions uniformly distributed in $[0, 2\pi] \times [-0.3, 0.3]$ with $\kappa^0 = 10^{-4}$, $\gamma_k = 3 \times 10^{-6}$, $\theta^0 = 0$ and $\Omega = 0$. The frames show the instantaneous coordinates of the N initial conditions, at $n = 2, 6, 12, 20$ and 66 in the region $[0, 2\pi] \times [-0.8, 0.8]$ of the (x, y) plane. The colors label the y-coordinate of the initial condition, with red denoting y_k^0 close to $y = 0$ and blue further away.

is closely related to the linear stability properties of the corresponding initial condition in the single wave model. In particular, Ref. [6] presents the necessary and sufficient conditions for the linear stability (i.e., exponential growth of the mean field amplitude) of a given initial condition in the context of the continuous, $N \to \infty$ limit. These ideas might help understand the conditions for the growth of κ^n. However, one must be careful before drawing conclusions as the self-consistent map model discussed here is obtained by simplifying drastically the single wave model by approximating the continuous limit when $N \to \infty$.

Alternatively, the evolution pictured in Fig. 1.4 and 1.5 can be pictured together as in Fig. 1.6, where the *instantaneous* hyperbolic invariant stable

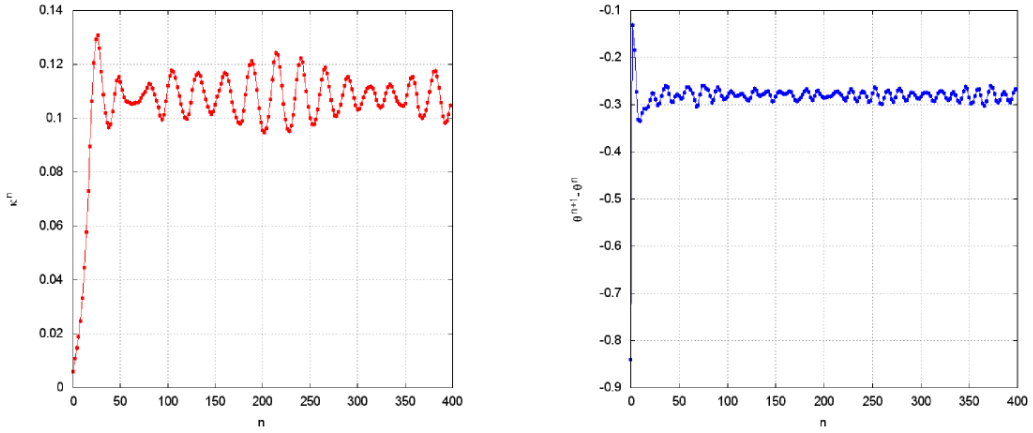

(a) (b)

Figure 1.5: Time evolution of the mean-field variables in the self-consistent map in Eq. (1.1) with initial conditions taken in a uniform grid in $[0, 2\pi] \times [-0.3, 0.3]$ with $N = 13440$, $\kappa^0 = 10^{-4}$, $\gamma_k = 3 \times 10^{-6}$, $\theta^0 = 0$ and $\Omega = 0$. κ^n is shown in (a) and $\vartheta^{n+1} = \theta^{n+1} - \theta^n$ in (b).

and unstable manifolds are drawn on top of the projected phase space coordinates (x_k, y_k). Here *instantaneous* means that the hyperbolic invariant manifolds drawn correspond to the fixed hyperbolic point in standard map computed with perturbation parameter equal to the value of κ^n and then displaced on x by the value of θ^n.

Perhaps contrary to the intuition, it was observed in these simulations that map (1.1) shows global diffusion even when $\bar{\kappa} < \kappa_G$. It is also worth mentioning that when the *instantaneous* coordinates (x_k^n, y_k^n) of each degree-of-freedom are plotted on the same plane like in Fig. 1.4, the amplitude and shape of the cat's eye structure is in good agreement with the invariant manifolds emanating from the hyperbolic fixed point of the standard map calculated with a perturbation parameter equal to the *instantaneous* value of κ^{n+1}. This gives rise to the following question: What is the mechanism that allows the diffusion across the invariant curves on the self-consistent map? In Figure 1.6, it can be observed the formation, for relatively small times, of the macro particle coherent structure trapped around the elliptic fixed point, and at the same time can be seen the formation of the heteroclinic tangle responsible for the high mixing region around the separatrix of the cat's eye.

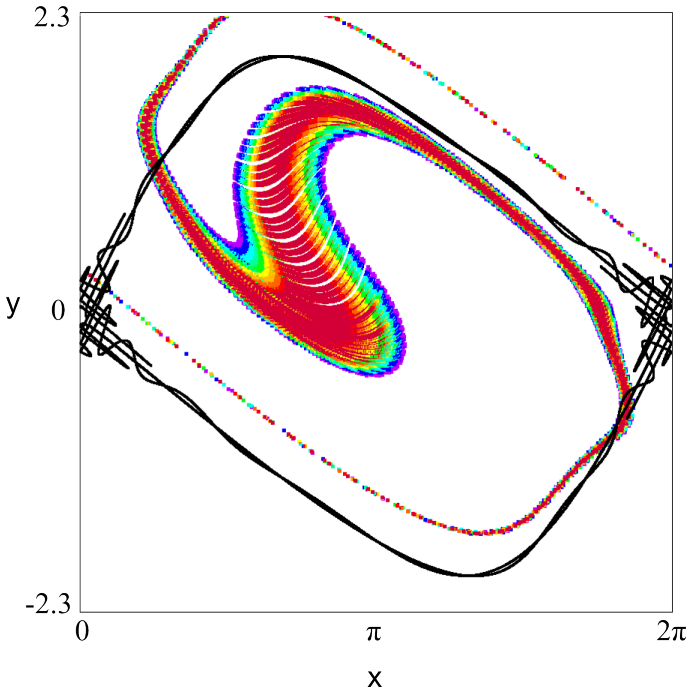

Figure 1.6: Plot of the projected phase space coordinates (x_i, y_i) on the (x, y)-plane of a simulation of the self-consistent map in Eq. (1.1) in the oscillatory κ regimen. Also shown in black is the heteroclinic tangle generated by the unstable invariant manifold of the hyperbolic fixed point of the standard map with perturbation parameter equal to κ^n. The initial conditions are the same as those in Fig. 1.4, except that to enhance the heteroclinic tangle the higher values $\kappa^0 = 0.005$ and $\gamma = 0.0005$ were used.

1.4 Low N cases

An approach that mimics the work from Refs. [1, 4, 19] to explain the apparent existence of coherent structures in a high dimensional dynamical system such as map (1.1) consists in the study of lower dimensional cases of the system that reduces to *robust* integrable systems. If these integrable cases are robust enough (as in Ref. [4]) then sets of particles with initial conditions (x_j^0, y_j^0) clustered around the stable regions (*macroparticles*) may persist in a coherent fashion. Again, following these two references, the easiest and simplest reduced cases of self-consistent map to study correspond to the $N = 1$ and $N = 2$. To simplify the algebra and facilitate the comparison

with results from Refs. [1] and [4], the implicit version of the self-consistent map, Eqs. (1.7), was chosen. The use the explicit symplectic version from Eqs. (1.31) yield similar results.

1.4.1 $N = 1$ Single wave map

For $N = 1$ the dimension of the map is $D = 4$,

$$x^{n+1} = x^n + \frac{\tau}{\Gamma}\, p^{n+1} \tag{1.35a}$$

$$p^{n+1} = p^n - 2\tau\Gamma\sqrt{J^{n+1}}\, \sin\left(x^n - \theta^n\right) \tag{1.35b}$$

$$\theta^{n+1} = \theta^n - \tau U - \frac{\tau\Gamma}{\sqrt{J^{n+1}}}\, \cos\left(x^n - \theta^n\right) \tag{1.35c}$$

$$J^{n+1} = J^n + 2\tau\Gamma\sqrt{J^{n+1}}\, \sin\left(x^n - \theta^n\right)\,. \tag{1.35d}$$

Introducing the symplectic change of coordinates (see Sec. 2.2.1) given by,

$$\phi = x - \theta\,, \qquad \psi = x + \theta \tag{1.36}$$

$$u = \frac{p - J}{2}\,, \qquad w = \frac{p + J}{2}\,, \tag{1.37}$$

the system transforms into:

$$\phi^{n+1} = \phi^n + \frac{\tau}{\Gamma} u^{n+1} + C^+ + \frac{\tau\Gamma}{\sqrt{w^0 - u^{n+1}}}\, \cos\left(\phi^n\right)\,, \tag{1.38a}$$

$$u^{n+1} = u^n - 2\tau\Gamma\sqrt{w^0 - u^{n+1}}\, \sin\left(\phi^n\right)\,, \tag{1.38b}$$

$$\psi^{n+1} = \psi^n + \frac{\tau}{\Gamma}\, u^{n+1} + C^- - \frac{\tau\Gamma}{\sqrt{w^0 - u^{n+1}}}\, \cos\left(\phi^n\right)\,, \tag{1.38c}$$

$$w^{n+1} = w^n\,. \tag{1.38d}$$

where $C^{\pm} = \tau\left(\frac{w^0}{\Gamma} \pm U\right)$. The Eqs. (1.38a)-(1.38b) constitute a 2-D map that preserves area, while (1.38c) is just a function of the map: $\psi^{n+1} = \psi^n + \mathcal{F}(\phi^n, u^{n+1})$ and w^n is a constant of motion (half of the total momentum $\mathcal{P}$).

And it is possible to write a generating function for the 2-D map (1.38a)-(1.38b):

$$S(\phi^n, u^{n+1}) = \left(\phi^n + C^+\right) u^{n+1} + \frac{\tau}{2\Gamma}\left(u^{n+1}\right)^2 - 2\tau\Gamma\sqrt{w^0 - u^{n+1}}\, \cos\left(\phi^n\right). \tag{1.39}$$

In Fig. 1.7 is possible to appreciate the phase space of the 2-D map (1.38a)-(1.38b) for different values of the parameters, while in Fig. 1.8 shows the 3-D dynamics of map (1.38).

Period one periodic orbits

A natural macroparticle state that intuitively should approximate the behavior observed in Fig. 1.3 and 1.4, should be around the linear elliptic stable period one periodic orbit. And because of this is worth assessing when it turns unstable. The period one periodic orbits from the 2-D map (1.38a)-(1.38b) are given by

$$\phi_* = m\pi, \qquad m = 0, 1\,, \tag{1.40}$$

and roots of,

$$\frac{\tau}{\Gamma}u_* + C^+ + \frac{(-1)^m\tau\Gamma}{\sqrt{w^0 - u_*}} = 2\ell\pi\,, \qquad \ell \in \mathbb{Z}\,, \tag{1.41}$$

which may have zero, one or two roots for each resonance ℓ depending on the values of the parameters: τ, Γ, C^+ and w^0, see Fig. 1.9. For $\phi^* = 0$ there is always one root, however for $\phi^* = \pi$ there is a bifurcation. Defining,

$$w_{crit} = \left(\frac{9}{32}\Gamma^4\right)^{1/3} - \frac{\Gamma}{2}U\,, \tag{1.42}$$

there will be two period one orbits if $w > w_{crit}$, none if $w < w_{crit}$ and only one if $w = w_{crit}$, for the $\ell = 0$ resonance[4].

The linear stability of the period one orbits is determined by Greene's residue (see Sec. 2.6), which in this case is,

$$R = \tau^2\sqrt{w^0 - u_*}\left((-1)^m + \frac{\Gamma^2}{2(w^0 - u_*)^{3/2}}\right)\,. \tag{1.43}$$

where

$$\begin{aligned} 0 < R < 1 \qquad &\rightarrow \qquad \text{stable} \\ R < 0 \quad \text{or} \quad R > 1 \qquad &\rightarrow \qquad \text{unstable} \end{aligned}$$

With this criteria, the orbit for $\phi_* = 0$ is always stable for small values of

[4]Here C^+ has been replaced for its definition in term of w and U to avoid inconsistencies.

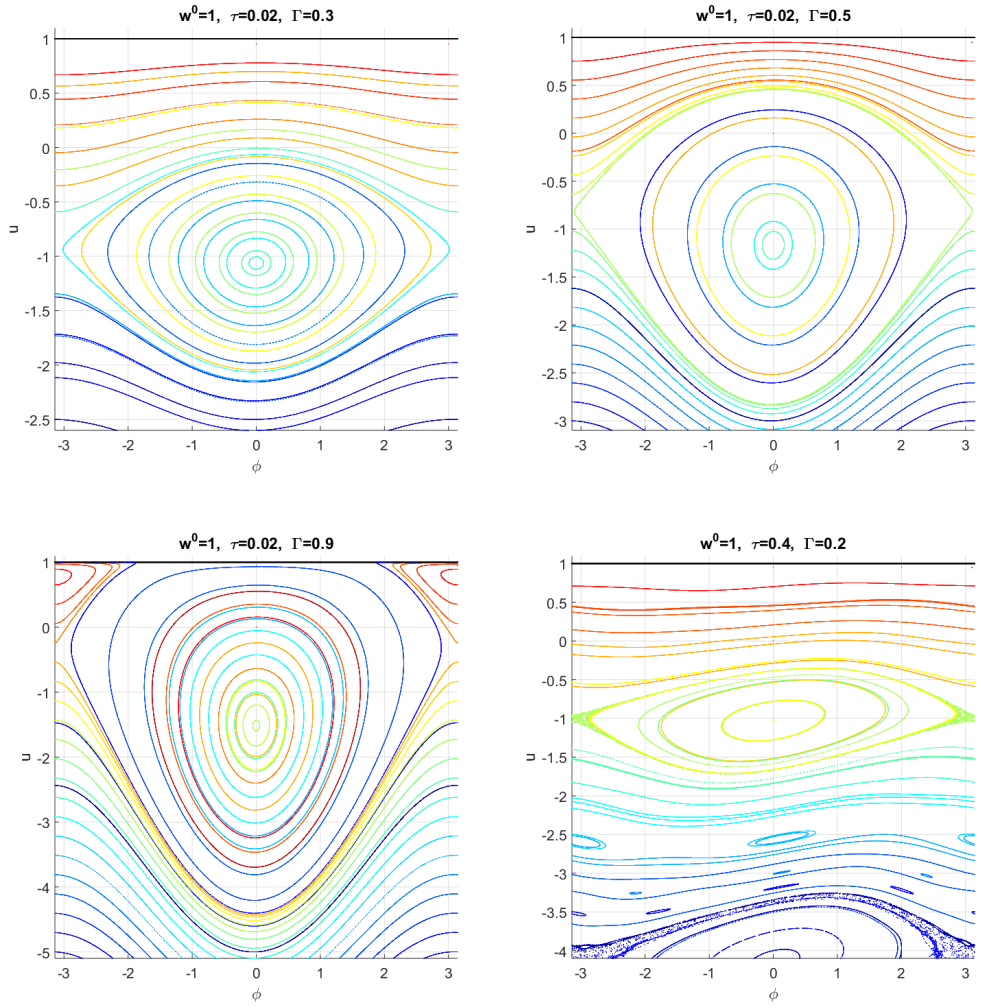

Figure 1.7: Samples of the phase space for the 2-D map (ϕ, u) from (1.38a)-(1.38b) for different values of w^0, τ and Γ, with $U = 0$.

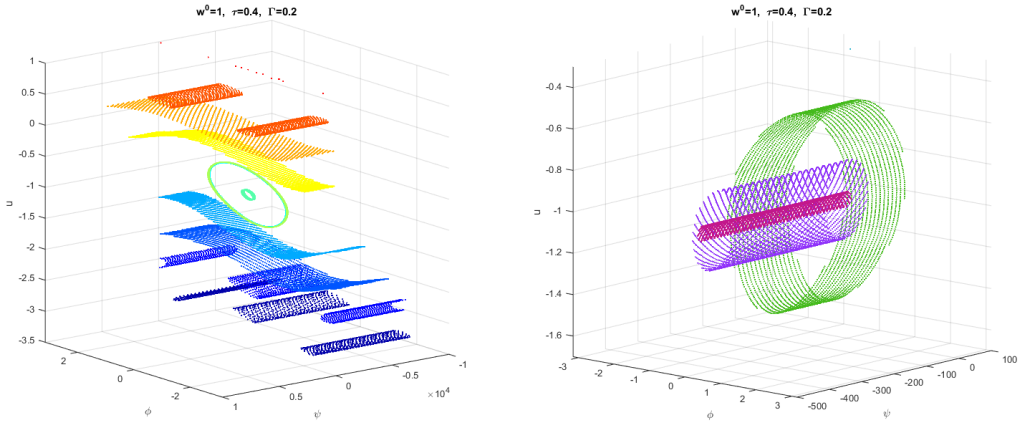

Figure 1.8: *Phase space* for the 3-D map (ϕ, ψ, u) from (1.38a)-(1.38c) and a detail on the *elliptic* regime. Note that the orientation is not the same; it was changed for appreciation purposes.

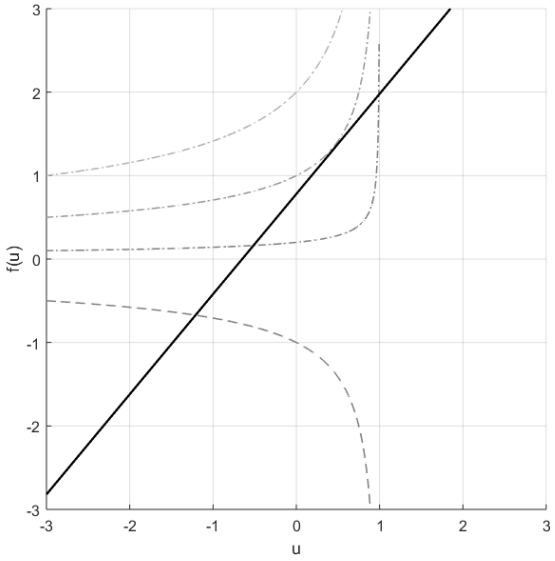

Figure 1.9: Possible roots in Eq. 1.41 in case $\ell = 0$, where the intersection between the solid line and the dashed curve always happens while the dot-dashed branch may have zero, one or two intersections.

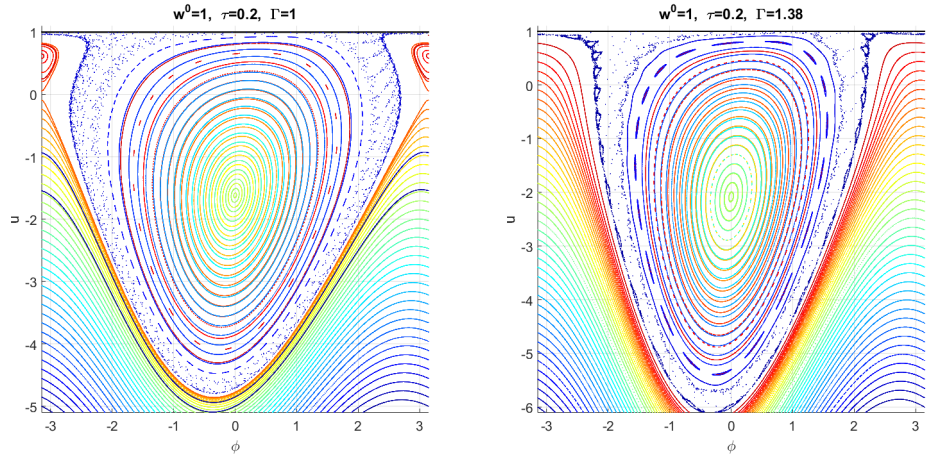

Figure 1.10: Phase space of the 2-D map (ϕ, u) from (1.38a)-(1.38b) for values of Γ around the bifurcation of the $\ell = 0$ resonance (with $U = 0$). Note that $\sqrt[4]{32/9} \sim 1.373178...$

τ and Γ. While for $\phi_* = \pi$, $R = 0$ for the critical value w_{crit} and $R = \pm\epsilon$ for the $w > w_{crit}$, in other words one point is stable while the other one is unstable. This can be appreciated from the third panel in Fig. 1.7 and in Fig. 1.10.

It should be noted that as $|\ell|$ increase (and so $\sqrt{w - u_*}$) the linear stability of the fixed point given by the residue in Eq. (1.43) will tend to make the fixed points unstable. Which is consistent with the *appreciation* that the map (1.38a)-(1.38b) should behave as a standard map with high perturbation parameter for high values of $-u$. This means that the map turns more "stochastic" as u decreases. This can be appreciated from the fourth panel in Fig. 1.7.

Macroparticle simulations

Inspired by Refs. [1] and [4], it may be physically relevant to find if a coherent structure that approximates the stable solutions for $N = 1$ can persist in the context of the single wave map model (1.1). The coherent structure that seems appropriate for the symmetry, is a set of initial conditions $(x_1^0, y_1^0, ...x_N^0, y_N^0, \kappa^0, \theta^0)$ *clustered* around a $(x^0, y^0, \kappa^0, \theta^0)$ equivalent to a stable fixed point of the 2-D map (1.38a)-(1.38b). The specific set of initial

conditions and parameters used, referred as *macroparticle*, consist in N pairs $\{(x_i^0, y_i^0)\}_{i\in[1,N]}$ with a 2-D Gaussian distribution,

$$f(x, y; x_0, y_0, \sigma_1, \sigma_2) = \frac{1}{2\pi\sigma_1\sigma_2} \exp\left(-\frac{1}{2}\left(\frac{x - x_0}{\sigma_1}\right)^2 - \frac{1}{2}\left(\frac{y - y_0}{\sigma_2}\right)^2\right), \tag{1.44}$$

and

$$\kappa^0 = 2\tau^2\sqrt{w^0 - u^0}\,, \qquad \theta^0 = 0\,, \tag{1.45}$$

with

$$\gamma_k = 2\tau^3\Gamma/N \qquad x_0 = \phi^0 \qquad y_0 = \frac{\tau}{\Gamma}\left(u^0 + w^0\right). \tag{1.46}$$

Where τ and Γ are parameters from the 2-D map (1.38a)-(1.38b) and (ϕ^0, u^0) correspond to the coordinates of a period 1 (elliptic) fixed point.

The election of γ_k in (1.46) guaranties that the total intensity (vorticity) Γ and initial amplitude of mean field κ (J) are the same in their respective units for maps (1.1) and (1.38a)-(1.38b). In Ref. [4] the parameters between the different equivalent systems were chosen in a way that the total energy was the same, this could not be translated entirely to the present case since both maps do not preserve energy and may change it at different rates.

With the scheme in (1.44)-(1.46) is possible to translate a given set of values of the parameters (w^0, τ, Γ) and fixed point (ϕ^0, u^0) from map (1.38a)-(1.38b) to initial conditions and parameters for (1.1). However this may not guaranty that the initial state persist in a coherent fashion. There are two main scenarios which may lead to deformation or destruction of the macroparticle state: an off centered initial distribution and big ratio between τ and Γ.

To illustrate them, we consider the map (1.38a)-(1.38b) for values of the parameters $w^0 = 1/\sqrt{2} \sim 0.707$, $\tau = \Gamma = 0.2$ and the first elliptic point $(\phi^0, u^0) = (0, -1/\sqrt{2})$, see Fig. 1.11. This election of values for the parameters yield thorough (1.44)-(1.46) a macroparticle centered in the origin $(x_0, y_0) = (0, 0)$ that after the iteration seems stable, as it can be appreciated in Figs. 1.12 and 1.13. However, when the macroparticle is not centered in the origin, it tends to be deformed even for small values of (σ_1, σ_2), as it can be seen in Fig. 1.14.

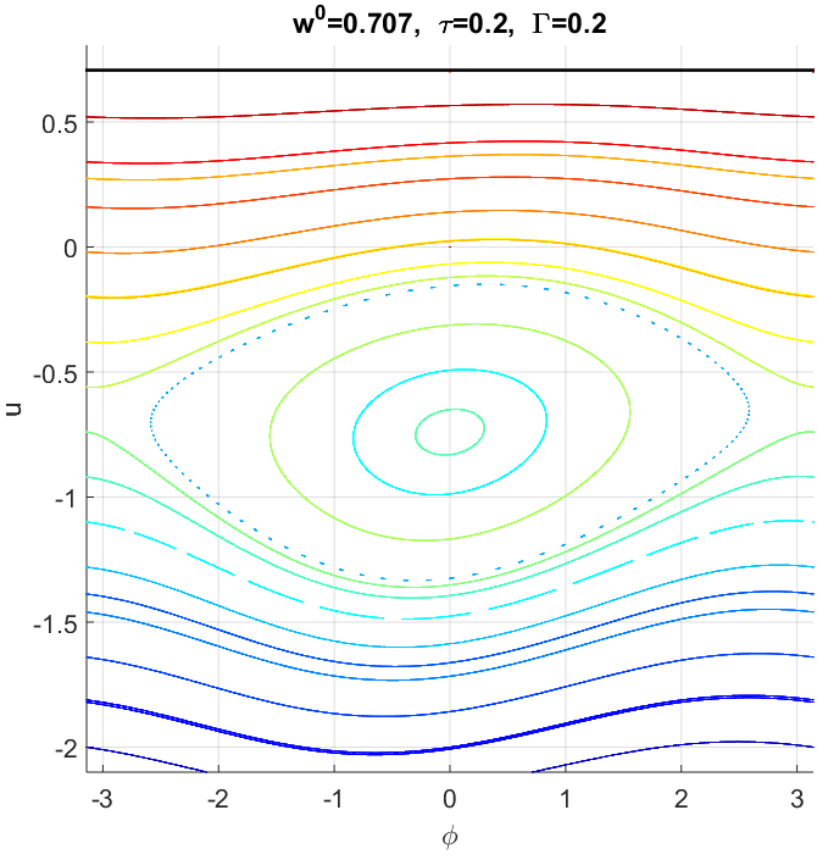

Figure 1.11: Phase space for the 2-D map (1.38a)-(1.38b) with values of the parameters (w, τ, Γ).

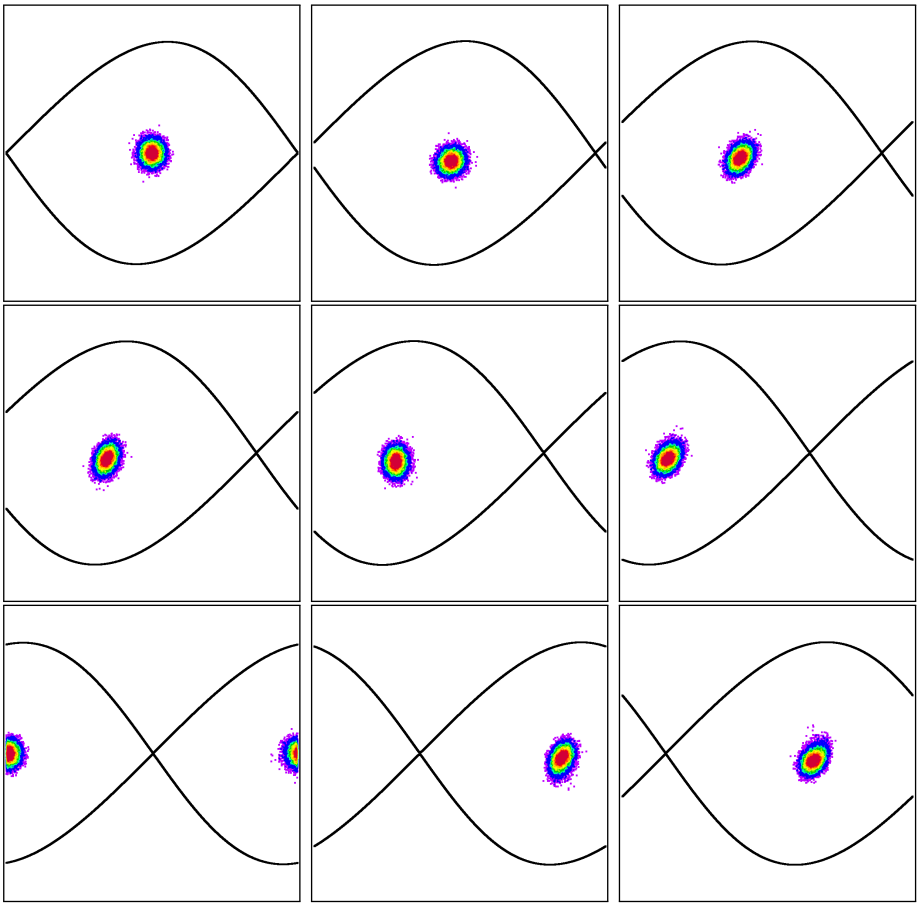

Figure 1.12: Evolution of the self-consistent map in Eq. (1.1) for macroparticle initial conditions (1.44) with $N = 13440$, $\kappa^0 = 0.113136$, $\gamma_k = 1.0714 \times 10^{-6}$, $\theta^0 = \Omega = x_0 = y_0 = 0$, $\sigma_1 = 0.444$ and $\sigma_2 = 0.2$. The frames show the instantaneous coordinates of the N initial conditions , at $n = 0, 8, 24, 32, 48, 80, 104, 138$ and 192 in the region $[-\pi, \pi] \times [-0.9, 0.9]$ of the (x, y) plane. Superposed on each frame it is plotted the instantaneous stable and unstable invariant manifolds of the hyperbolic fixed point. The colors represent the density of (x, y) points, with purple low density and red high density.

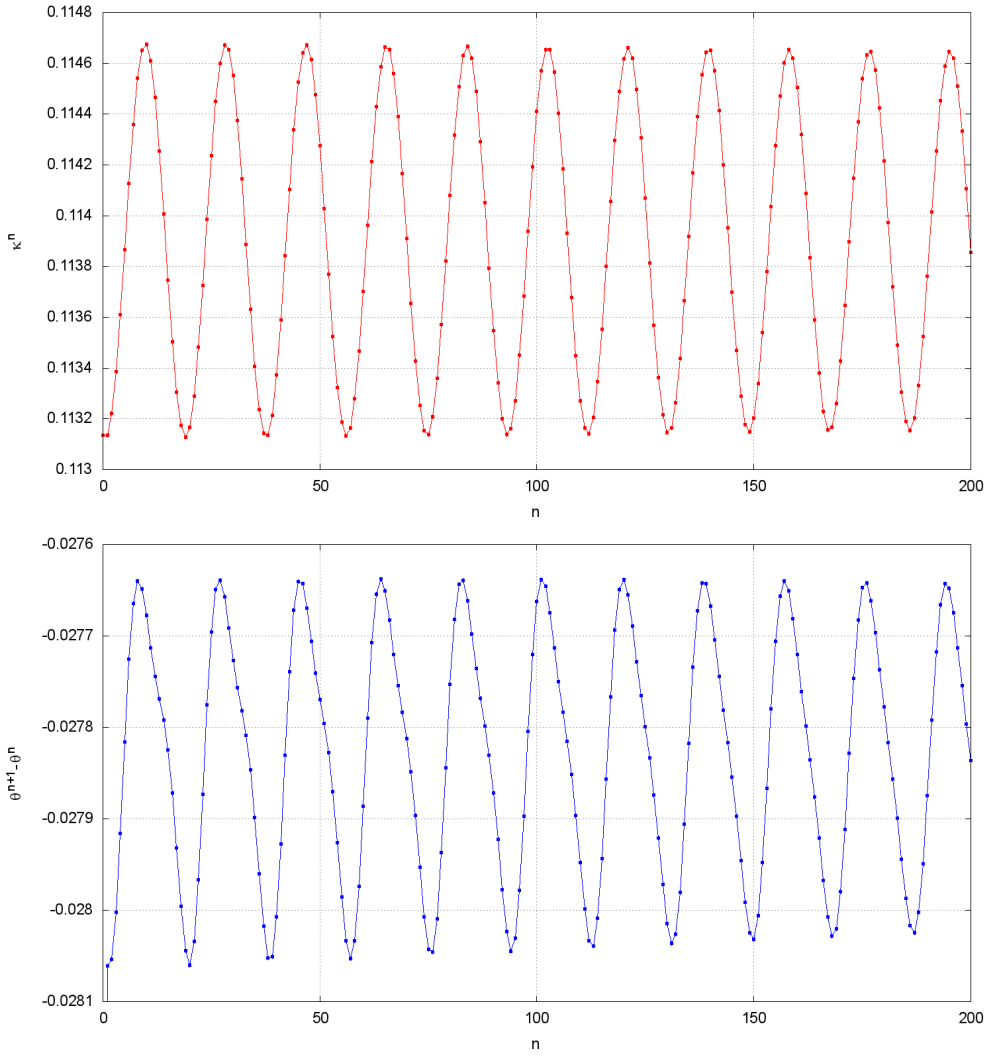

Figure 1.13: Evolution of the mean field (κ, θ) corresponding to Fig. 1.12 for the first 200 iterations.

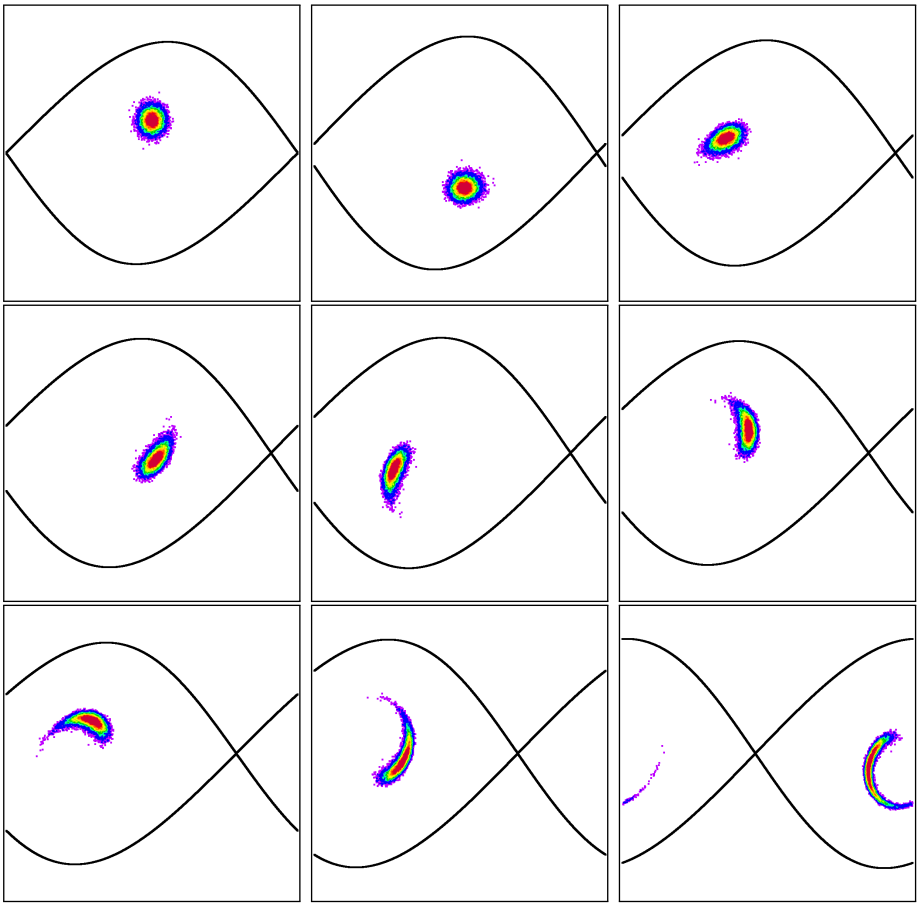

Figure 1.14: Evolution of the self-consistent map in Eq. (1.1) for almost identical macroparticle initial conditions to those in Fig. 1.12, only changing $y_0 = 0.1$. The frames show the instantaneous coordinates of the N initial conditions , at $n = 0, 8, 12, 16, 20, 28, 40$ and 72 in the region $[-\pi, \pi] \times [-0.9, 0.9]$ of the (x, y) plane.

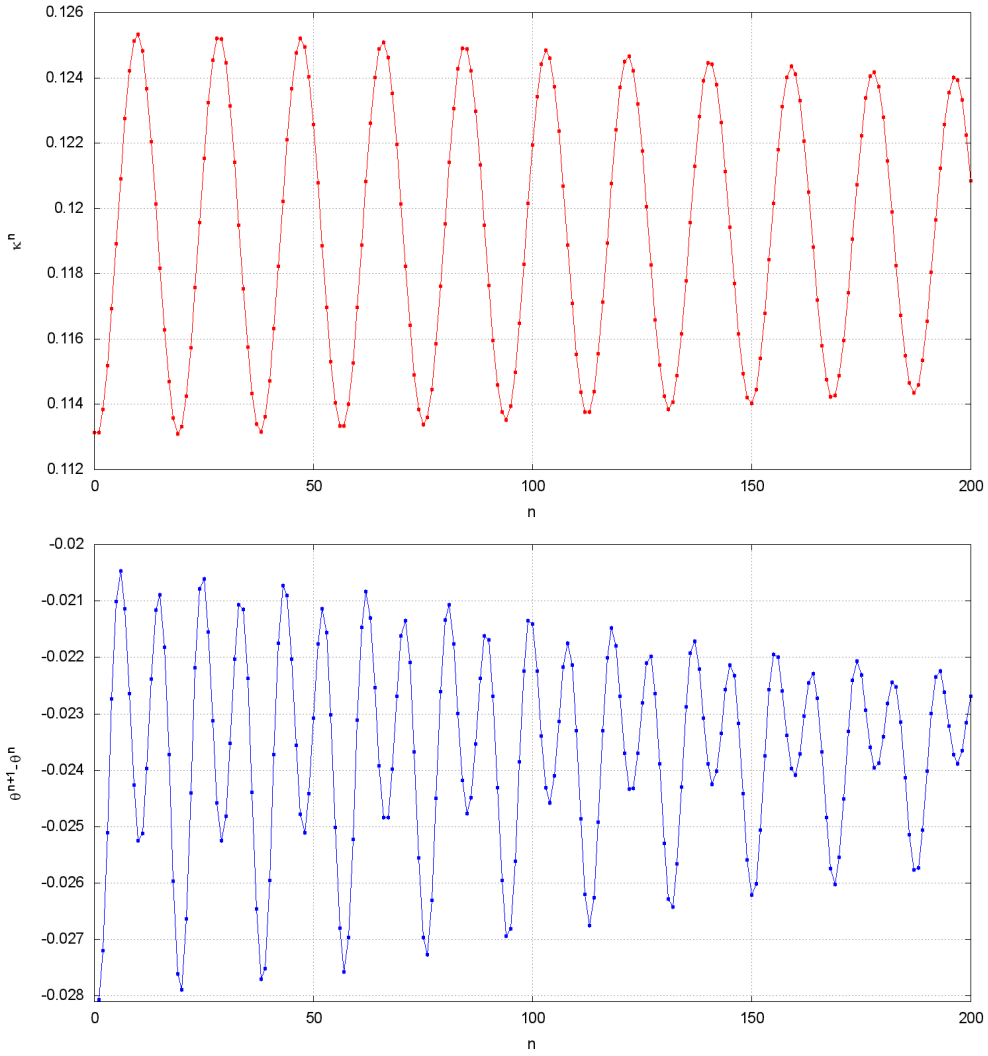

Figure 1.15: Evolution of the mean field (κ, θ) corresponding to Fig. 1.14 for the first 200 iterations.

The data obtained from phase space of the 2D map (1.38a)-(1.38b) served to find the parameter values for which the macroparticle remained coherent. However an extra criteria was needed to chose adequate values of τ and Γ since their ratio could impact directly on the values of κ^0 and γ_k, which cause the macroparticle to be *destroyed* in just a few iterations, as in Fig. 1.16. The values of $\{\kappa^0, \gamma_k\}$ of Fig. 1.16 were chosen to be analogous to the parameter values $\{w, \tau, \Gamma\}$ of first frame in Fig. 1.7, which does not look too dissimilar

to Fig. 1.11.

Additionally Fig. 1.16 shows that it is possible to find initial conditions that lead to the filamentation of the macroparticle observed in Ref. [4].

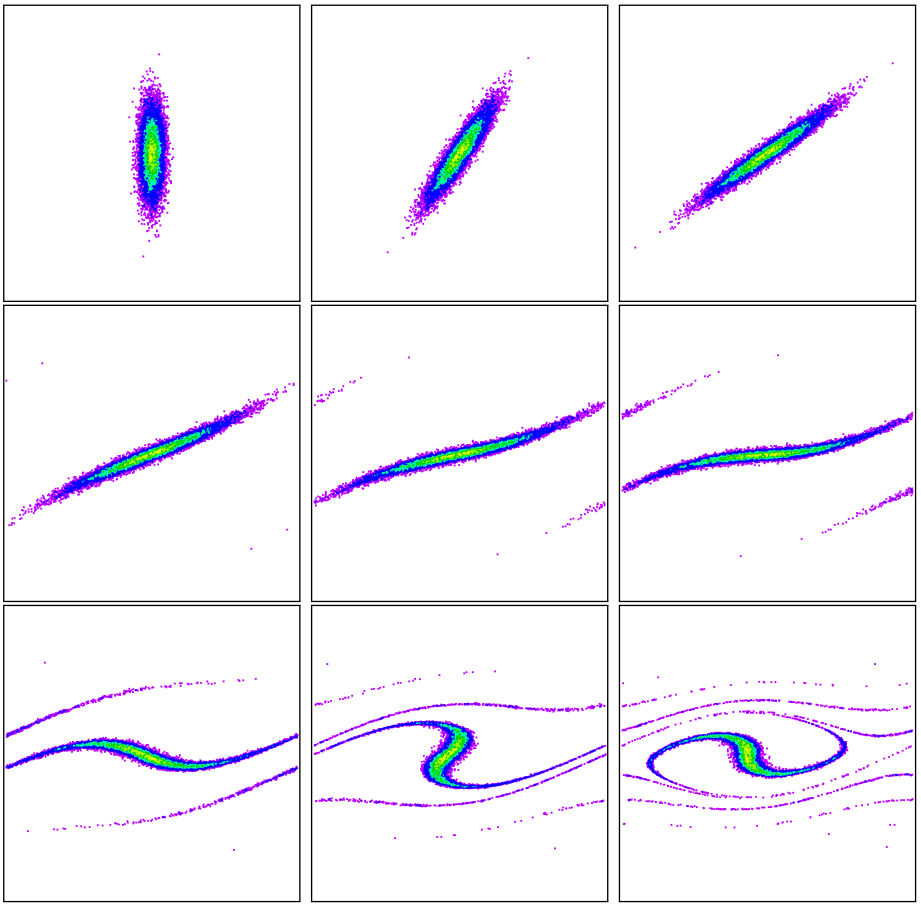

Figure 1.16: Evolution of the self-consistent map in Eq. (1.1) for the macroparticle initial conditions from Fig. 1.12 just varying $x_0 = -0.1$, $\kappa^0 = 1.1314 \times 10^{-3}$ and $\gamma_k = 3.57 \times 10^{-10}$. The frames show the instantaneous coordinates of the N initial conditions, at $n = 0, 8, 16, 24, 32, 40, 48, 100$ and 172 in the region $[-\pi, \pi] \times [-0.25, 0.25]$ of the (x, y) plane.

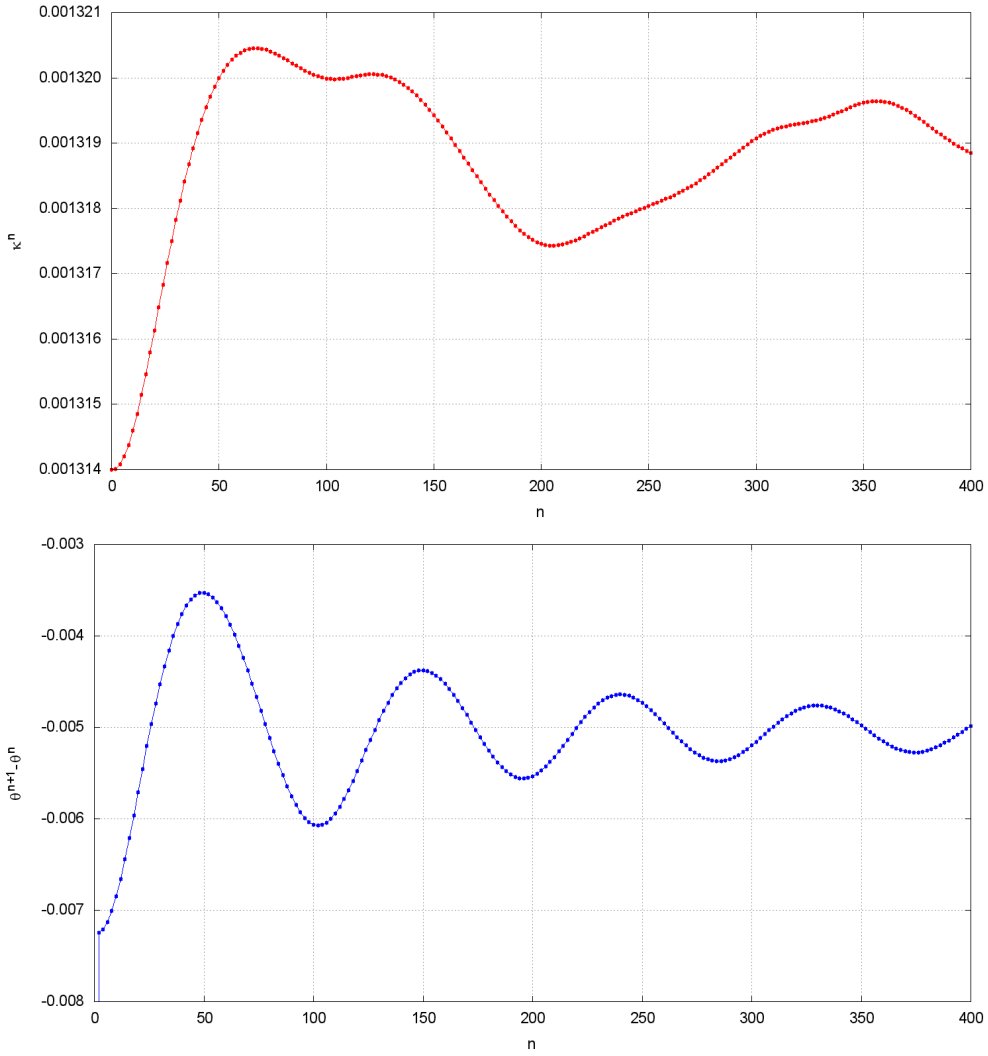

Figure 1.17: Evolution of the mean field (κ, θ) corresponding to Fig. 1.16 for the first 200 iterations.

1.4.2 $N = 2$ Standard mean-field map

For $N = 2$ the mean-field map becomes the 6-D map

$$x_1^{n+1} = x_1^n + \frac{\tau}{\Gamma_1} p_1^{n+1} \tag{1.47a}$$

$$x_2^{n+1} = x_2^n + \frac{\tau}{\Gamma_2} p_2^{n+1} \tag{1.47b}$$

$$p_1^{n+1} = p_1^n - 2\tau\Gamma_1\sqrt{J^{n+1}}\,\sin\left(x_1^n - \theta^n\right) \tag{1.47c}$$

$$p_2^{n+1} = p^n - 2\tau\Gamma_2\sqrt{J^{n+1}}\,\sin\left(x_2^n - \theta^n\right) \tag{1.47d}$$

$$\theta^{n+1} = \theta^n - \tau U - \frac{\tau}{\sqrt{J^{n+1}}}\left[\Gamma_1\cos\left(x_1^n - \theta^n\right) + \Gamma_2\cos\left(x_2^n - \theta^n\right)\right] \tag{1.47e}$$

$$J^{n+1} = J^n + 2\tau\sqrt{J^{n+1}}\left[\Gamma_1\sin\left(x_1^n - \theta^n\right) + \Gamma_2\sin\left(x_2^n - \theta^n\right)\right]. \tag{1.47f}$$

This map has one more degree of freedom and can not be reduced as in the $N = 1$ case, but it is possible to do it for the symmetrical case, as in Ref. [4]. The symmetry involved corresponding to the one in Eq. 1.22, warrants that if the initial conditions and parameters are chosen as,

$$x_2^0 = -x_1^0\,, \qquad p_2^0 = -p_1^0\,, \qquad \theta^0 = 0\,,$$
$$\Gamma_2 = -\Gamma_1\,, \qquad U = 0\,.$$

then $(x_2^n, p_2^n) = -(x_1^n, p_1^n)$ for all n. So the real dimension of the problem is reduced from 6 to 4.

It would be a natural choice for the reader to just substitute the symmetric case initial conditions and parameters in map (1.47) and then work with the reduced independent equations of the map, however this may lead to significant confusion about the properties or lack of them in the resultant 2-D map, since the reduced variables are not symplectic conjugates. Instead, the procedure chosen is to first modify through symplectic changes of coordinates the map (1.47) and then substitute the symmetric states conditions. The first change of coordinates for (1.47) proposed is,

$$\varphi = \frac{x_1 - x_2}{2}\,, \qquad \mu = \frac{x_1 + x_2}{2}\,, \tag{1.48}$$

$$u = p_1 - p_2\,, \qquad m = p_1 + p_2\,, \tag{1.49}$$

where φ (μ) is the symplectic conjugate of u (m). The resulting map is,

$$\varphi^{n+1} = \varphi^n + \frac{\tau}{4\Gamma_1}\left(m^{n+1} + u^{n+1}\right) - \frac{\tau}{4\Gamma_2}\left(m^{n+1} - u^{n+1}\right) \tag{1.50a}$$

$$u^{n+1} = u^n - 2\tau\sqrt{J^{n+1}}\left[\Gamma_1 \sin\left(\mu^n + \varphi^n - \theta^n\right) - \Gamma_2 \sin\left(\mu^n - \varphi^n - \theta^n\right)\right] \tag{1.50b}$$

$$\mu^{n+1} = \mu^n + \frac{\tau}{4\Gamma_1}\left(m^{n+1} + u_1^{n+1}\right) + \frac{\tau}{4\Gamma_2}\left(m^{n+1} - u^{n+1}\right) \tag{1.50c}$$

$$m^{n+1} = m^n - 2\tau\sqrt{J^{n+1}}\left[\Gamma_1 \sin\left(\mu^n + \varphi^n - \theta^n\right) + \Gamma_2 \sin\left(\mu^n - \varphi^n - \theta^n\right)\right] \tag{1.50d}$$

$$\theta^{n+1} = \theta^n - \tau U - \frac{\tau}{\sqrt{J^{n+1}}}\left[\Gamma_1 \cos\left(\mu^n + \varphi^n - \theta^n\right) + \Gamma_2 \cos\left(\mu^n - \varphi^n - \theta^n\right)\right] \tag{1.50e}$$

$$J^{n+1} = J^n + 2\tau\sqrt{J^{n+1}}\left[\Gamma_1 \sin\left(\mu^n + \varphi^n - \theta^n\right) + \Gamma_2 \sin\left(\mu^n - \varphi^n - \theta^n\right)\right] \tag{1.50f}$$

Imposing the conditions: $\Gamma_1 = -\Gamma_2 = \Gamma$ and $U = 0$, the map reduces to,

$$\varphi^{n+1} = \varphi^n + \frac{\tau}{2\Gamma} m^{n+1} \tag{1.51a}$$

$$u^{n+1} = u^n - 2\tau\Gamma\sqrt{J^{n+1}}\left[\sin\left(\mu^n + \varphi^n - \theta^n\right) + \sin\left(\mu^n - \varphi^n - \theta^n\right)\right] \tag{1.51b}$$

$$\mu^{n+1} = \mu^n + \frac{\tau}{2\Gamma} u^{n+1} \tag{1.51c}$$

$$m^{n+1} = m^n - 2\tau\Gamma\sqrt{J^{n+1}}\left[\sin\left(\mu^n + \varphi^n - \theta^n\right) - \sin\left(\mu^n - \varphi^n - \theta^n\right)\right] \tag{1.51d}$$

$$\theta^{n+1} = \theta^n - \frac{\tau\Gamma}{\sqrt{J^{n+1}}}\left[\cos\left(\mu^n + \varphi^n - \theta^n\right) - \cos\left(\mu^n - \varphi^n - \theta^n\right)\right] \tag{1.51e}$$

$$J^{n+1} = J^n + 2\tau\Gamma\sqrt{J^{n+1}}\left[\sin\left(\mu^n + \varphi^n - \theta^n\right) - \sin\left(\mu^n - \varphi^n - \theta^n\right)\right] \tag{1.51f}$$

From the expressions of (1.51d) and (1.51f), can be noted that: $\mathcal{P} = J^{n+1} + m^{n+1} = J^n + m^n$. So it is natural to introduce a new change of variables with a momentum variable proportional to that sum ($\mathcal{P}$),

$$\rho = \theta + \mu\,, \qquad \sigma = \mu - \theta\,, \tag{1.52}$$

$$r = \frac{J+m}{2}\,, \qquad s = \frac{m-J}{2}\,, \tag{1.53}$$

And the system reduces again to,

$$\varphi^{n+1} = \varphi^n + \frac{\tau}{2\Gamma}\left(r^{n+1} + s^{n+1}\right) , \tag{1.54a}$$

$$u^{n+1} = u^n - 2\tau\Gamma\sqrt{r^{n+1} - s^{n+1}}\left[\sin\left(\sigma^n + \varphi^n\right) + \sin\left(\sigma^n - \varphi^n\right)\right] , \tag{1.54b}$$

$$\sigma^{n+1} = \sigma^n + \frac{\tau}{2\Gamma}u^{n+1} + \frac{\tau\Gamma}{\sqrt{r^{n+1} - s^{n+1}}}\left[\cos\left(\sigma^n + \varphi^n\right) - \cos\left(\sigma^n - \varphi^n\right)\right] , \tag{1.54c}$$

$$s^{n+1} = s^n - 2\tau\Gamma\sqrt{r^0 - s^{n+1}}\left[\sin\left(\sigma^n + \varphi^n\right) - \sin\left(\sigma^n - \varphi^n\right)\right] , \tag{1.54d}$$

$$\rho^{n+1} = \rho^n + \frac{\tau}{2\Gamma}u^{n+1} - \frac{\tau\Gamma}{\sqrt{r^{n+1} - s^{n+1}}}\left[\cos\left(\sigma^n + \varphi^n\right) - \cos\left(\sigma^n - \varphi^n\right)\right] , \tag{1.54e}$$

$$r^{n+1} = r^n . \tag{1.54f}$$

And finally, the symmetric case initial conditions are imposed, which in these coordinates are: $u^0 = \sigma^0 = \rho^0 = 0$. So the map reduces to,

$$\varphi^{n+1} = \varphi^n + \frac{\tau}{2\Gamma}\left(r^0 + s^{n+1}\right) , \tag{1.55a}$$

$$u^{n+1} = u^n = 0 , \tag{1.55b}$$

$$\sigma^{n+1} = \sigma^n = 0 , \tag{1.55c}$$

$$s^{n+1} = s^n - 4\,\tau\Gamma\sqrt{r^0 - s^{n+1}}\sin\left(\varphi^n\right) , \tag{1.55d}$$

$$\rho^{n+1} = \rho^n = 0 , \tag{1.55e}$$

$$r^{n+1} = r^0 . \tag{1.55f}$$

This is a 2-D map on (φ, s) with parameters: (r^0, τ, Γ), that do not preserve area. This apparent contradiction is easily explained since these 2 variables are not symplectic conjugates. The effect of this lack of area-preserving can be observed in Figs. 1.18 and 1.19.

Furthermore, rewriting Eq. (1.54d) to be explicit for s^{n+1}, gives,

$$s^{n+1} = s^n - 8A^2 - 4A\sqrt{16A^2 + r - s^n} , \tag{1.56}$$

where,

$$A = \tau\Gamma\sin(\varphi^n) . \tag{1.57}$$

This *perturbation function* $V' = 8A^2 + 4A\sqrt{16A^2 + r - s^n}$ does not have in general average zero, so a drag is expected to be observed. In particular for

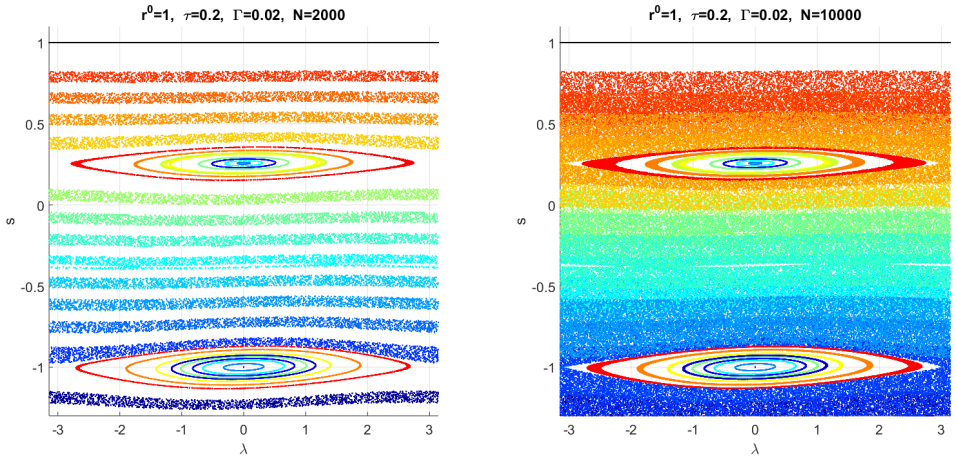

Figure 1.18: Sample of the phase space for the 2-D map (φ, s) from map (1.55a) and (1.55d) for different number N of iterations. The orbits with initial conditions taken between resonances display a monotonous drag towards negative values of s, while orbits with initial conditions inside the resonances behave as an stable focus.

the case $r - s^n \gg 1$, the perturbation function has the form,

$$V' \approx 8\tau^2\Gamma^2\left(1 - \frac{\cos(2\varphi^n)}{2}\right) + 4\tau\Gamma\sqrt{r - s^n}\sin(\varphi^n)\,, \tag{1.58}$$

that clearly does not have zero average, making this map dissipative for certain regions of the phase space.

The Jacobian matrix of this map is,

$$\mathcal{D}T = \begin{pmatrix} 1 + \frac{\tau}{2\Gamma}\mathfrak{a} & \frac{\tau}{2\Gamma}\mathfrak{b} \\ \mathfrak{a} & \mathfrak{b} \end{pmatrix}, \tag{1.59}$$

where,

$$\mathfrak{a} = \frac{\partial s^{n+1}}{\partial \varphi^n} = \frac{-4\tau\Gamma(r - s^{n+1})\cos(\varphi^n)}{\sqrt{r - s^{n+1}} - 2\tau\Gamma\sin(\varphi^n)}\,, \tag{1.60}$$

$$\mathfrak{b} = \frac{\partial s^{n+1}}{\partial s^n} = \frac{\sqrt{r - s^{n+1}}}{\sqrt{r - s^{n+1}} - 2\tau\Gamma\sin(\varphi^n)}\,. \tag{1.61}$$

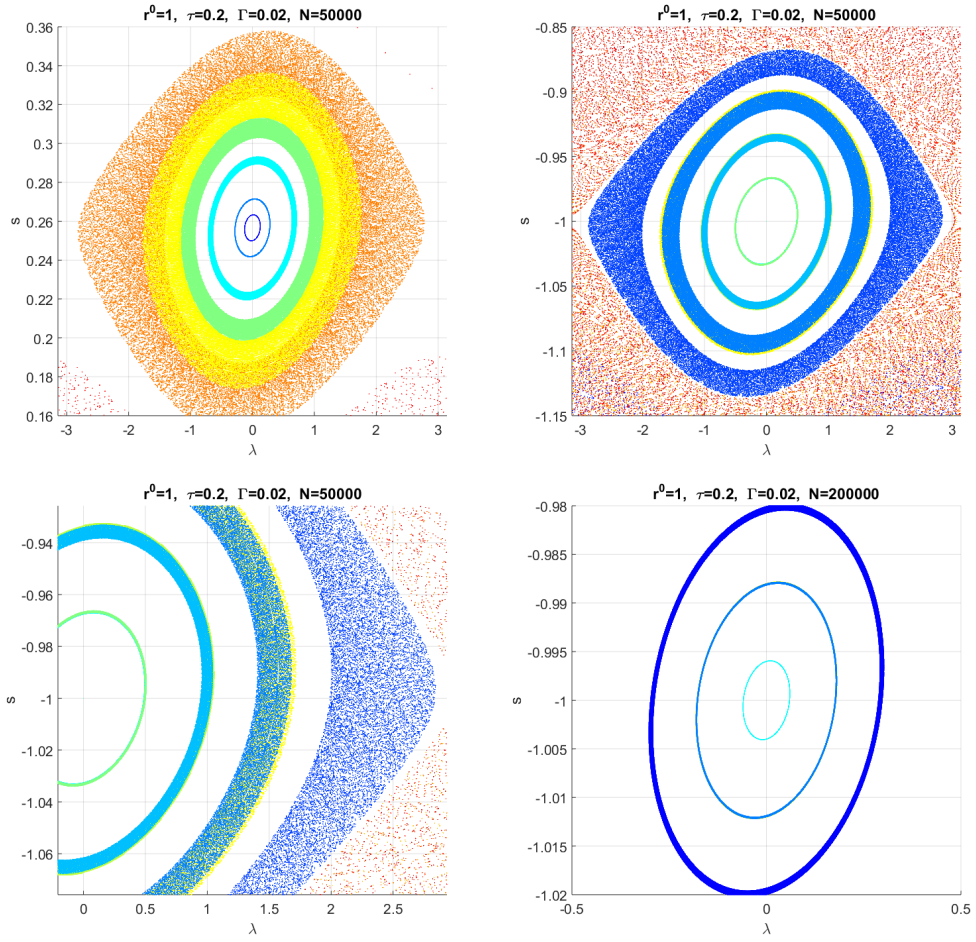

Figure 1.19: Detail of the structure inside the resonances $\ell = 1$ (first panel) $\ell = 0$ (second, third and forth panels) from figure 1.18 for different number of iterations N.

Curiously, there is an additional orbit for map (1.55a)-(1.55d) not present in previous section for map (1.38a)-(1.38b), the orbit corresponding to $s^n = r^0$. This orbit in the 2-D map (1.55a)-(1.55d) behaves as a standard orbit from the integrable map. The Jacobian matrix, $\mathcal{D}T$, around the orbit $s^n = r^0$ has the form,

$$\mathcal{D}T = \begin{pmatrix} 1 & \frac{\tau}{2\Gamma} \\ 0 & 1 \end{pmatrix} , \tag{1.62}$$

so the area is preserved (locally).

Period one periodic orbits, case $N = 2$ symmetric

The period one periodic orbits from the 2-D map (1.55a)-(1.55d) are given by,

$$\varphi_* = m\pi \, , \qquad m = 0, 1 \, , \tag{1.63}$$

and

$$s_* = -r^0 + \frac{2\Gamma}{\tau} 2n\pi \, , \qquad n = 0, 1, 2, \ldots \, . \tag{1.64}$$

The stability of these orbits can not be obtained from the Greene's residue since the map is not area preserving, however it is possible to obtain certain information around the fixed points. It is easy to show that the area around any of the fixed points is conserved since,

$$|\mathcal{D}T(\varphi_*, s_*)| = \left. \frac{\partial s^{n+1}}{\partial s^n} \right|_{(\varphi_*, s_*)} = 1 \, . \tag{1.65}$$

After performing simulations for different values of the parameters, it was observed that the iteration of this map cause to any initial condition outside a resonance to monotonically decrease s^n and transitioning (jumping) the resonances through the *hyperbolic point* ($m = 1$). The behavior inside the *resonances* is more complicate, any initial condition inside a *resonance* tends to *fall* to the *elliptic point* ($m = 0$) but not in an increasing slow yet monotonous manner.

Dipole simulations

As in the case of the macroparticle in last subsection and taking Ref. [4] as a guiding example, it may be physically relevant and insightful to find if a

coherent structure that approximates the stable solutions for $N = 2$ can also persist in the context of the single wave map model (1.1).

The initial conditions used are of two identical symmetric macroparticles with opposite charge γ and $\theta^0 = 0$. More in detail, these initial conditions consist of two set of N identical *particles* described by N points $\{(x_k, y_k)\}_{k=1,\dots,N}$ with $\gamma_k = \gamma$ and $\{(\tilde{x}_k, \tilde{y}_k)\}_{k=1,\dots,N}$ with $\tilde{\gamma}_k = -\gamma$, each following a Gaussian distribution (1.44) with the same width (σ_1, σ_2) but opposite centers $(x_0, y_0) = (-\tilde{x}_0, -\tilde{y}_0)$. Additionally the mean field initial values (κ_0, θ_0) and (γ, x_0, y_0) are set as,

$$\kappa^0 = \tau^2\sqrt{8r^0}\,, \qquad \theta^0 = 0\,, \tag{1.66}$$

$$\gamma = 2\tau^3\Gamma/N \qquad x_0 = \varphi^0 + \varepsilon \qquad y_0 = \frac{\tau}{\Gamma}s_0\,, \tag{1.67}$$

where r^0, τ and Γ are parameters from the 2-D map (1.55a)-(1.55d) and (φ^0, s^0) are the coordinates of a period 1 fixed point. Due the symmetry of the problem, it is necessary to add an small parameter ε to x_0 to ensure that both macroparticles are not overlapping, at least initially.

A typical evolution of a dipole around the (x, y)-origin can be appreciated in Fig. 1.20. As in Fig. 1.14, each macroparticle tends to be deformed even for small values of (σ_1, σ_2).

1.5 A true macroparticle: the *Water-Bag* mode

The coherent macroparticle simulation in Figs. 1.12 and 1.13, suggest that a gaussian macroparticle is an stable structure. To contrast this further, a different integrable limit is considered in the continuous case, that is the limit $N \to \infty$. The original PDE system of the single wave has exact solutions called Bernstein-Greene-Kruskal (BGK) modes [20] and they can be obtained (see Ref. [7]) in context of deduction of single wave model sketched here in Sec. 1.1.2. The ansatz to obtain the BGK modes is to propose the distribution f as a function of the hamiltonian (streamfunction) in the form,

$$f_{BGK}(\xi, v) = e^{-H}\,, \tag{1.68}$$

where $\xi = x - ct$,

$$H(\xi, v) = \frac{1}{2}(v - c)^2 + 2\rho\cos(\xi)\,, \tag{1.69}$$

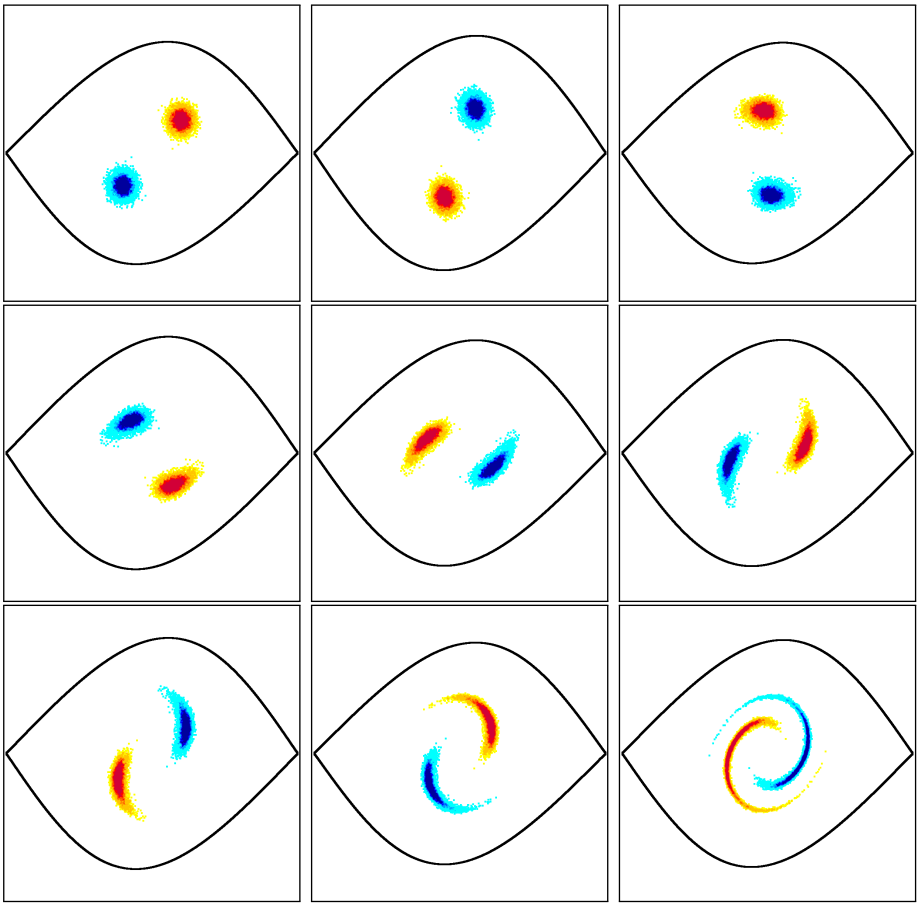

Figure 1.20: Evolution of the self-consistent map in Eq. (1.1) for dipole initial conditions with $N_1 = N_2 = 6720$, $\kappa^0 = 0.113136$, $\Gamma = 0.032$, $\theta^0 = \Omega = 0$, $x_0 = 0.1$, $y_0 = 0.2$, $\sigma_1 = 0.444$ and $\sigma_2 = 0.2$. The frames show the instantaneous coordinates of the N initial conditions at $n = 0, 4, 8, 12, 16, 20, 24, 38$ and 82 in the region $[-\pi, \pi] \times [-0.9, 0.9]$ of the (x, y) plane. Overposed on each frame it is plotted the instantaneous stable and unstable invariant manifolds of the hyperbolic fixed point. The colors represent the the density of points.

and $a = \rho e^{i\theta} e^{-ict}$. This leads to a particular condition for the value of c in terms of ρ (see Refs. [7, 19]). The shape of the BGK mode, f_{BGK}, and the contour plot of H can be appreciated in Figs. 1.21 and 1.22, respectively.

The constant c corresponds to a Galilean change of coordinates, but in

the context of (1.15), it correspond to an specific value[5] of U to make f_{BGK} an actual solution of the PDE single wave model (1.11)-(1.15).

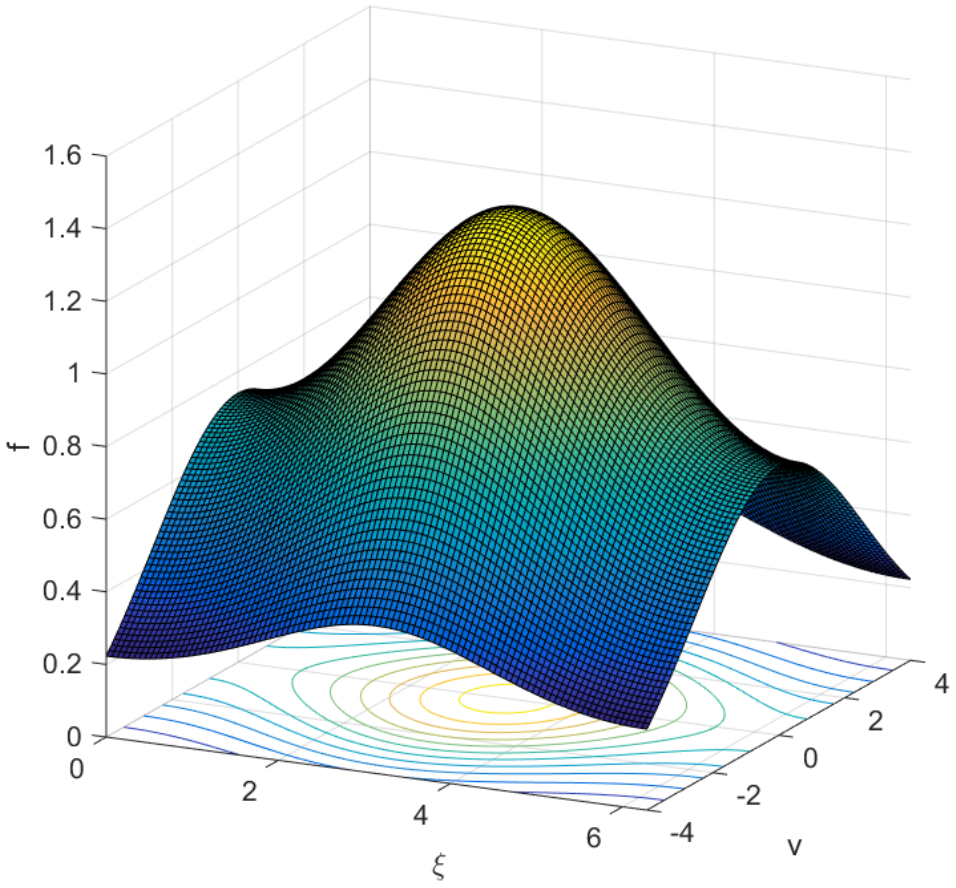

Figure 1.21: f corresponding to a BGK mode as a function of H: $f(\xi, v) = e^{-\alpha H}$, as in (1.68), with $c = 0$, $\rho = 1$ and $\alpha = 0.15$ for appreciation purposes.

In principle it is possible to test the BGK modes using the map (1.7) to numerically solve (1.3) as a point vortex representation of the PDE SWM (1.11)-(1.15). However the kind of initial state f of interest here is one

[5]Refs. [7] and [19] use slightly different definitions for the U used in this chapter, however in all cases $U \propto c$.

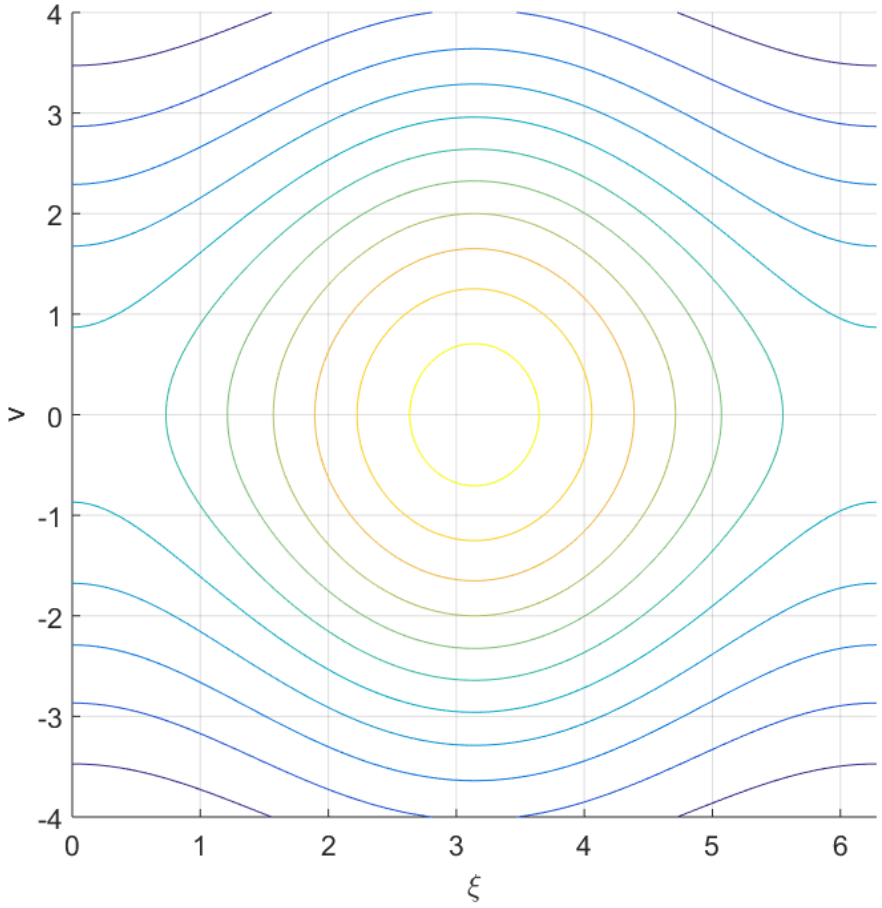

Figure 1.22: Contour plot of the function H from (1.69) for $c = 0$ and $\rho = 1$.

with compact support, similar to the discrete Gaussian macroparticle from previous section. A distribution f more appropriate to this end is the so called *Water-Bag modes*[21], that instead of Eq. (1.68), $f(H)$ is defined by,

$$f_{WB}(\xi, v) = \begin{cases} r\,, & H(\xi, v) \leq h_0\,, \\ \\ 0\,, & H(\xi, v) > h_0\,, \end{cases} \tag{1.70}$$

where h_0 is a fixed value in the range of H that has a single connected boundary, $h_0 \in [-2\rho, 2\rho)$ and r is fixed real number. The shape of f_{WB} can

be appreciated in Fig. 1.23.

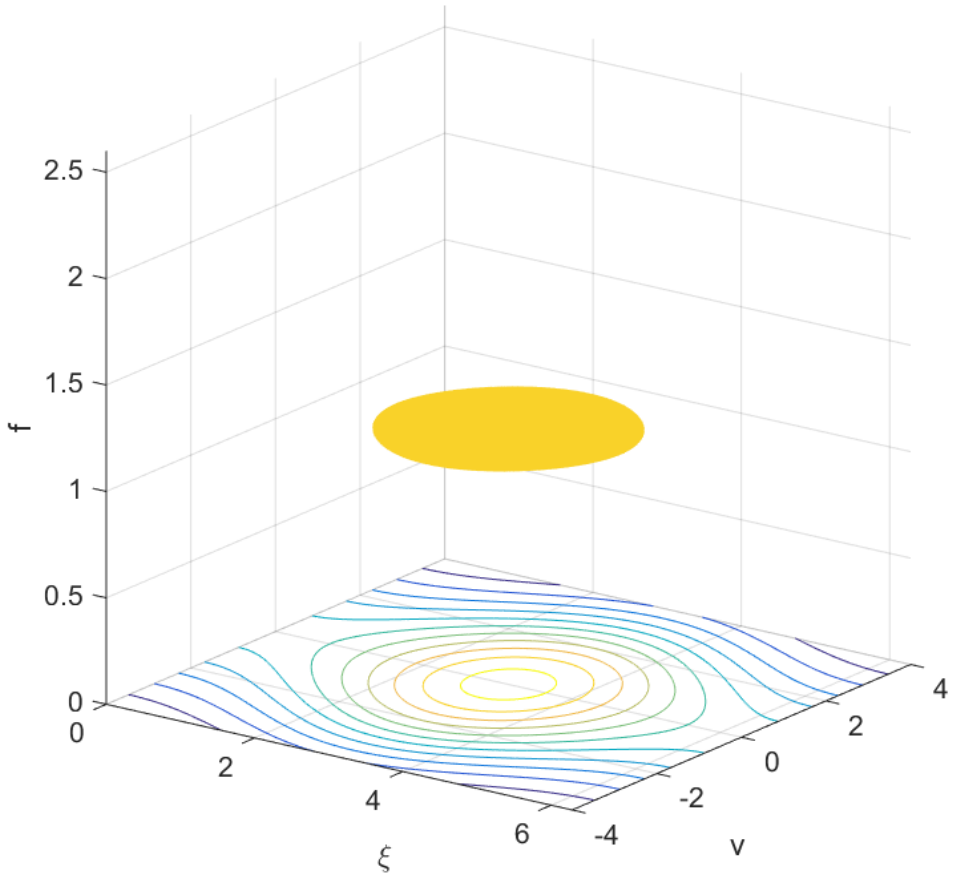

Figure 1.23: Plot of a Water-Bag mode f_{WB} defined as in (1.70) for $h_0 = -0.1$, $\rho = 1$ and $r = 1.2$.

Any function $f = f(H)$ solves trivially (1.11) since the PDE equation is equivalent to the Poisson bracket $\{f(H), H\}$, which is always zero. However (1.15) can only be satisfied by a specific value of $U = U_*$. The computation of (1.15) for f_{WB} with $a(t) = \rho e^{-ict}$ yields,

$$2\pi U_* \rho = 8r\sqrt{\rho} I_1(\chi)\,, \tag{1.71}$$

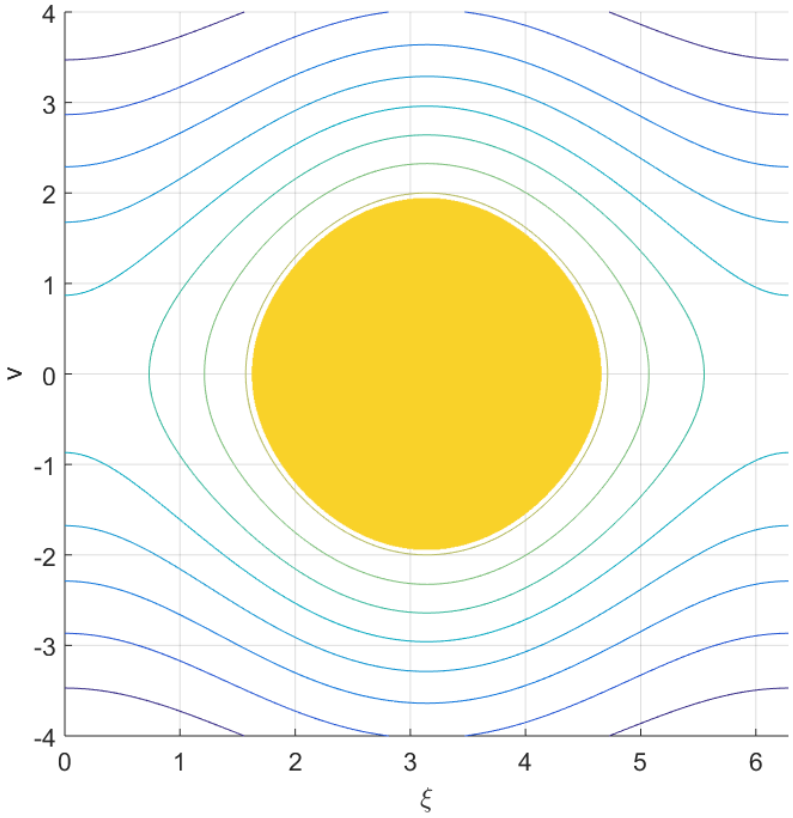

Figure 1.24: Shape of a Water-Bag mode f_{WB} defined as in (1.70) for $h_0 = -0.1$, $\rho = 1$ and $r = 1.2$.

where

$$I_1(\chi) = \int_{-\pi}^{\cos^{-1}(\chi)} \cos(\eta)\sqrt{\chi - \cos(\eta)}d\eta = -\frac{1}{2}\int_{-\chi}^{1} \frac{\sqrt{1-u^2}}{\sqrt{\chi+u}}du\,, \qquad (1.72)$$

where $\chi = h_0/2\rho$, so $\chi \in [-1, 1)$.

1.5.1 Numerical implementation of the Water-Bag modes

The use of the map (1.7) to simulate the Water-Bag modes requires to introduce a discretization of f_{WB}. Using the one suggested by Ref. [1],

$$f(x,y,t) = \sum_{j=1}^{N} \Gamma_j \delta[x - x_j(t)]\delta[y - y_j(t)]\,, \tag{1.73}$$

bridge the gap between the PDE system and the hamiltonian ODE system (1.3), however to ensure that both represent exactly the same system it is necessary Γ_j values are chosen such that the integral in (1.15) yield the same values for (1.70) and (1.73). The easiest way to ensure this is to make $\Gamma_j = \Gamma$ and,

$$\mathrm{Area}(\rho,\chi) = 8\sqrt{\rho}\mathrm{I}_2(\chi) = \sum_{\mathrm{j}=1}^{\mathrm{N}} \Gamma_{\mathrm{j}} = \mathrm{N}\Gamma\,, \tag{1.74}$$

where

$$I_2(\chi) = \int_{-\pi}^{\cos^{-1}(\chi)} \sqrt{\chi - \cos(\eta)}d\eta\,. \tag{1.75}$$

Nevertheless this is impractical because the values of Γ are relatively small and this forces to decrease τ to the same order to avoid introducing numerical error due the integrator[6]. So instead of choosing U_* as a function of ρ, r and h_0 like in (1.71), it is more convenient to introduce $\gamma = r\Gamma/2\pi$ an independent value fixed a priori and find U via numerical (Monte Carlo) integration, that is the following sum,

$$U_* = \frac{\tau\gamma}{\rho^2}\sum_{j=1}^{N}\left\{\frac{(y_j^0)^2}{2} - 2\rho\cos(x_j^0)\right\}\,. \tag{1.76}$$

where $\rho = 2\tau\sqrt{J^0}$ and $\left\{(x_j^0, y_j^0)\right\}_{j=1,\ldots,N}$ are points following an uniform distribution inside the water bag shape S,

$$S = \left\{(x,y)\middle|\frac{y^2}{2} - 2\rho\cos(x) \le h_0\right\}\,. \tag{1.77}$$

Eqs. (1.76) and (1.77) are written for $c = 0$ to simplify the coding, leading to stationary Water-Bag modes. If the interest were to find moving Water-Bag modes, it is only need to add $\tilde{c}$ to U_* and $\tilde{c}\tau$ to the right hand side of (1.7a) (or (1.31a)).

[6]The ratio of τ/Γ in (1.7a) has a direct impact in the accuracy of the simulation.

1.5.2 Numerical Water-Bag modes

The numerical integration of the Water-Bag mode by the iteration of map (1.7) (or (1.31)) with the (x_j^0, y_j^0)-initial conditions of (1.77), $\theta^0 = 0$ and $U = U_*$ from (1.76) yield stable coherent states, as it can be appreciated in Figs. 1.25-1.30 for the different values of the free parameters: τ, γ and J^0.

The first two cases presented in Figs. 1.25-1.28, both with $\chi = -0.8$, display the stationary Water-Bag mode predicted. The amplitude of the mean field J oscillates with an small ($\leq 10\%$) amplitude, much like the case of the stable macroparticle from Sec. 1.4, mean while the phase of the mean field θ oscillates with a small amplitude around $\theta = 0$.

The third case in Fig. 1.29-1.30, for $\chi = -0.4$, displays a coherent Water-Bag mode of bigger relative area,

$$\frac{\text{Area}(\rho, -0.4)}{\text{Area}(\rho, -0.8)} = \frac{I_2(-0.4)}{I_2(-0.8)} = \frac{2.779104}{0.900123} = 3.0874714\,, \tag{1.78}$$

with a drift on the phase that does not seem to affect the shape of the state. An hypothesis of the existence of this drift is that the *point vortex* representation (1.73) is not as good approximation to the f_{WB} (1.70) as χ increases. Additionally, Fig. 1.30 shows an unexpected decrease of the frequency of oscillation of the mean field variables that can be associated to the size of the water bag mode.

Additionally to illustrate the option in the model to describe a moving water-bag mode, a forth case is presented in Fig. 1.31, where $\tilde{c}\tau = 0.05$ is introduced.

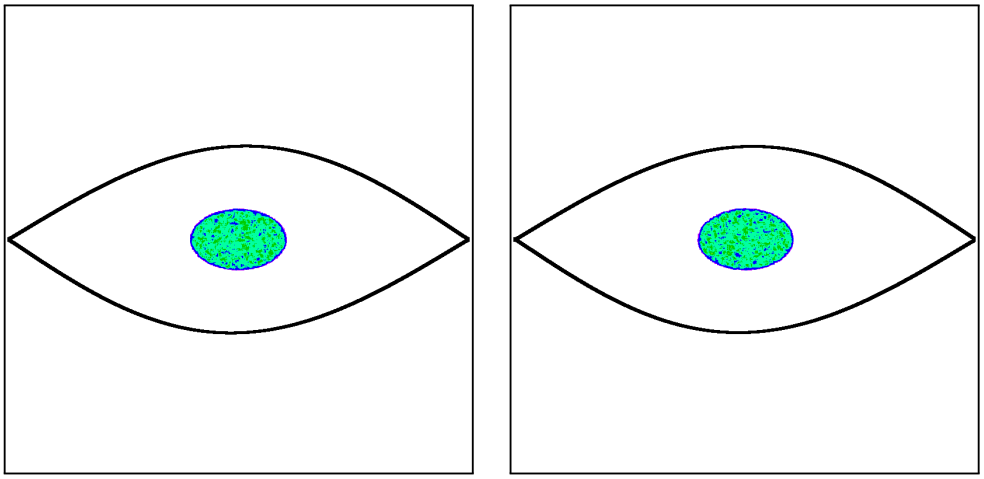

Figure 1.25: Iteration of a Water-Bag mode f_{WB} for $N = 13440$, $\chi = -0.8$, $\tau = \gamma = 0.005$ and $J^0 = 1$. Left frame corresponds to the initial state and right frame to the 100th iteration of the map (1.31), in the region $[-\pi, \pi] \times [-0.5, 0.5]$ of the (x, y) plane. The colors denote the relative density of points.

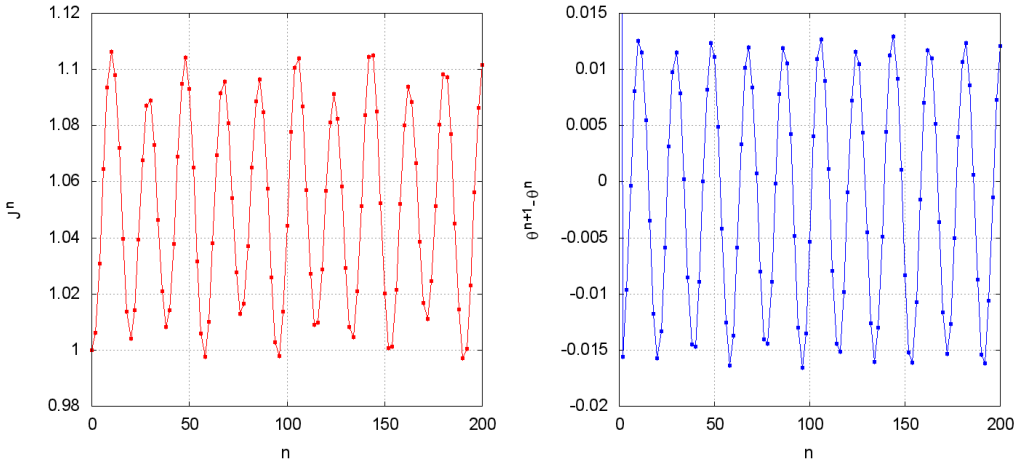

Figure 1.26: Evolution of the mean field (J, θ) corresponding to Fig. 1.25 for the first 200 iterations.

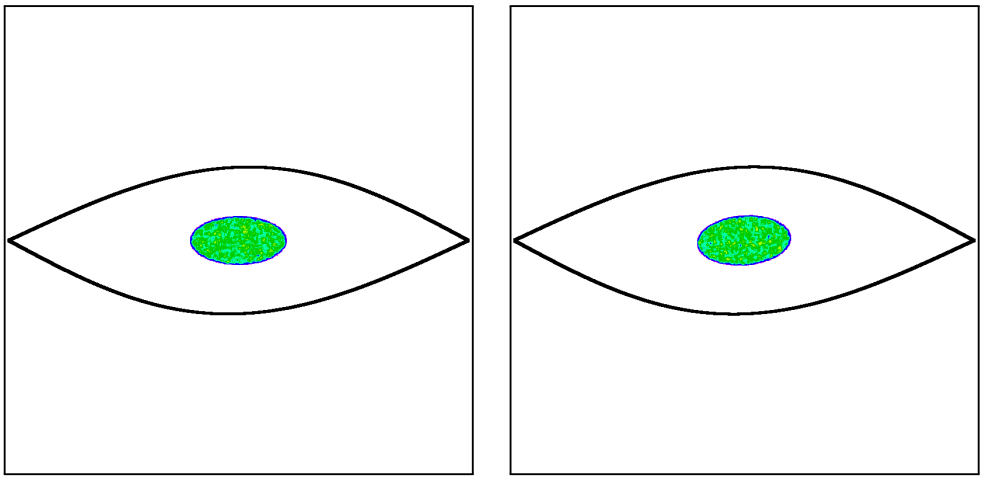

Figure 1.27: Iteration of a Water-Bag mode f_{WB} for $N = 13440$, $\chi = -0.8$, $\tau = \gamma = 0.01$ and $J^0 = 2$. Left frame corresponds to the initial state and right frame to the 100th iteration of the map (1.31), in the region $[-\pi, \pi] \times [-0.9, 0.9]$ of the (x, y) plane. The colors denote the relative density of points.

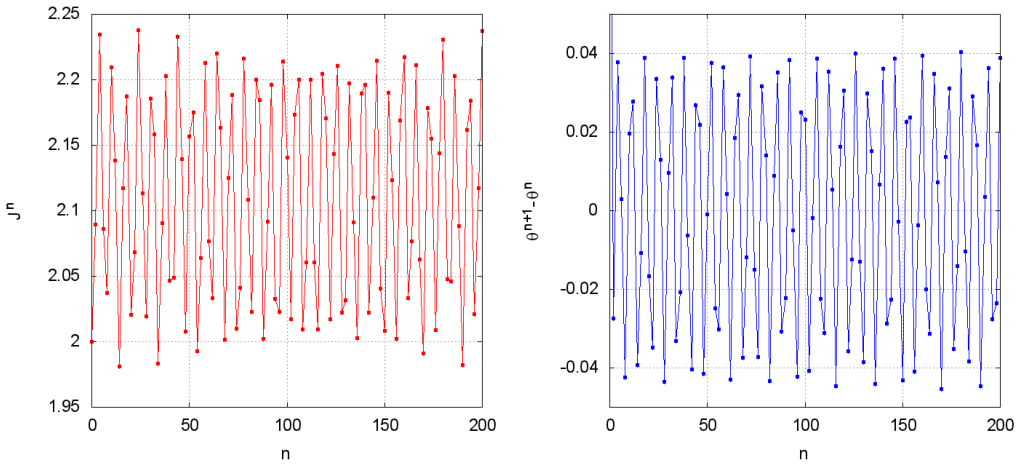

Figure 1.28: Evolution of the mean field (J, θ) corresponding to Fig. 1.27 for the first 200 iterations.

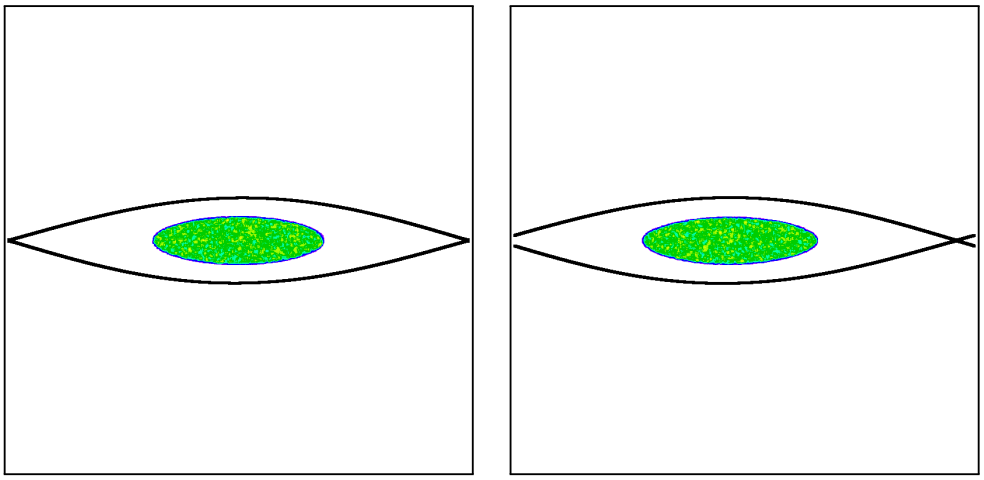

Figure 1.29: Iteration of a Water-Bag mode f_{WB} for $N = 26880$, $\chi = -0.4$, $\tau = \gamma = 0.0015$ and $J^0 = 1$. Left frame corresponds to the initial state and right frame to the 100th iteration of the map (1.31), in the region $[-\pi, \pi] \times [-0.6, 0.6]$ of the (x, y) plane. The colors denote the relative density of points.

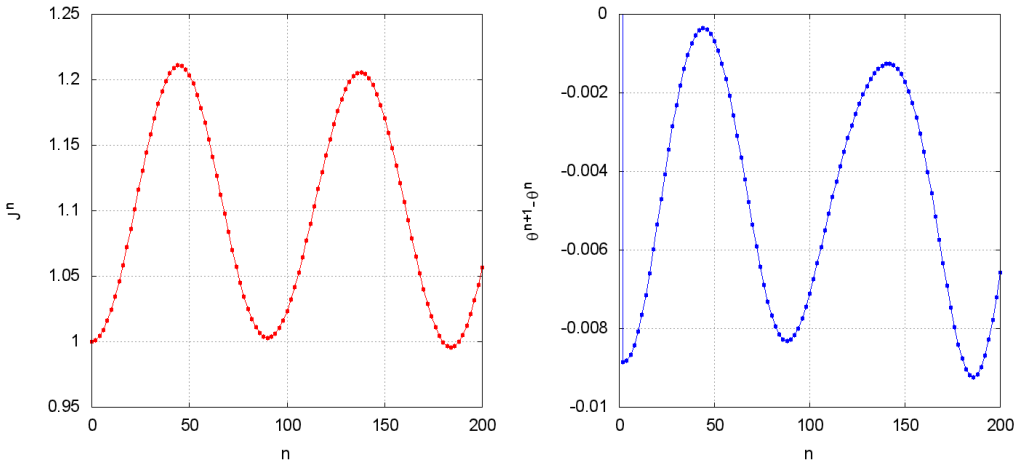

Figure 1.30: Evolution of the mean field (J, θ) corresponding to Fig. 1.29 for the first 200 iterations.

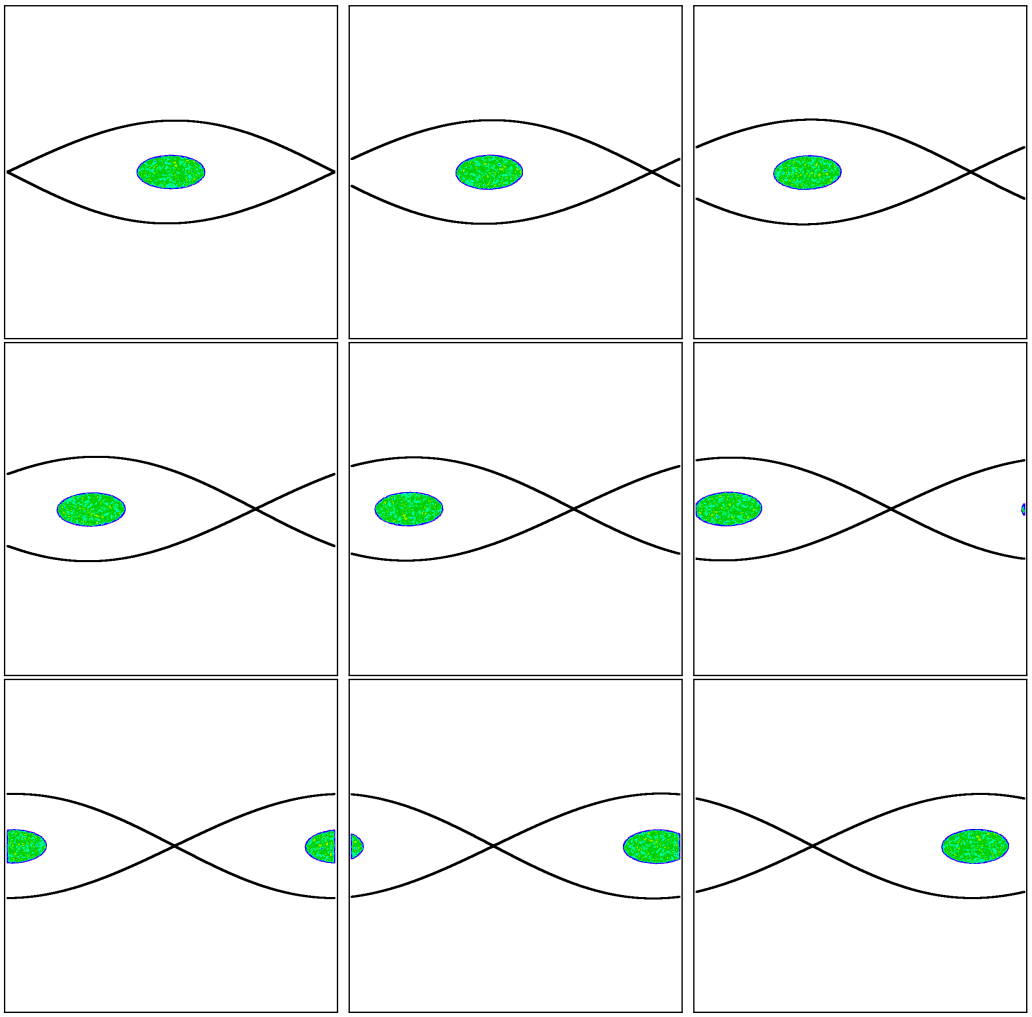

Figure 1.31: Iteration of a Water-Bag mode f_{WB} for $N = 13440$, $\chi = -0.8$, $\tau = \gamma = 0.03$, $J^0 = 1$ and $\tilde{c}\tau = 0.05$. The frames show the instantaneous coordinates of the N initial conditions at $n = 0, 10, 20, 30, 40, 50, 60, 70$ and 80 in the region $[-\pi, \pi] \times [-0.5, 0.5]$ of the (x, y) plane. The colors denote the relative density of points.

Chapter 2

Hamiltonian flows and dynamical systems

This chapter reviews the mathematical concepts, definitions and theorems that are used in the present work. The discussion has a bias toward the use of maps as a tool to study the behavior of solutions of a particular kind of differential equations: the *near-integrable hamiltonian dynamical systems*. Although it is assumed certainly familiarity on these topics from the reader, a more detailed exposition of the content of this chapter can be found in Refs. [22], [23] and [24].

2.1 Dynamical systems

A dynamical system consist of a *phase space* that describes the allowed states of the system and a *rule* that defines the evolution of such states. The evolution can be continuous, as in the case of differential equations, or discrete, as the case of maps. All physical phenomena are in principle susceptible to be modeled by a dynamical system of some sort and moreover, many of the fundamental models in physics are Hamiltonian dynamical systems[1], and from this particular kind is where the *symplectic maps* are inspired and/or obtained. The canonical example is the map defined by the hamiltonian flow applied to an initial condition $\mathbf{x}(0)$ and the final state $\mathbf{x}(t)$ is achieve after a finite time t, this is a sympletic map (see figure 2.1). More examples of sym-

[1] In particular at astronomical and microscopic scales, where friction is non-existent or negligible.

plectic maps obtained from Hamiltonian dynamical systems can be found in Ref. [22, 23, 25].

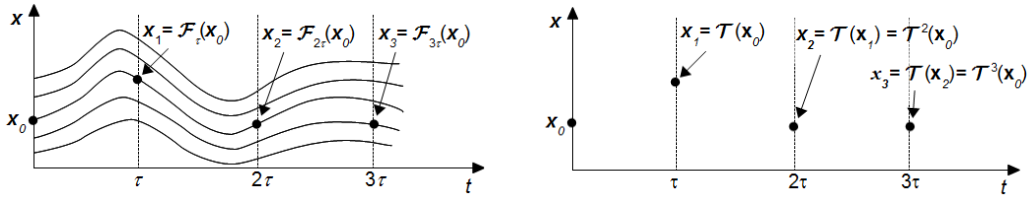

(a) (b)

Figure 2.1: Example of a *symplectic map* $\mathcal{T}$ constructed from the hamiltonian flow: $\mathbf{x}_{n+1} = \mathcal{T}(\mathbf{x}_n) = \mathcal{F}_\tau(\mathbf{x}_n)$.

Maps can be useful in many cases since they are easier to study than a differential equation and in principle, all numerical solution involves a map.

Two of the typical questions that arise in the study of dynamical systems are: the stability of the orbits for longer times and to determine the accessible regions of movement. Both questions can be approached using maps.

2.2 Hamiltonian flow and symplectic maps

A hamiltonian flow is described by a function $H(\mathbf{p}, \mathbf{q}, t)$ and a set of differential equations:

$$\frac{dq_i}{dt} = \frac{\partial H}{\partial p_i}, \quad \frac{dp_i}{dt} = -\frac{\partial H}{\partial q_i} \tag{2.1}$$

where q_i correspond to the *configuration coordinates* and p_i to the *canonical momenta*, $i = 1, 2, ...N$, for a system of N degrees of freedom. A more compact form of write (2.1) is using the Poisson bracket as,

$$\dot{z} = \{z, H\}, \tag{2.2}$$

where $z = (q_1, ..., q_N, p_1, ..., p_N)$ and $\{,\}$ is defined as,

$$\{f, g\} = \sum_{m,n=1}^{2N} \frac{\partial f}{\partial z_m} \mathbb{J}_{mn} \frac{\partial g}{\partial z_n} = \sum_{k=1}^{N} \left(\frac{\partial f}{\partial q_k} \frac{\partial g}{\partial p_k} - \frac{\partial g}{\partial q_k} \frac{\partial f}{\partial p_k} \right), \tag{2.3}$$

where $\mathbb{J}$, the *symplectic matrix*, a $2n \times 2n$ matrix that in the Darboux coordinates has the form,

$$\mathbb{J} \;=\; \begin{pmatrix} 0 & \mathbb{I} \\ -\mathbb{I} & 0 \end{pmatrix} \;, \tag{2.4}$$

where $\mathbb{I}$ is the $n \times n$ identity matrix.

The hamiltonian flow can also be obtained from a variational principle. Let $\gamma = \{(\mathbf{q}(t), \mathbf{p}(t))|\ t_0 < t < t_1\}$ be a test trajectory in the phase space that connects $(\mathbf{q}_0, \mathbf{p}_0)$ with $(\mathbf{q}_1, \mathbf{p}_1)$. The functional *action* of such trajectory is defined as,

$$S[\gamma] = \int_{t_0}^{t_1} [\mathbf{p} \cdot \dot{\mathbf{q}} - H(\mathbf{p}, \mathbf{q}, t)] dt \,. \tag{2.5}$$

The hamiltonian flow is the one that minimizes the action, i.e. $\delta S = 0$. Using this definition of hamiltonian flow and the Stoke's theorem, it is easy to prove the *Poincaré integral invariant*: the action of a loop is an invariant for Hamiltonian flow, see Ref. [22]. For the particular case when H is independent of t, the action of a (closed) loop $\mathcal{L}$ contractable to a point reduces to,

$$S[\mathcal{L}] = \oint_{\mathcal{L}} \mathbf{p} \cdot d\mathbf{q} = \int_{\mathcal{A}} d\mathbf{p} \wedge d\mathbf{q} \,. \tag{2.6}$$

By Stokes theorem, last term in the equality implies that the invariance of the action of a loop is equivalent to the preservation of the *symplectic area*, the sum of the areas obtained by the projection of $\mathcal{L}$ onto each canonical plane (p^i, q^i).

For example, the area of a parallelogram with sides made of vectors δz and $\delta \bar{z}$ is given by,

$$\omega(\delta z, \delta \bar{z}) = \delta \mathbf{p} \cdot \delta \bar{\mathbf{q}} - \delta \mathbf{q} \cdot \delta \bar{\mathbf{p}} = \delta z^i \omega_{ij} \delta \bar{z}^j \,. \tag{2.7}$$

The antisymmetric form ω is called the *symplectic form*. In Darboux coordinates, it is represented by the matrix,

$$\omega \;=\; \begin{pmatrix} 0 & -\mathbb{I} \\ \mathbb{I} & 0 \end{pmatrix} \tag{2.8}$$

which is the inverse of $\mathbb{J}$.

2.2.1 Symplectic maps

A *map* is a transformation in the phase space ($z = (\mathbf{q}, \mathbf{p})$),

$$z' = \mathcal{T}(z)\,. \tag{2.9}$$

and an *orbit* is a sequence,

$$\{..., z_n, z_{n+1}, ...\} \tag{2.10}$$

such that $z_{n+1} = \mathcal{T}(z_n)$.

A map $\mathcal{T}$ is *symplectic* if it preserves the loop action integral (2.6),

$$S[\mathcal{L}'] = S[\mathcal{T}(\mathcal{L})] = S[\mathcal{L}]\,. \tag{2.11}$$

From this definition it follows a local (differential) definition with the use of the symplectic form ω, a map $\mathcal{T}$ is *locally symplectic* or *exact symplectic* if,

$$[D\mathcal{T}]^t \omega D\mathcal{T} = \omega \tag{2.12}$$

where $D\mathcal{T}$ is the Jacobian matrix of $\mathcal{T}$,

$$(D\mathcal{T})_{i,j} = \frac{\partial z'_i}{\partial z_j}\,. \tag{2.13}$$

2.3 *Twist* maps

A *twist* map (with *twist* to the right) is a particular case of a symplectic two dimensional map with a phase space (x, y) homeomorfic to a cylinder, such that it fulfills the *twist condition*,

$$\left.\frac{dx'}{dy}\right|_x \geq K \geq 0 \tag{2.14}$$

where x corresponds to the angular coordinate. The condition implies that x' is a monotonic growing function of y, see Fig. 2.2.

The twist condition has a natural physical interpretation: y is the coordinate that represents the *linear momentum* and the twist condition implies that as y grows bigger, the displacement x will be longer, because its *velocity* will be higher. However in generalized hamiltonian systems, like in the one of streamfunctions, this may not hold true since y can be unrelated to $\dot{x}$.

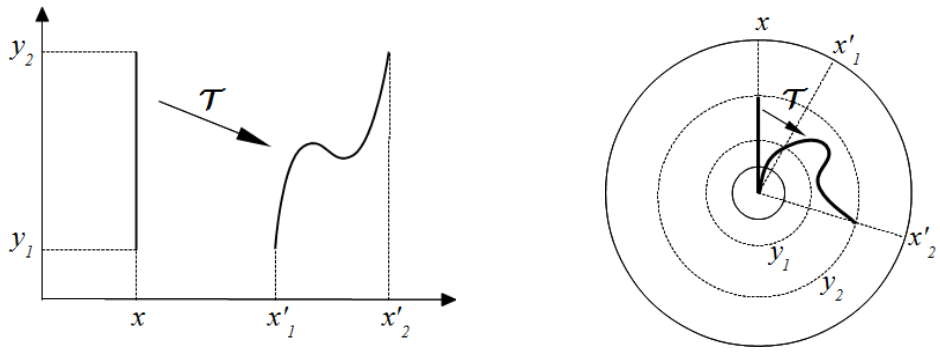

Figure 2.2: Geometric interpretation of the *twist* condition (2.14), in cartesian (a) and polar (b) coordinates.

It must be noted that even if a map $\mathcal{T}$ is *twist*, its iteration $\mathcal{T}^2$ will not necessarily be too. However, its inverse $\mathcal{T}^{-1}$ is a *twist* map, with *left twist*. The composition of (positive) twist maps is denoted as *positive tilt map*[26] in the literature. Although, tilt maps share many features with twist maps it is easy to see that in general tilt maps in general are not twist.

Commonly it is assumed that *twist* maps are particular cases of *symplectic* maps, even though it is possible to have two-dimensional maps that are only twist. To avoid confusion, the *twist* maps that are symplectics are named *area preserving twist maps* (or APTM). An important result on these maps is the following,

Theorem 2.1. *(Birkhoff 1920; Herman 1983; Mather 1984)*
Suppose $\mathcal{T}$ is a C^1 APTM on the cylinder. Let U be an open invariant set homeomorphic to the cylinder such that there are $a < b$ satisfying

$$\{x, y : y < a\} \subset U \subset \{x, y : y < b\}$$

then the boundary of U (∂U)is the graph $\{x, Y(x)\}$ of some continuous function Y.

Proof: See Ref. [22].

2.4 Near-integrability results

The systems described in previous sections have been subject of study since times of Newton if not before and to study them several classifications have been introduced, the most useful one between integrable and non-integrable systems. Paraphrasing Ref. [22], a system is called *integrable* when the motion is "simple" in some way. Among the many different definitions of integrability, the notion used in this work is the integrability in sense of Liouville.

An *integral* is a function of the $2N$-dimensional phase space $I(z)$, which is invariant under the dynamics of the system (a hamiltonian flow or the map),

$$I(\mathcal{T}(z)) = I(z)\,. \tag{2.15}$$

To exclude trivial numerical constants, it is assumed $\nabla I \neq 0\ \forall z$. This implies $I =$constant defines a $2N-1$-dimensional surfaces in the phase space. A set of N integrals are *independent* if their gradients span an $N-$dimensional vector space at each point in the phase space and the set is in *involution* if all mutual Poisson brackets vanish,

$$\{I^j, I^k\} := \sum_{\ell=1}^{N} \left[\frac{\partial I^j}{\partial q_\ell}\frac{\partial I^k}{\partial p_\ell} - \frac{\partial I^j}{\partial p_\ell}\frac{\partial I^k}{\partial q_\ell}\right] = 0\,. \tag{2.16}$$

A map is integrable in the sense of Liouville if it satisfies the following theorem.

Theorem 2.2. *(Arnol'd-Liouville)*
If there are N independent integrals in involution, then the motion lies on a nested family of N-dimensional tori, and there exist angle coordinates θ such that the map can be written in the form,

$$I' = I\,, \tag{2.17}$$
$$\theta' = \theta + \Omega(I)\,. \tag{2.18}$$

Proof: See Refs. [22] and [23].

Although integral systems are present in some relatively simple physical models, they are not the norm. Nevertheless many systems susceptible to be studied can be written as a special kind of non-integrable systems, the

near-integrable systems. The later are in most cases systems that depend on one or more parameters such that for some ranges of values, the systems are integrable. The perturbed map $\mathcal{T}_\epsilon$ is written,

$$I' = I + f_\epsilon(I, \theta)\,, \tag{2.19a}$$
$$\theta' = \theta + \Omega(I) + g_\epsilon(I, \theta)\,, \tag{2.19b}$$

and for simplicity we can consider that for $\epsilon = 0$ the map (2.19) becomes integrable.

A useful definition to characterize and label orbits of a map on a cylinder is the *rotation number*, originally intrduced by Poincaré for orientation preserving homeomorphisms of the circle[99].

Definition 1. *Let $\mathcal{T}$ be map in the cylinder, $\mathcal{T} : \mathbb{S} \times \mathbb{R} \to \mathbb{S} \times \mathbb{R}$. The lift of $\mathcal{T}$ is the map $T : \mathbb{R}^2 \to \mathbb{R}^2$ such that $\mathcal{T} = T \circ h$, where h is just the* mod 1 *function in the first variable, the angle variable for $\mathcal{T}$.*

Definition 2. *The rotation number ω of an orbit is defined as the limit*

$$\lim_{n\to\infty} \frac{\phi_n - \phi_0}{n}\,, \tag{2.20}$$

where ϕ is the lift *of the* angle variable. *When the limit exist, it is independent of the choice of the starting point ϕ_0.*

It can be proved that if the map is twist, then for all orbits for which the limit exist, are labeled and ordered by this quantity. An obvious remark is that all periodic orbits that may exist in a twist map have $\omega \in \mathbb{Q}$.

Theorem 2.3. *(Birkhoff 1927; Berry 1978)*
Suppose $\mathcal{T}_\epsilon$ is a APTM on the cylinder such that $\mathcal{T}_\epsilon|_{\epsilon=0} = \mathcal{T}_0$ is an integrable map. Let $\mathcal{C}$ and invariant circle with rotation number $\omega = p/q$ (p ad q prime relatives) for $\mathcal{T}_0$. Then for a sufficient small ϵ, there will exist an even number: $2kq$, $k \in \mathbb{N}$ of fixed points for the map $(\mathcal{T}_\epsilon)^q$, where half of the fixed points will have elliptic linear stability and the other hyperbolic linear stability.

Proof: See Ref. [24].

This theorem gives a picture of the shape of the phase space near the periodic orbits, however, as illustrated in Fig. 2.3, there are many ways to

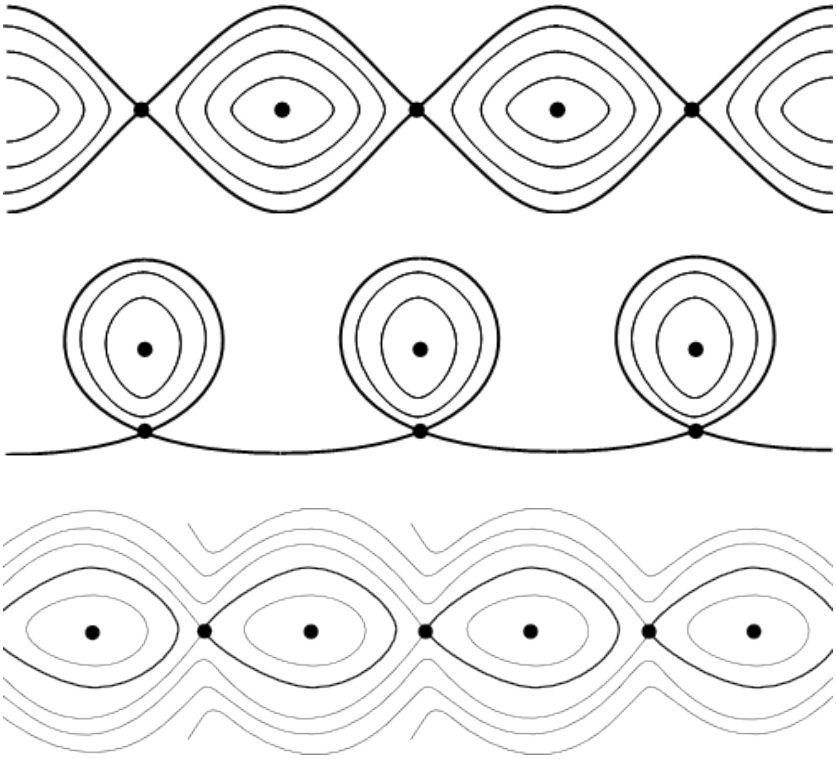

Figure 2.3: Illustration of different ways to *connect* the points of a periodic orbit of a APTM.

connect the hyperbolic points. The structures around the periodic orbit points is called "resonance" and one of the few possible ways to analitically characterize its shape is by asympthotic tools like the normal forms (discussed in chapter 3).

One more definition is needed to state the last result,

Definition 3. *An irrational number ω is said to be Diophantine if for a given τ there is a constant ν such that,*

$$|\omega \cdot q - p| \geq \nu |q|^{-\tau},\ p \in \mathbb{Z},\ q \in \mathbb{Z} \setminus \{0\}.$$

We will denote the set of all numbers satisfying Definition 3 by $\mathcal{D}(\nu, \tau)$.

Theorem 2.4. *(Moser, 1973)*
Let $\mathcal{T}_\epsilon$ be a 1-parameter family of C^j twist maps of the form of (2.19), then

there is a $\epsilon > 0$ *such that if* $f(I,\theta)$ *has zero average,*

$$\int_0^1 f(I,\theta)d\theta = 0\,, \tag{2.21}$$

with

$$\sup_{m+n<j}\left|\frac{\partial^{m+n}f}{\partial I^m\partial\theta^n}\right| + \sup_{m+n<j}\left|\frac{\partial^{m+n}g}{\partial I^m\partial\theta^n}\right| < \epsilon K\nu^2 \tag{2.22}$$

have rotational[2] *invariant circles for all rotation numbers that satisfy a Diophantine condition with*

$$1 < \tau < \frac{j-1}{2}\,. \tag{2.23}$$

Proof: See Ref. [22].

This theorem implies among many things, that all the rotation circles with rational rotation number are "destroyed" as soon as $\epsilon \neq 0$. There are however examples non C^1 maps in which this does not happen, however these are not a generic kind of maps [27].

2.5 The standard map

The standard map or Chirikov-Taylor map is a locally symplectic map defined by

$$x_{n+1} = x_n + y_{n+1}\,, \tag{2.24a}$$
$$y_{n+1} = y_n + \epsilon V'(x_n)\,, \tag{2.24b}$$

where $x_n \in \mathbb{S}^1$, $y_n \in \mathbb{R}$ and $V' : \mathbb{S}^1 \to \mathbb{R}$ is a function with zero average:

$$\int_0^{2\pi} V'(x)\,dx = 0\,. \tag{2.25}$$

One of the most popular choices of potential is $V(x) = \cos(x)$ (or $V(x) = \frac{1}{(2\pi)^2}\cos(2\pi x)$ for a different scaling), which yields,

$$x_{n+1} = x_n + y_{n+1}\,, \tag{2.26a}$$
$$y_{n+1} = y_n - \epsilon\,\sin(x_n)\,. \tag{2.26b}$$

[2]Circles in the cylinder not homotopic to points.

For notation purposes, the map (2.24) will be referred as the *standard map* and the specific form of the map (2.26) as the *Chirikov-Taylor map*.

This map can be obtained from different physical system models (see Ref. [22, 25]), but what gives it the surname of "standard" is the fact that it is usually the result of the linearization almost any twist map around a resonance.

The main relevance of this map is that it is a very simple model that displays very clearly the behavior of near integrable systems. For $\epsilon = 0$, the map (2.26) is *integrable*, which in this case means that its evolution from any initial condition and the general structure of its phase space is know at all times. And for $\epsilon \ll 1$, all theorems from previous sections apply and additionally others results, like the Aubry-Mather theory.

2.6 Greene residue

J. Greene developed a criteria (Ref. [18]) to predict the (existence/persistence) of invariant circles that is closely related to the renormalization group theory. It start with the definition of the (Greene's) *residue*.

The linear stability around the fixed point of periodic orbit $\omega = m/n$ of a given twist map $\mathcal{T}$ can be determined by the behavior of the eigenvalues of the iterated map $\mathcal{T}^q$ around each point,

$$\begin{aligned} \delta z &= \left[\frac{d}{dz_0}\mathcal{T}(\mathcal{T}(\cdots(\mathcal{T}(z_0)))\right]\delta z_0 \\ &= \mathcal{M}(z_{n-1})\mathcal{M}(z_{n-2})\cdots\mathcal{M}(z_0)\delta z_0 \\ &= \mathcal{M}^n\delta z_0\,. \end{aligned} \tag{2.27}$$

where $\mathcal{M}(z)$ is the Jacobian matrix. Since $\mathcal{M}(z)$ is symplectic, so is $\mathcal{M}(z)^n$, which implies that if λ is an eigenvalue, then so is λ^{-1}, which implies that $det(\mathcal{M}^n) = 1$. From the characteristic polynomial $\lambda^2 - \lambda\mathrm{Tr}(\mathcal{M}^n) + 1 = 0$, we obtain,

$$\lambda = \frac{1}{2}\left\{\mathrm{Tr}(\mathcal{M}^n) + \sqrt{(\mathrm{Tr}(\mathcal{M}^n))^2 - 4}\right\}\,. \tag{2.28}$$

The possible stability properties are shown in table 2.1, in which it has been introduced the (Greene's) *residue*, defined as,

$$R = \frac{1}{4}[2 - \mathrm{Tr}(\mathcal{M}^n)]\,. \tag{2.29}$$

Stability	λ	R	$\mathrm{Tr}(\mathcal{M}^n)$
hyperbolic	> 0	< 0	> 2
elliptic	$e^{2\pi i\omega}$	(0,1)	$(-2, 2)$
reflection hyperbolic	< 0	> 1	< -2

Table 2.1: Stability classification.

With this classification, the only (neutral) stable case is the elliptic. And from this Greene developed a method for determining the existence of an invariant circle by looking at the stability of nearby periodic orbits. The conjecture is that if there is an infinite set of periodic orbits ordered by their period whose rotation numbers $\{\omega_i\}_{i\in\mathbb{I}}$ limit on the invariant circle,

$$\lim_{i\to\infty} \omega_i \to \omega \,, \tag{2.30}$$

and which have residues between zero and 1, then the invariant circle will exist. The "residue conjecture" has been proved in some cases [28] and used in many many works in the past. However this method requires to be able to compute periodic orbits of very high order ($n \gtrsim 10^5$) as in Ref. [29], which can only be done efficiently on maps with symmetries (more of this on chapter 5). This method gives rise to the introduction of renormalization theory in symplectic maps and the finding of universal critical exponents related to critical invariant circles.

2.7 Other methods: converse KAM theory

There exist other methods to prove that a certain invariant circle no longer exist. Many of them are based in the converse KAM theory: for a sufficient high value of the perturbation parameter ϵ in Thm. 2.4, there will not exist any invariant circle[3]. It is possible to use the Thm. 2.1 to find cases when KAM theory as stated on Thm. 2.4 is no longer valid.

[3]From here on, the term *invariant circle* will always be used for an invariant circle not homotopic to a point, which is the same as the *rotation invariant circle* (RIC) used in Ref. [22].

2.7.1 Resonances overlap method

The first method called Chirikov's overlap method[10] or *climbing orbits* argument[22] or simply *brute force* by some experts in the field. The argument is that if an orbit can climb arbitrary far up in the cylinder, then there are no invariant circles. The reason for this, is the incompatibility between the invariance of the circles and the area preserving property of the map for climbing orbits. If an orbit has one point bellow and down and another above an invariant circle it would imply that the image of any open compact set containing the first point would contain the second point. But if any of those sets contains a point from the invariant circle it implies that the other set and all iterations contain also a point of the circle, which can not happen.

In practice this method is very hard to implement efficiently for a couple of reasons. The first is that the map needs to have some symmetry to guarantee that a displacement on the y-axis is enough to consider that the orbit can *climb* arbitrary on the cylinder. The second is related with Aubry-Mather theory's result: when a change on the parameters cause a critical invariant circle to cease to exist, it transform into an orbit with Cantor structure and the *transit* through it may require an exponential number iterations as the perturbation parameter approaches a critical value. This has been associated with the observed algebraic convergence of the method to estimate critical values[22, 9], which translates in the need of an immense amount of iterations as the perturbation parameter gets close to a critical value. And lastly this method requires the use of a *generic* set of initial conditions that guaranties that not all of them are *trapped* inside resonances.

The concept of this method is illustrated on Fig. 2.4 and an example of the phase space of map

2.7.2 Obstruction method

Another method relevant for the discussion of this work is the *obstruction method* [30], related with the *heteroclinic connection* argument in Ref. [22] and the *overlap criterion* given by Chirikov[10]. The main idea, proved in Lemma 1 of Ref. [30], is that if there exist two hyperbolic periodic points (HPP) x_0 and x_1 with rotation numbers ω_0 and ω_1, such that the unstable invariant manifold ($W^u x_0$) of x_0 has a non empty intersection with the stable invariant manifold ($W^s x_1$) of x_1 (i.e. there exist heteroclinic points), then

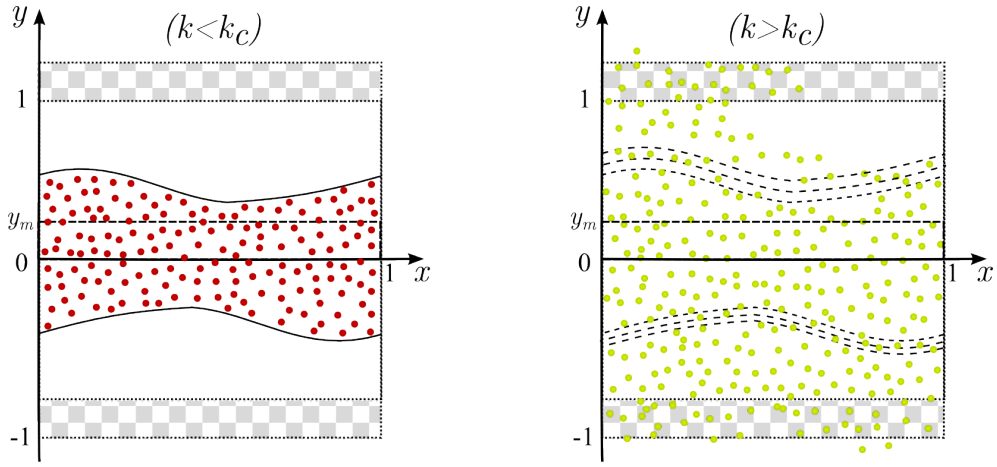

Figure 2.4: Illustration of the crossing method. The left picture depicts the case of the arbitrary iteration of a generic compact set of initial conditions (red dots) for a perturbation parameter value bellow critical, which is bounded by a topological barrier, and invariant circle. The right picture depicts the complementary case.

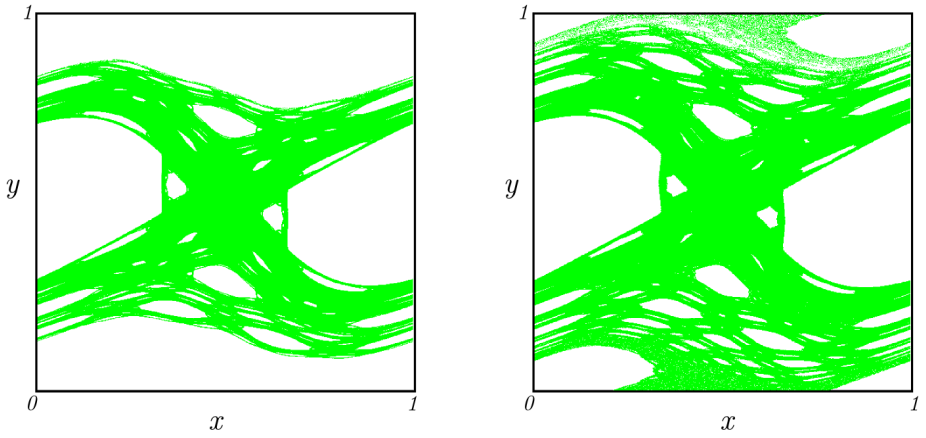

Figure 2.5: Example of the crossing method. Both figures show 3×10^6 iterations of the same single initial condition on a symplectic map (studied in chapter 4) for similar values of the parameters (κ_1, κ_2): $(-0.69, 0.525)$ on left and $(-0.73, 0.525)$ on right.

there is no invariant circle in between (with rotation number $\omega \in (\omega_0, \omega_1)$). This idea is illustrated in Fig. 2.6.

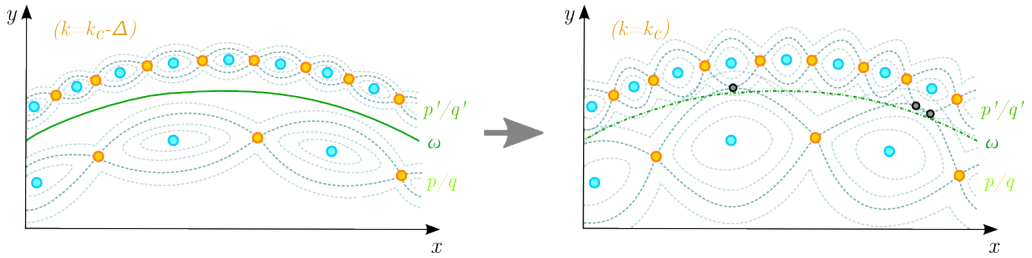

Figure 2.6: Illustration of the obstruction method. Any invariant circle (with irrational rotation number ω) that may exist between two periodic orbits ($\omega_1 = p/q$ and $\omega_2 = p'/q'$) will be destroyed if the invariant manifolds of different hyperbolic points cross.

This method can give upper bounds for critical values of the perturbation parameter for the destruction of a given invariant circle and also rescaling relations related to the invariant circle. However the method also requires to compute periodic orbits of the map and then compute the stable and unstable invariant manifolds of the hyperbolic points.

2.7.3 Cone-crossing criterion

The *Lipschitz criteria*[22], later refined in Refs. [31, 32, 33] and sometimes called *(MacKay) cone-crossing criterion*, consist in the use of Lipschitz bounds on slopes. It can be proved that the function $Y(x)$ from theorem 2.1 is Lipschitz[32], which implies that if an orbit of $(\mathrm{T}, D\mathrm{T})$,

$$(\mathrm{T}, D\mathrm{T})(z, v) = (\mathrm{T}(z), D\mathrm{T}_z v) \qquad \text{where} \qquad \begin{cases} z = (x, y) \\ v = (\delta x, \delta y) \end{cases} \tag{2.31}$$

has the n-iteration a change of sign on δx, then the orbit of z is not on an invariant circle. This is illustrated in Fig. 2.7.

This method and its refinements have been used to give upper bounds for the critical value of perturbation parameter for the standard map (2.26), with the best estimate of $\epsilon^* = 63/64 = 0.984375$, close to the optimal value calculated by Greene[18], $\kappa_G = 0.971635406....$

Although this method can give rigorous analytic bounds for the destruction of invariant circles of a given map, the computation can turn cumbersome for even for simple maps.

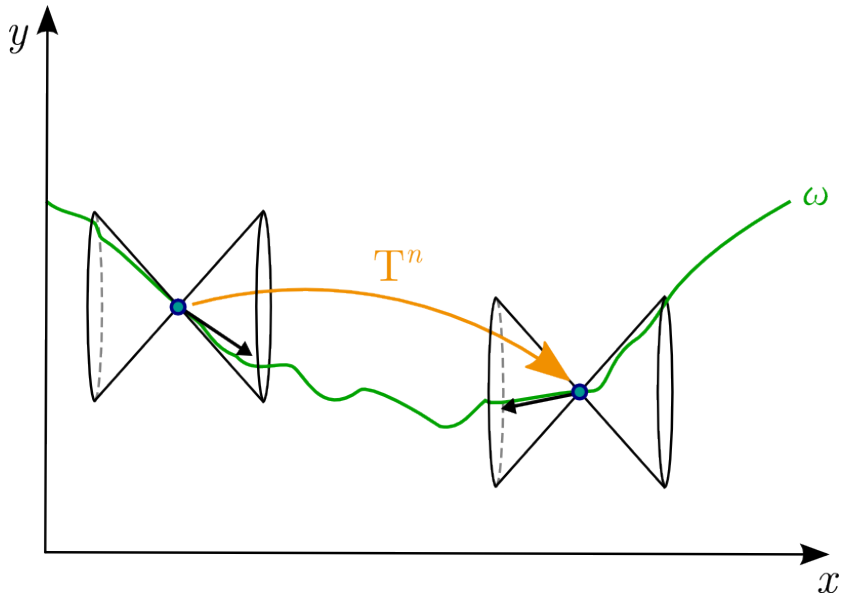

Figure 2.7: Illustration of an impossible situation in cone-crossing criterion. The x-component of a tangent vector to a point of an invariant circle can not change the sign if there exist a Lipschitz uniform bound for the invariant circle.

2.8 The parameterization method

This section describes the numerical implementation of the computation and continuation of invariant circles for a given twist map T by the so called *parameterization method*. Most of the technical details are omitted and the discussion is done over the tools that are used. For further mathematical details (e.g. function spaces, geometric preliminaries, and Diophantine properties) the reader is referred to Ref. [34, 13, 35, 11].

2.8.1 The goal

The goal of the method is to find invariant circles of T on which the dynamics is conjugated to a rigid rotation by a fixed Diophantine rotation number ω, R_ω.

The rationale of the method is best understood in the constructive proof of the KAM theorem in Ref. [35], which relies among other things on a Newton iteration in the spirit of Nash-Moser theory, see Ref. [36]. A second ingredient for the particular implementation described here is related with the area preserving properties of the type of map considered that allows the use of a symplectic change of coordinates, referred in Ref. [35] as *automatic reducibility*.

Nash-Moser techniques can be used in algorithms that allow to continue smooth functions $K : \mathbb{S}^1 \to \mathbb{S}^1 \times \mathbb{R}$ satisfying the invariance equation,

$$T \circ K(\theta) = K(\theta + \omega)\,, \tag{2.32}$$

where $T : \mathbb{S}^1 \times \mathbb{R} \to \mathbb{S}^1 \times \mathbb{R}$ is a given twist map and ω is a Diophantine number, an irrational real number such that for a given τ there is a constant ν such that,

$$|\omega \cdot q - p| \geq \nu |q|^{-\tau},\ p \in \mathbb{Z},\ q \in \mathbb{Z} \setminus \{0\}\,. \tag{2.33}$$

Starting from the integrable case of the map T, the continuation moves the parameter as close to the breakdown of analyticity of the invariant circles as possible. The criterion of breakdown in Ref. [13] is used to determine when the invariant circle ceases to exist. This criterion states that close to the breakdown of analyticity the derivatives of the solution K start to blow up at points of $K(\mathbb{S}^1)$, in the sense that all the Sobolev $||\cdot||_{H^n}$ norms diverge.

Continuation methods like the one presented here have already been used in several contexts. See for instance, Ref. [37, 12], for models in statistical mechanics, Ref. [38, 39, 40] for examples in symplectic maps, Ref. [41, 42] for conformally symplectic models, and Ref. [43] for volume preserving maps.

2.8.2 The method

The main idea of the method is to start from an approximate solution of the invariance equation applied to T and then produce a "better" approximate solution by adding a small correction. K_0 is said to be approximately invariant if

$$e_0(\theta) = T \circ K_0(\theta) - K_0(\theta + \omega)\,, \tag{2.34}$$

where $\|e_0\|$ is a small function with respect to the norm $\|\cdot\|$ of the Banach space of smooth functions.

An approximate solution is said to be "better" if it approximates the invariance equation (2.32) with a smaller error. The idea is to add a periodic function $\Delta : \mathbb{S}^1 \to \mathbb{R} \times \mathbb{S}^1$ so that $K_1(\theta) = K_0(\theta) + \Delta(\theta)$ has an error

$$e_1(\theta) = T \circ K_1(\theta) - K_1(\theta + \omega) \tag{2.35}$$

with $\|e_1\| \approx \|e_0\|^2$.

This is possible according to Nash-Moser theory, adding an appropriate correction Δ can provide an error satisfying the quadratic property above. The correction Δ that could be used, would solve the Newton step equation,

$$DT(K_0(\theta))\Delta(\theta) - \Delta(\theta + \omega) = -e_0(\theta)\,, \tag{2.36}$$

which, if we were able to solve for Δ from equation (2.36), then the norm of the new error, $\|e_1\|$ will be of order $\|e_0\|^2$.

In principle, one could try to solve numerically the Newton equation in (2.36) for Δ, but this would require $O(n^3)$ operations, where n is the number of points that one uses to represent the invariant circle. The alternative to follow is to reduce the Newton step equation (2.36) by introducing a symplectic change of coordinates around the approximate solutions. The implementation will yield methods that require $O(n \log n)$ operations.

The change of coordinates is done around an approximate solutions K_0 is given by a 2 by 2 matrix composed of two column vectors. The first 2 by 1 column is the vector $u_0 = DK_0(\theta)$ representing the tangent bundle to the approximate solution with base at every point $K(\theta)$. The second column vector $v_0(\theta)$ is a symplectic conjugate bundle which in this case of one dimensional circles reduces to a vector orthogonal to the tangent bundle, namely $v_0(\theta) = J^{-1}DK_0(\theta)N_0(\theta)$, where J is the matrix representation of the symplectic form Ω and

$$N_0(\theta) := [DK_0(\theta)^t DK_0(\theta)]^{-1}\,. \tag{2.37}$$

So the matrix can be written as follows,

$$M_0(\theta) = \Big(\ DK_0(\theta)\ \Big|\ J^{-1}DK_0(\theta)N_0(\theta)\ \Big)\,. \tag{2.38}$$

This change of coordinates is symplectic and transforms approximately the matrix $DF(K_0(\theta))$ into an upper triangular matrix with ones along the

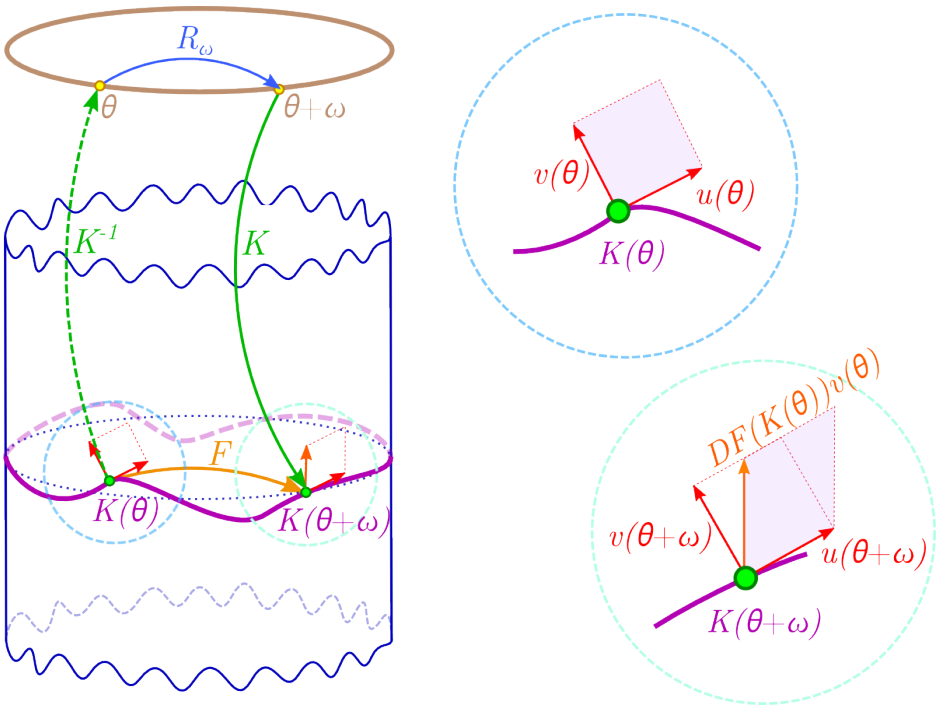

Figure 2.8: Illustration of the main components in the symplectic change of coordinates used in the implementation of parameterization method.

diagonal, namely,

$$DF(K_0(\theta))M_0(\theta) = M_0(\theta+\omega)\begin{pmatrix} 1 & S_0(\theta) \\ 0 & 1 \end{pmatrix}, \tag{2.39}$$

where

$$S_0(\theta) = N_0(\theta+\omega)DK_0^T(\theta+\omega)DF(K_0(\theta))DK_0(\theta)N_0(\theta)\,. \tag{2.40}$$

And this is consequence of the *automatic reducibility*: the map T preserves area and u_0 approximately is preserved, then v_0 must satisfy,

$$DF(K_0(\theta))v_0(\theta) = v_0(\theta+\omega) + S_0(\theta)u_0(\theta)\,. \tag{2.41}$$

The function $S_0(\theta)$ is related to the local twist condition on the invariant circle K_0. It is possible to apply the change of coordinates to the Newton

step, $\Delta(\theta) = M_0(\theta)W(\theta)$, to reduce approximately the Newton step equation. The new Newton step now requires to solve the equation,

$$\begin{pmatrix} 1 & S_0(\theta) \\ 0 & 1 \end{pmatrix} \begin{pmatrix} W_1(\theta) \\ W_2(\theta) \end{pmatrix} - \begin{pmatrix} W_1(\theta+\omega) \\ W_2(\theta+\omega) \end{pmatrix} = -M_0^{-1}(\theta+\omega)e_0(\theta)\,. \quad (2.42)$$

Now, spliting the equation (2.42) into components there are two cohomological equations to be solved, namely

$$W_2(\theta) - W_2(\theta+\omega) = -[M_0^{-1}(\theta+\omega)e_0(\theta)]_2 \quad (2.43)$$

and

$$W_1(\theta) - W_1(\theta+\omega) = -[M_0^{-1}(\theta+\omega)e_0(\theta)]_1 - S(\theta)W_2(\theta). \quad (2.44)$$

To solve the functional system of equations (2.43)-(2.44) in the Fourier space a necessary condition is that the right hand side on both equations have average zero (or of the order of $O(\|e_0\|^2)$. This can be done easily for (2.44) if the map is twist since average of W_2 is free parameter that can be adjusted as needed[4], however for the right hand side of (2.43) needs to introduce extra properties. The case of interest in the present work is when T is exact, because it can be shown that in that case by *Lemma 9* from Ref. [35],

$$\int_{\mathbb{S}^1} [M_0^{-1}(\theta+\omega)e_0(\theta)]_2\, d\theta = O(\|e_0\|^2)\,. \quad (2.45)$$

Therefore, it is possible to solve for Δ for (2.42) by following the algorithm described below.

Algorithm 2.1.

1) *Let* $e_0(\theta) = T \circ K_0(\theta) - K_0(\theta+\omega)$

2) *Compute the matrix* $M(\theta)$ *from equation* (2.38).

3) *Solve for* $W_2(\theta)$ *from* (2.43).

4) *Choose the average* $\int_{\mathbb{S}^1} W_2(\theta)d\theta$ *so that* $-[M_0^{-1}(\theta+\omega)e_0(\theta)]_1 - S_0(\theta)W_2(\theta)$ *has an average close to zero.*

5) *Solve for* $W_1(\theta)$ *from* (2.44).

[4]If the map were not twist, it could be the case that $S_0(\theta) = 0$.

6) Compute the step Δ,

$$\Delta(\theta) = M_0(\theta)W(\theta)$$

7) Obtain the new parameterization K_1,

$$K_1(\theta) = K_0(\theta) + \Delta(\theta)$$

8) Set $K_0(\theta) = K_1(\theta)$ *and go to step 1).*

Chapter 3

Periodic orbits and normal forms

A general first step to characterize a dynamical system is the study of its periodic orbits. The knowledge gained from periodic orbits can lead to understand existence and stability of quasi-periodic and more generic type of orbits, and in some cases to find very significant relations between the parameters of the complete system. In particular for the case of study, the map displays after a transient and for a particular kind of initial conditions, an oscillatory bounded evolution in its variables, see figure 1.5(a). It could be relevant for this particular behavior to know if there exist periodic orbits with the period displayed in the evolution and if these are correlated. Even if the behavior were to be quasi-periodic, the knowledge about the periodic orbits that approximate the orbit could give a hint of the stability and dependence on the initial conditions and parameters.

One of the original purposes of the present work was to determine values of the parameters for which the self-consistent map would display *global transport*, i.e. unbouded evolution of some coordinate y_k. With the approach on this chapter, it was possible to determine the asymptotic value of $\bar{\kappa}$ and $\Delta\,\kappa$ for an special kind of initial conditions and parameter values. To do this, the specific form of the mean field auxiliary variable η^n in Eq. (1.2) is taken into account to try to discriminate sets of initial conditions that let η^n to start and stay with very small values, and thus perturbing just a little the initial configuration.

One of the two approaches used to study this type of configurations was an asymptotic method known as normal form. The normal form of system

is in general the result of change of variables done over a system with the purpose of simplifying it in some way [44]. The type of normal form used in this chapter have as its final purpose to find relations between the systems dynamics and the parameters and to allow a better understanding of the dynamics of the system at different scales. This kind of parameter relations can also be found by performing a high number of simulations and performing parameters correlations, but this type of analysis can be very time consuming and often not as accurate as the results of an asymptotic method.

This chapter reviews the results from Ref. [8], in which a normal form was introduced to study the existence of certain type of discrete choreography[1]-like periodic orbits named *sequential periodic orbits* (*SPO's*).

3.1 Periodic orbits

In general, the structure of periodic solutions help determining the behavior of a dynamical system. Our goal is to show that periodic orbits are closely related to the mean-field variables (in particular $\bar{\kappa}$ and $\Delta\,\kappa$) and the choice of values of the parameters (γ_k, Ω). However, finding periodic orbits for high dimensional maps is a complex problem and numerical simulation is in principle the only procedure to estimate the values of the mean field variables. The use of simulations to study a system has the implicit problem to predict or associate the results to the initial conditions, which usually requires a large number of iterations to give substantial evidence. In the case of study, the dimension of the self-consistent map (1.1) has to be rather big (of order 10^4) and very small time steps[2] so the system can achieve similar patterns to that of the continuous single-wave model. In practice it is not possible to approach this problem in general using analytic or asymptotic tools.

One way to reduce the complexity of finding periodic orbits is to use symmetries or doing numerical continuation over a known periodic solution.

In the case of low-dimensional maps, the use of symmetries can greatly simplify the search of periodic orbits [46]. For the self-consistent map, the problem simplifies by assuming $\gamma_k = \gamma$ constant, for $k = 1, \ldots, N$ in (1.1c) which implies the following properties:

[1] In the sense of the choreographic orbits found in celestial mechanics by Chenciner and Montgomery [45].

[2] Which translates to a very large number of map iterations.

1. Let $\mathbf{z}$ be a periodic orbit of map (1.1) with dimension $2N+2$. If the initial condition of this orbit is,

$$\mathbf{z}^0 = (x_1^0, y_1^0, x_2^0, y_2^0, \ldots, x_N^0, y_N^0, \kappa^0, \theta^0)\,, \tag{3.1}$$

then any permutation of the pairs (x_i^0, y_i^0), for $i = 1, \ldots, N$, produces a new periodic orbit with the same period. This is because the term that couples the standard maps only depends on the average of the variables x_i.

2. For any periodic orbit $\mathbf{z}$ of the map (1.1) with dimension $2N+2$, it is possible to increase the dimension of the solution by replicating the orbit $\mathbf{z}$ and reducing the strength of γ by one half. Thus, for any $\mathbf{z}$ given in (3.1), a new periodic solution of dimension $2N$ is generated with the form,

$$\mathbf{z}^0 = (\underbrace{x_1^0, y_1^0, x_2^0, y_2^0, \ldots, x_N^0, y_N^0}_{2N}, \underbrace{x_1^0, y_1^0, x_2^0, y_2^0, \ldots, x_N^0, y_N^0}_{2N}, \kappa^0, \theta^0)\,,$$

with the strength of vorticity equal to $\gamma/2$. The dimension of this new orbit is $4N+2$ and the period of the orbits is the same as (3.1). In this case, since γ is rescaled by a factor of $1/2$, the function η in (1.2) preserves the value given when it is calculated at the orbit (3.1) since the N terms twice are summed twice.

With these two properties, it is possible to generate a large set of periodic orbits: starting with low dimensional map corresponding to $N = 1$ and a strength parameter γ, periodic orbits of period M can be found. Using the property 2, the orbit can be replicated s times, such that an orbit of dimension 2^s is obtained for a reduced strength in the parameter $\gamma' = \gamma/2^s$.

Another possibility is to construct a periodic orbit by imposing that the iteration of each oscillator pair (x_i^{n+1}, y_i^{n+1}) almost coincides with the next point in the orbit of the previous pair. This is, if (x_i^n, y_i^n) are the values of the i-th oscillator for the n-th iteration and (x_{i+1}^n, y_{i+1}^n) is the next point in the periodic orbit, then $(x_i^{n+1}, y_i^{n+1}) \approx (x_{i+1}^n, y_{i+1}^n)$. This kind of periodic orbits will be referred as *sequential periodic orbits* (SPO's). To generate this kind of orbits, a periodic orbit of period τ of the standard map was computed for a fixed value of κ^* and θ^*. The iterations of this orbit give the following set of pairs of coordinates:

$$(\mathsf{x}_0, \mathsf{y}_0)\ \ (\mathsf{x}_1, \mathsf{y}_1)\ \ \ldots\ \ (\mathsf{x}_{\tau-1}, \mathsf{y}_{\tau-1})\,. \tag{3.2}$$

With this sequence of points, a periodic orbit of dimension $2\tau + 2$ with period τ for the map (1.1) is constructed, giving as its initial condition,

$$\mathbf{z}^0 = (\mathsf{x}_0, \mathsf{y}_0, \mathsf{x}_1, \mathsf{y}_1, \ldots, \underbrace{\mathsf{x}_{i-1}, \mathsf{y}_{i-1}}_{i-\text{th}}, \ldots, \mathsf{x}_{\tau-1}, \mathsf{y}_{\tau-1}, \kappa^*, \theta^*)\,. \tag{3.3}$$

For $\gamma = 0$, this orbit follows a sequential pattern, the i-th pair (x_i, y_i) are shifted to the position $i-1$ in a cyclic way, for each iteration of the map.

$$\mathbf{z}^1 = (\mathsf{x}_1, \mathsf{y}_1, \mathsf{x}_2, \mathsf{y}_2, \ldots, \underbrace{\mathsf{x}_i, \mathsf{y}_i}_{i-\text{th}}, \ldots, \mathsf{x}_0, \mathsf{y}_0, \kappa^*, \theta^*)\,.$$

It is clear that this is not a periodic orbit for $\gamma \neq 0$ because the mean-field variables, κ and θ, are going to change while the orbit is iterated. Nevertheless, this is a good guess for finding a periodic orbit using numerical or asymptotical procedures for small values of γ.

Based on the previous ideas, the numerical procedure used to find a periodic orbit of (1.1) with period τ and dimension $2\tau + 2$ consists of the following steps:

Algorithm 3.1.

1. *For given values of θ^* and κ^*, a symmetric periodic orbit of period τ of the standard map is found using the symmetry lines of the map [18].*

2. *With this orbit, a sequential periodic orbit (3.2) is formed. For $\gamma = 0$ this is a periodic orbit of the self-consistent map (1.1), as in (3.3).*

3. *Using a continuation method, the sequential periodic orbit is computed for small values of γ [47] and continued for large values of γ.*

4. *The dimension of the orbit is then increased using the replication property of the map (1.1). For each replication, the strength parameter γ is divided by two.*

Note that the value of the auxiliary variable η^n is small in all iterations due the almost equidistribution on the angular variables x_i^n. Following this procedure, it is possible to compute periodic solutions for small periods. The convergence of the continuation–method requires adjusting the value of the parameter Ω in (1.1d), otherwise the variable θ might not converge to

a value. After some numerical experiments, it was concluded that for the method to converge, Ω should be a function of κ^0. Therefore, the parameter Ω was included in the numerical method as a free parameter which has to be determined by the continuation process.

In a similar way, a perturbative method was used to determine periodic orbits. The idea was to compute a sequential periodic orbit in an asymptotic way. Begin the process with an integrable map, in this case, map is (1.1) with the parameter γ and the variable κ^n are zero. For this integrable case, the periodic solution with period q is:

$$\begin{aligned} \mathbf{z}^0 &= (x_1^0, y_1^0, x_2^0, y_2^0, \ldots, \underbrace{x_j^0, y_j^0}_{j-\text{th}}, \ldots, x_q^0, y_q^0, \kappa^0, \theta^0) \\ &= (\rho, \rho, 2\rho, \rho, \ldots, \underbrace{j\rho, \rho}_{j-\text{th}}, \ldots, q\rho, \rho, 0, \theta_0)\,. \end{aligned} \tag{3.4}$$

where $\rho = 2\pi p/q$, $p, q \in \mathbb{Z}^+$ and θ_0 is a constant. The iteration of this initial orbit has simple dynamics: $x_i^j \to x_i^{j+1} = x_{i+1}^j$, $y_i^j = y_i^{j+1}$, $\kappa^j = 0$ and $\theta^j = \theta_0$, where the variables x and θ are defined in the interval $[0, 2\pi)$. The integrable periodic orbit (3.4) is the initial point of the asymptotic procedure. The small parameter in the method is γ and the variable κ^j has to be small as well. κ^j is also set to be of order $O(\gamma)$.

3.2 Normal Forms

As mentioned before, the normal form of system is generally speaking, the result of change of variables done over a system with the purpose of simplifying it in some way [44]. The concept of normal form goes back to Poincaré and for this reason, there are many different approaches for different problems [48]. The type of normal form used in this chapter have as its final purpose to find relations between the systems dynamics and the parameters. The particular normal form approach used on this work, is the one from Ref. [49]. The proposed change of variables is written as an infinite series such that the initial evolution equations are rewritten as a Poincaré-Lindstedt system ordered by a small parameter. In this case of study, the small parameter corresponds to the initial value of $\varepsilon = \kappa^0$, where γ is also assumed small. Of course, this choice is arbitrary since the objects of interest are periodic orbits. Therefore it is always possible to take a different choice, for instance κ^1.

A big difference with [49] is that instead of introducing a single change of variables for a 2-dimensional map, for the $2N+2$-dimensional map, a change of variables is proposed for each oscillator (x_k, y_k) with the *a priori* condition that all the oscillators and the mean field (κ, θ) have the same *rational* winding number $\omega = 2\pi p/q$, $p/q \in \mathbb{Q}$. The reason of this condition is that the effective number of variables needed is decreased and it avoids the introduction of an extra change of variables for the *mean field* map. In order to prepare the map (1.1) in a suitable form, equations (1.1a) and (1.1b) are rewritten in a Lagrangian form,

$$x_k^{n+1} - 2x_k^n + x_k^{n-1} = -\kappa^{n+1} \sin(x_k^n - \theta^n) \tag{3.5a}$$

$$\kappa^{n+1} = \sqrt{(\kappa^n)^2 + (\eta^n)^2} + \eta^n \tag{3.5b}$$

$$\theta^{n+1} = \theta^n - \Omega + \frac{1}{\kappa^{n+1}} \frac{\partial \eta^n}{\partial \theta^n} \tag{3.5c}$$

The proposed change of variables for each oscillator is

$$x_k = \zeta + \omega k + g(\zeta + \omega k, \kappa^0), \tag{3.6}$$

where ω is a given winding number and $g(\phi, \varepsilon)$ is given by

$$g(\phi, \varepsilon) = \sum_{j=0}^{\infty} \varepsilon^j \sum_{m \in \mathbb{Z}} g_{j,m}\, e^{im\phi}. \tag{3.7}$$

Substituting (3.6)-(3.7) in (3.5a) yields for each oscillator the *same* homological equation[3]:

$$\sum_{j=0}^{\infty} (\kappa^n)^j \sum_{m \in \mathbb{Z}} g_{j,m}\, e^{im\zeta_k^n} c_m = \frac{\sqrt{(\kappa^n)^2 + (\eta^n)^2} + \eta^n}{2i} \{ e^{i(x_k^n - \theta^n)} - e^{-i(x_k^n - \theta^n)} \}, \tag{3.8}$$

where

$$c_m := 2(1 - \cos(2\pi m p/q)), \tag{3.9}$$

$$\eta^n = \frac{\gamma}{2} \sum_{k'=1}^{N} \left\{ \exp\left(i(x_{k'}^n - \theta^n)\right) + \exp\left(-i(x_{k'}^n - \theta^n)\right) \right\}. \tag{3.10}$$

[3]The equation still depends on the label k of each oscillator, but it can be absorbed in the angular variable: $\zeta_k := \zeta + \omega k$

To solve (3.8), a relation between the two *small* parameters (γ and κ^0) is imposed [4] so the homological equation can be organized hierarchically in terms of a single variable $\varepsilon = \kappa^0$, as in the Poincaré-Lindstedt method. This relation is added in order to have a well ordered set of equations for the perturbation analysis, and it is not a physical constraint that the system must necessarily obey. The lowest order at which the problem can be solved is: $\gamma \propto \kappa^0$ or $\gamma = \alpha\kappa^0$, $\alpha \in \mathbb{R}$. Also, for (3.10) to be summable at order $O(1)$, the mean value of g must be zero on each change of variables.

From (3.9), it is obvious that there will be cases were (3.8) will not be solvable. The terms on the right hand side that can not be eliminated, give the *normal resonant form* of (3.5a). In general the normal form has the following structure,

$$x_k^{n+1} - 2x_k^n + x_k^{n-1} = \sum_{\ell=q}^{\infty} \left(\kappa^0\right)^\ell \left\{ c_\ell^+(\alpha)\, e^{i\ell\left(\zeta_k^n - \theta^n\right)} + c_\ell^-(\alpha)\, e^{-i\ell\left(\zeta_k^n - \theta^n\right)} \right\}. \quad (3.11)$$

The next step is to substitute the computed $g(\phi, \varepsilon)$ in the map to find the needed initial conditions and additional parameters to have these p/q-*periodic orbits*, will be referred as *sequential periodic orbits* (SPO's).

After such substitution on the map and its next q iterations, it was found that for given κ^0 and α small, the *sequential periodic orbits* exist only for a certain value of the parameter $\Omega = \Omega(\kappa^0, \alpha)$, if the initial conditions of the oscillators are taken *near* the *fixed points*[5]: hyperbolic, elliptic or a mixed type.

3.2.1 Normal form compared with numerical continuation

In order to compare the results from normal forms with a numerical continuation procedure (based in a Newton method), the two different kinds (hyperbolic and elliptic) of initial conditions were computed for period three SPO, that is period $\tau = 2\pi/3$. Appendix 3.A contains the detailed calculations from the normal form for this period. The most significant results are

[4] For the perturbation analysis to work, it must be assumed that both parameters are small. Notice that this assumption is consistent since both parameters can be traced back to the perturbation parameter of the standard map.

[5] Actually fixed points for the map iterated q times.

the change of variables[6],

$$g(\zeta^0,\kappa^0) = \frac{\kappa^0}{3}\sin(\phi^0)+\frac{(\kappa^0)^2}{18}\sin(2\phi^0)+\frac{(\kappa^0)^3}{216}\sin(\phi^0) + \frac{\alpha(\kappa^0)^3}{48}\big(\cos(2\phi^0)-\cos(4\phi^0)\big)+O((\kappa^0)^4)\,, \tag{3.12}$$

the resonant normal form,

$$\zeta^1-2\zeta^0+\zeta^{-1} = -\frac{(\kappa^0)^3}{24}\sin(3\phi^0)+O((\kappa^0)^4), \tag{3.13}$$

and relations among the parameters for the existence of the SPO's

$$\Omega = \frac{\alpha\kappa^0}{2}-\frac{\alpha(\kappa^0)^2}{8}+\frac{\alpha(\kappa^0)^3}{324}+O(\alpha(\kappa^0)^4), \tag{3.14}$$

for the SPO *around* the linear elliptic fixed points of the standard map and

$$\Omega = \frac{\alpha\kappa^0}{2}+\frac{\alpha(\kappa^0)^2}{8}+\frac{\alpha(\kappa^0)^3}{324}+O(\alpha(\kappa^0)^4), \tag{3.15}$$

for the SPO *around* the linear hyperbolic fixed points.

A numerical continuation method, based in a Newton method, was used to compute the previous sequential periodic orbits. Following Algorithm 3.1 a periodic orbit with the same rotation number as the sequential periodic orbit was computed for the standard map (2.26) with value of the parameter $\varepsilon = \kappa^0$ and $\theta* = 0$. However, in order to have convergence in the Newton method, it was necessary to define Ω as a free parameter. So in this way, the numerical procedure converges for a specific value of Ω.

The results from normal forms and the continuation method matched to machine precision, in particular, as it can be appreciated in Figures 3.1 and 3.2, there was a very good agreement in the relations between κ^0 and Ω for the existence of the computed SPO's.

A conclusion obtained of the use of normal forms is that the existence of this particular kind of periodic orbits, the SPO's, is tied to specific values of one parameter Ω as function of γ and κ^0, depending on the type of initial conditions. Nevertheless due the periodicity of the orbits, the same can be

[6]Where: $\phi^k := \zeta^k - \theta^k$.

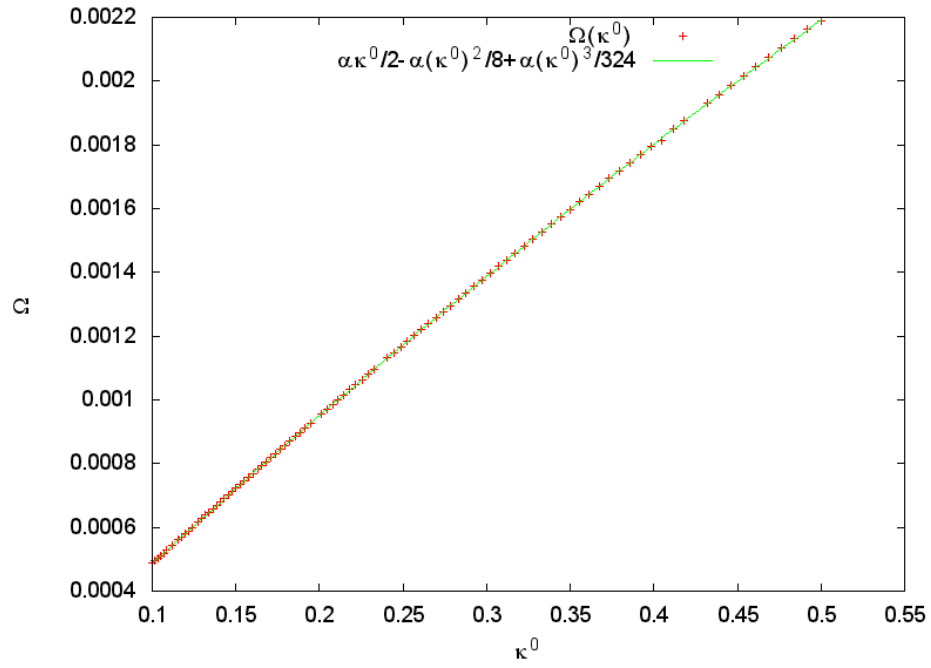

Figure 3.1: The figure displays in red the values of Ω for a given κ^0 (with $\alpha = \frac{1}{100}$) found by using numerical continuation of a sequential periodic orbit with winding number $\omega = \frac{2\pi}{3}$, that started from the linear elliptic *fixed* points. The overlapped green line correspond to parameter relation (3.14) found with normal forms.

said for any iteration of the orbit. However, it is possible to calculate the first variation on κ^n:

$$\Delta\kappa = \kappa^1 - \kappa^0 \simeq \frac{\alpha^2(\kappa^0)^4}{64}\,. \tag{3.16}$$

This implies that κ^0 and $\Delta\kappa$ can be calculated as functions of the parameters Ω and γ, and so $\bar{\kappa}$ (average of κ^n). This is evidence that a simple oscillatory behavior of the mean field variable κ is tied to a relation between the parameter values and critical value κ^0.

In a more general dynamics, the oscillatory evolution of the variable κ (as the observed in Fig. 1.5) can be pictured as if it is driven by a set of orbits close to periodic orbits, periodic orbits associated to particular ratios of the parameters of the evolution and the variable κ. Due this hypothesis,

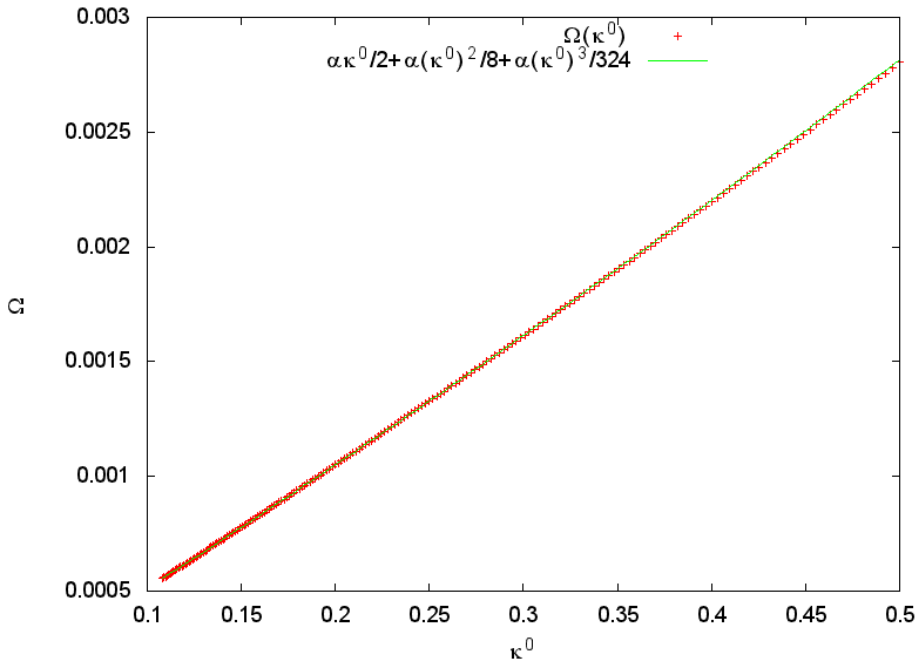

Figure 3.2: The figure displays in red the values of Ω for a given κ^0 (with $\alpha = \frac{1}{100}$) found by using numerical continuation of a sequential periodic orbit with winding number $\omega = \frac{2\pi}{3}$, that started from the linear hyperbolic *fixed* points. The overlapped green line correspond to parameter relation (3.15) found with normal forms.

a study on the frequency space of κ for long times is deemed relevant. *It will be presented in a future chapter...*

Appendix 3.A

As an example in detail of how is the homological equation solved, this appendix contains the steps to compute the first terms of the change of variables $g(\phi, \varepsilon)$, the resonant normal form and the corresponding dependence of $\Omega(\kappa^0)$ for the sequential periodic orbit with period $\tau = 2\pi/3$.

1. Write the zeroth order of the homological equation (3.8), substituting

$(\gamma = \alpha\,\kappa^0)$[7],

$$\sum_{m\in\mathbb{Z}} g_{0,m}\, e^{im\zeta^0} c_m = 0, \tag{3.17}$$

where for this case is,

$$c_k = \begin{cases} 0, & \text{k=3m} \\ 3, & \text{k=3m+1} \\ 3, & \text{k=3m+2} \end{cases}, \quad m \in \mathbb{Z} \tag{3.18}$$

and the sub-index k on ζ_k^n has been omitted since the value of ζ does not change with k in this case. There exist several free parameters that can be used later, but for the moment let assume them all to zero, meaning

$$g_{0,m} = 0 \qquad \forall m \in \mathbb{Z}. \tag{3.19}$$

2. Write the next order, (κ^0) of the homological equation,

$$\sum_{k\in\mathbb{Z}} g_{1,k} e^{ik\zeta^0} c_k = \frac{1}{2i}\left(e^{i(\zeta^0-\theta^0)} - e^{-i(\zeta^0-\theta^0)}\right). \tag{3.20}$$

From which, by orthogonality of the functions, it is obtained,

$$g_{1,1} = \frac{1}{6i} e^{-i\theta^0}, \qquad g_{1,-1} = \frac{-1}{6i} e^{i\theta^0}. \tag{3.21}$$

and set the remaining $g_{1,m}$ to 0.

3. Repeat the process for the following orders.

Up to order $((\kappa^0)^3)$, compute,

$$g_{2,2} = \frac{1}{36i} e^{-i2\theta^0}, \qquad g_{2,-2} = \frac{-1}{36i} e^{i2\theta^0}, \tag{3.22}$$

$$g_{3,\pm4} = -\frac{\alpha}{96} e^{\mp 4i\theta^0}, \quad g_{3,\pm2} = \frac{\alpha}{96} e^{\mp 2i\theta^0}, \quad g_{3,\pm1} = \mp\frac{1}{432i} e^{\mp i\theta^0}. \tag{3.23}$$

At this order appears the first resonant terms,

$$c_3\Big|_0\, g_{3,\pm3} = \pm\frac{1}{48i} e^{\mp 3i\theta^0} \tag{3.24}$$

[7]It is important to remind that the upper index 0 is just a reference, the value of γ will not change from iteration to iteration even though the change of variables g and the *normal form* are used to evaluate iterations of the map.

4. Adding these results gives the change of variables[8],

$$g(\zeta^0,\kappa^0) = \frac{\kappa^0}{3}\sin(\phi^0)+\frac{(\kappa^0)^2}{18}\sin(2\phi^0)+\frac{(\kappa^0)^3}{216}\sin(\phi^0) + \frac{\alpha(\kappa^0)^3}{48}\big(\cos(2\phi^0)-\cos(4\phi^0)\big)+O((\kappa^0)^4), \quad (3.25)$$

and the resonant normal form,

$$\zeta^1-2\zeta^0+\zeta^{-1} = -\frac{(\kappa^0)^3}{24}\sin(3\phi^0)+O((\kappa^0)^4). \quad (3.26)$$

5. Substituting (3.25) and (3.26) in the map (3.5), it is possible to solve the mean field or, in other words, to establish the needed initial conditions and the parameters to have the same period for the variables κ and θ.

   (a) κ^n: Substitute (3.25) into map in (3.5b), to obtain,

   $$\kappa^1 = \kappa^0\Big(1+\frac{\alpha(\kappa^0)^2}{6}\sin(3\phi^0)+O((\kappa^0)^4)\Big), \quad (3.27)$$

   and then substitute in the following iterates,

   $$\kappa^3 = \kappa^0+\frac{\alpha(\kappa^0)^3}{6}\Big(\sin(3\phi^0)+\sin(3\phi^1)+\sin(3\phi^2)\Big)+O((\kappa^0)^5) \quad (3.28)$$

   So, the condition to have period 3 in κ^n is,

   $$\sin(3\phi^0)+\sin(3\phi^1)+\sin(3\phi^2) = O((\kappa^0)^2). \quad (3.29)$$

   (b) (x^n,y^n): After substituting (3.26) into (3.5a) and imposing $\zeta_3-\zeta_0-2\pi=0$, a similar condition is found,

   $$\sin(3\phi^0)+\sin(3\phi^1)+\sin(3\phi^2) = O(\kappa^0). \quad (3.30)$$

   (c) θ^n: Substituting (3.25) and the results for κ^n into the map in (1.1d), yields a different condition[9],

   $$\theta^3 = \theta^0-3\Omega+\frac{3}{2}\alpha\kappa^0-\frac{\alpha(\kappa^0)^2}{8}\Big[\sum_{j=0}^{2}\mathrm{c}(3\phi_j)+\frac{1}{2}\sum_{j=0}^{2}\mathrm{s}(3\phi_j)\Big] + \frac{3\alpha(\kappa^0)^3}{324}+\frac{\alpha^2(\kappa^0)^3}{24}[4\mathrm{s}(3\phi^0)+3\mathrm{s}(3\phi^1)-\mathrm{s}(3\phi^2)]+O(\alpha(\kappa^0)^4)\,. \quad (3.31)$$

[8]Where: $\phi^k := \zeta^k-\theta^k$.

[9]Where $\mathrm{s}(\phi)\equiv\sin(\phi)$ and $\mathrm{c}(\phi)\equiv\cos(\phi)$.

The conditions (3.29), (3.30) and (3.31) can only be solved in the general case when restricted to the fixed points (of the map iterated q times). After the change of variables, $\phi = \frac{2n\pi}{3}$ ($\phi = \frac{(2n+1)\pi}{3}$) corresponds to the linear elliptic (hyperbolic) fixed points at least at order κ^0.

Then (3.29) and (3.30) are satisfied and (3.31) yields,

$$\Omega = \frac{\alpha\kappa^0}{2} - \frac{\alpha(\kappa^0)^2}{8} + \frac{\alpha(\kappa^0)^3}{324} + O(\alpha(\kappa^0)^4), \tag{3.32}$$

for linear elliptic *fixed* points and

$$\Omega = \frac{\alpha\kappa^0}{2} + \frac{\alpha(\kappa^0)^2}{8} + \frac{\alpha(\kappa^0)^3}{324} + O(\alpha(\kappa^0)^4), \tag{3.33}$$

for linear hyperbolic *fixed* points.

If $\kappa^1 = \sqrt{(\kappa^0)^2 + (\eta^0)^2} + \eta^0 \simeq \kappa^0 + \eta^0 + O((\eta^0)^2/\kappa^0)$, it is possible to expand $\eta^0 = \gamma \sum \sin(x_k^0 - \theta^0)$, from which after substituting x_k^0 from (3.6), it is obtained

$$\kappa^1 - \kappa^0 \simeq \frac{\alpha^2(\kappa^0)^4}{64}. \tag{3.34}$$

Table 3.1 shows the change of variables, normal resonant form and $\Omega(\kappa^0)$ relations for two kinds of initial conditions (elliptic and hyperbolic fixed points) for given rotation numbers.

The three examples show that the relation of the asymptotic value of the mean field variables with the parameters of the self–consistent map (1.1). For each rotation number of the sequential periodic orbit it is obtained a specific value of the average of κ and the amplitude of its oscillation. Table 3.1 shows these values for rotation numbers 1/2, 1/3 and 1/6. The main point is the relation between Ω and κ^0. Fixing the values of the parameters γ and Ω, the average value of kappa can be found, where $\bar{\kappa} = \kappa^0$ by using equations (3.14) and (3.15) and the relation $\gamma = \alpha\kappa^0$. The amplitude of the variation of κ is given by $\Delta\,\kappa = \max|\kappa^i - \kappa^0|$, for $i = 1, \ldots, N$, which first approximation is written in (3.16). This method can be used for any sequential periodic orbits of period τ.

$1/q$	
$1/2$	$g(\zeta^0,\kappa^0) = \frac{\kappa^0}{4}\sin(\phi^0) + \frac{\alpha(\kappa^0)^2}{32}\left(\cos(\phi^0) - \cos(3\phi^0)\right) - \frac{(3-\alpha^2)(\kappa^0)^3}{512}\sin(\phi^0) + \frac{(1+\alpha^2)(\kappa^0)^3}{512}\sin(3\phi^0) - \frac{\alpha^2(\kappa^0)^3}{512}\sin(5\phi^0) + O((\kappa^0)^4)$ $\zeta^1 - 2\zeta^0 + \zeta^{-1} = -\frac{(\kappa^0)^2}{a}\sin(2\phi^0) + \frac{\alpha(\kappa^0)^3}{32}\left(\cos(4\phi^0) - 1\right) + O((\kappa^0)^4)$ *Elliptic:* $\Omega = O((\kappa^0)^4)$ *Hyperbolic:* $\Omega = \frac{\alpha\kappa^0}{2} - \frac{\alpha(\kappa^0)^2}{64}(1+\alpha^2) + \frac{3\alpha(\kappa^0)^3}{128} + O(\alpha(\kappa^0)^4)$
$1/3$	$g(\zeta^0,\kappa^0) = \frac{\kappa^0}{3}\sin(\phi^0) + \frac{(\kappa^0)^2}{18}\sin(2\phi^0) + \frac{(\kappa^0)^3}{216}\sin(\phi^0) + \frac{\alpha(\kappa^0)^3}{48}\big(\cos(2\phi^0) - \cos(4\phi^0)\big) + O((\kappa^0)^4)$ $\zeta^1 - 2\zeta^0 + \zeta^{-1} = -\frac{(\kappa^0)^3}{24}\sin(3\phi^0) + O((\kappa^0)^4)$ *Elliptic:* $\Omega = \frac{\alpha\kappa^0}{2} - \frac{\alpha(\kappa^0)^2}{8} + \frac{\alpha(\kappa^0)^3}{324} + O(\alpha(\kappa^0)^4)$ *Hyperbolic:* $\Omega = \frac{\alpha\kappa^0}{2} - \frac{\alpha(\kappa^0)^2}{8} + \frac{\alpha(\kappa^0)^3}{324} + O(\alpha(\kappa^0)^4)$
$1/6$	$g(\zeta^0,\kappa^0) = \kappa^0\sin(\phi^0) + \frac{(\kappa^0)^2}{6}\sin(2\phi^0) - \frac{7(\kappa^0)^3}{24}\sin(3\phi^0) + \frac{(\kappa^0)^3}{96}\sin(3\phi^0) - \frac{43(\kappa^0)^4}{576}\sin(2\phi^0) + \frac{17(\kappa^0)^4}{576}\sin(4\phi^0) + \frac{25(\kappa^0)^5}{288}\sin(\phi^0) - \frac{185(\kappa^0)^5}{1152}\sin(3\phi^0) + \frac{51(\kappa^0)^5}{384}\sin(5\phi^0) + \frac{211(\kappa^0)^6}{864}\sin(2\phi^0) - \frac{4227(\kappa^0)^6}{34560}\sin(4\phi^0) + \frac{1077\alpha(\kappa^0)^6}{3840}\left(\cos(7\phi^0) - \cos(5\phi^0)\right) + O((\kappa^0)^7)$ $\zeta^1 - 2\zeta^0 + \zeta^{-1} = -\frac{1077(\kappa^0)^6}{3840}\sin(6\phi^0) + O((\kappa^0)^7)$ *Elliptic:* $\Omega = \alpha\kappa^0 + \frac{9}{24}\alpha(\kappa^0)^3 - \frac{379}{1151}\alpha(\kappa^0)^5 + \frac{1077}{3840}\alpha(\kappa^0)^5 + O((\kappa^0)^7)$ *Hyperbolic:* $\Omega = \alpha\kappa^0 + \frac{9}{24}\alpha(\kappa^0)^3 - \frac{379}{1151}\alpha(\kappa^0)^5 - \frac{1077}{3840}\alpha(\kappa^0)^5 + O((\kappa^0)^7)$

Table 3.1: Normal forms for some sequential periodic orbits with ration rotation numbers. The table displays: (i) the change of variables g, (ii) the resonant normal form and needed parameter relations for (iii)*elliptic* and (iv)*hyperbolic* fixed points.

Chapter 4

A non-autonomous standard map

The oscillatory behavior of the mean field variable κ in Fig. 1.5(a) and the observation that the cat's eye structure is contained in the instantaneous invariant stable and unstable manifolds of the hyperbolic point lead to further study the relation of an *oscillatory perturbation parameter* in the standard map and the possible critical global transport. For this reason an even simpler map model of transport is considered in this chapter. The results presented are discussed in detail in Ref. [9].

4.1 Map definition.

The starting point is the nonautonomous standard map (NASM), defined as

$$\hat{x}_{n+1} = \hat{x}_n + \hat{y}_{n+1} \qquad \text{mod } (1), \tag{4.1a}$$

$$\hat{y}_{n+1} = \hat{y}_n + \frac{\kappa_n}{2\pi} \sin(2\pi \hat{x}_n)\,. \tag{4.1b}$$

where κ_n is a function of n. The change in the scaling of the definition of map (2.26) and the change of sign is done to simplify some calculations.

Motivated by the asymptotic dynamics of the single wave map (Sec.1.3) the case of interest in this chapter is κ_n a periodic function of n. The periodic case always allows to give an autonomous representation of the nonautonomous map in Eq. (4.1) as the consecutive iteration of a whole period. A

high period variation of κ_n could allow to mimic more complex models and establish hierarchy of relevance between the parameters. However there exist evidence that adding one more parameter cause a transcendental change in the critical global transport problem[1, 8]. The properties and relations between the nonautonomous map (4.1) and the autonomous version are presented for the simplest periodic case in this section.

As a first step, a "triangular wave" periodic dependence is considered in which κ_n can only take two values:

$$\kappa_n = \begin{cases} \kappa_1 & \text{if } n \text{ is odd,} \\ \\ \kappa_2 & \text{if } n \text{ is even.} \end{cases} \tag{4.2}$$

The map $\mathcal{T}_{\kappa_1\kappa_2}$ is defined such that its iterates (x_n, y_n) $n = 1, 2, ...$ coincide with the even iterations of (4.1), i.e.,

$$(x_n, y_n) = (\hat{x}_{2n}, \hat{x}_{2n})\,. \tag{4.3}$$

By construction, the map $\mathcal{T}_{\kappa_1\kappa_2}$ is autonomous and can be written as,

$$x_{n+1} = x_n + 2y_n + \mathcal{F}_1(x_n, y_n; \kappa_1, \kappa_2) \qquad \text{mod } (1) \tag{4.4a}$$

$$y_{n+1} = y_n + \mathcal{F}_2(x_n, y_n; \kappa_1, \kappa_2) \tag{4.4b}$$

where the functions $\mathcal{F}_1$ and $\mathcal{F}_2$ are defined as,

$$\mathcal{F}_1(x, y; \kappa_1, \kappa_2) = \frac{\kappa_1}{2\pi}\sin(2\pi x) + \mathcal{F}_2\,, \tag{4.5a}$$

$$\mathcal{F}_2(x, y; \kappa_1, \kappa_2) = \frac{\kappa_1}{2\pi}\sin(2\pi x) + \frac{\kappa_2}{2\pi}\sin\left\{2\pi\left[x + y + \frac{\kappa_1}{2\pi}\sin(2\pi x)\right]\right\}\,. \tag{4.5b}$$

It should be noted that this new autonomous map preserves orientation and depends of an infinite number of harmonics when the term $\sin[a + \sin(b)]$ is expanded in Bessel functions and because of this, the map is not reducible to the extensively studied Refs. [50, 51, 12, 41] two frequency standard map.

As Fig. 4.1(c) shows, due to its non autonomous nature, the map in (4.1) exhibits self-intersection of trajectories, something that as Fig. 4.1(a) and Fig. 4.1(b) illustrates, never happens in autonomous maps. Fig. 4.1(d) shows, the non autonomous dynamics of an initial condition inside an *island* of (4.1)

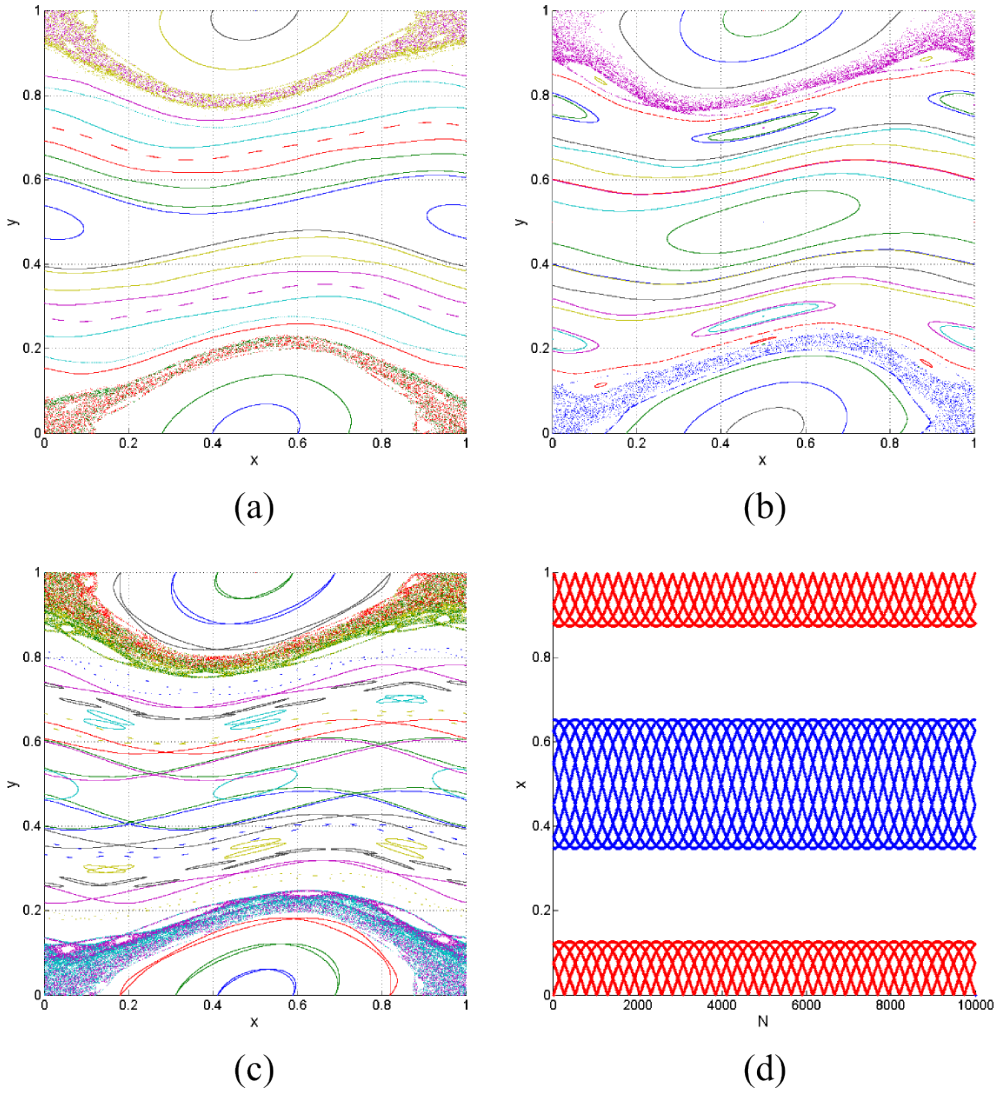

Figure 4.1: Comparison between the phase space of maps (4.4) and (4.1). (a) and (b) correspond to (4.4) with (κ_1, κ_2): $(0.35, 0.5)$ and $(0.5, 0.35)$ respectively, and (c) corresponds to map (4.1) with the same parameters. (d) shows to the time series of the initial condition $z_0 = (0, 0.55)$, where blue (red) corresponds to the even (odd) iterates of map (4.1).

alternates between $(0, 1/2)$ elliptic point of $\mathcal{T}_{\kappa_1\kappa_2}$ and $(1/2, 1/2)$ elliptic point

of $\mathcal{T}_{\kappa_2\kappa_1}$.

The map in Eq. (4.4) is equivalent to the composition of two standard maps, i.e., $\mathcal{T}_{\kappa_1\kappa_2} \equiv \mathcal{S}_{\kappa_2} \circ \mathcal{S}_{\kappa_1}$, where $\mathcal{S}_\epsilon$ denotes the standard map with perturbation parameter ϵ from Sec. 2.5 in the form,

$$\mathcal{S}_\epsilon \begin{pmatrix} x \\ y \end{pmatrix} = \begin{pmatrix} x + y + \frac{\epsilon}{2\pi}\sin(2\pi x) \\ y + \frac{\epsilon}{2\pi}\sin(2\pi x) \end{pmatrix} . \tag{4.6}$$

with $(x, y) \in \mathbb{S}^1 \times \mathbb{R}$. The composition of (positive) twist maps is denoted as *positive tilt map*[26] in the literature. Although, tilt maps share many features with twist maps it is easy to see that in general tilt maps are not twist. It is straightforward to show that $\mathcal{T}_{\kappa_1\kappa_2}$ and $\mathcal{T}_{\kappa_2\kappa_1}$ are diffeomorphic, since,

$$\mathcal{S}_{\kappa_2}^{-1} \circ \mathcal{T}_{\kappa_1\kappa_2}^n \circ \mathcal{S}_{\kappa_2} = \mathcal{T}_{\kappa_2\kappa_1}^n . \tag{4.7}$$

where $\mathcal{S}_\epsilon^{-1}$ denotes the inverse of the standard map,

$$\mathcal{S}_\epsilon^{-1} \begin{pmatrix} x \\ y \end{pmatrix} = \begin{pmatrix} x - y \\ y - \frac{\epsilon}{2\pi}\sin(2\pi(x - y)) \end{pmatrix} . \tag{4.8}$$

Note that, as shown in Fig. 4.1, the two autonomous representations have the same invariant sets. This important remark, that results from the conjugacy in Eq. (4.7), is discussed in Secs. 4.2.2 and 4.5.1 where it is proved that if an invariant circle exists in one of the representations then an invariant circle with the same rotation number exists in the other representation.

This implies that if there exist an invariant circle in any of the autonomous representations, then there exists a barrier for the transport in the nonautonomous map (4.1), since the autonomous representations are also stroboscopic maps of (4.1). By invariance, the invariant circles of $\mathcal{T}_{\kappa_1\kappa_2}$ and $\mathcal{T}_{\kappa_2\kappa_1}$ limit the vertical displacement (drift) of any orbit in the map, so, if there is no unbounded drift in any of the stroboscopic maps, there is not for the whole map, even if in general there is not a defined invariant circle for map (4.1), as it is required in the argument in Ref. [52].

The *twist* of $\mathcal{T}_{\kappa_1\kappa_2}$ is given by,

$$\left.\frac{\partial x_{n+1}}{\partial y_n}\right|_{x_n} = 2 + \kappa_2 \cos\left\{2\pi\left[x_n + y_n + \frac{\kappa_1}{2\pi}\sin(2\pi x_n)\right]\right\} . \tag{4.9}$$

and the twist condition $\left.\frac{\partial x_{n+1}}{\partial y_n}\right|_{x_n} > 0$, is satisfied in the whole cylinder when $|\kappa_2| < 2$. Based on this, the *twist region* in the parameter space is defined

as the square: $\{(\kappa_1, \kappa_2) : |\kappa_i| < 2, i = 1, 2\}$, where both $\mathcal{T}_{\kappa_1\kappa_2}$ and $\mathcal{T}_{\kappa_2\kappa_1}$ are twist. It must be noted that, if the map is twist for small values of the parameters, the Moser's Twist Theorem [53] guarantees the existence of invariant circles well ordered with the rotation number.

Let $\Omega = dy \wedge dx$ be a symplectic form on the cylinder, then it is clear that $\mathcal{T}_{\kappa_1\kappa_2}$ is symplectic with respect to Ω since each one of the standard maps is symplectic. In particular,

$$(\mathcal{T}_{\kappa_1\kappa_2})^*\Omega = (\mathcal{S}_{\kappa_2} \circ \mathcal{S}_{\kappa_1})^*\Omega = \mathcal{S}^*_{\kappa_1}\mathcal{S}^*_{\kappa_2}\Omega = \Omega\,, \tag{4.10}$$

where $(\mathsf{F})^*$ is the pullback via a function F. It can also be noted that since both $\mathcal{S}_{\kappa_2}$ and $\mathcal{S}_{\kappa_2}$ are exact, then $\mathcal{T}_{\kappa_1\kappa_2}$ is also exact. Notice that if $d\alpha = \Omega$, then

$$\mathcal{S}^*_{\kappa_i}\alpha - \alpha = dP_i \qquad i = 1, 2$$

where P_i is the generating functions of $\mathcal{S}_{\kappa_i}$. The simple computation is as follows (see Ref. [54]).

$$\begin{aligned} \mathcal{T}^*_{\kappa_1\kappa_2}\alpha &= (\mathcal{S}_{\kappa_2} \circ \mathcal{S}_{\kappa_1})^*\alpha = \mathcal{S}^*_{\kappa_1}\mathcal{S}^*_{\kappa_2}\alpha = \mathcal{S}^*_{\kappa_1}(\alpha + dP_2) \\ &= \alpha + d(P_1 + \mathcal{S}^*_{\kappa_1}P_2) \end{aligned} \tag{4.11}$$

Therefore $\mathcal{T}_{\kappa_1\kappa_2}$ is exact with generating function $P = P_1 + \mathcal{S}^*_{\kappa_1}P_2$. Using Mather's *conjunction* operation[55] it is possible to give an implicit expression for this generating function P as,

$$P = P_1 * P_2\,, \tag{4.12}$$

where $*$ stands for,

$$P_1 * P_2(x, x') = \min_{\xi}(P_1(x, \xi) + P_2(\xi, x')). \tag{4.13}$$

In this case, the ξ that minimizes the conjunction is the unique solution to the equation,

$$\xi = \frac{x + x'}{2} + \frac{\kappa_2}{4\pi}\sin(2\pi\xi)\,. \tag{4.14}$$

And this last expression has clearly only one solution whenever $|\kappa_2| < 2$, which as mentioned before corresponds to the region in the parameter space where the twist condition is satisfied.

4.2 Symmetries.

The symmetries of the NASM, help to reduce different possible cases and to infer the existence of invariant circles and their rotation numbers from the existence of invariant circle with different parameter values. Since the autonomous representation of the NASM in (4.4) is the composition of two standard maps (4.6), it is expected to have the symmetries of the standard map. However there are other symmetries of $\mathcal{T}_{\kappa_1\kappa_2}$.

The functions $\mathcal{F}_i$ in Eqs. (4.5a) and (4.5b) have the following symmetries.

$$P1. \quad \mathcal{F}_i(-x,-y;\kappa_1,\kappa_2) = -\mathcal{F}_i(x,y;\kappa_1,\kappa_2). \tag{4.15}$$

$$P2. \quad \mathcal{F}_i(x+n,y+m;\kappa_1,\kappa_2) = \mathcal{F}_i(x,y;\kappa_1,\kappa_2), \quad \text{for } n,m \in \mathbb{Z}. \tag{4.16}$$

$$P3. \quad \mathcal{F}_i(x,y;\kappa_1;\kappa_2) = \mathcal{F}_i(x+1/2,y;-\kappa_1,-\kappa_2). \tag{4.17}$$

$$P4. \quad \mathcal{F}_i(x,y;\kappa_1;\kappa_2) = \mathcal{F}_i(x,y+1/2;\kappa_1,-\kappa_2). \tag{4.18}$$

Whereas Eqs. (4.15) and (4.16) are coordinate symmetries directly inherited from the standard map, Eqs. (4.17) and (4.18) are symmetries of the non-autonomous map that involve both coordinates and parameter transformations. From, (4.17) and (4.18) it follows that,

$$\mathcal{F}_i(x,y;\kappa_1;\kappa_2) = \mathcal{F}_i(x+1/2,y+1/2;-\kappa_1;\kappa_2). \tag{4.19}$$

In the remaining of this section, (x,y) denotes the variables of the *lift* of map (4.4). In other words, $x \in \mathbb{R}$.

4.2.1 Orbit symmetries.

Let $x_n(x_0,y_0;\kappa_1,\kappa_2)$ and $y_n(x_0,y_0;\kappa_1,\kappa_2)$ denote the x and y coordinates of the n-th iterate of the NASM with parameters (κ_1,κ_2) and initial condition (x_0,y_0). Then, from the properties of $\mathcal{F}_i$, it follows that the orbits exhibit the following symmetries (see Fig. 4.2).

1. Coordinate reflection [from Eq. (4.15)],

$$x_n(-x_0,-y_0;\kappa_1,\kappa_2) = -x_n(x_0,y_0;\kappa_1,\kappa_2)\,, \tag{4.20a}$$

$$y_n(-x_0,-y_0;\kappa_1,\kappa_2) = -y_n(x_0,y_0;\kappa_1,\kappa_2)\,. \tag{4.20b}$$

2. Coordinate translation [from Eq. (4.16)],

$$x_n(x_0 + r, y_0 + s; \kappa_1, \kappa_2) = x_n(x_0, y_0; \kappa_1, \kappa_2) + r + 2ns\,, \tag{4.21a}$$
$$y_n(x_0 + r, y_0 + s; \kappa_1, \kappa_2) = y_n(x_0, y_0; \kappa_1, \kappa_2) + s\,, \tag{4.21b}$$

for $r, s \in \mathbb{Z}$.

3. Coordinate translation and reflection [from Eqs. (4.20)-(4.21)],

$$x_n(1 - x_0, 1 - y_0; \kappa_1, \kappa_2) = 1 - x_n(x_0, y_0; \kappa_1, \kappa_2) + 2n\,, \tag{4.22a}$$
$$y_n(1 - x_0, 1 - y_0; \kappa_1, \kappa_2) = 1 - y_n(x_0, y_0; \kappa_1, \kappa_2)\,. \tag{4.22b}$$

4. Coordinate translation and parameter reflexion twice [from Eq. (4.17)],

$$x_n(x_0 + 1/2, y_0; -\kappa_1, -\kappa_2) = x_n(x_0, y_0; \kappa_1, \kappa_2) + 1/2\,, \tag{4.23a}$$
$$y_n(x_0 + 1/2, y_0; -\kappa_1, -\kappa_2) = y_n(x_0, y_0; \kappa_1, \kappa_2)\,. \tag{4.23b}$$

5. Coordinate translation and parameter reflexion [from Eq. 4.18],

$$x_n(x_0, y_0 + 1/2; \kappa_1, -\kappa_2) = x_n(x_0, y_0; \kappa_1, \kappa_2) + n\,, \tag{4.24a}$$
$$y_n(x_0, y_0 + 1/2; \kappa_1, -\kappa_2) = y_n(x_0, y_0; \kappa_1, \kappa_2) + 1/2\,. \tag{4.24b}$$

6. Coordinate translation and parameter reflexion [from Eq. 4.19],

$$x_n(x_0 + 1/2, y_0 + 1/2; -\kappa_1, \kappa_2) = x_n(x_0, y_0; \kappa_1, \kappa_2) + 1/2 + n\,, \tag{4.25a}$$
$$y_n(x_0 + 1/2, y_0 + 1/2; -\kappa_1, \kappa_2) = y_n(x_0, y_0; \kappa_1, \kappa_2) + 1/2\,. \tag{4.25b}$$

Note that property $P3$ in (4.17) implies that if there is an invariant circle above the line $y = 0.5$, then there is an invariant circle corresponding to its *reflected* image bellow $y = 0.5$. This same property exists in the standard map, so its invariant circle γ has a reflected image (with rotation number $1 - \gamma$) in the lower half of the cell, and both break up for the same value of the parameter $\kappa_G = 0.971635406...$

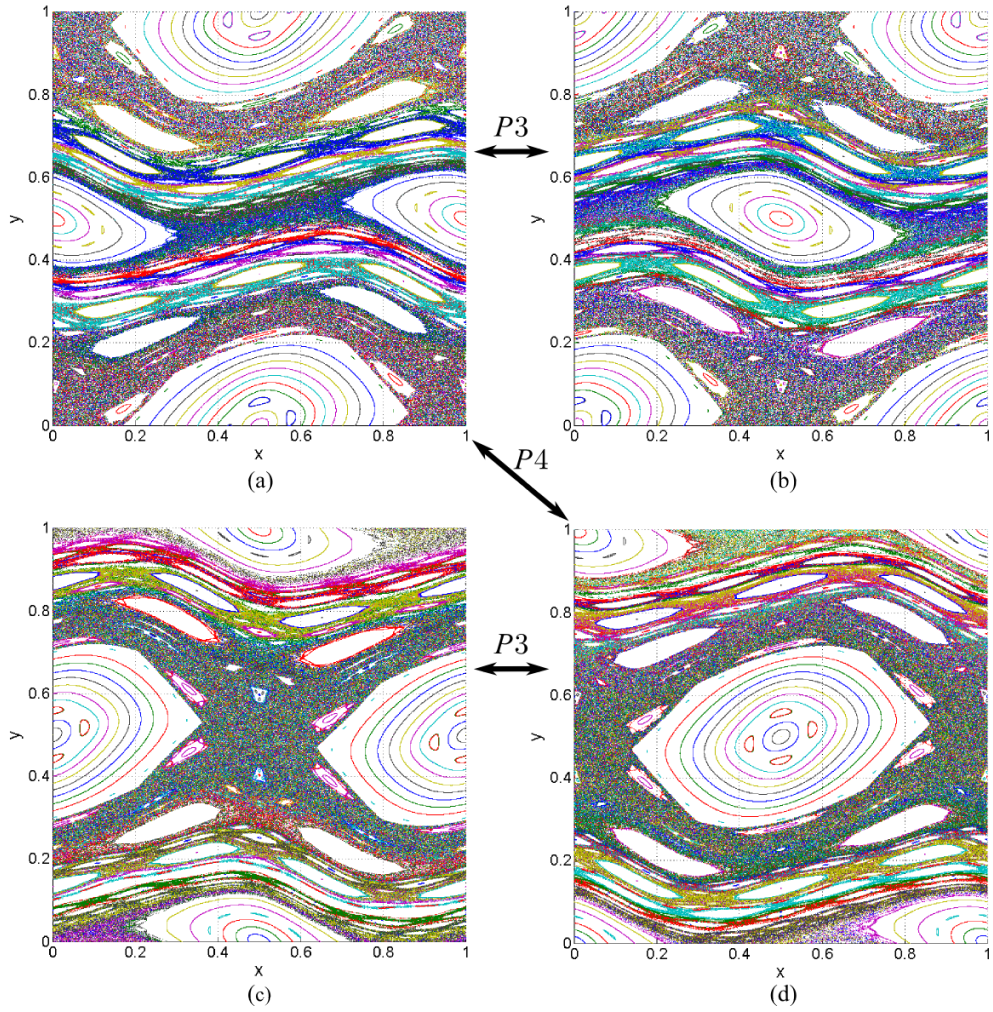

Figure 4.2: Phase space of the map (4.4) for different values of the parameters (κ_1, κ_2): (a) $(0.5, 0.7)$,(b) $(-0.5, -0.7)$, (c) $(-0.5, 0.7)$ and (d) $(0.5, -0.7)$, related by the symmetries $P3$ and $P4$, in Eq. (4.17) and (4.18) respectively.

4.2.2 Rotation number symmetries.

The rotation number of an orbit of the map (4.4) with parameters (κ_1, κ_2) is defined as,

$$\omega(x_0, y_0; \kappa_1, \kappa_2) = \lim_{n\to\infty} \frac{x_n(x_0, y_0; \kappa_1, \kappa_2) - x_0}{n}\,, \tag{4.26}$$

whenever the limit exist.

Then from Eqs. (4.23a), (4.24a) and (4.25a), respectively, it follows that

$$\omega(x_0 + 1/2, y_0; -\kappa_1, -\kappa_2) = \omega(x_0, y_0; \kappa_1, \kappa_2)\,, \tag{4.27}$$

$$\omega(x_0, y_0 + 1/2; \kappa_1, -\kappa_2) = \omega(x_0, y_0; \kappa_1, \kappa_2) + 1\,, \tag{4.28}$$

$$\omega(x_0 + 1/2, y_0 + 1/2; -\kappa_1, \kappa_2) = \omega(x_0, y_0; \kappa_1, \kappa_2) + 1\,. \tag{4.29}$$

.

Therefore, for each invariant circle passing through (x_0, y_0) with rotation number ω in the NASM with parameters (κ_1, κ_2), there exist up to three other associated invariant circles: one with rotation number $\omega + 1$ for $(-\kappa_1, \kappa_2)$ passing through $(x_0 + 1/2, y_0 + 1/2)$, one also with rotation number $\omega + 1$ for $(\kappa_1, -\kappa_2)$ passing through $(x_0, y_0 + 1/2)$, and one with rotation number ω for $(-\kappa_1, -\kappa_2)$ passing through $(x_0 + 1/2, y_0)$.

In addition, for a given (κ_1, κ_2), from Eq. (4.22) it can be shown that,

$$\omega(1 - x_0, 1 - y_0; \kappa_1, \kappa_2) = 2 - \omega(x_0, y_0; \kappa_1, \kappa_2)\,, \tag{4.30}$$

which is a property that also applies to the standard map (4.6), but with a different shift[1].

Finally from Eq. (4.7) and the definition of rotation number in (4.26), it follows that,

$$\omega(\mathcal{S}_{\kappa_2}(\mathbf{z}_0); \kappa_2, \kappa_1) = \omega(\mathbf{z}_0; \kappa_1, \kappa_2)\,, \tag{4.31}$$

where $\mathbf{z}_0 = (x_0, y_0)^T$.

4.3 Periodic orbits.

The periodic orbits are sets that in many cases offer information that can be used to characterize maps, approximate invariant sets and study linear stability. For these reasons, it is important to study them in the case of the NASM.

The close relationship between $\mathcal{T}_{\kappa_1\kappa_2}$ and $\mathcal{T}_{\kappa_2\kappa_1}$ reflects on the fact that if $\mathbf{z} = (x, y)^T$ is an n-periodic orbit, on the lift of the map[2] with rotation

[1] 1 instead of 2 on the right hand side of Eq. (4.30).

[2] To the universal cover of $\mathbb{S}^1 \times \mathbb{R}$.

number m/n of $\mathcal{T}_{\kappa_1\kappa_2}$, that is,

$$\mathcal{T}^n_{\kappa_1\kappa_2}(\mathbf{z}) = \mathbf{z} + (m, 0)^T \,, \tag{4.32}$$

then from Eq. (4.7) it follows that,

$$\mathbf{w} = \mathcal{S}^{-1}_{\kappa_2}\mathbf{z} \,, \tag{4.33}$$

is an m/n-periodic orbit of $\mathcal{T}_{\kappa_2\kappa_1}$, i.e.

$$\mathcal{T}^n_{\kappa_2\kappa_1}(\mathbf{w}) = \mathbf{w} + (m, 0)^T \,. \tag{4.34}$$

Note that the linear stability properties of $\mathbf{z}$ and $\mathbf{w}$ are the same because the trace of a product of matrices is invariant under the product commutation.

4.3.1 Period-one orbits

There are six primary period-one orbits. By primary it must be understood that they exist for any values of κ_1 and κ_2. In addition there are bifurcated period-one orbits that exist only for certain values of κ_1 and κ_2. The primary orbits are

$$\mathcal{P}_1 = \{(1/2, 0)\,, (0, 0)\,, (0, \pm 1/2)\,, (1/2, \pm 1/2)\} \,. \tag{4.35}$$

The stability of these orbits is determined by the residue

$$R = \frac{1}{4}\left[2 - \mathrm{Tr}\left(\nabla\mathcal{T}_{\kappa_1\kappa_2}\right)\right] \,, \tag{4.36}$$

where Tr denotes the trace, and $\nabla\mathcal{T}_{\kappa_1\kappa_2}$ is the derivative of the map evaluated at the fixed point. A fixed point (x_*, y_*) is stable if and only if $0 < R < 1$. From this it follows that,

$$\text{I.} \quad (0,0) \quad \text{is stable iff } 0 < -\kappa_1 - \kappa_2 - \frac{\kappa_1\kappa_2}{2} < 2 \,, \tag{4.37}$$

$$\text{II.} \quad \left(\tfrac{1}{2}, 0\right) \quad \text{is stable iff } 0 < \kappa_1 + \kappa_2 - \frac{\kappa_1\kappa_2}{2} < 2 \,, \tag{4.38}$$

$$\text{III.} \quad \left(0, \pm\tfrac{1}{2}\right) \quad \text{is stable iff } 0 < \kappa_2 - \kappa_1 + \frac{\kappa_1\kappa_2}{2} < 2 \,, \tag{4.39}$$

$$\text{IV.} \quad \left(\tfrac{1}{2}, \pm\tfrac{1}{2}\right) \quad \text{is stable iff } 0 < \kappa_1 - \kappa_2 + \frac{\kappa_1\kappa_2}{2} < 2 \,. \tag{4.40}$$

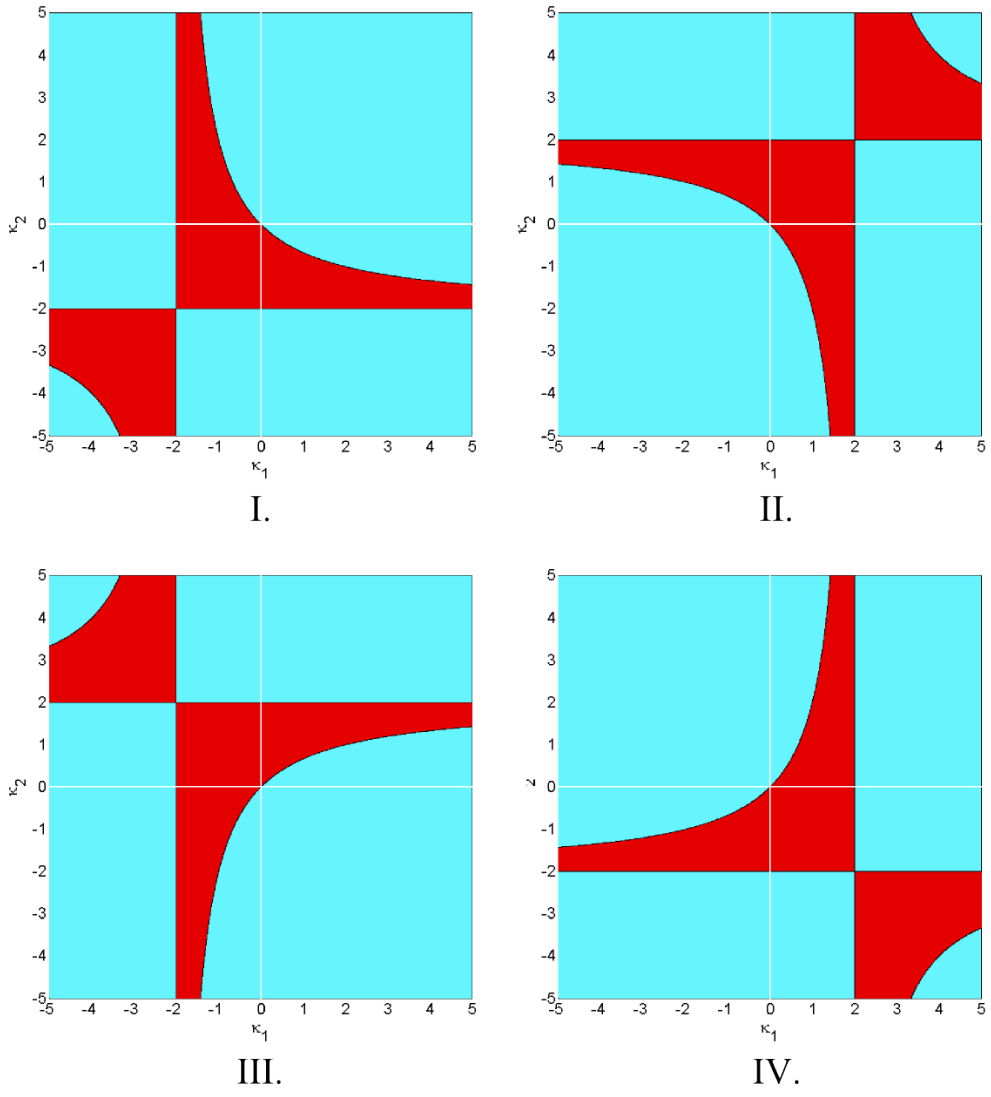

Figure 4.3: Stability of primary period-one fixed points. Red regions correspond to stable orbits. As expected, the stability diagrams satisfy the symmetry relations in Eqs. (4.15)-(4.18).

Figure 4.3 shows the stability regions of the primary period-one fixed points in the (κ_1, κ_2) space, according to (4.37)-(4.40). As expected, the results in Fig. 4.3 are consistent with the symmetries in (4.15)-(4.18).

The secondary period-one orbits (x_*, y_*) are solutions to the system,

$$2y_* = -\frac{\kappa_1}{2\pi}\sin(2\pi x_*) \qquad \mathrm{mod}(1)\,, \tag{4.41a}$$

$$\kappa_1 \sin(2\pi x_*) = -\kappa_2 \sin\left(2\pi x_* + \frac{\kappa_1}{2}\sin(2\pi x_*)\right)\,. \tag{4.41b}$$

A Taylor expansion of (4.41b) around the elliptic point $(1/2, 0)$, neglecting fifth order terms, around $|z_*| = |2\pi x_* - \pi| \ll 1$, allows to estimate z_* as

$$z_*^2 = \frac{6\kappa_1 + 6\kappa_2 + 3\kappa_1\kappa_2}{\kappa_1 - \frac{\kappa_1\kappa_2}{2} + \kappa_2\left(1 - \frac{\kappa_1}{2}\right)^3} + O(z_*^4)\,. \tag{4.42}$$

Figure 4.4 shows the region in the positive quadrant of the parameter space where it is possible to find these associated periodic orbits of period 1 around the primary period-one fixed point $\left(\frac{1}{2}, 0\right)$. It should be noted that the limiting curve in the figure coincides with the limiting curve in Fig. 4.3 for the same point. These secondary families of periodic orbits appear after a pitchfork bifurcation of the primary fixed point $\left(\frac{1}{2}, 0\right)$. The value of Greene's residue evaluated at the orbits correspond to the region shaded in red tells us that these orbits are stable.

4.4 Transport barriers: known limit cases and direct computation.

Our goal is to find the critical parameter values of the map (4.4) for which *global transport* occurs. We will say that there is global transport when there exists at least one initial condition (x_0, y_0) such that the y variable is unbounded. We have observed in (4.9)-(4.11) that the map in (4.4) is symplectic, exact and twist for small values of the parameters. It is established, see Ref. [56], that for twist maps of the cylinder the only barriers to global transport are invariant circles that are not homotopic to a point. Because of these properties, Moser's Twist Theorem guarantees the existence invariant circles for sufficiently small values of the parameters κ_i in a neighborhood in parameter space of the origin which corresponds to the case in which the

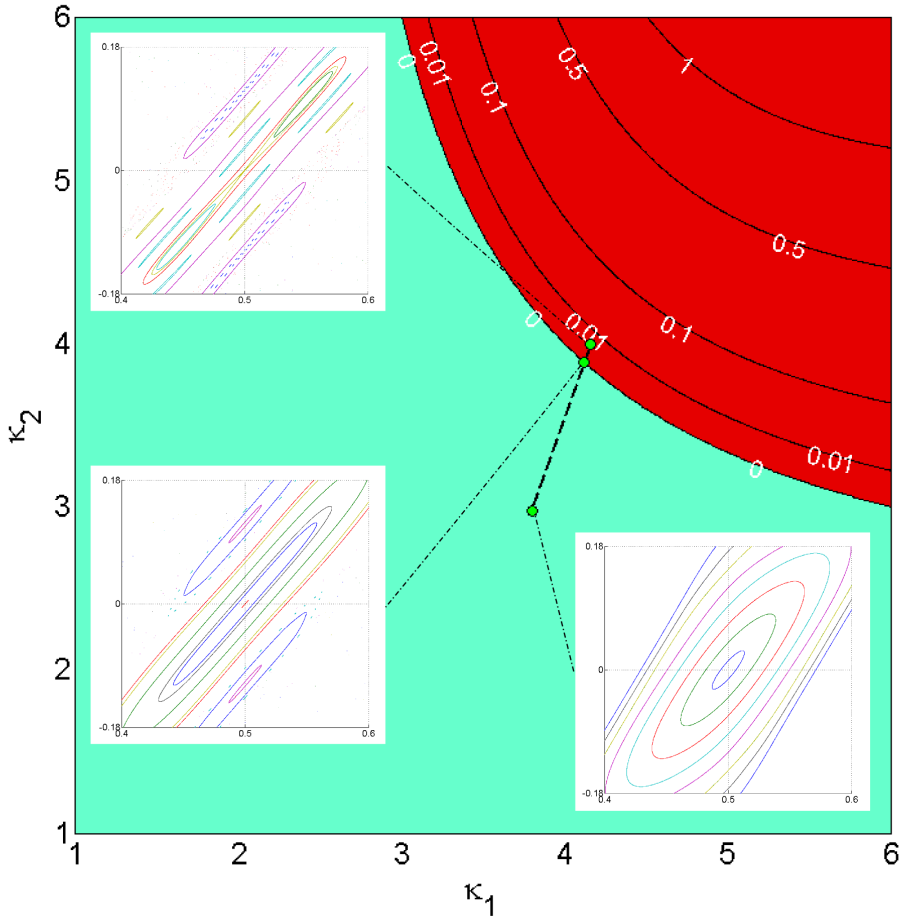

Figure 4.4: Region of existence of the secondary period 1 periodic orbits around the elliptic point $\left(\frac{1}{2}, 0\right)$ in the positive quadrant of the parameter space. The light green shaded region corresponds to values of the parameters where the secondary periodic orbits do not exist. The figure displays in red the increasing values of the absolute error of the approximate value of z_* from (4.42), when substituted into (4.41b). The red colored region also coincides with values of the Greene's residue, Eq. (4.36), for when the orbits are stable.

map is integrable. Then it is reasonable to compute the critical boundaries (CB) in the parameter space for the onset of global transport (CB_{gt}) and for

the destruction of invariant circles with a fixed rotation number, ω, (CB_ω). By CB we mean the boundary of the open region $\mathcal{R}$ in the parameter space (assumed to be simply connected) such that for (κ_1, κ_2) values in $\mathcal{R}$ there is not global transport in the case of (CB_{gc}) or a given invariant circle with rotation number ω exists in the case of (CB_ω).

We propose three different approaches to find these transport barriers: analytical reductions of the map for particular values of the parameters, direct numerical iteration for a range of values of the parameters which gives upper bounds, and a continuation method over invariant circles with an a priori chosen rotation number in the parameter space which gives lower bounds to global transport.

4.4.1 Known limit cases.

In the standard map, the term *critical parameter value*, κ_c, is established in the literature[18] as the value for with any further increment $|\kappa| > |\kappa_c|$ there are no invariant curves. We call *critical invariant curve* to such invariant curve that exist for $\kappa = \kappa_c$ and cease to exist after the critical value. It is a known conjecture[18] that for the standard map, the rotation number of the critical invariant curve is equal to the golden mean $\gamma = \frac{\sqrt{5}-1}{2}$.

We present some particular cases of map (4.4).

1. $(\kappa_1, \kappa_2) = (\kappa_1, 0)$, $\kappa_1 \geq 0$.

   In this case the map (4.4) reduces to,

$$x_{n+1} = x_n + 2y_n + \frac{2\kappa_1}{2\pi}\sin(2\pi x_n) \tag{4.43a}$$

$$y_{n+1} = y_n + \frac{\kappa_1}{2\pi}\sin(2\pi x_n) \tag{4.43b}$$

   which upon the change of coordinates: $\{X = x, Y = 2y\}$, becomes the standard map (4.6) with $\epsilon = 2\kappa_1$. And it is well known in this case that the critical invariant circle has rotation number equal to the golden mean γ and breaks at the critical value $\kappa_G \approx 0.971635406$ [18, 22]. This implies that the critical invariant circle for the case $(\kappa_1, \kappa_2) = (\kappa_1, 0)$ has rotation number $\omega_c = \gamma$ and breaks for $\kappa_{1c} = \kappa_G/2$. Applying Eq. (4.30) to the standard map reduction and the NASM, it follows that there are also three more critical invariant circles with rotation numbers: $1 - \gamma$, $2 - \gamma$ and $\gamma + 1$.

2. $(\kappa_1, \kappa_2) = (0, \kappa_2)$, $\kappa_2 \geq 0$.

   In this case the map (4.4) reduces to,

$$x_{n+1} = x_n + 2y_n + \frac{\kappa_2}{2\pi} \sin(2\pi\,(x_n + y_n)), \tag{4.44a}$$

$$y_{n+1} = y_n + \frac{\kappa_2}{2\pi} \sin(2\pi\,(x_n + y_n)). \tag{4.44b}$$

   As before, with the change of coordinates: $\{X = x + y, Y = 2y\}$, the map reduces to the standard map (4.6) with perturbation parameter $\epsilon = 2\kappa_2$. Therefore the critical invariant circle has rotation number $\omega_c = \gamma$ and breaks for $\kappa_{2c} = \kappa_G/2$. From Eq. (4.30), there are three more critical invariant circles: $1-\gamma$, $2-\gamma$ and $\gamma+1$. This case can also be considered a consequence of the Eq. (4.31) applied to the previous case.

3. $(\kappa_1, \kappa_2) = (\kappa, \kappa)$, $\kappa \geq 0$.

   In this case the map reduces to the standard map iterated twice, which that the critical invariant circle of map (4.4), has rotation number $\omega_c = 2\gamma$ and breaks at $\kappa_c = \kappa_G$. By the symmetry (4.30), there exists also the invariant circle with rotation number: $\omega_{c_2} = 2 - 2\gamma$.

   Furthermore, applying the results of section III.B we can give the rotation numbers of the critical circles in the other quadrants. For example, for $(-\kappa, \kappa)$, the critical invariant circles are: $\omega_{c_1} = 2\gamma - 1$ and $\omega_{c_2} = 3 - 2\gamma$ for $\kappa_c = \epsilon_c$.

It should be noted that the change of variables used in the first two cases are homotopic to the identity, so the barriers in the cylinder for the standard map reductions are barriers for the NASM as well.

4.4.2 Direct computation.

We formally define a barrier to global transport as an invariant circle not homotopic to a point, which geometrically are circles that go around the cylinder $\mathbb{S}^1 \times \mathbb{R}$. An invariant circle of this kind, when it exists, always divides the phase space in two unbounded invariant regions, due to its invariance and the continuity of the map. This method is basically a modified version of the overlap method introduced by Chirikov[10].

The numerical computation of the threshold to global transport is based on the following criteria:

Proposition 4.1. *(Global transport criterion)*
If for a set value of the parameters (κ_1, κ_2), there is an initial condition (x_0, y_0) with $y_0 \in (0,1)$, for which $|y_n - y_0| > 2$ for some n and all the invariant circles of the map have an amplitude[3] *$\mathcal{A} < 1$, then the map has global transport.*

Proof. Lets assume that for the map with (κ_1, κ_2), there exists an initial condition (x_0, y_0) such that $|y_n - y_0| > 2$ for a certain n but there still exists an invariant circle fully contained in the cell $[0,1] \times (Q, Q+1)$ for $Q \in \mathbb{R}$. By the orbit symmetry property in Eq. (4.21), using $r = 0$ and $s = -\lfloor Q \rfloor := -\max\{m \in \mathbb{Z} | m \leq Q\}$, there exists a *copy* of the invariant circle in $[0,1] \times [0,2]$. Then, either the invariant circle or one of its *copies* $(s = -\lfloor Q \rfloor \pm 1)$ lies between y_0 and y_n. Which is a contradiction because y_0 and y_n must be in the same connected component of the cylinder.

□

Numerical evidence, see e.g. Fig. 4.2(a), shows that at least for parameter values $|\kappa_i| < 1$, the hypothesis, $\mathcal{A} < 1$, holds. A different argument to support the hypothesis is that the invariant stable and unstable manifolds of the hyperbolic fixed point around $(0,0)$ obstruct the path of the invariant curve, and so do its integer translates in the y-direction.

We performed several series of N-iterations of the map (4.4) on M initial conditions taken uniformly distributed in the rectangle $[0,1] \times [0, 0.3]$ to determine, using the proposed transport criteria (Proposition 1) when the map displayed global transport for a wide range of the parameters (κ_1, κ_2) inside the *twist region*. Different number of initial conditions, M, were used, finding $M = 10^4$ to be a reasonable balance between the computing capabilities and the consistency of the results. The procedure was repeated for an increasing number of iterations N. The convergence of the method is shown in Figure 4.7. Figures 4.5 and 4.6 show the critical boundary for the global transport (CB_{gt}) found with these calculations, i.e. the locus of points in parameter space for which no critical invariant curves were detected.

In all the cases studied, the CB_{gt} in the upper half plane of the parameter space were symmetric (up to machine precision) on the right (left) quadrant with respect to the line $\kappa_2 = \kappa_1$ $(\kappa_2 = -\kappa_1)$, Fig. 4.6.

The slope of the adjusted line to the convergence data obtained with the *direct method* for a variable number of iterations N, Fig. 4.7, suggests

[3] Where $\mathcal{A}$ is the height difference between the highest and lowest point of the invariant circle.

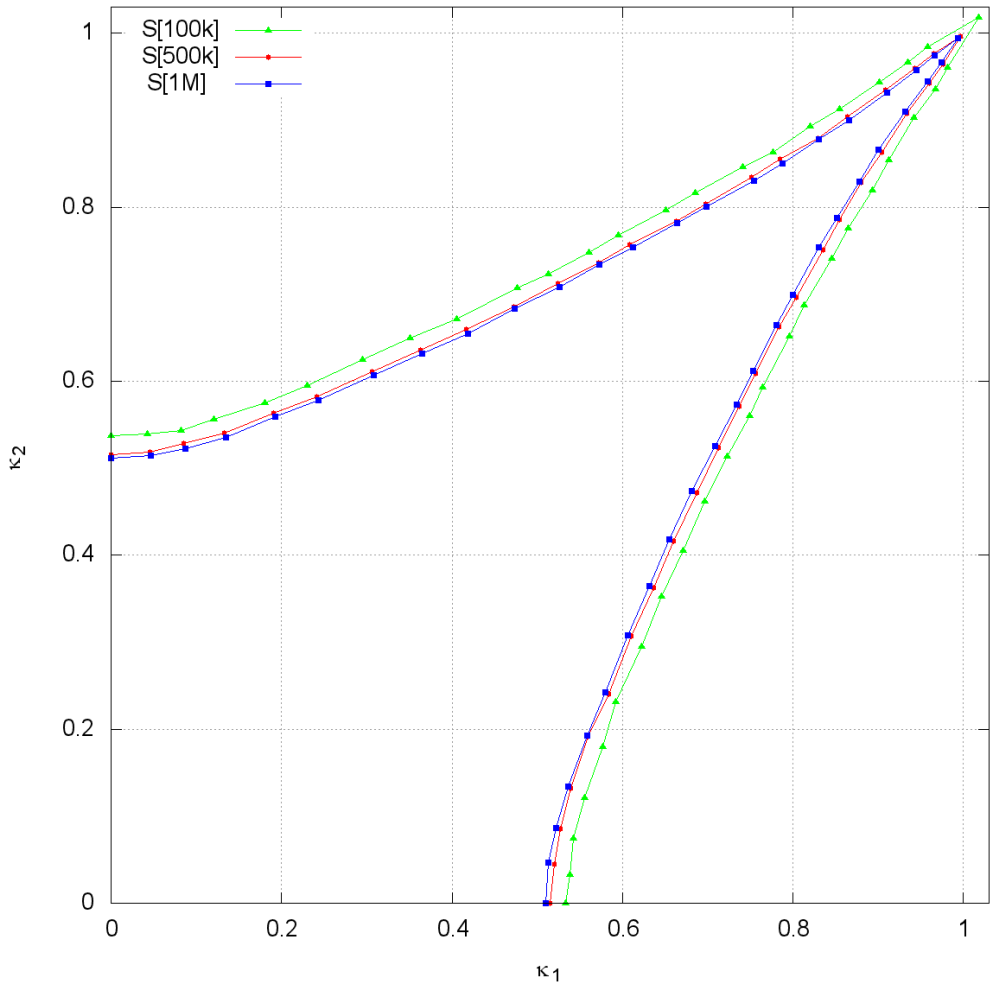

Figure 4.5: Critical boundary for global transport (CB_{gt}) in the non-autonomous standard map in Eq. (4.4), in the positive quadrant. The area outside the "horn" corresponds to parameter values for which there is *global transport*, in the sense that at least one of 10^4 initial condition uniformly distributed on the rectangle $[0, 1] \times [0, 0.3]$ exhibited a displacement with: $y > 0.3 + 2$ or $y < -2$ after 10^5 (green triangles), 5×10^5 (red circles) and 10^6 (blue squares) iterations of the map.

that the convergence of the method is algebraic: $(\kappa_N - \kappa_G) \propto N^{-1/\eta}$, with

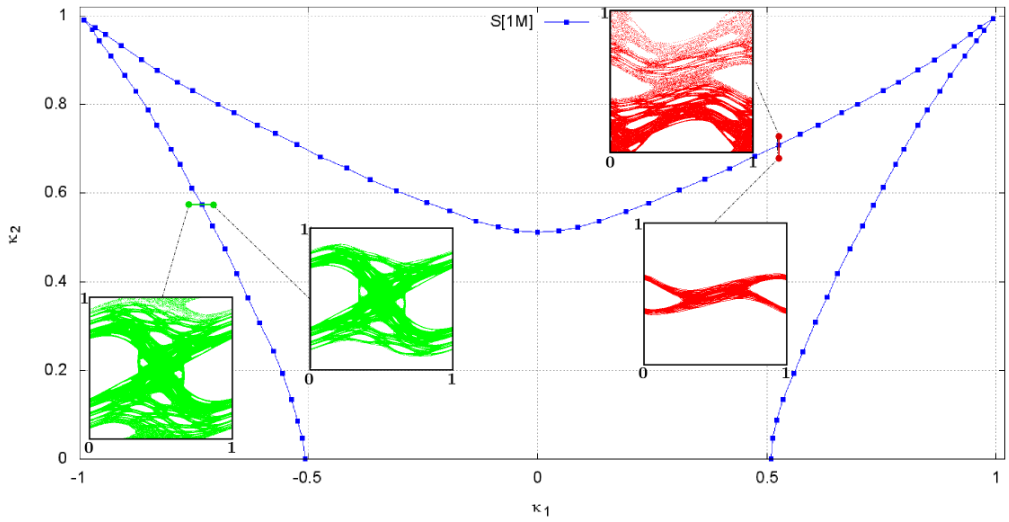

Figure 4.6: Critical boundary for global transport (CB_{gt}) in the non-autonomous standard map in Eq. (4.4) in the upper half plane of parameter space, obtained by the direct method with $M = 10^4$ and $N = 10^6$. As in Figure 4.5, the area outside the "horns" corresponds to *global transport*, for the same conditions as in Fig. 4.5. The insets are images of the cell $[0,1]\times[0,1]$ of the phase space (x, y) obtained from the iteration ($N = 3\times10^6$) of the NASM for the initial condition $(0.5, 0.44)$ for parameter values close the computed boundary: $(0.526, 0.69)$, $(0.526, 0.73)$, $(-0.69, 0.525)$ and $(-0.73, 0.525)$.

$\eta = 2.681$ (and $\eta = 3.322$ for large N), which is close to the value,$\eta = 3.012$, reported in literature[22] for transport in the standard map.

4.5 Transport barriers: continuation method.

This section reviews the numerical implementation of the parameterization method presented in Sec. 2.8 to do the numerical continuation of invariant circles of the map in Eq. (4.4).

The main idea of the method is, as stated previously, to start from an approximate solution of the invariance equation applied to $\mathcal{T}_{\kappa_1\kappa_2}$,

$$e_0(\theta) = \mathcal{T}_{\kappa_1\kappa_2} \circ K_0(\theta) - K_0(\theta + \omega)\,, \tag{4.45}$$

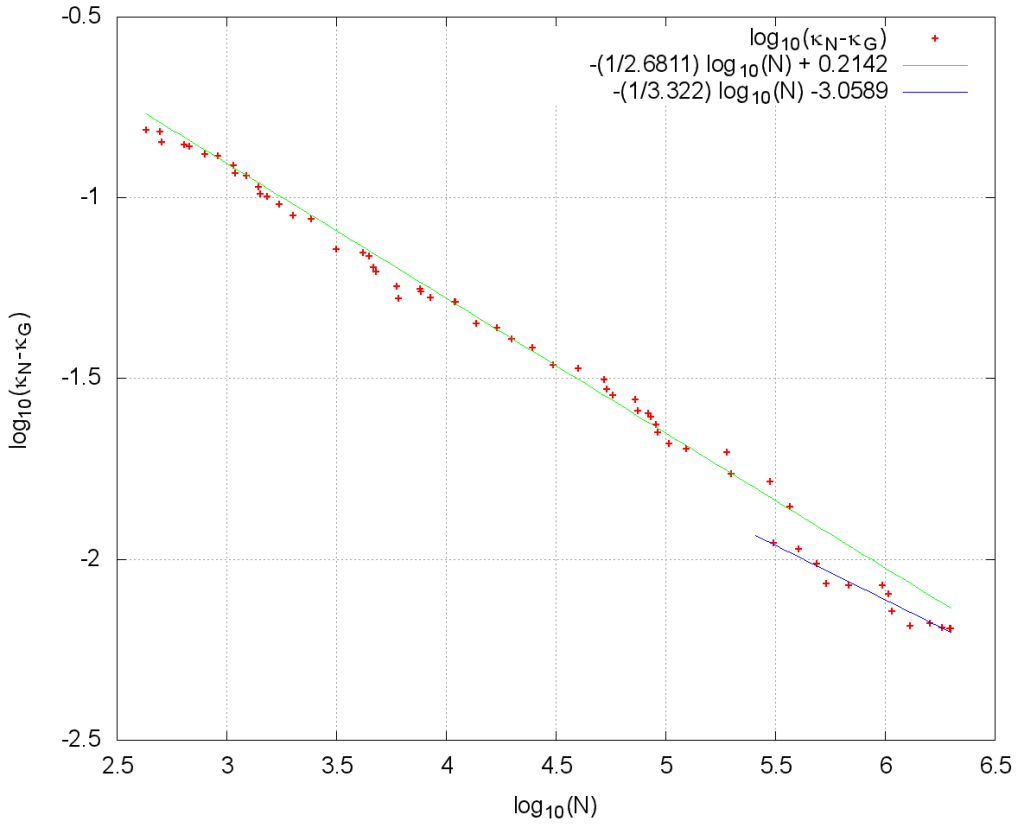

Figure 4.7: Convergence of the critical parameter value κ_c as function of the number of iterates N, observed using the *direct method* at the cusp of the *horn*, along the diagonal $(\kappa_1, \kappa_2) = (\kappa, \kappa)$. To better display the results, the plotted quantity on the vertical axis is $\kappa_N - \kappa_G$.

where $\|e_0\|$ is small. And then "improve" the approximate solution by adding a periodic function $\Delta : \mathbb{S}^1 \to \mathbb{R} \times \mathbb{S}^1$ so that $K_1(\theta) = K_0(\theta) + \Delta(\theta)$ has an error

$$e_1(\theta) = \mathcal{T}_{\kappa_1 \kappa_2} \circ K_1(\theta) - K_1(\theta + \omega)\,, \tag{4.46}$$

with $\|e_1\| \approx \|e_0\|^2$. Which according to Nash-Moser theory is possible.

Instead of solving numerically the Newton equation in (4.46) for Δ, the method opts for a symplectic change of coordinates that reduces the Newton step equation (4.46) with the benefit to have an implementation that require only $O(n \log n)$ operations, where n is the number of points that one uses to

represent the invariant circle.

The proposed change of coordinates applied to the Newton step, $\Delta(\theta) = M_0(\theta)W(\theta)$, reduces approximately the Newton step equation to,

$$W_2(\theta) - W_2(\theta+\omega) = -[M_0^{-1}(\theta+\omega)e_0(\theta)]_2\,, \tag{4.47}$$

$$W_1(\theta) - W_1(\theta+\omega) = -[M_0^{-1}(\theta+\omega)e_0(\theta)]_1 - S(\theta)W_2(\theta)\,, \tag{4.48}$$

that are the system of Eqs.(2.43)-(2.44) discussed at end of Sec. 2.8. An this time, because equation (4.11) guaranties that $\mathcal{T}_{\kappa_1\kappa_2}$ is exact, the right hand side of (4.47) has average zero, so both homological equations can be solved.

The algorithm to solve for Δ from the reduced Newton equation is again described below.

Algorithm 4.1.

1) Let $e_0(\theta) = \mathcal{T}_{\kappa_1\kappa_2} \circ K_0(\theta) - K_0(\theta+\omega)$

2) Compute the matrix $M(\theta)$ *from equation* (2.38).

3) Solve for $W_2(\theta)$ *from* (2.43).

4) Choose the average $\int_{\mathbb{S}^1} W_2(\theta)d\theta$ *so that* $-[M_0^{-1}(\theta+\omega)e_0(\theta)]_1 - S_0(\theta)W_2(\theta)$ *has an average close to zero.*

5) Solve for $W_1(\theta)$ *from* (2.44).

6) Compute the step Δ,

$$\Delta(\theta) = M_0(\theta)W(\theta)$$

7) Obtain the new parameterization K_1,

$$K_1(\theta) = K_0(\theta) + \Delta(\theta)$$

8) Set $K_0(\theta) = K_1(\theta)$ *and go to step 1).*

Remark. *In order to implement the computations in step 5, one has to make sure that the twist condition is satisfied, so* $S_0(\theta) \neq 0$. *Verifying the twist condition might be a drawback when the algorithm is applied to maps that do not have a uniform twist condition. However in the present case, it is only required to perform the continuation in parameter regions where the maps satisfied the twist condition uniformly.*

Remark. *One can verify that all the operations required to implement algorithm 4.1, are either diagonal in Fourier space or in real space. To transform from real space to Fourier space one can use a Fast Fourier Transform (FFT), which is the most expensive operation in the Algorithm 4.1 in terms of arithmetic operations. Therefore, the cost of implementing Algorithm 4.1 is $O(n \log n)$ operations with $O(n)$ storage requirements, where n is the number of points used to represent the circle.*

between the parameterization method exposed here and the symmetries that were introduced in Section 4.2.

4.5.1 Symmetries of the parameterization of an invariant circle

This subsection presents some of the symmetries discussed in Section 4.2 from the point of view of the parameterization method. The goal is to rewrite the symmetries in terms of compositions of functions. In this way, the composition formulation can be used to rewrite the invariance equation that a parameterization of a circle with a certain symmetry should satisfy. This way if a map has an invariant circle, then it is possible to use the parameterization function, K, and transform it using the composition operators with respect to a given symmetry. In this way, a new parameterization can be constructed such that it satisfies the invariance equation of a new map with the given symmetry. The starting point is to verify that the invariant circles of the map $\mathcal{T}_{\kappa_1,\kappa_2}$ are expected to exist and to have the rotation numbers found in Section 4.4.1.

First, let the map T has an invariant circle with rotation number ω, whenever Eq. (2.32) is satisfied. For instance, if S_κ in Eq. (4.6), has an invariant circle of rotation number ω, with graph K, then $\mathcal{T}_{\kappa\kappa}$ will have an invariant torus with rotation number 2ω as described above. Since,

$$S_\kappa \circ K(\theta) = K(\theta + \omega)$$

and

$$S_\kappa \circ K(\theta + \omega) = K(\theta + 2\omega),$$

then

$$S_\kappa \circ S_\kappa \circ K(\theta) = S_\kappa \circ K(\theta + \omega) = K(\theta + 2\omega). \tag{4.49}$$

It can be noticed that by defining the rigid rotation the following function for $\phi \in \mathbb{R}$,

$$R_\phi(x, y) = (x + \phi \mod 1, y),$$

then the standard map (4.4) satisfies that,

$$S_\epsilon \circ R_{-\frac{1}{2}} = R_{-\frac{1}{2}} \circ S_{-\epsilon}, \tag{4.50}$$

for any ϵ. There exist one more symmetry of the parameterization that will be important. To see this, the components of the parameterization K is rewritten as follows. Let $u(\theta)$ be a 1-periodic function of $\mathbb{S}^1$, then

$$K(\theta) = \begin{pmatrix} \theta + u(\theta) \\ \omega + u(\theta) - u(\theta - \omega) \end{pmatrix}. \tag{4.51}$$

It is clear from (4.51) and the periodicity of u, that

$$R_{-1} \circ K(\theta) = K(\theta - 1). \tag{4.52}$$

In particular, if K is the parameterization of an invariant circle of $S_\kappa \circ R_{-\frac{1}{2}}$ then by the property (4.49) of the square of a map above, we have that

$$S_\kappa \circ R_{-\frac{1}{2}} \circ S_\kappa \circ R_{-\frac{1}{2}} \circ K(\theta) = K(\theta + 2\omega).$$

So by the symmetry property in (4.50) of the standard map together with the symmetry (4.52) of the invariant circle, we have that

$$\begin{aligned} S_\kappa \circ S_{-\kappa} \circ R_{-1} \circ K(\theta) = K(\theta + 2\omega) \\ \implies S_\kappa \circ S_{-\kappa} \circ K(\theta - 1) = K(\theta + 2\omega) \end{aligned}$$

This is equivalent to saying that K is an invariant circle of $S_\kappa \circ S_{-\kappa}$ with rotation number $2\omega + 1$, where K is the invariant circle of $S_\kappa \circ R_{-\frac{1}{2}}$ with rotation number ω, which is the same as the symmetry in Eq. (4.28).

It is possible to verify the properties formulated in Section 4.4 that state that the maps $\mathcal{T}_{\kappa_1 0}$ and $\mathcal{T}_{0\kappa_2}$ can be rescaled to standard maps with twice the perturbation parameter.

If we define the transformation

$$P_\xi(x, y) = (x \mod 1, \xi y),$$

a simple computation tells us that

$$\mathcal{T}_{\kappa_1 0} = S_0 \circ S_{\kappa_1} = P_{1/2} \circ S_{2\kappa_1} \circ P_2$$

So if $S_{2\kappa_1}$ has an invariant circle, then the invariance equation is

$$S_{2\kappa_1} \circ K(\theta) = K(\theta + \omega).$$

We immediately know that $P_{1/2} \circ K(\theta)$ is an invariant circle for $\mathcal{T}_{\kappa_1 0}$. Namely,

$$P_2 \circ S_0 \circ S_{\kappa_1} \circ P_{1/2} \circ K(\theta) = K(\theta + \omega),$$

is equivalent to

$$\mathcal{T}_{\kappa_1 0} \circ P_{1/2} \circ K(\theta) = P_{1/2} \circ K(\theta + \omega).$$

The case of the map $\mathcal{T}_{0\kappa_1}$ is obtained for the above since when we use (4.7), we have that $\mathcal{T}_{0\kappa_1} = S_0^{-1} \circ \mathcal{T}_{\kappa_1 0} \circ S_0$. Then, it is clear that the circle $S_0^{-1} \circ P_{1/2} \circ K$ is invariant for $\mathcal{T}_{0\kappa_1}$. In fact, from Eq. 4.7 it is easy to see that if $\mathcal{T}_{\kappa_1\kappa_2}$ has an invariant circle with rotation number ω, then $\mathcal{T}_{\kappa_2\kappa_1}$ has an invariant circle with the same rotation number. This result was also stated in Eq. (4.31).

4.5.2 Results from the parameterization method

The parameterization method was applied using the rotation numbers obtained from section 4.4: γ, $\gamma + 1$, 2γ and $2\gamma + 1$ and also with $\frac{5\gamma+6}{4\gamma+5}$ and $\frac{\gamma+1}{4\gamma+5}$ which were found heuristically. The method produced in all the cases as critical boundaries between the existence and *breaking* of a given invariant circles with rotation number ω, (CB_ω), a *two horn*-shaped asymmetrical curve in the upper plane of the parameter space (κ_1, κ_2). The points obtained in the CB_ω correspond to the blow-up of the Sobolev norms of the parameterization function K. The critical boundaries are displayed in Figure 4.8 with the addition of the a curve of the first method to contrast the results. All the critical boundaries agree with the results from section 4.4 and are contained in the *tightest* curve from previous subsection. Notice that the CB corresponding to γ is related to the one of $\gamma + 1$ and the CB of 2γ is related to the one of $2\gamma + 1$ by a reflection with respect to the κ_2-axis.

Additionally to the rotation numbers that were predicted to be of importance in section 4.4.1, the parameterization method was applied to two

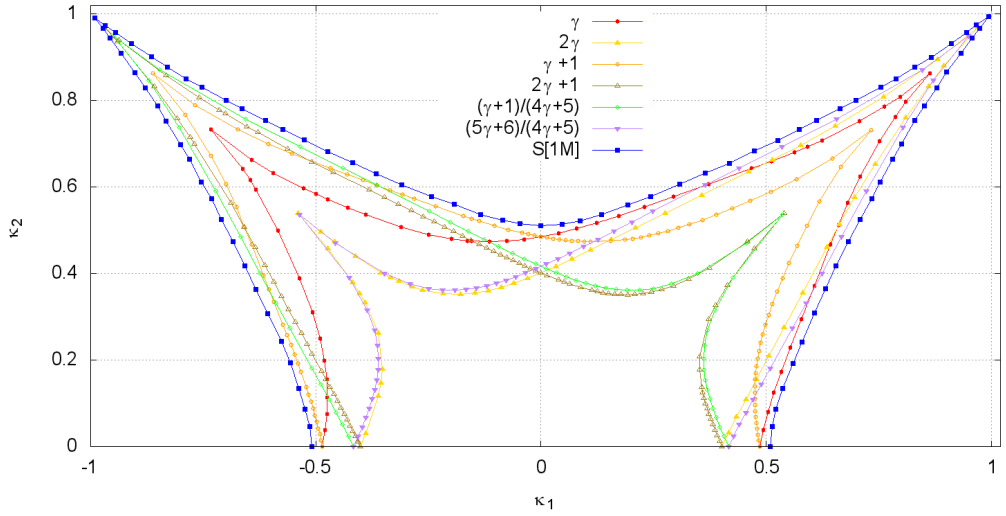

Figure 4.8: Critical boundaries for the existence of four KAM tori (CB_ω) $\{\gamma,\ \gamma+1,\ 2\gamma,\ 2\gamma+1,\ \frac{5\gamma+6}{4\gamma+5}$ and $\frac{\gamma+1}{4\gamma+5}\}$ found with the *parameterization method* contrasted with the critical boundary (CB_{gt}) found via direct simulation of the NASM.

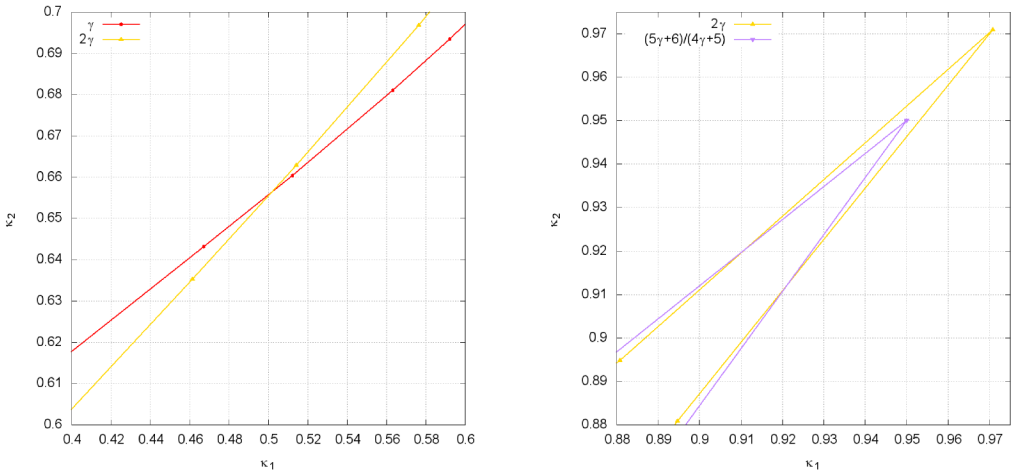

Figure 4.9: Details on the intersection between the critical boundaries $\{\gamma$, 2γ and $\frac{5\gamma+6}{4\gamma+5}\}$ from Fig. 4.8.

additional ones: $\frac{5\gamma+6}{4\gamma+5}$ and $\frac{\gamma+1}{4\gamma+5}$. These numbers were obtained empirically by iterating the map close to the invariant circle, obtaining a few digits by approximating the limit in (4.26) and then adding a tail of ones to the continued fraction. Neither of these two numbers correspond to a known reduced case of the map (4.4), however the results displayed on Figure 4.8 show that the corresponding CB_ω's give reasonable lower bounds to the CB_{gt} found by direct method in some regions of the parameter space. There exist more robust numerical methods[57, 58] to estimate rotation numbers of invariant sets, however at the time the concern was in corroborating the consistency of the previous analytic and numeric results. A numerical characterization of the rotation number of the most robust invariant circle as function of the parameters may be leaved to a further publication.

4.6 Discussion and conclusions

In section 4.4 was founded from the direct computation a horn shaped critical boundary for global transport, CB_{gt}, giving the threshold between bounded evolution of a set of initial conditions and global transport. Using the parameterization method in Sec. 4.5 was founded that the critical boundaries for the existence of invariant curves with given rotation numbers, the CB_ω's. All the CB_ω were found to be fully contained inside the CB_{gt}. It is expected that the CB_{gt} is minimal envelope of all the CB_ω associated to the invariant circles that exist for the map $\mathcal{T}_{\kappa_1\kappa_2}$.

CB's were also computed using a Greene's residue method in Ref. [59] for the $3D$ map,

$$\mathcal{F}_{k,\Delta k}\begin{pmatrix} x \\ y \\ \phi \end{pmatrix} = \begin{pmatrix} x + y + \frac{k'}{2\pi}\sin(2\pi x) & \mod 1 \\ y + \frac{k'}{2\pi}\sin(2\pi x) & \\ \phi + \Omega & \mod 1 \end{pmatrix}, \tag{4.53}$$

where $k' = \bar{\kappa} + \Delta\kappa\cos(2\pi\phi)$, which corresponds to a more general (quasi-periodic) variation of κ than the one in Eq. (4.2). In the case $\Omega = 1/2$, the map (4.53) is equivalent to the map in Eq. (4.1) with the appropriate choice of parameters. If the initial value of ϕ is 0 and $\Omega = 1/2$, the parameters of the map (4.53) and map (4.1) are related by:$\bar{\kappa} = \frac{\kappa_1+\kappa_2}{2}$, $\Delta\kappa = \frac{\kappa_2-\kappa_1}{2}$. Additionally in the special case when the initial value of ϕ is $1/4$, the map reduce to the Chirikov-Taylor map (4.6). In Ref. [59] the CB displayed correspond to the critical values of the Greene's residue[18] in the parameter

space $(\bar{\kappa}, \Delta\kappa)$ for map (4.53) for different periodic orbits with rotation vectors that approximate a two dimensional invariant torus. These *CB*'s have a diamond shape similar to the curves obtained in Sec. 4.4 in $(\bar{\kappa}, \Delta\kappa)$ parameter variables (see Fig. 4.10), which represent the threshold of global transport and disappearance of all invariant one dimensional tori for map (4.53) with rotation vectors of the form $(\omega, 1/2)$. In figure 4.11 we compare our CB_{gt} with one of the *CB* from Ref. [59] corresponding to the periodic orbit with rotation vector $(\frac{1705}{3136}, \frac{2631}{3136})$ with period 3136, that approximates a golden rotation vector. The critical curve is contained inside ours except for a few points that do not belong inside the region we computed.

To explore the phenomenon of the protruding regions in the parameter space that possibly exist for non autonomous maps with periods greater than two, we have studied map (4.53) with $\Omega = 1/3$, which correspond to a κ_n variation for map (4.1) with three values. Finding also critical boundaries that surpassed in a small region the one found for map (4.4).

Reference [60] computed the CB for a given rotation number in a *driven standard map* similar to Eq.(53). As in the previous case, the results are consistent with ours. In particular, they also found a diamond shaped *CB* in the $(\bar{\kappa}, \Delta\kappa)$ parameter space.

It is important to remark that in map (4.53) the two dimensional and the one dimensional tori are topological barriers to global transport due the uncoupled variation of ϕ with respect to (x, y). In general, Fig. 4.11 suggests that the destruction of the one dimensional tori implies the breaking of the two dimensional ones except for a few *peaks* that stand outside of our curve in the parameter space. It remains to study why are the two dimensional tori more robust that the one dimensional ones in these *peak* regions. Numerical evidence leads us to think that the critical boundary for global transport in the map (4.53) with $\Omega = p/q$ might fully contain the ones in Ref. [59].

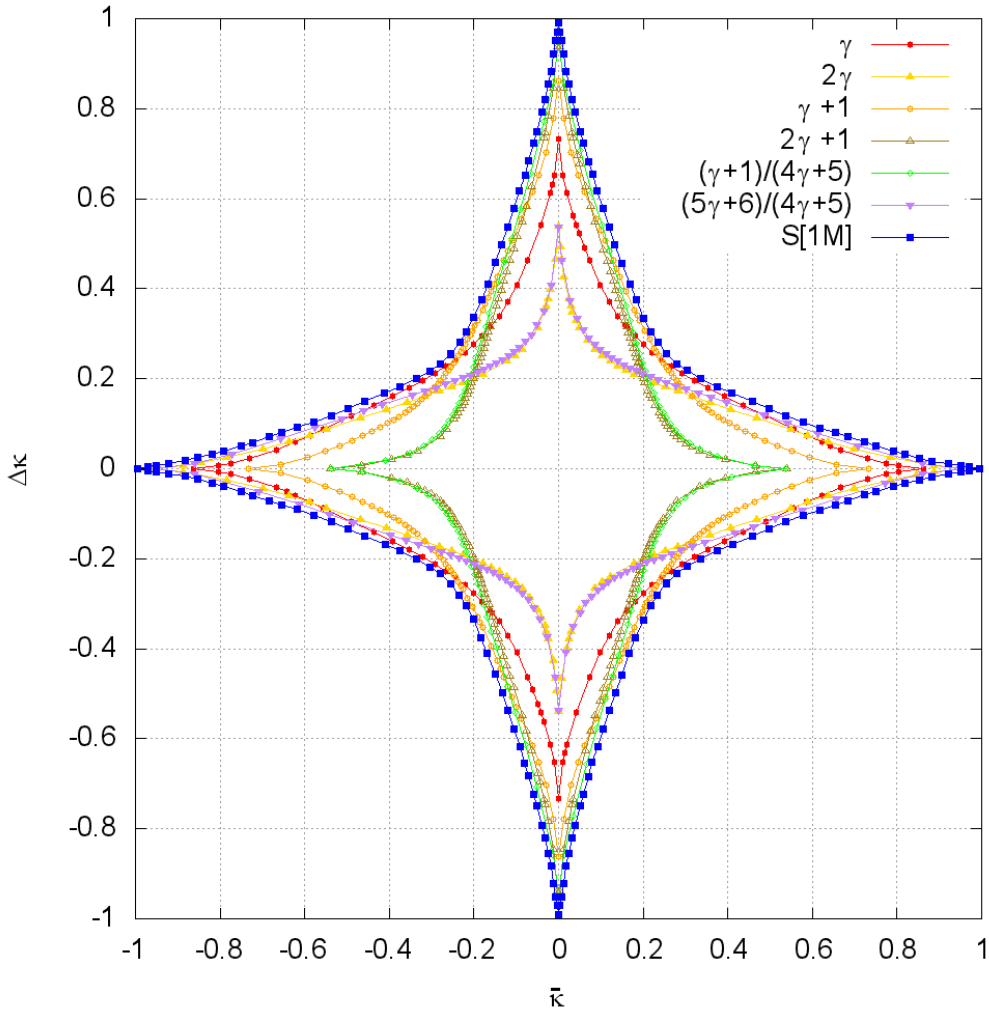

Figure 4.10: Plot in the $(\bar{\kappa}, \Delta\kappa)$ parameter variables of the CB_ω of four KAM tori $\{\gamma,\ \gamma+1,\ 2\gamma,\ 2\gamma+1,\ \frac{5\gamma+6}{4\gamma+5}$ and $\frac{\gamma+1}{4\gamma+5}\}$ found with the *parameterization method* and the CB_{gt} found via direct simulation of the NASM. The extension to the whole parameter space is obtained using the Eq. (4.27).

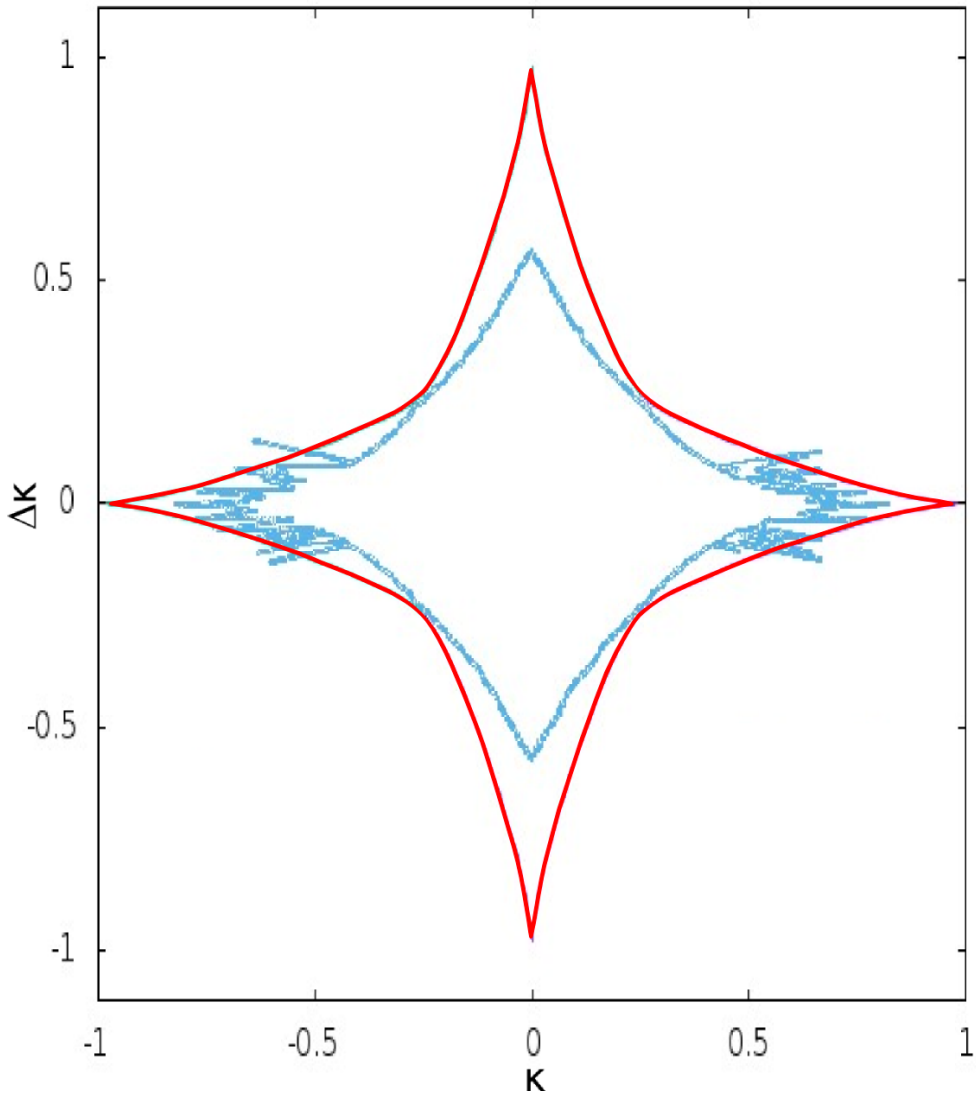

Figure 4.11: Critical boundary curve (CB_{gt}) found via direct simulation of the NASM (red) compared with one of the *CB* for a periodic orbit with rotation vector $(\frac{1705}{3136}, \frac{2631}{3136})$ for map (4.53) (blue) taken directly from Ref. [59] [*Exp. Math.* **5**(3):211-230,1996].

Chapter 5

Periodic orbits in twist maps

As mentioned before in chapter 3, the study of periodic orbits gives an insightful first approach to dynamical systems that can provide fundamental understanding of the behavior of many systems. Low order periodic orbits are usually the easiest to recognize structures in the phase space of any twist map but the high order ones (order $> 10^3$) are the ones that may give the most useful information. Since the early 60's with works from Newel[61], Greene[18], Ford[62, 63], Chirikov[10], the study of periodic orbits allowed to introduce powerful frameworks as the renormalization theory. Periodic orbits have been used to many ends, some of the most noticeable are: to determine the existence of an invariant circle as function of the parameter values[18], to determine the topology and dynamic of invariant sets[22, 24], to prove the existence of universal properties on maps close to critical[64, 24], to study the behavior of invariant sets with rotation numbers with a periodic structure in their continued fraction expansion (PACSE)[65], to give bounds for the gaps in invariant circles turned in cantori[22] and more. Notwithstanding the many results and applications, the search of periodic orbits of high order period has been always restricted to problems with symmetries that help to reduce the dimension of the search space, in particular reversible maps. Extension or mere corroboration of some of universal properties for maps without symmetries has not been possible due the inability to compute high order periodic orbits. The approach proposed in this chapter describes a **compound method** that modifies the parameterization method from Secs. 2.8 and 4.5 to estimate periodic orbits of high order $(10^2 - 10^6)$ and then use a 2D-Newton algorithm to improve the accuracy. The original motivation to develop this new method is to apply it to maps like (4.4), for

which there are no known useful symmetries that help to simplify the search of periodic orbits. By doing this, it would possible to round up the previous chapter having a tool to study and verify properties not guarantied to exist by the renomalization theory in tilt maps. The proposed method does not require any additional symmetry and in principle can be applied to any area preserving twist map (APTM).

5.1 Some results with periodic orbits

Although periodic orbits appear in many results in dynamical systems, their calculation is not always included in the theory. Even in more general (2-D) results like Mather theory, it is not proved if the *symmetric* periodic orbits that can be actually computed are the same *monotone orbits* predicted to exist by the theory. The first kind could be just a subset of the second.

The monotonicity and existence of periodic orbits (Birkhoff's theorem) are used in KAM results like Moser's Theorem (Thm. 2.4) to describe properties or prove the persistence of invariant circles for sufficient enough small values of the parameters, where among other hypothesis, a series of periodic orbits with rotation numbers $\{p_i/q_i\}_{i\in\mathbb{N}}$ such that $p_i/q_i \to \omega$ can be establish, this is illustrated in Fig. 5.1(a). This analytic perturbative result should be contrasted with the conjecture given by Green[18], mentioned in Chap. 2, that works outside the small parameter regime. Both use the existence of periodic orbits in twist maps but the second use a residue (a quantity computed over the periodic orbit points) to give numerical bounds to parameter values for the existence of an invariant circle. Greene's method uses a scaling rule of the residue and bifurcation of the stability of periodic orbits that can be only appreciated for high order periodic orbits with the critical behavior of invariant circle.

A complementary result, when $p_i/q_i \to P/Q$, found by Katok[66] and MacKay[67], affirm that the periodic orbits close to the monotonous intersection of the stable and unstable manifolds of the hyperbolic points of the P/Q resonance, not the P/Q-periodic orbit itself. This result too was corroborated by the computation of high order periodic orbits.

One more remarkable result of periodic orbits, treated in detail in next chapter, is the self similar behavior of critical invariant circles found by Shenker and Kadanoff[64, 68] which was the numerical evidence to back the introduction of renormalization theory by MacKay [67, 69] to twist maps.

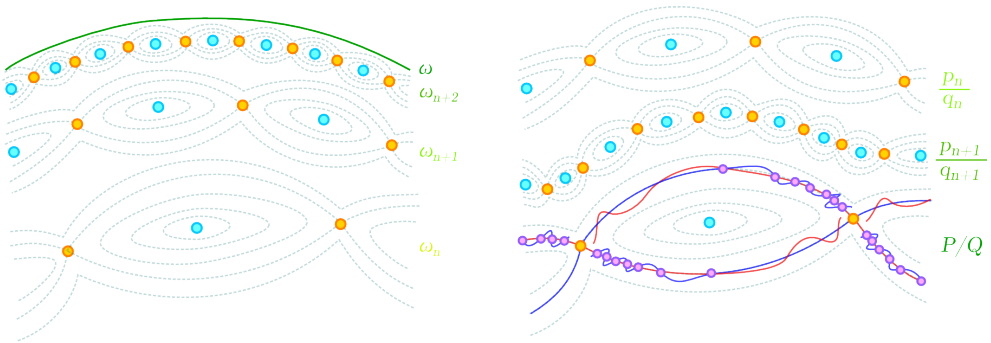

(a) (b)

Figure 5.1: Illustration of the periodic orbits uses in (a) KAM theory and (b) Katok-Mather result.

From renormalization theory, the critical behavior observed for the standard map is found to be universal behavior of invariant circles with rotation number ω in area preserving twist maps for critical parameter values and it is related to a critical point in the renormalization group. And again, the computation of self-similar universal bounds for twist maps require the computation of high-order periodic orbits.

One last result that is worth mentioning due to its importance and novelty is the *Principle of Approximate Combination of Scaling Exponents* (PACSE), Ref. [65], that basically found, through computation of high order periodic orbits, numerical evidence of relations between critical exponents and rotation numbers with periodic structure in their continuous fraction expansion.

The computation of high order periodic orbits have been restricted a very limited set of twist and non-twist maps, namely the reversible maps. There has been no attempt to study the properties of periodic orbits in non-reversible maps due the lack of reliable methods to compute them. In the following section will describe the nature of reversible maps.

5.2 Reversible maps

A map T is called *reversible*[70, 71, 46] if it can be written as the composition, $T = I_2 \circ I_1$, of two functions I_1 and I_2 with the property,

$$I_k \circ I_k = Id\,, \qquad k = 1, 2\,, \tag{5.1}$$

where Id is the identity. Functions that fulfill this property are called *involutions*. A list of properties of reversible maps can be found in Ref. [72] and further properties of involutions in Refs. [73, 74].

The invariant sets of involutions are called symmetry lines[1]. It can be proved (see Refs. [24, 68, 73]) that for any periodic orbit[2] of a reversible map with rotation number $\omega = p/q$, at least two points of the orbit lay on the symmetry lines.

The existence of symmetry lines allows to reduce the search of periodic orbits of a reversible twist map [18, 29] and non twist map [75] from a 2-D problem to a 1-D search on the symmetry line. In 1-D there are plenty of methods to search for zeros of a equation and in particular the quasi-Newton methods are efficient and well behaved [76]. This is why it is possible to find periodic orbits of high order period, $q \sim 10^6 - 10^7$. The only limit for their computation is the machine precision and not the complexity of the perturbation function presented, as it can be appreciated in Ref. [29] for different (reversible) maps.

The work done by Greene on twist (reversible) maps was extended to non-twist maps [75, 77, 78] and other more general cases [29] but always in problems with symmetries for which it is possible to reduce the search of periodic orbits to one dimension.

Studies of the same kind for maps in higher dimensions (like Refs. [46, 79]) or two dimensional maps without symmetry lines have to search the periodic orbits in at least two dimensions, where the basin of attraction more often than not have a very complicate (fractal) structure[80] which makes methods like a 2D-Newton very unstable and sometimes unreliable unless the seed is already very close to the periodic orbit, see Fig. 5.2. Additionally we mention that the problem of the computation of periodic orbits via continuation methods over a newton-like method can be very complex[80, 79] due adjacent invariant structures like invariant manifolds.

This problem has been sometimes approached by reducing the search to orbits with some kind of symmetry, as in chapter 3 with the sequential periodic orbits (SPO's), but the results rarely are as general as in the work of Greene.

[1] In Ref. [73] a more general definition is used for symmetry lines.

[2] At least periodic orbits that approximate invariant circles not homotopic to a point.

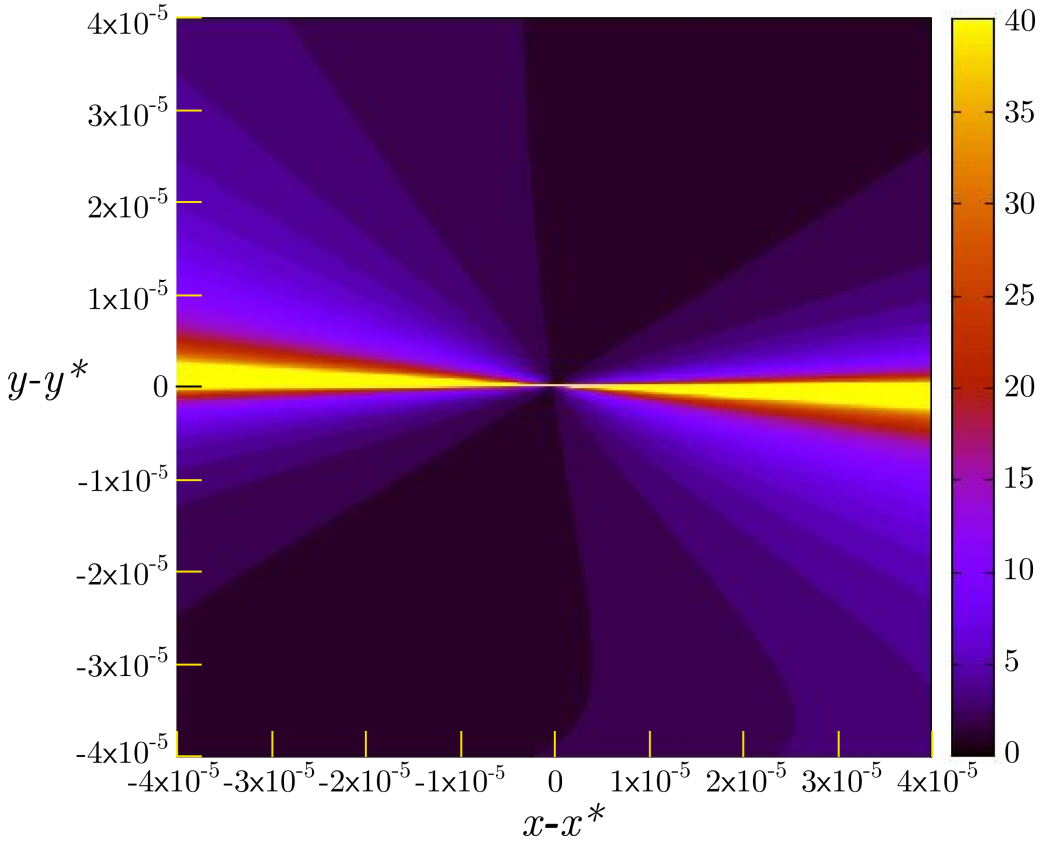

Figure 5.2: Basin of attraction around a hyperbolic periodic point (x^*, y^*) of the 34/55-periodic orbit of the Chirikov-Taylor map (4.6) with $\kappa = 0.9707$. The colors reflects the number of iterates of a 2D-Newton of a given point would persist around the region. Yellow indicates that the point stays in the region (basin).

5.2.1 The case of the standard map

In Ref. [18], heavily inspired by deVogelaere[81] work on flows, Greene gave to the Chirikov-Taylor map Eqs. (4.6)[3], a decomposition in two involutions I_1 and I_2, $\mathcal{S}_\kappa = I_2 \circ I_1$, defined as,

$$I_1 \begin{pmatrix} x \\ y \end{pmatrix} = \begin{pmatrix} -x \\ y - \frac{\kappa}{2\pi}\sin(2\pi x) \end{pmatrix}, \qquad I_2 \begin{pmatrix} x \\ y \end{pmatrix} = \begin{pmatrix} y - x \\ y \end{pmatrix}. \tag{5.2}$$

[3]In this chapter considered with the opposite sign, $\kappa = -\epsilon$ respect the definition in Eqs. (4.6).

Considering that x is an angular variable ($x \in [0, 1)$), the symmetry lines for I_1 are: $x = 0$ and $x = 1/2$, and for I_2: $x = \frac{y}{2}$ and $x = \frac{y+1}{2}$. These lines can be appreciated in Fig. 5.3 superposed over the phase space of Chirikov-Taylor map for $\kappa = 0.97$. In the same figure a few of the low order periodic orbits are signaled by colored O and X marks for linear elliptic and hyperbolic stability, respectively. It can be appreciated that the line $x = 0$ contains only linear elliptic periodic points and for this reason is called the *dominant* symmetry line[64], although sometimes the name is also used also for the $x = 1/2$ line.

5.3 Non-reversible maps

In the present work, a *non-reversible map* refers to any map for which there is **no known** decomposition into two involutions. It is an open problem to characterize when it is possible to write a map as a composition of **two** involutions.

The study of periodic orbits in non-reversible maps is not a purely academic exercise, in the literature very often the dynamical system (not just symplectic maps) have no known symmetries to simplify their analysis. In particular, twist maps of the form of Eq. (2.19) in which the perturbation functions depend on both variables, it seems to be impossible to write them as the composition of two involutions. There exist a collocation-like method [82] that can be used for general symplectic maps but it has not been yet published.

5.4 A new method to find periodic orbits: *the compound method*

The parameterization method in the spirit of Ref. [83, 12, 13, 11, 37] and the works of Percival[84] and MacKay[85] use Fourier series to asymptotically find quasi-periodic rotation circles, namely KAM tori. This approach does not require the use of symmetry lines, however by its construction, it can only approximate continuous objects never discrete structures like periodic orbits. The norm of parametrization function K blows-up when the invariant circle ceases to exist (as a continuous object) breaks into a cantorus, a feature used extensively in Sec. 4.5.2 to obtain the Figs. 4.8 and 4.9. However in twist

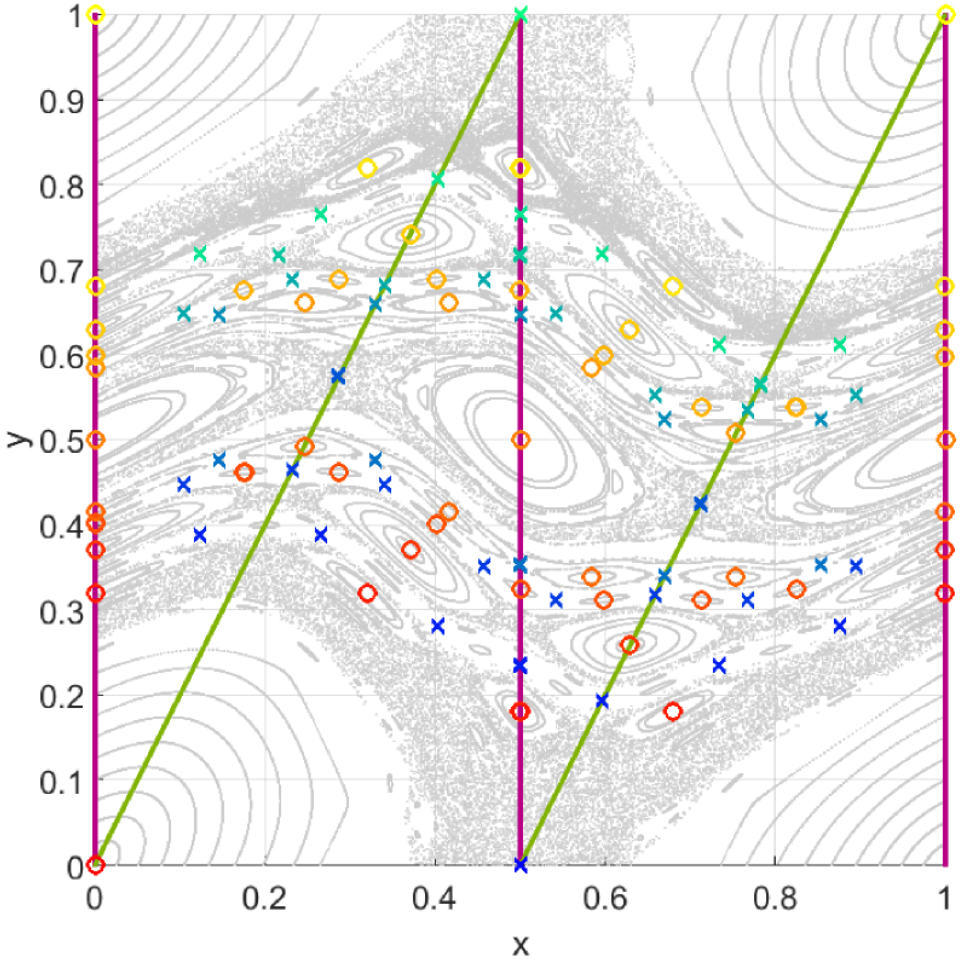

Figure 5.3: Example of symmetry lines and periodic orbits in the Chirikov-Taylor map (4.6) with $\kappa = 0.97$. The purple lines correspond to the symmetry lines of I_1 and green lines to I_2. Low order periodic orbits are signaled by colored O and X marks for linear elliptic and hyperbolic stability respectively, corresponding to rotation numbers: 1/5, 2/7, 3/8, 2/5, 1/2, 3/5, 5/8, 2/3, 5/7 and 4/5.

maps, the monotone periodic orbits always exist for all values of the parameters (Birkhoff theorem 2.3 and Aubry-Mather theory[22]). The discussion in this section omits to review the material on the parameterization method

from Sec. 2.8 and proceeds to expose the problems to adapt the scheme to the search of periodic orbits.

If one naively attempts to apply the parameterization method to a non-diophantine rotation number the result will not converge due the "small denominators" problem and it is worse for rational rotation numbers, where there is a "zero denominators" problem. To be more clear on what "zero denominators" means, lets review how to solve a reduced invariant equation like (2.43) and (2.44). The kind of homological equation to solve is the following,

$$W(\theta) - W(\theta + \omega) = \tilde{e}(\theta)\,, \tag{5.3}$$

where $\tilde{e}$ has zero average. On a Fourier series representation,

$$W(\theta) = \sum_{k=-\infty}^{\infty} a_k e^{2\pi i k\theta}\,, \qquad \tilde{e}(\theta) = \sum_{k=-\infty}^{\infty} b_k e^{2\pi i k\theta}\,, \tag{5.4}$$

the problem reduces to find a_k as function of b_k with a_0 is a free parameter and $b_0 = 0$. This can be done for almost all coefficients by,

$$a_k = \frac{b_k}{1 - e^{2\pi \imath \omega k}}\,, \qquad \text{if } e^{2\pi i \omega k} \neq 1\,. \tag{5.5}$$

However to ensure the convergence of the series is needed the Diophantine hypothesis of ω.

If $\omega = P/Q$, there exists a *zero denominators problem* for every a_k with $k = mQ$, $m \in \mathbb{Z}$, this is a resonance. The problem is similar to finding the periodic orbit with the resonant normal form in Sec. 3.2, although now it is not clear what would be the meaning of a *resonant approximate parameterization.*

There are two possible ways to avoid this: a blunt approach to find $\tilde{\theta}$ such that,

$$\tilde{e}(\tilde{\theta}) = \sum_{m=-\infty}^{\infty} b_{mQ} e^{2\pi i m Q \tilde{\theta}} = 0\,, \tag{5.6}$$

which can be very complicate and may not be well posed problem because the frame of work is an approximate solution. A second approach would be setting a priori all coefficients $b_{mQ} \equiv 0$. This is, eliminating the resonance eliminates the denominator zero. This transforms the goal of parameterization method to find a continuous parametric curve $K(\theta)$ that contains all

the periodic points (hyperbolic and elliptic) from the monotone periodic orbit $\omega = P/Q$ up to an error of $O(||\tilde{e}||)$. However this does not guaranty the convergence of the series.

A quantitative aspect not explicitly mentioned in Secs. 2.8 and 4.5 is that the number of Fourier modes considered is for practical reasons always finite. However it is guarantied by the theory behind the parametererization method that for a fixed upper bound for the error of the approximate solution, $||\tilde{e_1}|| < \tilde{\varepsilon}$ there is an optimal maximum number of Fourier coefficients $N(\tilde{\varepsilon})$ to be considered so the norm of the remaining tail of harmonics can always be safely included inside the error of the approximate solution[13]. A proof in the convergence of the new method is still pending so there is not a clear argument of how many harmonics is convenient to use. If the number of harmonics N^* is fixed a priori, then the method, when it converges, should give an optimal trigonometric polynomial of degree N^* such that the parametric curve pass close to the points of the periodic orbit. And even if the method does not converge and gives an approximate value of a point of the periodic orbit with a bounded error, it may suffice to be used as seed for 2-D methods. So a convergence theorem may not be needed at this point for the implementation of the method.

For obvious reasons, if this curve K exists, it can not be an invariant subset of the phase space of the map. The curve has no dynamical meaning for the map except for the points of it that approximate the points of the periodic orbit of the corresponding rotation number. Only these points can be considered as approximating an invariant object. Extra conditions must added to find where are the periodic orbits approximately embedded in the curve. However, it must be kept in mind that a good approximation of a periodic orbit point can be used as a seed for a 2D root finder to improve the error. As in any other numerical implementation, the use of a finite number of terms in the approximations, a finite number of Fourier modes in this case, and the machine rounding error guaranties that the computed curve K will yield only approximate results.

Although the hypothesis of the existence of $K_{P/Q}$ does not seem unreasonable for maps like the standard map (2.26) or the period two NASM (4.4) and probably any locally twist map, it is an open problem to prove its existence. The numerical evidence indicates that it should be possible to write a theorem to prove this, nevertheless for now this chapter focus only on the implementation of the hybrid method and presenting the numerical evidence.

If an existence theorem is proven or if its error can be bounded, an in-

teresting question would be to relate properties such as the regularity of the parametric curves K_{P_n/Q_n} to a K_ω, when $\{P_n/Q_n\}_{n\in\mathbb{N}}$ is a sequence that converge to a Diophantine rotation number ω. A different approach could be to use an a-posteriori theorem (like the one in Appendix 2) to prove the existence and uniqueness of these periodic orbit points.

5.4.1 Phase tracking

The method described in last section yields a parametric curve $K_{P/Q}$ that in some sense is "close" to the periodic orbit that we are looking for. The problem now turns into finding the correct phase, a value $\tilde{\theta} \in [0, 1/2q_n)$ such that,

$$T^Q(K_{P/Q}(\tilde{\theta})) \approx K_{P/Q}(\tilde{\theta})\,. \tag{5.7}$$

Because theorem 2.3, there must exist at least $2Q$ equidistant values of $\tilde{\theta}$ in $[0, 2\pi)$ that satisfy (5.7), but in most of cases[4] it is only needed to find two independent $\tilde{\theta}_1$ and $\tilde{\theta}_2$, since if $K_{P/Q}(\tilde{\theta}_1)$ is a periodic point then $K_{P/Q}(\tilde{\theta}_1 + nP/Q)$, $n = 1, 2, ..., Q$ are also periodic points of the same orbit, see Fig. 5.4.

There are two candidates to find the *correct* phases $\tilde{\theta}$: the error of the approximate periodic point,

$$E(\theta) = ||T^Q(K(\theta)) - K(\theta)|| \tag{5.8}$$

and the (Greene's) residue $R(\theta)$ (Sec. 2.6),

$$R(\theta) = \frac{1}{4}\Big[2 - \mathrm{Tr}\Big(DT^Q(K(\theta))\Big)\Big]\,. \tag{5.9}$$

for $\theta \in [0, 2\pi]$, however it is enough to restrict the search for $\theta \in [0, P/Q]$. Both present problems in their computation and the residue in particular has a very well known unstable behavior when computed *not close enough* of a periodic orbit, see Fig. 5.6. Nevertheless the underlying idea behind the parameterization method is that the exact dynamic of the map T is conjugated to a rigid rotation over a parametric curve K. So it is expected that

[4]There are cases in which there can be more than one set of elliptic (hyperbolic) fixed points connected by iteration of the map, like the map (4.4) for the case $\kappa_1 = \kappa_2$. When the Aubry-Mather theory is applicable, it is guarantied that there can only exist two monotone orbits for a fixed rotation number, one minimal orbit and one minimax orbit, see Ref. [22].

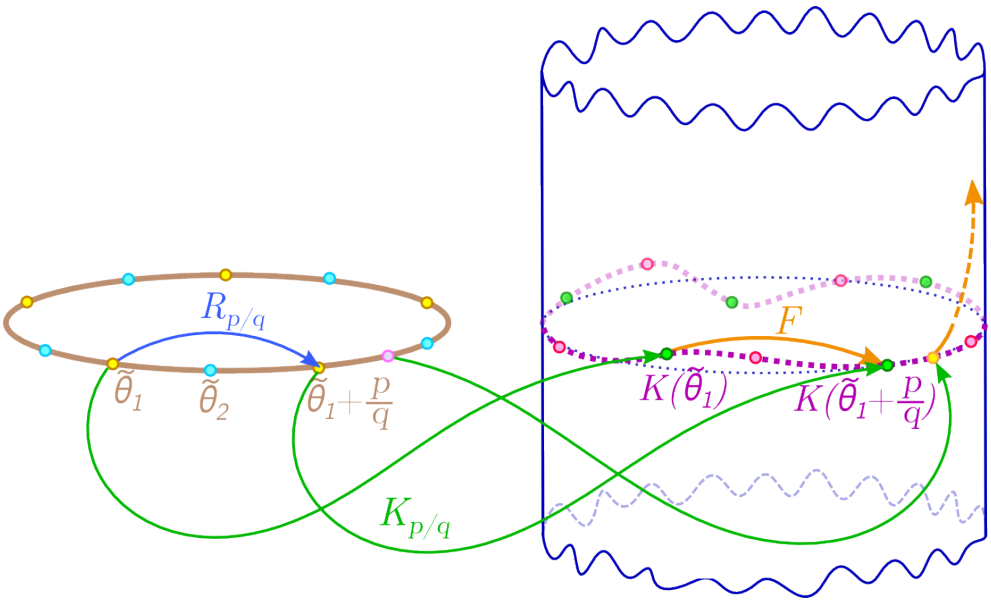

Figure 5.4: Illustration of the components of the modified parameterization method, for which the parameterization $K_{p/q}$ is only dynamically consistent with the map F for periodic orbits points.

for the current case that for values of θ for which $K_{P/Q}(\theta)$ is close to a fixed periodic point the dynamic will be also approximated by the conjugation,

$$T(K_{P/Q}(\theta)) \approx K_{P/Q}(\theta + P/Q)\,, \tag{5.10}$$

while for other values of θ the dynamic may radically differ. However the later points of the parametric curve $K_{P/Q}$ are not relevant for the search of periodic orbits and the dynamic of T can be interchanged with the one of the conjugation $K_{P/Q}(\theta + \ell P/Q)$ for the present case. The benefit of using the dynamic of the conjugation $(K_{P/Q} \circ R^{\ell}_{P/Q})$ is to compute approximate versions E and R is that both will be computed over smooth functions over bounded (compact) domains, so both are expected be also regular. So we define,

$$\tilde{E}(\phi) = ||K_{P/Q}(\theta + P) - K_{P/Q}(\theta)|| \tag{5.11}$$

$$\tilde{R}(\theta) = \frac{1}{4}[2 - \mathrm{Tr}(\tilde{\mathcal{M}}^{Q}(\theta))]\,, \tag{5.12}$$

where $\tilde{\mathcal{M}}^{Q}(\theta)$ is computed as,

$$\tilde{\mathcal{M}}^{Q}(\theta) = DT[K_{P/Q}(\theta + (Q-1)P/Q)] \cdots DT[K_{P/Q}(\theta)]\,, \tag{5.13}$$

Fig. 5.5 illustrates the difference between computing DT over an exact iterate of the map $T^{\ell}(K_{P/Q}(\theta))$ and over the $K_{P/Q}(\theta + \ell P/Q)$, as in (5.13). The acumulative error of using a bad approximation of the periodic point to compute R can be appreciated in Fig. 5.6. This is the main reason of why the residue is not usually used as an estimator, the iterates may diverge exponentially if the seed is not close enough to the exact value and their subsequent evaluation in DT only make the calculation more inexact.

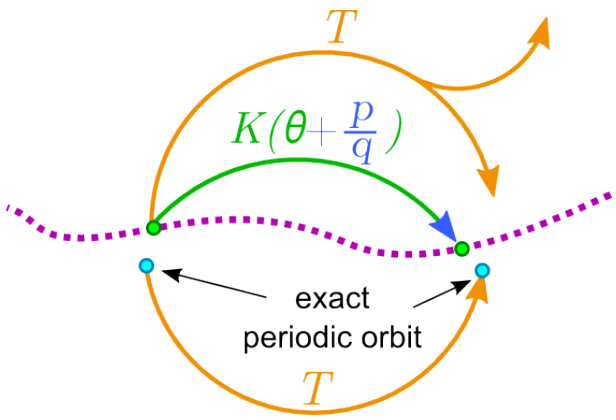

Figure 5.5: Illustration of the difference of using the parameterization K over the map T to estimate the iterate of an approximate periodic orbit point.

$\tilde{E}(\theta)$ and $\tilde{R}(\theta)$ are expected to be more regular than their exact counterparts $E(\theta)$ and $R(\theta)$, since the first ones are computed in a bounded domain and K and $\mathcal{M} = DT$ have some regularity. However the numerical implementation of (5.11) is also not a good option because for high values of $Q \sim 10^5$, it can yield values close to the machine precision[5]. So instead, the following two error estimators are used,

$$\hat{E}_1(\theta) = \sum_{n=0}^{Q-1} |T \circ K(\theta + nP/Q) - K[\theta + (n+1)P/Q]| \,, \tag{5.14}$$

$$\hat{E}_2(\theta) = \left\{ \sum_{n=0}^{Q-1} \{T \circ K(\theta + nP/Q) - K[\theta + (n+1)P/Q]\}^2 \right\}^{1/2} \tag{5.15}$$

These error functions are also regular for the same reason as $\tilde{E}$ but yield not too small values thanks to the sum over all the iterates, see Fig. 5.7.

[5]We are working with quadruple precision.

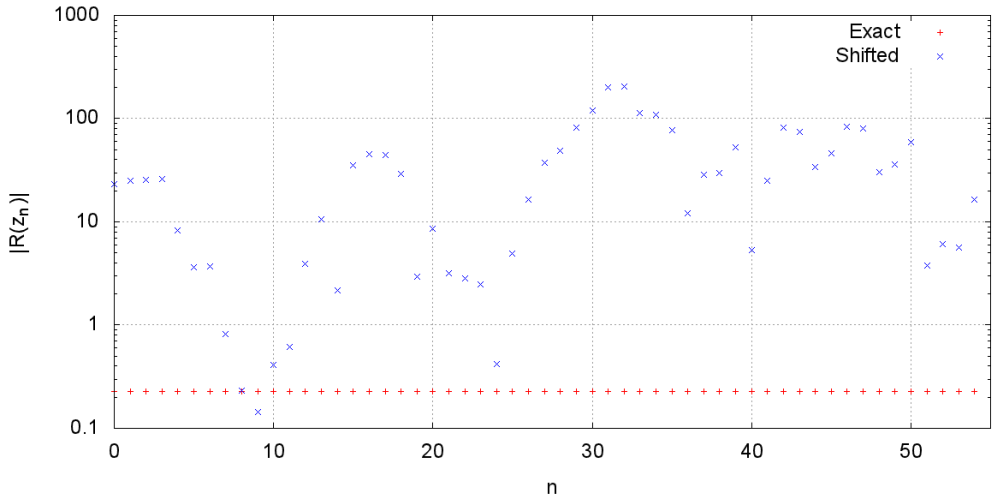

Figure 5.6: Greene residue $|R(z_n)|$, Eq. (4.36), of 55 iterates $z_k = T^k(z_0)$ $k = 0, 1, ..., 54$ of two approximations of a point of the 34/55-periodic orbit in the Chirikov-Taylor map for $\kappa = 0.9700$. The "exact" point has an error of 7.5809×10^{-09} and residue 2.278622×10^{-01} that remains constant on all iterates. The "shifted" point has an initial error of 1.1591×10^{-02} and a residue varies on every iterate.

Although in the numeric calculations of high order periods ($Q \gtrsim 10^3$), $\hat{E}_1$ is better behaved for values close to machine precision.

The regularity of the function $\tilde{R}$ and the fact that it should be positive (negative) close to the elliptic (hyperbolic) periodic points, guaranties that $\tilde{R}$ is an oscillatory function with mean close to zero, as it can be appreciated in Fig. 5.8.

As it can be appreciated in Figs. 5.7 and 5.8, it was found for all the computed cases that the minima $\{\theta_n^{(min)}\}_{n=1,...,2Q}$ of $\hat{E}_1$ are placed always in the vicinity of the maxima and minima $\{\theta_n^{(crit)}\}_{n=1,...,2Q}$ of $\tilde{R}$. The numerical evidence consistently suggest that there exist an analytic relation between the critical points of $\tilde{R}$ and the minima of $\hat{E}_1$ but there is not yet a complete proof to this fact. The numerical evidence is in agreement with an a-posteriori Newton-Kantorovich theorem that relates the critical points of the approximate residue $\tilde{R}$ with the existence of periodic orbits, the detailed statement of the theorem can be found in Appendix 2. The a-posteriori theorem guaranties the existence of a unique fixed point (a periodic orbit point

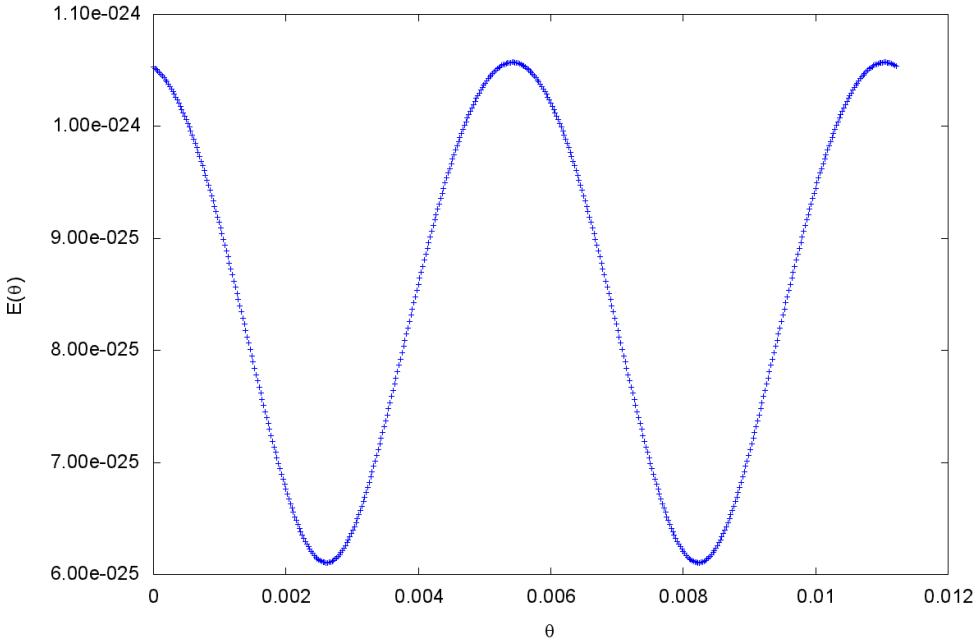

Figure 5.7: Error $\hat{E}_1$ of the approximated solution for the 55/89-periodic orbit of the rational harmonic map (5.23) with the values of the parameters: $\kappa = 0.4$, $p_a = 2.5$ and $p_m = 0.37$.

for $G(x) = T^Q(x) - x = 0$) in an open ball $B_r(\bar{x})$ around of a given $\bar{x}$, if some bounds hold and a polynomial function of these bounds on r admits negative values for $r > 0$. Restricting the theorem to the present case, the polynomial function have the form,

$$p(r) = Z_2(r)r^2 - r + Y_0\,, \tag{5.16}$$

where $Z_2(r)$ is a positive function of r and Y_0 is positive real constant that in their definition appear the modulus of the residue R dividing. So it is more likely for $p(r)$ to be negative in an interval $(0, \tilde{r})$ for $\bar{x} = K_{P/Q}(\theta)$ around the critical points of $\tilde{R}(\theta)$ for which Z_2 and Y_0 are smaller. This not a proof but an argument that will be addressed in a future work.

Although there is not yet a complete explanation of this "numerical coincidence", it is convenient to use the critical points of $\tilde{R}$ as an estimator of the position $\tilde{\theta}_n$ of the periodic points in $K_{P/Q}(\theta)$ when $\hat{E}_1$ is unreliable due to numerical error.

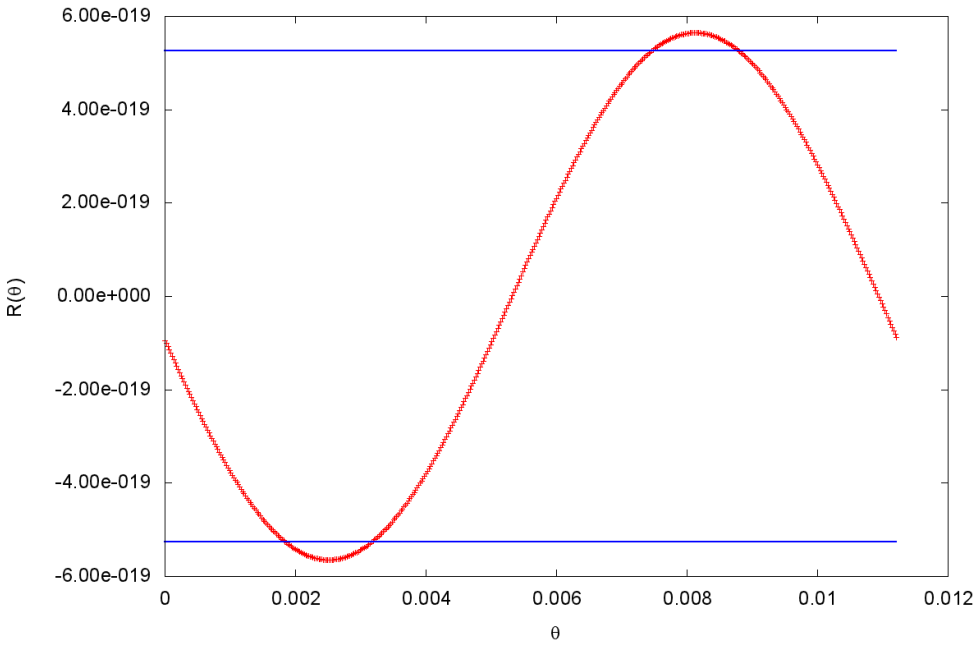

Figure 5.8: Regularized residue $\tilde{R}$ of the approximated solution for the 55/89-periodic orbit of the rational harmonic map (5.23) with the values of the parameters: $\kappa = 0.4$, $p_a = 2.5$ and $p_m = 0.37$. The blue horizontal lines correspond to the exact value residue for the hyperbolic (-5.253×10^{-19}) and elliptic (5.254×10^{-19}) orbits.

Table 5.1 displays data from a few periodic orbits of the Chirikov-Taylor map, in which it is possible to observe the agreement between the minima of $\hat{E}_1$ and the critical points of $\tilde{R}$.

5.4.2 Refining the results

There are several sources of error in the method previously described, however in almost of the cases tested it has yielded a reasonable approximation of the periodic orbit ($E \sim O(10^{-8})$ for $Q \sim O(10^3)$ with $\tilde{R} \lesssim O(10^{-1})$). A natural step to refine the results of the modified parameterization method is to use a 2-D root finder such as a 2-D Newton method. Even if the Newton basin is irregular or fractal, if the initial guess is *close enough*[6] the method converge.

[6]Inside an open convex set containing the zero, see theorem 5.2.1 from Ref. [76].

$\frac{P}{Q}$		$\hat{E}_{1,min}$	x_{min}	$\tilde{R}_c$	x_c
$\frac{5}{8}$	(h)	1.689×10^{-10}	0.000×10^{-00}	2.520×10^{-01}	0.000×10^{-00}
	(e)	1.689×10^{-10}	6.250×10^{-02}	-2.573×10^{-01}	6.250×10^{-02}
$\frac{55}{89}$	(h)	3.118×10^{-08}	0.000×10^{-00}	2.133×10^{-01}	0.000×10^{-00}
	(e)	3.079×10^{-08}	5.595×10^{-03}	-2.172×10^{-01}	5.618×10^{-03}
$\frac{377}{610}$	(h)	6.762×10^{-10}	0.000×10^{-00}	8.328×10^{-02}	0.000×10^{-00}
	(e)	6.404×10^{-10}	8.098×10^{-04}	-8.391×10^{-02}	8.197×10^{-04}
$\frac{987}{1597}$	(h)	2.015×10^{-11}	0.000×10^{-00}	1.380×10^{-02}	0.000×10^{-00}
	(e)	1.909×10^{-11}	3.093×10^{-04}	-1.381×10^{-02}	3.131×10^{-04}

Table 5.1: Comparison of the localization in the angular variable x of a local minimum of $\hat{E}_1$ and a critical point of $\tilde{R}$ for a few periodic orbits of the Chirikov-Taylor map (4.6) with $\epsilon = 0.9700$, computed by the *modified parameterization method*.

In 2-D, the Newton method reduces to iterating the following contracting map,

$$\begin{pmatrix} x_{n+1} \\ y_{n+1} \end{pmatrix} = \begin{pmatrix} x_n \\ y_n \end{pmatrix} - \lambda \cdot \big(DG\big)^{-1} \begin{pmatrix} x_n \\ y_n \end{pmatrix} \cdot G \begin{pmatrix} x_n \\ y_n \end{pmatrix}, \tag{5.17}$$

where $\lambda = 1$, DG is the Jacobian matrix G, defined as,

$$G \begin{pmatrix} x \\ y \end{pmatrix} = T^Q \begin{pmatrix} x \\ y \end{pmatrix} - \begin{pmatrix} x \\ y \end{pmatrix}, \tag{5.18}$$

where T is the map assumed to have a point of the P/Q periodic orbit close to (x_0, y_0), a point obtained by the modified parameterization method.

Due the quadratic convergence of the Newton method, with a few iterations of (5.17) is possible to reduce the initial error of order $O(10^{-8})$ to $O(10^{-32})$, the machine error for quadruple precision. However in most of cases it seems necessary to use a pseudo-Newton method, assigning a constant value $\lambda < 1$ (or a function $\lambda(n) \leq 1$) to improve the chance of convergence from the seed data at the cost of reducing a little the rate convergence. Some of the functions $\lambda(n)$ tested are shown in figure 5.9.

It should be remarked to the reader that if the seed data is not sufficiently close enough to the root, even damped pseudo-Newton method can yield unwanted results like local minima. There exist many other strategies

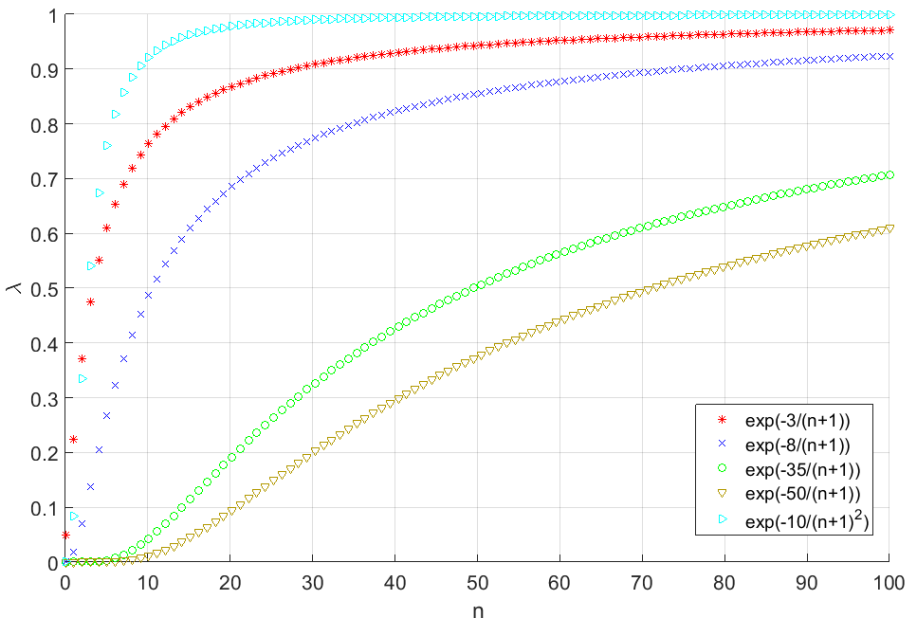

Figure 5.9: Example of a few $\lambda(n)$ used in implementations of pseudo-Newton algorithm.

that may help to improve the rate of convergence of a pseudo-Newton algorithm: Armijo's rule, quadratic backtracking, steepest descent method, etc. Some specialized texts to consult on the subject are Refs. [76] and [86]. An alternative to a Newton method is the method developed by Haro[82] but the work is not yet published.

5.4.3 The compound method

Summarizing the method described in this section and taking into account the numerical evidence given by earlier implementations, the original algorithm 2.1 for the parameterization method is modified into the following algorithm described below.

Algorithm 5.1.

1) Let $e_0(\theta) = T \circ K_0(\theta) - K_0(\theta + P/Q)$.

2) *Find* $\tilde{\theta}$ *such that* $\tilde{R}(\tilde{\theta})$ *is a local minimum.*

3) *Compute the matrix* $M(\tilde{\theta})$ *from equation* (2.38).

4) *Solve for* $W_2(\tilde{\theta})$ *from* (2.43)*, after eliminating all resonant terms of the Fourier series of* e_0 *and* W_2*, that is the terms of the form* $c_{nQ}e^{\pm inQ\tilde{\theta}}$.

5) *Choose the average* $\int_{\mathbb{S}^1} W_2(\theta)d\theta$ *so that* $-[M_0^{-1}(\theta+\omega)e_0(\theta)]_1 - S_0(\theta)W_2(\theta)$ *has an average close to zero.*

6) *Solve for* $W_1(\tilde{\theta}_0)$ *from* (2.44)*, eliminating all the resonant terms.*

7) *Compute the step* Δ*,*

$$\Delta(\tilde{\theta}) = M_0(\tilde{\theta})W(\tilde{\theta})$$

8) *Obtain the new parameterization* K_1*,*

$$K_1(\theta) = K_0(\theta) + \Delta(\theta)$$

9) *Set* $K_0(\theta) = K_1(\theta)$ *and go to step 1) until an a priori fixed bound* $|\min e_0(\theta)| < T$ *is satisfied.*

10) *Find two adjacent local minimum and maximum* $\left\{\tilde{\theta}_1, \tilde{\theta}_2\right\}$ *of* $e_0(\theta)$.

11) *Apply the contracting map (5.17) to* $(x_0, y_0) = K_0(\tilde{\theta}_k)$*,* $k = 1, 2$ *to obtain a point from each one of the hyperbolic and elliptic periodic orbits.*

The steps $1) - 9)$ from algorithm 5.1 will be called the *modified parameterization method* and the $10) - 11)$ the 2D-Newton method.

5.5 Implementation of the compound method

5.5.1 Error and residue behavior

To test the capabilities of the compound method as a continuation method to obtain periodic orbits from an integrable case, the *modified parameterization method* was used alone to make the continuation on the Chirikov-Taylor map. From earlier tests of the code it was found the need to perform the

computations with quadruple precision ($O \sim 10^{-30}$), particularly in the FFT computation. Figure 5.10 shows the error $\tilde{E}_1$ as function of the perturbation parameter κ. Notice that the horizontal lines in the figure are close to the machine error ($O \sim 10^{-30}$) and should be considered spurious.

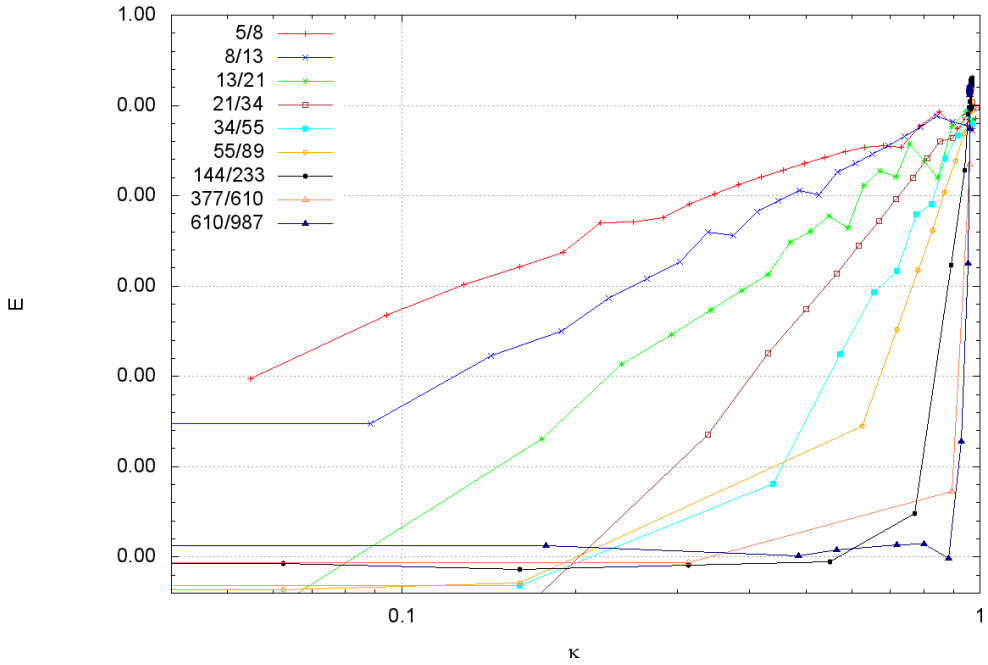

Figure 5.10: Global minimum of the error E of the approximated solution for the Chirikov-Taylor map (4.6) as function of the parameter κ, for different rotation numbers using only the *modified parameterization method*.

A first observation from Fig. 5.10 is that the error of E grows as a power of κ to a given exponent. This is to be expected since the *modified parameterization method* is attempting to approximate with a smooth continuous curve a periodic orbit that tends to have a self-similar (fractal) structure as $\kappa \to \kappa_G$ and Q increase. The next feature appreciable in the figure and in the table 5.2, that seems counterintuitive, is that for $\kappa < \kappa_G$ the error reduces as the period of the orbit increase. Although this is easily explained by considering that the stability of the periodic orbit, given by the residue, modulates the behavior of the error (Fig. 5.11). It can also be appreciated from Fig. 5.10 that working in quadruple precision, the *modified parameterization method* gives reasonable good estimates of the periodic orbits for values of κ away

$\frac{P}{Q}$	$\tilde{E}_1$	E	$\tilde{R}$	R
$\frac{5}{8}$	6.0450×10^{-08}	5.3007×10^{-09}	-2.3412×10^{-01}	-2.3637×10^{-01}
$\frac{8}{13}$	3.6744×10^{-09}	7.2300×10^{-10}	-2.12062×10^{-01}	-2.13982×10^{-01}
$\frac{13}{21}$	1.7126×10^{-08}	1.7767×10^{-10}	-1.9657×10^{-01}	-1.9822×10^{-01}
$\frac{21}{34}$	5.1154×10^{-09}	1.9298×10^{-08}	-1.64352×10^{-01}	-1.6552×10^{-01}
$\frac{34}{55}$	3.3095×10^{-09}	1.5404×10^{-08}	-1.2680×10^{-01}	-1.2751×10^{-01}
$\frac{55}{89}$	1.6056×10^{-09}	1.9979×10^{-08}	-8.2585×10^{-02}	-8.2893×10^{-02}
$\frac{89}{144}$	9.3009×10^{-10}	1.2959×10^{-08}	-4.1153×10^{-02}	-4.1232×10^{-02}
$\frac{144}{233}$	1.7206×10^{-10}	6.9020×10^{-09}	-1.3033×10^{-02}	-1.3042×10^{-02}
$\frac{233}{377}$	4.5521×10^{-11}	5.6428×10^{-11}	-2.0967×10^{-03}	-2.0969×10^{-03}
$\frac{377}{610}$	8.5157×10^{-12}	9.8185×10^{-12}	-1.0800×10^{-04}	-1.0798×10^{-04}
$\frac{610}{987}$	5.1989×10^{-25}	5.1215×10^{-23}	-8.9148×10^{-07}	-8.9147×10^{-07}
$\frac{987}{1597}$	3.5981×10^{-26}	1.6107×10^{-23}	-3.7914×10^{-10}	-3.7914×10^{-10}

Table 5.2: Progression of the errors $(\tilde{E}_1, E)$ and residues $(\tilde{R}, R)$ for the first P/Q hyperbolic periodic orbits that approximate the golden mean invariant circle in the Chirikov-Taylor map (4.6) for $\kappa = 0.9600$, computed by the modified parameterization method alone.

from the critical. The 2D-Newton method may only be required, depending of the precision needs, for calculations with κ near critical.

As a complement to the error behavior, the amplitude of the approximate residue $\tilde{R}$ of the computed periodic orbits behaves as expected. Fig. 5.11 displays the amplitude of the approximate residue $\tilde{R}$ of the same periodic orbits from Fig. 5.10. Even for the unrefined periodic orbit data, the four lowest order periodic orbits that incidentally have the lowest error near the critical region, cross at $\kappa \approx 0.971$ and $\max|\tilde{R}| \approx 0.25$.

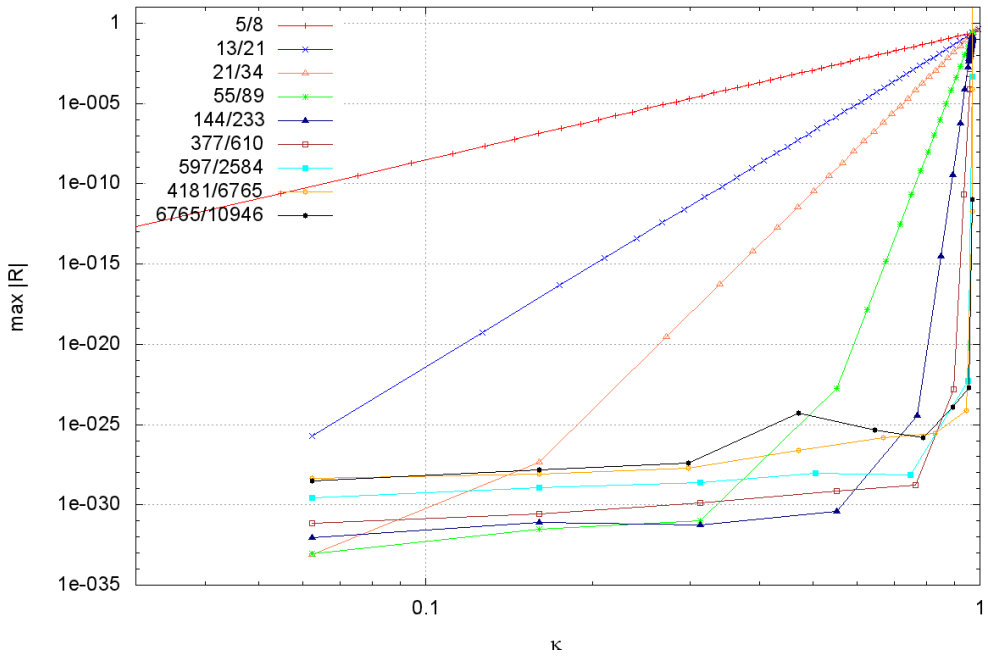

Figure 5.11: Amplitude of $\tilde{R}$ of the approximated solution for the Chirikov-Taylor map (4.6) as function of the parameter κ, for different rotation numbers using only the *modified parameterization method*.

5.5.2 An a-posteriori argument

There exist a-posteriori Newton-like theorems that have been used in the literature to validate the existence and uniqueness of solutions found numerically [87, 88, 89, 90, 91].

Applying an a-posteriori Newton-Kantorovich theorem in a radii polynomial approach[91, 89] (see Appendix 2) to the problem of finding an approximated periodic orbit from the modified parameterization method reduces after some algebra to finding a positive real constant Y_0 and a positive real function $Z_2(r)$ such that,

$$\frac{1}{|4R|}\left|\Big((DT^Q)^{-1} - Id\Big)F(\bar{x})\right|_X \leq Y_0\,, \tag{5.19}$$

$$\sup_{x\in\overline{B_r(\bar{x})}} \frac{1}{|4R|}\left|\Big((DT^Q)^{-1} - Id\Big)\Big(DF(\bar{x}) - DF(x)\Big)\right|_{B(X)} \leq Z_2(r)r\,, \tag{5.20}$$

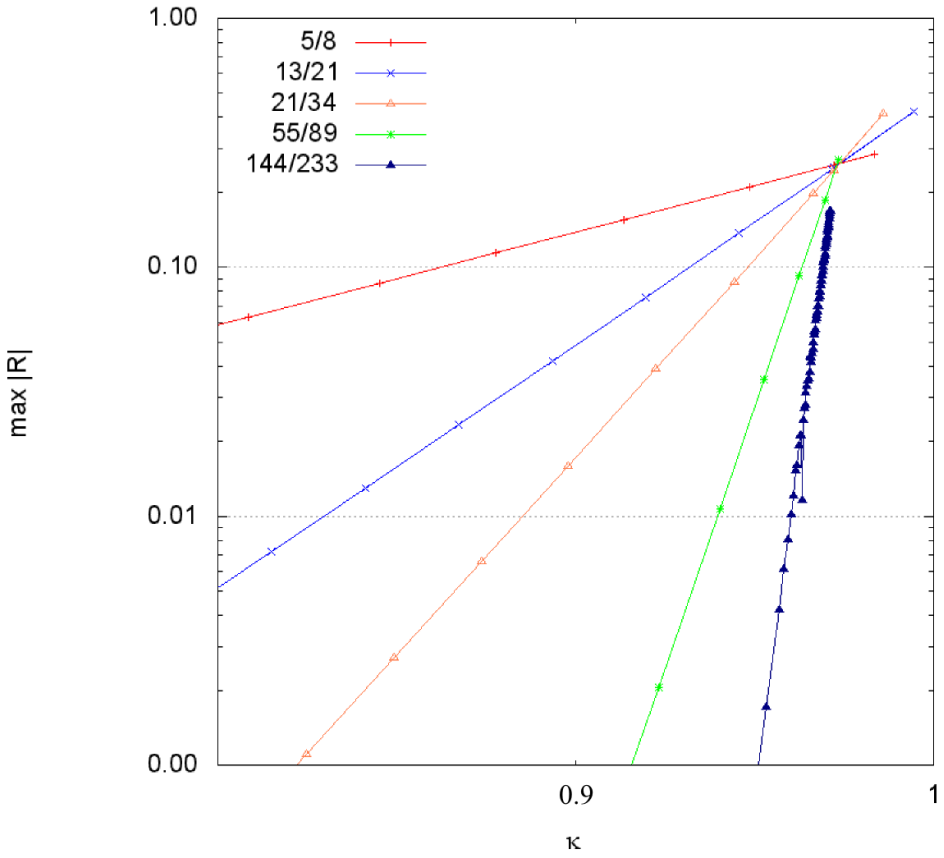

Figure 5.12: Detail of figure 5.11 around $\kappa \approx 0.971$ and $\max|\tilde{R}| \approx 0.26$.

where R is the Greene's residue, $|\cdot|_X$ is the distance in the cylinder, $|\cdot|_{B(X)}$ is an adequate matrix norm and F is defined as,

$$F(x) = T^Q(x) - x\,. \tag{5.21}$$

And then determine if there exist $r > 0$ such that the polynomial,

$$p(r) = Z_2(r)r^2 - r + Y_0\,, \tag{5.22}$$

is negative.

It is still a work in progress to find appropriate bounds for the contents of the norms in (5.19) and (5.20) although for the analytic maps T considered in this chapter, does not seem to be an insurmountable challenge.

The observation that can be made from (5.19)-(5.22) is that if $|R|$ has a bigger value then bounds Y_0 and $Z_2(r)$ can be taken smaller which implies that the polynomial $p(r)$ is more likely to be negative for r in an interval $[0, \tilde{r}]$.

5.6 Results of the compound method

The compound method was tested for three symplectic maps: the standard map (4.6) (in the Chirikov-Taylor map case), a three parameter analytic map (5.23) with no known useful decomposition into two involutions and the two-periodic NASM (4.4). The results are presented in this section.

Additionally invoking the renormalization theory, we had the following hypothesis about the critical behavior or periodic orbits in general area preserving twist maps (APTM's).

Claim 1. *For twist maps of the form (2.19), the residues of the set of periodic orbits with rotation numbers $\{P_n/Q_n\}_{n\in\mathbb{N}}$ such that $P_n/Q_n \to \omega$, $n \to \infty$, follow an scaling rule as function of the perturbation parameter ϵ. Additionally the residues $R_{p/q}(\epsilon)$ cross at the same critical values of the residue R_c and ϵ_c.*

The first part of claim 1, the scaling rule in terms of ϵ is a well stablish behavior of this kind of maps[22] but the unique critical value of the residue has been dosumented only in the Chirikov-Taylor map (4.6) with $|R_c| \approx 0.25$ for $\omega = \gamma$, see Ref. [18]. The critical value of the residue is known to be a periodic series of values and not unique for the standard non-twist map [92], so it is a non trivial assertion.

5.6.1 On the standard map

The first test of the *compound method* was done over the Chirikov-Taylor map Eq. (4.6) to compare with the orbits obtained by symmetry lines. The test allowed to identify some initial problems of the code and discover the surprising agreement between the critical points of $\tilde{R}$ and the minima of $\hat{E}$. Also it was possible to compare the difference between using different number N^* of harmonics in the approximation. For small values of Q, the total number of harmonics N^* was taken as $2Q$, while for larger values $N^* \sim 4Q$.

Increasing the value of N^* over $4Q$ did not reflect in a better convergence of the method and in some cases increase it since the extra terms were spurious.

The results of performing a first numerical continuation by the *modified parameterization method* and then using the data as seed for the 2D-Newton method are contained in table 5.3 and in a more complete form in table 5.6 in the appendix at the end of chapter.

$\frac{P}{Q}$	Orbit x	E	R
$\frac{5}{8}$	$1.04262381263415710544 \times 10^{-01}$	1.7776×10^{-33}	-2.3618×10^{-01}
$\frac{8}{13}$	$7.2292421040641022513 \times 10^{-02}$	3.8240×10^{-45}	-2.1396×10^{-01}
$\frac{13}{21}$	$5.06992260762055879603 \times 10^{-02}$	1.4227×10^{-30}	-1.9779×10^{-01}
$\frac{21}{34}$	$3.5022447826195364453 \times 10^{-02}$	3.0469×10^{-30}	-1.6521×10^{-01}
$\frac{34}{55}$	$2.4048789198498598295 \times 10^{-02}$	1.5432×10^{-29}	-1.2748×10^{-01}
$\frac{55}{89}$	$1.62171825022147208409 \times 10^{-02}$	2.8721×10^{-32}	-8.2110×10^{-02}
$\frac{89}{144}$	$1.0731773004662365072 \times 10^{-02}$	6.7440×10^{-52}	-4.0823×10^{-02}
$\frac{144}{233}$	$6.9344882456917456713 \times 10^{-03}$	5.2130×10^{-55}	-1.3101×10^{-02}
$\frac{233}{377}$	$4.39068507873134101191 \times 10^{-03}$	1.9267×10^{-32}	-2.0969×10^{-03}
$\frac{377}{610}$	$2.74217144026659842688 \times 10^{-03}$	9.5578×10^{-30}	-1.0800×10^{-04}
$\frac{610}{987}$	$1.70222914399736324091 \times 10^{-03}$	9.8163×10^{-45}	-8.9147×10^{-07}
$\frac{987}{1597}$	$1.05402094177906953965 \times 10^{-03}$	6.5275×10^{-46}	-3.7914×10^{-10}

Table 5.3: Angular component x of the closest point to $x = 0$ of the first few golden mean approximates P/Q hyperbolic periodic orbits of the Chirikov-Taylor map (4.6) for $\kappa = 0.9600$, computed by the modified parameterization method (table 5.2) and then refined by a 2D-Newton method up to $|E| < 10^{-28}$.

As mentioned before in Sec. 5.4.2, the convergence of the pseudo-Newton method can be sometimes troublesome. Last row on table 5.3 is an example

of this, the error of the seed had to be taken very low (10^{-26}) so the method converge to the lower bound ($< 10^{-28}$). To improve this scenario a first step is to use the whole compound method to do the continuation, that means not using the 2D-(pseudo)-Newton method at the end but every time the modified parameterization method's error reach a fixed threshold. Nevertheless there are cases in which the pseudo-Newton method need a very fine tuning to ensure its convergence, which may be caused by multiple causes: a seed close to the fractal boundary of the basin, multiple local minima in the neighborhood, etc. Additionally, to improve the chances of convergence of all the 2D-pseudo-Newton implemented variations were coded using an octuple precision ($O \sim 10^{-64}$) library in C++. This was observed to be useful for p/q-periodic orbits of periods of order $q \gtrsim F_{19} = 6765$.

5.6.2 On the *rational harmonic map*

A more interesting case to test the compound method is a standard-like map,

$$x_{n+1} = x_n + y_{n+1}\,, \tag{5.23a}$$
$$y_{n+1} = y_n + \frac{\kappa}{2\pi} V'(x_n)\,, \tag{5.23b}$$

with the perturbation function,

$$V'(x) = f(x) - \int_0^1 f(s)ds\,, \tag{5.24}$$

where,

$$f(x) = \frac{\sin(2\pi x + p_a)}{1 - p_m \cos(2\pi x)}\,. \tag{5.25}$$

This map is known to be reversible for $p_a = n\pi$, $n \in \mathbb{Z}$ and thus in these cases can be written as the product of involutions,

$$I_1^n \begin{pmatrix} x \\ y \end{pmatrix} = \begin{pmatrix} -x \\ y - (-1)^r \frac{\kappa}{2\pi} \frac{\sin(2\pi x)}{1-(-1)^r p_m \cos(2\pi x)} \end{pmatrix}, \qquad I_2^n \begin{pmatrix} x \\ y \end{pmatrix} = \begin{pmatrix} y - x \\ y \end{pmatrix}. \tag{5.26}$$

Note also that for $p_m \neq 0$ the perturbation function $V'(x)$ can be expressed as an infinite series of Fourier harmonics and is singular at $p_m = 1$. This perturbation function was studied before by [93] and [29] to test different

kind twist maps universality results. Recently it was possible to find a generic two involutions decomposition of this map following Ref. [94], however the invariant sets of this generic involutions are not useful to compute periodic orbits, so for all the intended purposes this map is treated as non-reversible. The numerical continuation for this map in Ref. [29] was found to be very sensitive to the variation of parameters p_a and p_m, this can be appreciate in Fig. 5.13. For notation purposes this map is called *rational harmonic* map due the form of the pertubation function.

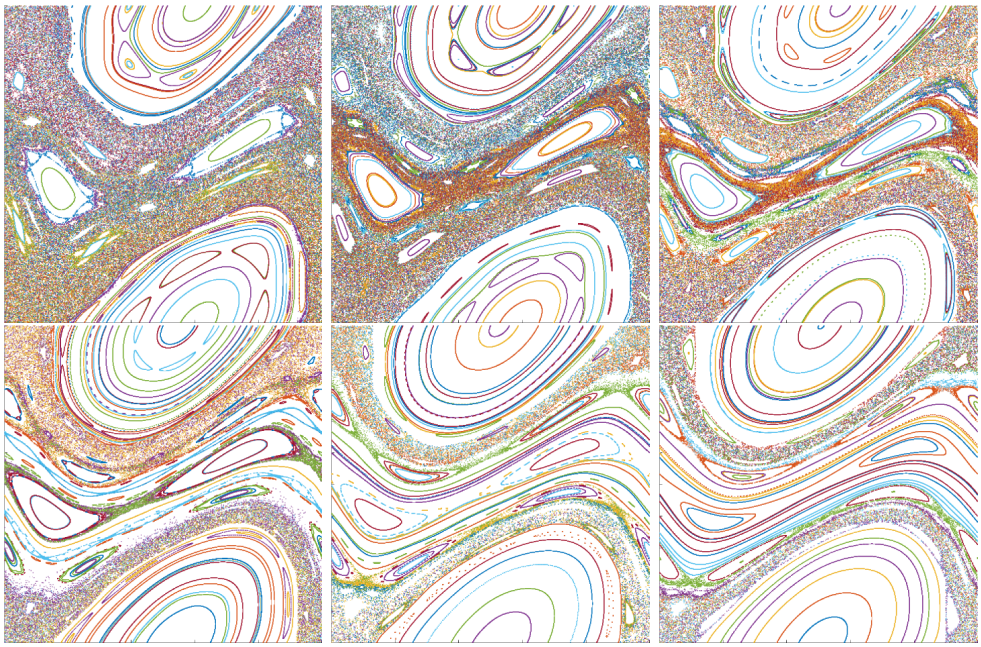

Figure 5.13: Examples of the phase space (x, y) in the unitary cell $[0, 1]^2$ of the *rational harmonic* map (5.23)-(5.25) for $(\kappa, p_m) = (1.4, 0.4)$ and different values of p_a, from left to right: 2.6, 2.7, 2.8, 2.9, 3.0, and 3.1.

This map can help to study the role of reversibility and persistence of symmetry lines in twist maps and we believe it has not been studied in detail in the past due its apparent lack of symmetries. This map has the symmetry

$$(x, y; \kappa, p_a, p_m) \mapsto (x - 1/2, y; \kappa, p_a + \pi, -p_m)\,, \tag{5.27}$$

which can be used to reduce the search in the parameter space from $\mathbb{R}^3$ to $\mathbb{R}^2 \times \mathbb{R}^+$. To better characterize the map and know where in the parameter

space would be more profitable to compute periodic orbits, the modified parameterization method (MPM) was applied as a continuation method over the parameter κ starting from the integrable case $\kappa = 0$ over an uniform mesh in (p_a, p_m) for 987/1597-periodic orbit, stopping at $|\tilde{R}| \sim 0.25$. The results can be appreciated in Fig. 5.14. The stopping criterion comes from Claim 1, that was found numerically to be true for the rational harmonic map for periodic orbits with rotation numbers of the from F_{n-1}/F_n for all the values of the parameters (p_a, p_m) used.

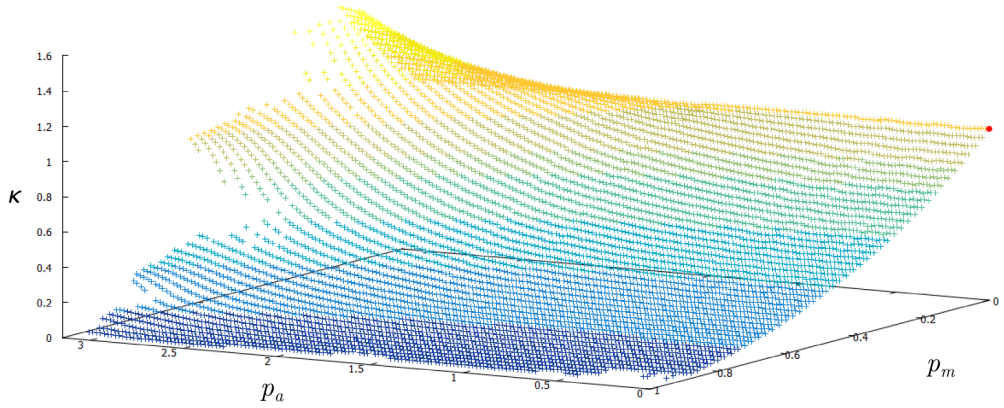

Figure 5.14: Critical manifold on the parameter space for the 987/1597-periodic orbit of the rational harmonic map (5.23)-(5.25), obtained by continuation over parameter κ and fixed values of (p_a, p_m), starting from the integrable case $\kappa = 0$. The points on the manifold are marked by + colored as function of κ. The red dot correspond to the case of the standard map.

Extra computations performed for rotation numbers of the form F_{n-1}/F_n, found that the shape of Fig. 5.14 unchanged and thus agreeing with the renormalization theory and Claim 1.

From Fig. 5.14, the behavior of the critical value of κ as function of p_m seems to agree with what could be expected from the perturbation function (5.25), bigger values of p_m should yield lower values of κ_*. However for $p_a \sim \pi$ there appear irregularities that suggest that the critical surface may have folds around which the κ_* rise to values bigger than the $\kappa_* = \kappa_G$, the standard map critical parameter value to which the map reduces in $(p_a, p_m) = (0, 0)$. Because of this observation, it seemed insightful to compute periodic orbits for $(p_a, p_m) = (3.0, 0.4)$, parameter values close to a fold but not in a trivial

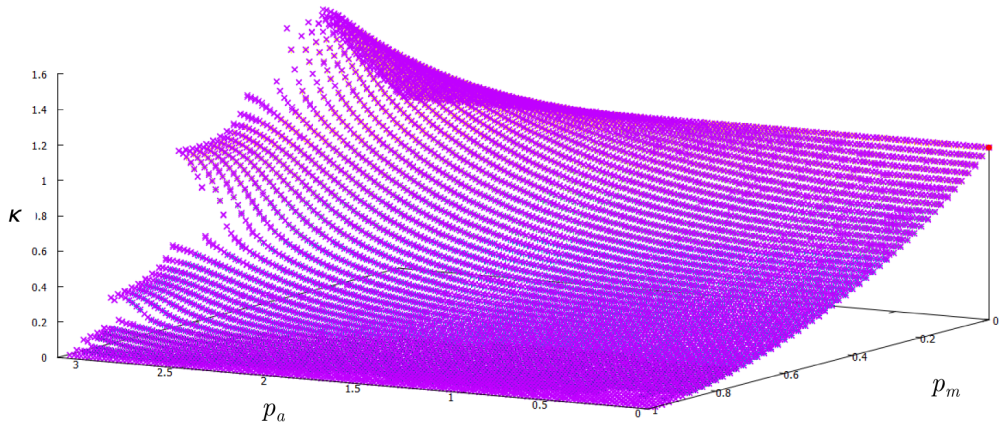

Figure 5.15: Superimpose of the critical manifold on the parameter space for the 144/233-periodic orbit (magenta X) of the rational harmonic map (5.23)-(5.25) over the manifold from Fig.5.14, for the same values of (p_a, p_m).

reversible case. Some of the computed orbits are presented in table 5.4 and in a more complete form in table 5.8 at the appendix.

A surprising benefit not originally considered in the implementation of this method, is that it is possible to continue the periodic orbits **beyond** the breaking of the invariant circle. It is increasingly difficult for high order periodic orbits, but it is possible to compute them and in cases like the present map can yield new information about the resurgence of invariant circles. This can be appreciated in Fig. 5.16.

5.6.3 On the two periodic NASM

The two periodic NASM in its two parameter autonomous reduction, Eq. (4.4) is another good candidate to test the method. This map does not have symmetry lines for a general election of the parameters, so the only possible validation of the found periodic orbit was the direct iteration of the points.

The periodic orbits found by the compound method are in table 5.5 and in a more complete form in table 5.9 in the appendix at the end of chapter.

The results found are similar to the previous case, although it was needed to prove with several different damping functions to ensure the converge of the 2D-pseudo-Newton method. This can be appreciated on the error of 377/610-periodic orbit, which have a considerable lower value thanks to a

$\frac{P}{Q}$	Orbit x	E	R
$\frac{8}{13}$	$9.84400324333751592206 \times 10^{-01}$	1.5314×10^{-04}	-2.1690×10^{-01}
	$9.84194430418146115882 \times 10^{-01}$	4.8935×10^{-39}	-2.1777×10^{-01}
$\frac{21}{34}$	$9.97753743054888484767 \times 10^{-01}$	1.3827×10^{-05}	-1.8059×10^{-01}
	$9.97722363363172234098 \times 10^{-01}$	1.6284×10^{-47}	-1.8095×10^{-01}
$\frac{55}{89}$	$4.35066410514029663774 \times 10^{-04}$	2.8190×10^{-03}	-2.8817×10^{-01}
	$4.42076348408883988105 \times 10^{-04}$	1.8242×10^{-37}	-1.0589×10^{-01}
$\frac{144}{223}$	$4.09885888135278521212 \times 10^{-04}$	8.3211×10^{-11}	-1.3204×10^{-01}
	$4.54519288406945185848 \times 10^{-04}$	8.2324×10^{-29}	-2.5599×10^{-02}
$\frac{377}{610}$	$4.54770852734730605323 \times 10^{-04}$	8.6265×10^{-05}	-2.5479×10^{-02}
	$5.10890552501945729879 \times 10^{-04}$	1.2373×10^{-29}	-6.2363×10^{-04}
$\frac{987}{1597}$	$2.18102889348964055253 \times 10^{-04}$	9.4507×10^{-11}	-9.2787×10^{-08}
	$2.88969724223810721485 \times 10^{-04}$	9.5395×10^{-31}	-4.0099×10^{-08}
$\frac{2584}{4181}$	$5.70931653171076079438 \times 10^{-03}$	1.1379×10^{-24}	-3.2521×10^{-19}
	$5.70811191353601822914 \times 10^{-03}$	1.1872×10^{-31}	-3.2944×10^{-19}
$\frac{6765}{10946}$	$1.23693970334899424212053377 7 \times 10^{-02}$	3.1733×10^{-28}	-8.6237×10^{-24}
	$1.23693970334899424212053376 9 \times 10^{-02}$	9.5204×10^{-29}	-2.0985×10^{-24}

Table 5.4: Angular component x of the point closets to $x = 0$ of a few P/Q hyperbolic periodic orbits found for the *rational harmonic* map (5.23) with $(\kappa, p_a, p_m) = (1.7150, 3.0, 0.4)$, computed by the modified parameterization method (white rows) and then refined by a 2-D Newton method (gray rows) until $E < 10^{-28}$.

fortuitous converge of the non-damped Newton method. A possible reason for the increased difficulty of convergence is due characteristics of the map, this is addressed in the discussion at end of the chapter.

The numerical evidence proved Claim 1 to be true for the two period NASM (4.4) for periodic orbits which rotation number were obtained from the **continuous fraction expansion** of γ and 2γ[7]. Plots illustrating this finding are in Figs. 5.17 and 5.18.

Using the Claim 1 it was possible to verify the most part of the critical bounds for the existence of the invariant circles of rotation γ and 2γ found in Sec. 4.5.2, see Fig.5.19. There was a systematic error in the calculation of

[7]The claim was found to be false if the rational rotation numbers are not obtained from the continuous fraction.

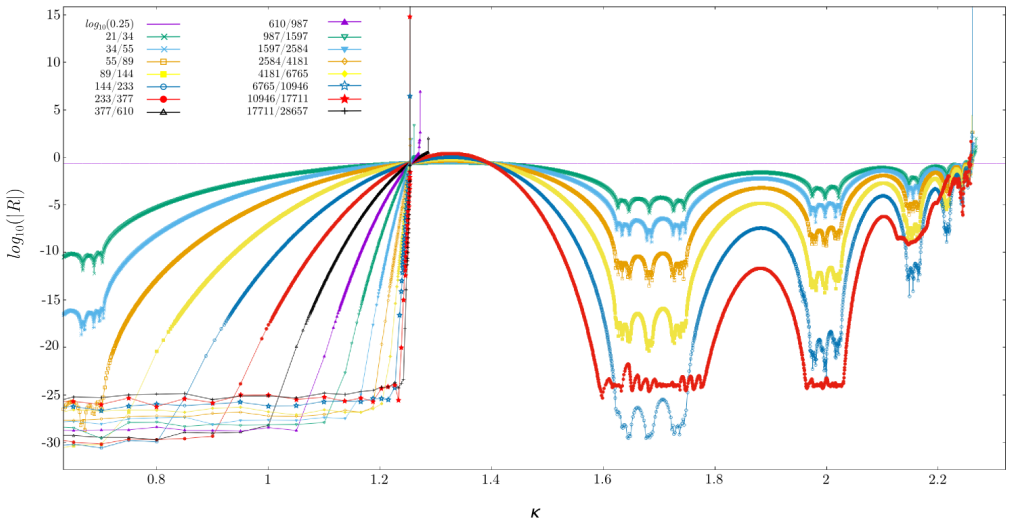

Figure 5.16: Residue of periodic orbits as function of the parameter κ in the rational harmonic map (5.23)-(5.25) for $(p_a, p_m) = (3.0, 0.4)$.

the critical parameter values near the "tips" of the graphs of the CB_ω. The value displayed on the diagonal for Fig. 5.19 correspond to the last value for which the continuation with the compound method converged, not critical parameter values near the reported values of $|R_c|$ for $\omega = \gamma$ or 2γ. A more accurate implementation of the compound method near critical regions of the parameters may be required to improve the results.

5.7 Discussion and conclusions

The method presented in this chapter was used successfully to find periodic orbits for different non-reversible maps. For parameter close to criticality the error in the *modified parameterization method* (MPM) seems to grow and the use of a 2D-(pseudo)-Newton method is necessary. The convergence of the later method is not optimal for high order periodic orbits and the implementation of different "line search algorithms" or more complex "descent methods" (see Refs. [76, 86]) may be needed to improve the results.

There is also a possible unwanted complexity in our implementation of the MPM for maps with multiple sets of periodic orbits, like in the case of the two periodic NASM, Eq. (4.4), for even-period periodic orbits. Although

$\frac{P}{Q}$	Orbit x	E	R
$\frac{8}{13}$	$9.28474979533394032586 \times 10^{-01}$	1.1092×10^{-04}	-2.0267×10^{-01}
	$9.28282103136275594876 \times 10^{-01}$	1.9774×10^{-47}	-2.0242×10^{-01}
$\frac{21}{34}$	$3.43315315162867085860 \times 10^{-02}$	3.3857×10^{-05}	-1.3650×10^{-01}
	$3.42428358234278121403 \times 10^{-02}$	7.4463×10^{-33}	-1.3778×10^{-01}
$\frac{55}{89}$	$9.845994366358192656317 \times 10^{-01}$	9.8675×10^{-08}	-5.0321×10^{-02}
	$9.845604550754948539836 \times 10^{-01}$	1.7139×10^{-44}	-5.0358×10^{-02}
$\frac{144}{223}$	$6.40268038613412254345 \times 10^{-02}$	1.5581×10^{-07}	-3.5953×10^{-03}
	$6.38468012310526810880 \times 10^{-02}$	2.2965×10^{-45}	-3.6373×10^{-03}
$\frac{377}{610}$	$9.97522710673880868038 \times 10^{-01}$	6.9444×10^{-11}	-3.7328×10^{-06}
	$9.97515492433739096197 \times 10^{-01}$	9.3468×10^{-29}	-3.7721×10^{-06}
$\frac{987}{1597}$	$9.54696825841002350864 \times 10^{-04}$	3.7585×10^{-19}	-5.7485×10^{-14}
	$9.52145748283865826621 \times 10^{-04}$	1.3876×10^{-30}	-5.8138×10^{-14}
$\frac{2584}{4181}$	$1.39055807882423202186 \times 10^{-03}$	1.4745×10^{-28}	-6.7894×10^{-24}
	$1.39055807882415784826 \times 10^{-03}$	9.8595×10^{-29}	-4.5398×10^{-25}
$\frac{6765}{10946}$	$3.44008191828690524568657547 3 \times 10^{-03}$	1.0906×10^{-27}	-1.3708×10^{-23}
	$3.44008191828690524568657508 0 \times 10^{-03}$	9.5496×10^{-29}	-1.2003×10^{-24}

Table 5.5: Angular component x of the point closest to $x = 0$ of a few P/Q hyperbolic periodic orbits found for the two periodic NASM (4.4) for $\kappa_1 = 0.5350$ and $\kappa_2 = 0.2000$, computed by the modified parameterization method (white rows) and then refined by a 2D-Newton method (gray rows).

it is mentioned in the Birkhoff theorem 2.3, that the periodic orbits have "an even number: $2kq$, $k \in \mathbb{N}$" of points, in most of the available examples in the literature, maps display only two sets ($k = 1$) of points. This complexity can be appreciated in Fig. 5.20 for the periodic orbit with rotation number $1/2$. Further study on of these *phantom* curves containing the periodic orbits may help to clarify this point.

The search for higher order periodic orbits than $F_{23} = 46368$ and for parameters values close to critical would help to obtain better bounds for Kadanoff's coefficients.

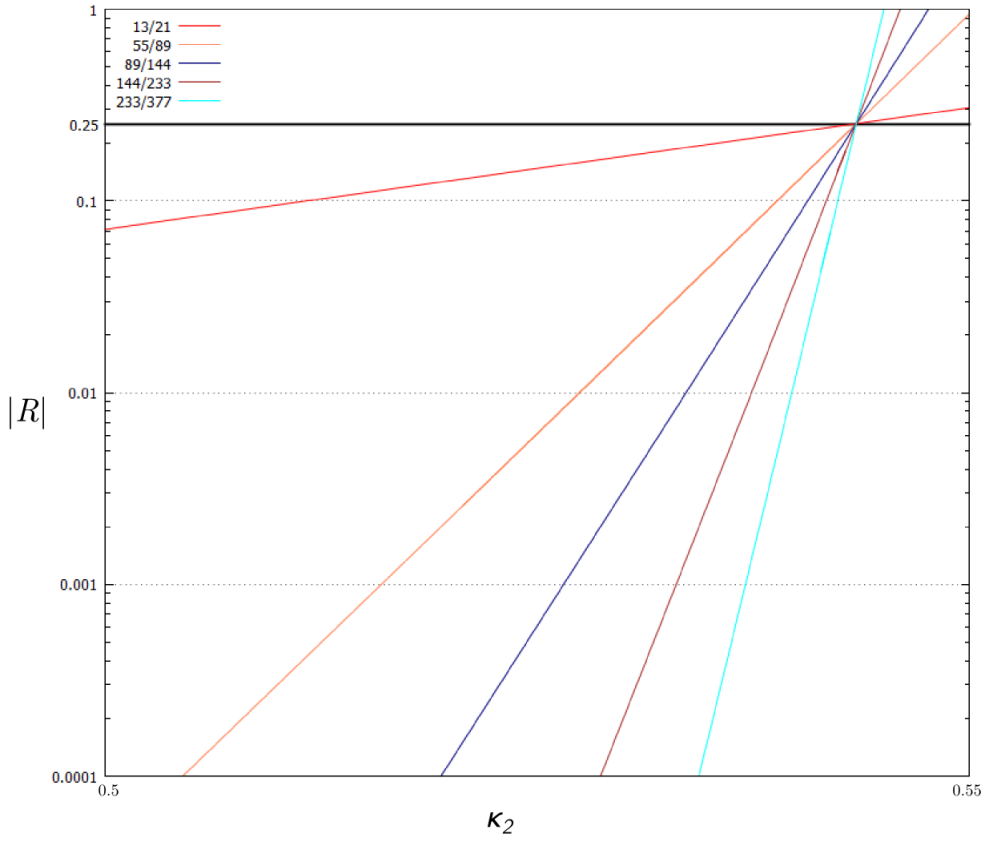

Figure 5.17: Log-Log plot around (0.5432,0.25) of the absolute residue $|R|$ versus parameter κ_2 for fixed $\kappa_1 = 0.2$, for different periodic orbits that approximate invariant circle γ for map (4.4).

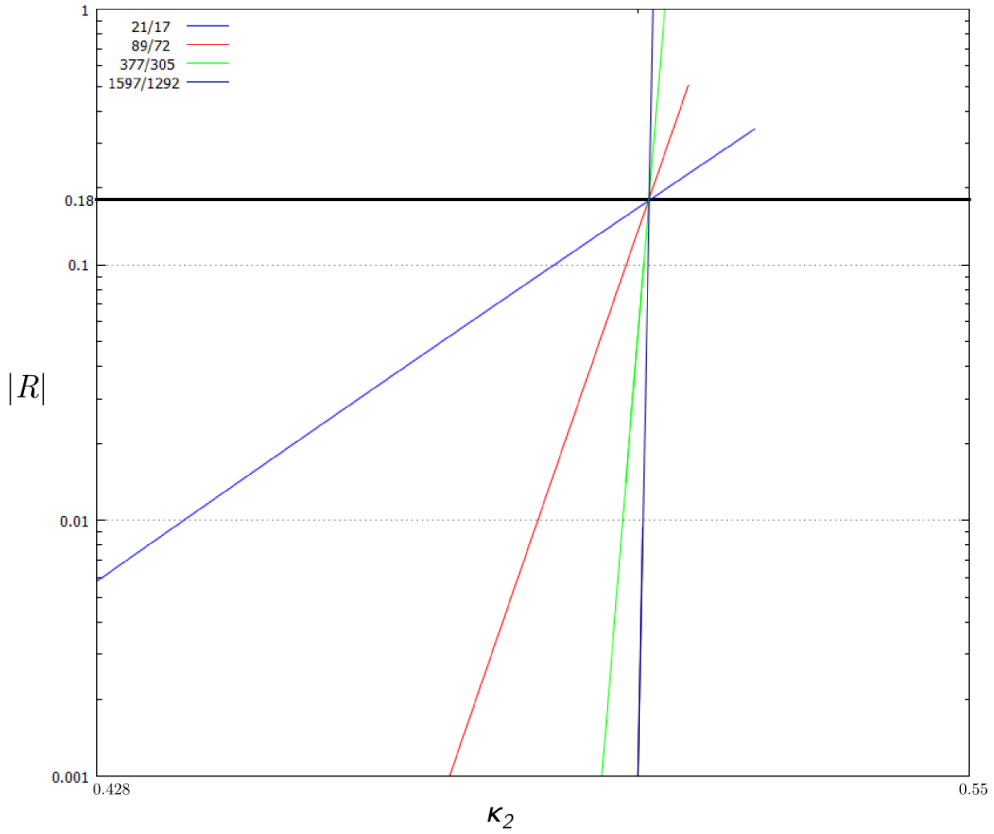

Figure 5.18: Log-Log plot around (0.5016,0.18) of the absolute residue $|R|$ versus parameter κ_2 for fixed $\kappa_1 = 0.2$, for different periodic orbits that approximate invariant circle 2γ for map (4.4).

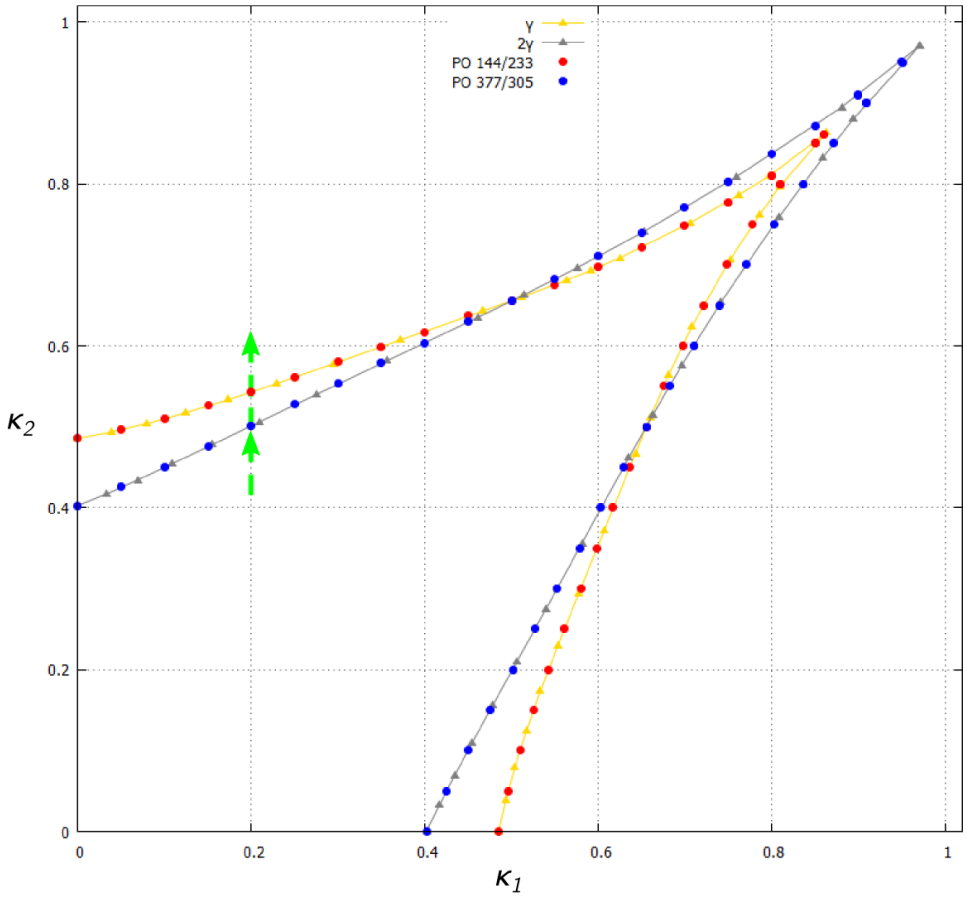

Figure 5.19: Comparison of the critical boundaries for the existence of KAM tori (CB_ω) $\{\gamma, 2\gamma\}$ from Fig. 4.8 and the critical parameter values obtained by computation of periodic orbits for map (4.4). The dashed line represent the continuation trajectory used for the computation of Figs. 5.17 and 5.18.

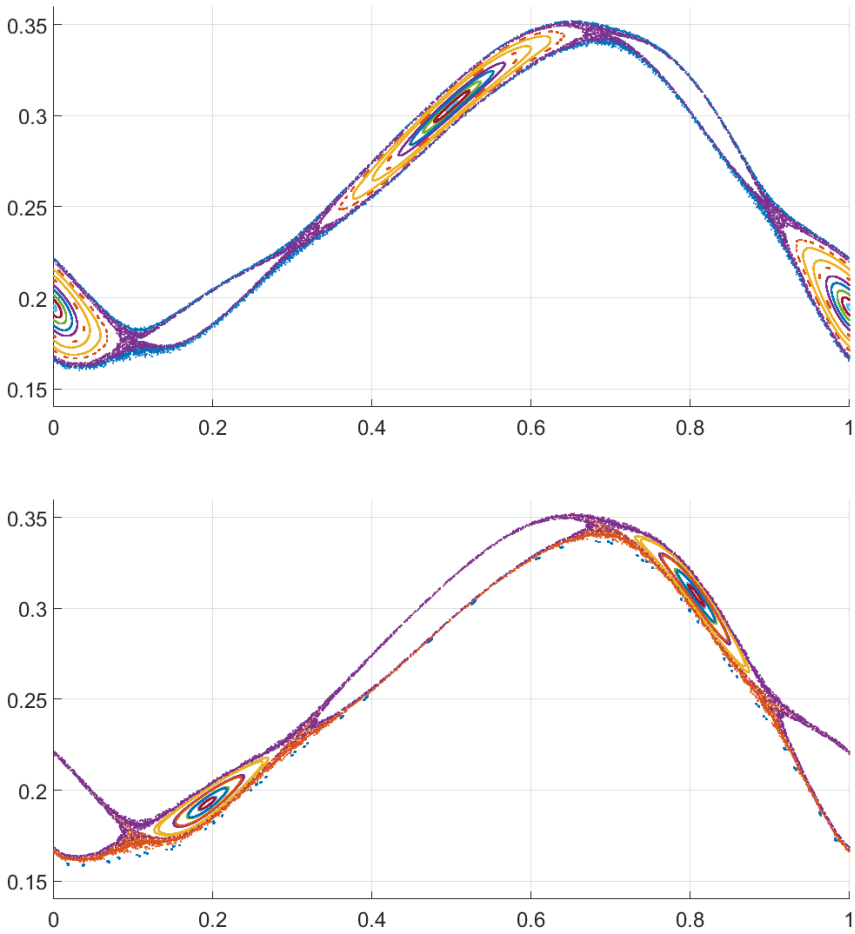

Figure 5.20: Phase space (x, y) of the map (4.4) for $(\kappa_1, \kappa_2) = (0.77, 0.74)$ around the 1/2-resonance. In both frames there are 11 initial conditions iterated 5000 times, taken uniformly over a segment of a vertical line: (up) $\{x_0 = 0\}$ and (down) $\{x_0 = 0.2\}$.

Appendix 1: Tables

Chirikov-Taylor map

$\frac{P}{Q}$	Orbit x	Orbit y	E	R
$\frac{5}{8}$	$1.0425864779590223499 \times 10^{-01}$	$6.4747224210571066960 \times 10^{-01}$	5.3007×10^{-09}	-2.3618×10^{-01}
	$1.0426238126341571054 \times 10^{-01}$	$6.4747456489474714699 \times 10^{-01}$	1.7776×10^{-33}	
$\frac{8}{13}$	$7.2279124021473426907 \times 10^{-02}$	$6.2793957476881539400 \times 10^{-01}$	7.2300×10^{-10}	-2.1397×10^{-01}
	$7.2292421040641022512 \times 10^{-02}$	$6.2794766832716750640 \times 10^{-01}$	3.8240×10^{-45}	
$\frac{13}{21}$	$5.0699225521116481782 \times 10^{-02}$	$6.1988229835423964450 \times 10^{-01}$	5.8869×10^{-09}	-1.9779×10^{-01}
	$1.0426238126341571054 \times 10^{-01}$	$6.4747456489474714699 \times 10^{-01}$	1.4227×10^{-30}	
$\frac{13}{21}$	$3.5022448053712375426 \times 10^{-02}$	$6.1182499955187100242 \times 10^{-01}$	3.2796×10^{-09}	-1.6521×10^{-01}
	$3.5022447826195364453 \times 10^{-02}$	$6.1182499943126210007 \times 10^{-01}$	3.0469×10^{-30}	
$\frac{34}{55}$	$2.4048789575376183242 \times 10^{-02}$	$6.0677333591129369932 \times 10^{-01}$	1.7770×10^{-08}	-1.2748×10^{-01}
	$2.4048789198498598295 \times 10^{-02}$	$6.0677333569657200390 \times 10^{-01}$	1.5432×10^{-29}	
$\frac{55}{89}$	$1.6217182600037420486 \times 10^{-02}$	$6.0293190380476556478 \times 10^{-01}$	1.9150×10^{-09}	-8.2110×10^{-02}
	$1.6217182502214720840 \times 10^{-02}$	$6.0293190375588490861 \times 10^{-01}$	2.8720×10^{-32}	
$\frac{89}{144}$	$1.0731773140643800112 \times 10^{-02}$	$6.0031353992141050667 \times 10^{-01}$	8.3944×10^{-09}	-4.0823×10^{-02}
	$1.0731773004662365072 \times 10^{-02}$	$6.0031353985180357670 \times 10^{-01}$	6.7440×10^{-52}	

Table 5.6: Coordinates of the point closest to $x = 0$ of the first few P/Q hyperbolic periodic orbits found for the Chirikov-Taylor map (4.6) for $\kappa = 0.9600$, computed by the modified parameterization method (white rows) and then refined by a 2D Newton method (gray rows).

$\frac{P}{Q}$	Orbit x	Orbit y	E	R
$\frac{144}{233}$	$6.93448825249725679923 \times 10^{-03}$	$5.98476282938418771477 \times 10^{-01}$	7.9917×10^{-10}	-1.3101×10^{-02}
	$6.93448824569174567128 \times 10^{-03}$	$5.98476282934934402710 \times 10^{-01}$	5.2130×10^{-55}	
$\frac{233}{377}$	$4.39068507839071845976 \times 10^{-03}$	$5.97255345454513903314 \times 10^{-01}$	5.6428×10^{-11}	-8.2110×10^{-02}
	$4.39068507873134101191 \times 10^{-03}$	$5.97255345454679880141 \times 10^{-01}$	1.9267×10^{-32}	
$\frac{377}{610}$	$2.74217144017497626263 \times 10^{-03}$	$5.96461591696472635425 \times 10^{-01}$	9.8185×10^{-12}	-1.0800×10^{-04}
	$2.74217144026659842688 \times 10^{-03}$	$5.96461591696517509924 \times 10^{-01}$	9.5578×10^{-30}	
$\frac{610}{987}$	$1.70222914399736324091 \times 10^{-03}$	$5.95962281948688779372 \times 10^{-01}$	5.1215×10^{-23}	-8.9148×10^{-07}
	$1.70222914399736324090 \times 10^{-03}$	$5.95962281948688779372 \times 10^{-01}$	9.8163×10^{-45}	
$\frac{987}{1597}$	$1.05402094177906953965 5127 \times 10^{-03}$	$5.95650761237369267913 7456 \times 10^{-01}$	1.6107×10^{-23}	-8.2110×10^{-02}
	$1.05402094177906953965 5189 \times 10^{-03}$	$5.95650761237369267913 7456 \times 10^{-01}$	6.5275×10^{-46}	

Table 5.7: Continuation of Table 5.6: coordinates of the point closest to $x = 0$ of the first few P/Q hyperbolic periodic orbits found for the Chirikov-Taylor map (4.6) for $\kappa = 0.9600$, computed by the modified parameterization method (white rows) and then refined by a 2D Newton method (gray rows).

Rational harmonic map

$\frac{P}{Q}$	Orbit x	Orbit y	E	R
$\frac{8}{13}$	$9.84400324333751592206 \times 10^{-01}$	$7.10244575221834431331 \times 10^{-01}$	1.5314×10^{-04}	-2.1690×10^{-01}
	$9.84194430418146115882 \times 10^{-01}$	$7.10392043464016943770 \times 10^{-01}$	4.8935×10^{-39}	-2.1777×10^{-01}
$\frac{21}{34}$	$9.97753743054888484767 \times 10^{-01}$	$7.02996822339558759884 \times 10^{-01}$	1.3827×10^{-05}	-1.8059×10^{-01}
	$9.97722363363172234098 \times 10^{-01}$	$7.03019856000149092831 \times 10^{-01}$	1.6284×10^{-47}	-1.8095×10^{-01}
$\frac{55}{89}$	$4.35066410514029663774 \times 10^{-04}$	$6.98385176038193858882 \times 10^{-01}$	2.8190×10^{-03}	-2.8817×10^{-01}
	$4.42076348408883988105 \times 10^{-04}$	$6.98347918557877904235 \times 10^{-01}$	1.8242×10^{-37}	-1.0589×10^{-01}
$\frac{144}{223}$	$4.09885888135278521212 \times 10^{-04}$	$7.01387396939671391725 \times 10^{-01}$	8.3211×10^{-11}	-1.3204×10^{-01}
	$4.54519288406945185848 \times 10^{-04}$	$7.01356932134908000753 \times 10^{-01}$	8.2324×10^{-29}	-2.5599×10^{-02}
$\frac{377}{610}$	$4.54770852734730605323 \times 10^{-04}$	$7.01363476798029161659 \times 10^{-01}$	8.6265×10^{-05}	-2.5479×10^{-02}
	$5.10890552501945729879 \times 10^{-04}$	$7.01321982171575674078 \times 10^{-01}$	1.2373×10^{-29}	-6.2363×10^{-04}
$\frac{987}{1597}$	$2.18102889348964055253 \times 10^{-04}$	$7.01549235896928450828 \times 10^{-01}$	9.4507×10^{-11}	-9.2787×10^{-08}
	$2.88969724223810721485 \times 10^{-04}$	$7.01496774128756488963 \times 10^{-04}$	9.5395×10^{-31}	-4.0099×10^{-08}
$\frac{2584}{4181}$	$5.70931653171076079438 \times 10^{-03}$	$6.97412780846434903470 \times 10^{-01}$	1.1379×10^{-24}	-3.2521×10^{-19}
	$5.70811191353601822914 \times 10^{-03}$	$6.97413699282616497981 \times 10^{-01}$	1.1872×10^{-31}	-3.2944×10^{-19}
$\frac{6765}{10946}$	$1.23693970334899424212053377 7 \times 10^{-02}$	$6.92176093384234520527742 9672 \times 10^{-01}$	3.1733×10^{-28}	-8.6237×10^{-24}
	$1.23693970334899424212053376 9 \times 10^{-02}$	$6.92176093384234520527742 9672 \times 10^{-01}$	9.5204×10^{-29}	-2.0985×10^{-24}

Table 5.8: Coordinates of the point closest to $x = 0$ of a few P/Q hyperbolic periodic orbits found for the *rational harmonic* map (5.23) with $(\kappa, p_a, p_m) = (1.7150, 3.0, 0.4)$, computed by the modified parameterization method (white rows) and then refined by a 2-D Newton method (gray rows) until $E < 10^{-28}$.

Two periodic NASM

$\frac{P}{Q}$	Orbit x	Orbit y	E	R
$\frac{8}{13}$	$9.28474979533394032586 \times 10^{-01}$	$2.93340815766706400724 \times 10^{-01}$	1.1092×10^{-04}	-2.0267×10^{-01}
	$9.28282103136275594876 \times 10^{-01}$	$2.93290138858783618713 \times 10^{-01}$	1.9774×10^{-47}	-2.0242×10^{-01}
$\frac{21}{34}$	$3.43315315162867085860 \times 10^{-02}$	$3.22071935161442124497 \times 10^{-01}$	3.3857×10^{-05}	-1.3650×10^{-01}
	$3.42428358234278121403 \times 10^{-02}$	$3.22049573810215720065 \times 10^{-01}$	7.4463×10^{-33}	-1.3778×10^{-01}
$\frac{55}{89}$	$9.845994366358192656317 \times 10^{-01}$	$3.090337502419617722444 \times 10^{-01}$	9.8675×10^{-08}	-5.0321×10^{-02}
	$9.845604550754948539836 \times 10^{-01}$	$3.090232200443436087788 \times 10^{-01}$	1.7139×10^{-44}	-5.0358×10^{-02}
$\frac{144}{223}$	$6.40268038613412254345 \times 10^{-02}$	$3.14891818598682725495 \times 10^{-01}$	1.5581×10^{-07}	-3.5953×10^{-03}
	$6.38468012310526810880 \times 10^{-02}$	$3.14887036187162437704 \times 10^{-01}$	2.2965×10^{-45}	-3.6373×10^{-03}
$\frac{377}{610}$	$9.97522710673880868038 \times 10^{-01}$	$3.12522279722287901968 \times 10^{-01}$	6.9444×10^{-11}	-3.7328×10^{-06}
	$9.97515492433739096197 \times 10^{-01}$	$3.12520344653005398089 \times 10^{-01}$	9.3468×10^{-29}	-3.7721×10^{-06}
$\frac{987}{1597}$	$9.54696825841002350864 \times 10^{-04}$	$3.12775071232490569362 \times 10^{-01}$	3.7585×10^{-19}	-5.7485×10^{-14}
	$9.52145748283865826621 \times 10^{-04}$	$3.12773919100896876768 \times 10^{-01}$	1.3876×10^{-30}	-5.8138×10^{-14}
$\frac{2584}{4181}$	$1.39055807882423202186 \times 10^{-03}$	$3.13441098550719471904 \times 10^{-01}$	1.4745×10^{-28}	-6.7894×10^{-24}
	$1.39055807882415784826 \times 10^{-03}$	$3.13440416749303693270 \times 10^{-01}$	9.8595×10^{-29}	-4.5398×10^{-25}
$\frac{6765}{10946}$	$3.44008191828690524568657547 3 \times 10^{-03}$	$3.13557583474995027752449176 2 \times 10^{-01}$	1.0906×10^{-27}	-1.3708×10^{-23}
	$3.44008191828690524568657508 0 \times 10^{-03}$	$3.13557583474995007937184727 7 \times 10^{-01}$	9.5496×10^{-29}	-1.2003×10^{-24}

Table 5.9: Coordinates of the point closest to $x = 0$ of a few P/Q hyperbolic periodic orbits found for the two periodic NASM (4.4) for $\kappa_1 = 0.5350$ and $\kappa_2 = 0.2000$, computed by the modified parameterization method (white rows) and then refined by a 2D-Newton method (gray rows).

Appendix 2: Newton-Kantorovich theorem

The Newton-Kantorovich theorem is a classical result in nonlinear analysis giving information about the convergence behaviour of the Newton iteration. The original version of the theorem can found in Refs. [95] and [76], however the version of interest here is a more general one used by Mireles-James and Lessard in various papers[88, 89, 90, 91] for computer assisted proofs, in the the tradition of Ref. [87].

Theorem 5.1. *(a-posteriori Newton-Kantorovich theorem, radii polynomial approach* [91, 89]*)*
Let $(X, ||\cdot||_X)$ and $(Y, ||\cdot||_Y)$ be Banach spaces and $F : X \to Y$ a Fréchet differentiable mapping. Let $B(X, Y)$ be the space of bounded linear operators from X to Y with the operator norm $||\cdot||_{B(X)}$. Consider $\bar{x} \in X$, $A^\dagger \in B(X, Y)$, and $A \in B(Y, X)$, with A one-to-one. Let Y_0, Z_0, Z_1 be positive constants, and $Z_2 : [0, \infty) \to [0, \infty)$ be a positive function, all satisfying the following conditions:

- $||AF(\bar{x})||_X \leq Y_0$, *(small defect/a-posteriori error)*
- $||Id - AA^\dagger||_{B(X)} \leq Z_0$, *(approximate inverse)*
- $||A(A^\dagger - DF(\bar{x}))||_{B(X)} \leq Z_1$, *(approximate derivative)*
- $\sup_{x \in \overline{B_r(\bar{x})}} ||A(DF(\bar{x}) - DF(x))||_{B(X)} \leq Z_2(r)r$, *(local control)*

Define the function $p(r) = Z_2(r)r^2 - (1 - Z_0 - Z_1)r + Y_0$. If there is an $r > 0$, so that $p(r) < 0$, then there exist a unique $\tilde{x} \in B_r(\bar{x})$ so that

$$F(\tilde{x}) = 0\,.$$

Applied to modified parameterization method for the search of periodic orbit of period q on a twist map T, then $X = Y = \mathbb{S} \times \mathbb{R}$ and,

$$F(x) = T^q(x) - x\,. \tag{5.28}$$

Using the exact derivative $A = DF$ and inverse $A^\dagger = (DF)^{-1}$, we have the expressions,

$$A = DT^q - Id\,, \qquad A^\dagger = \frac{1}{4R}\Big[(DT^q)^{-1} - Id\Big]\,,$$

where R is the (Greene's) residue (2.29) and Id is the identity. Also the coefficients Z_0 and Z_1 in the theorem are identically zero. So the polynomial $p(r)$ now reduce to,

$$p(r) = Z_2(r)r^2 - r + Y_0\,,$$

where the remaining coefficients now are,

$$\frac{1}{|4R|}\Big|\Big|\Big((DT^q)^{-1} - Id\Big)F(\bar{x})\Big|\Big|_X \leq Y_0\,, \tag{5.29}$$

$$\sup_{x\in\overline{B_r(\bar{x})}} \frac{1}{|4R|}\Big|\Big|\Big((DT^q)^{-1} - Id\Big)\Big(DF(\bar{x}) - DF(x)\Big)\Big|\Big|_{B(X)} \leq Z_2(r)r\,, \tag{5.30}$$

where now $||\cdot||_X$ is the distance in the cylinder. Considering that we have an appropriate 2×2-matrix norm definition for $||\cdot||_{B(X)}$, it is clearly more likely that the polynomial $p(r)$ can be negative for an interval $(0,\tilde{r})$ if the modulus of the residue $|R|$ is as big as possible. Restricting the search of periodic orbits to the parametric curve $K_{P/Q}$ and using the definition of $\tilde{R}$ (5.12) in terms of the parameterization, the more likely values of θ for which there may be periodic orbit points is around the critical points of $\tilde{R}$.

Chapter 6

Critical behavior of periodic orbits

The behavior of invariant circles in twist maps for critical values of the parameters has been a topic of interest for many years. Many names like Poincaré [96], Denjoy[97], Arnold[98], Herman[99], Mather[100], MacKay[101] among others worked on the subject and its applications [102]. Since the work from Greene [18] and subsequent works on renormalization theory like the ones from MacKay [67, 69, 85], it is clear that universal properties arise on invariant circles of twist maps around critical values of the parameters, that is, before the invariant circle cease to exist and becomes a Cantor set (cantorus) for any small variation of the parameters values. One of the first numerical observations of these universal properties are the universal critical *exponents* or *coefficients* (depending on the definition) was found by Kadanoff and Shenker for the Chirikov-Taylor map in Refs. [64, 68]. These *universal critical coeffients* or *universal scaling factors* characterize point-wise the self-similar behavior of critical invariant circles from twist maps around certain points, usually points lying in symmetry lines. The scaling factors can be appreciated and estimated only from high order periodic orbits. The goal of this chapter is to describe the procedure to find numerical bounds to these *universal critical exponents* mentioned in Sec. 2.6 to non-reversible maps like the two periodic NASM (4.4) studied in Chp. 4, maps for which there is no known decomposition into two involutions. These coefficients can be estimated using periodic orbits, so the use of the *compound method* introduced in previous chapter is of primordial importance, although some considerations must be done to choose critical values for the parameters and to find

suitable points to compute them.

6.1 Kadanoff's geometrical coefficients

In Refs. [64, 68], Kadanoff and Shenker computed a pair of geometrical coefficients (α_0, β_0) for the standard map $\mathcal{S}_\kappa$, Eq. (4.6), that characterizes the self-similar behavior of the golden invariant circle around a symmetry line and for a parameter value close to the critical breaking, $\kappa_G = 0.971635406...$, a behavior predicted by the renormalization theory. The scaling law found is,

$$\mathcal{S}_{\kappa_G}^{F_n} \begin{pmatrix} x \\ y \end{pmatrix} = \beta_0^{-n}\, \mathcal{S}^* \begin{pmatrix} \alpha_0^n\, x \\ \beta_0^n\, y \end{pmatrix}, \tag{6.1}$$

where F_n is the n-element in the Fibonacci sequence[1] and $\mathcal{S}^*$ describe the behavior near the dominant symmetry line at $x = 0$. In the context of the parameterization method, where $\mathcal{S}(x, y) = \mathcal{S}(K(\theta)) = K(\theta + \omega)$, Eq. (6.1) is equivalent to,

$$\begin{pmatrix} \alpha_0^n K_x(t + \tau_n) \\ \beta_0^n (K_y(t + \tau_n) - K_y(t)) \end{pmatrix} = \begin{pmatrix} \alpha_0^{n+1} K_x(t + \tau_{n+1}) \\ \beta_0^{n+1} (K_y(t + \tau_{n+1}) - K_y(t)) \end{pmatrix}, \tag{6.2}$$

where $K_x(t) = 0$, and $\tau_n \equiv q_n\omega - p_n$ is a geometrically decreasing sequence $(p_n/q_n \to \omega)$. In the case of the Chirikov-Taylor map: $\omega = \gamma = \frac{\sqrt{5}-1}{2}$ and $p_n/q_n = F_{n-1}/F_n$.

Similar coefficients (α_1, β_1) were found for the other dominant symmetry line at $x = 0.5$, although the exact coefficients (α_3, β_3) are found by a "step-3" scaling (see Ref. [29]),

$$\begin{pmatrix} \alpha_3^n (K_x(\tilde{t} + \tau_n) - 0.5) \\ \beta_3^n (K_y(\tilde{t} + \tau_n) - K_y(\tilde{t})) \end{pmatrix} = \begin{pmatrix} \alpha_3^{n+1} (K_x(\tilde{t} + \tau_{n+3}) - 0.5) \\ \beta_3^{n+1} (K_y(\tilde{t} + \tau_{n+3}) - K_y(\tilde{t})) \end{pmatrix}, \tag{6.3}$$

where now $K_x(\tilde{t}) = 0.5$. The values of Kadanoff's coefficients computed for the Chirikov-Taylor map reported in the literature[29] are presented in table 6.1.

The self-similar behavior of the continuous torus and its neighboring periodic orbits is illustrated on figure 6.1. Actual figures of the self-similar behavior and scaling of periodic orbits for a more complicate case ("step-6" scaling) can found in Ref. [92]. It should be noted that there are different

[1] $\{F_n\}_{n\in\mathbb{N}}$ such that $F_{n+1} = F_n + F_{n-1}$, $F_0 = F_1 = 1$.

Map	x_{rar}	α_0	β_0
	x_{den}	α_3	β_3
Chirikov- Taylor	0.0000	-1.414836	-3.0668882
	0.5000	-4.84581	-16.8597

Table 6.1: Kadanoff's geometrical coefficients reported in the literature[29] for the Chirikov-Taylor map.

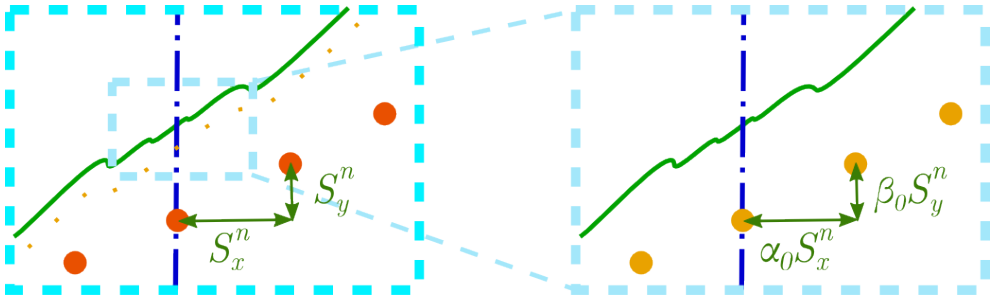

Figure 6.1: Illustration of the geometrical coefficients around a symmetry line for two successive approximants.

definitions in the literature for these geometric coefficients which may lead to confusions. For example the author in Ref. [24] define them as exponents: $\alpha_0 = \gamma^{\mathfrak{x}_0}$ and $\beta_0 = \gamma^{\mathfrak{y}_0}$.

It is important to remind that in the integrable case, for $p_n/q_n \to \omega$, the distance between a point $z_0 = (x_0, y_0)$ of the invariant circle C_ω and its q_n-iterate decreases monotonically,

$$||z_{q_n} - z_0|| = |x_{q_n} - x_0| = \tau_n \,, \tag{6.4}$$

and this continues to happen for big enough n in the perturbed non-critical regime while C_ω is an analytic curve, see Ref. [24]. And also in the non-critical regime, the separation between consecutive points of high order periodic orbits is also smooth, with the scaling rules[2],

$$|x_{i+1} - x_i| \sim (q_n)^{-1} \,, \qquad |y_{i+1} - y_i| \sim (q_n)^{-2} \,. \tag{6.5}$$

Just in the critical case, $\kappa = \kappa_G$ for the Chirikov-Taylor map, these regular separation breaks into the self-similar scaling described in this section.

[2]These scaling rules imply that the estimation of α and β in the non-critical regime for the golden mean invariant circle give: $\alpha \sim \gamma^{-1}$ and $\beta \sim \gamma^{-2}$.

Although Kadanoff's coefficients are a quantitative local analysis of the self-similar behavior on two points of a critical torus, they can be used to give bounds over global properties such as the regularity. In Ref. [29] a pointwise Holder norm was used to characterize the regularity of the limiting curve (invariant torus) and found interesting relations between their results and the numerical bounds given by Kadanoff's coefficients. It should be mentioned that the methods in Ref. [29] also required to compute periodic orbits of high order period ($Q \sim 10^6$) to give accurate estimations.

On the other hand the discovery of these coefficients inspired important analytic results as the earlier works on renormalization in area-preserving maps [67, 69] from MacKay. Another consequence of the scaling properties of periodic orbits is the proof the existence of hyperbolicity beyond the stable manifold of the critical point of the renormalization group [103].

In the particular frame of the present work, the main motivation to look for a new method to find periodic orbits was to determine the coefficients (α, β) for different rotation numbers for the map (4.4) to help to characterize better the topological barriers in the non-autonomous transport.

6.2 Strategies to compute the coefficients

There exist several ways to compute the values of the (α_0, β_0) coefficients, with the use of the parameterization $K_\omega(\theta)$ as the most direct one. However the big drawback is that the values of $K_x(0) = 0$ and $K_x(\tilde{\theta}) = 0.5$ will be different for non-reversible maps. The use of periodic orbits to compute the coefficients may help to solvent this inconvenience. But before addressing *where*, lets review *how* to compute them. Assuming there are symmetry lines to discriminate two convenient points, two strategies to compute the coefficients are the following:

- *Strategy #1: compute many periodic orbits*
  Find and order, in such manner that the component x_j is monotonous, the periodic orbits that passes through a symmetry line,

$$\{(x_0, y_0), (x_1, y_1), ..., (x_{q_n-1}, y_{q_n-1})\}_{\omega_n} \tag{6.6}$$

  corresponding to the rotation numbers $\{\omega_n = p_n/q_n\}_{n\in\mathbb{N}}$ that converge to the rotation number ω of the critical invariant circle for a value of the parameter close to the critical. Let (x_m, y_m) be the point in the

orbit that lies in the symmetry line and (x_*, y_*) the closest point in the orbit to it. Then the estimation of the coefficients consists in comparing the ratios of $x_* - x_m$ of successive (or "step-n") rotation numbers. For example,

$$\frac{[x_* - x_m]_{\omega_n}}{[x_* - x_m]_{\omega_{n+1}}} \approx \frac{[x_* - x_m]_{\omega_{n+1}}}{[x_* - x_m]_{\omega_{n+2}}} \approx \cdots \to \alpha_0 \,, \tag{6.7}$$

$$\frac{[y_* - y_m]_{\omega_n}}{[y_* - y_m]_{\omega_{n+1}}} \approx \frac{[y_* - y_m]_{\omega_{n+1}}}{[y_* - y_m]_{\omega_{n+2}}} \approx \cdots \to \beta_0 \,. \tag{6.8}$$

- *Strategy #2: compute a* **large** *periodic orbit*
  Use a large period periodic orbit to approximate the dynamic on the invariant circle. If the periodic orbits with rotation numbers $\{\omega_n = p_n/q_n\}_{n\in\mathbb{N}}$ approximate the invariant circle with rotation number ω, then, around a principal symmetry line $x = x_s$, the q_m-iteration of the map over the point (x_s, y_0) from the p_n/q_n-periodic orbit $(n > m)$ should approximate $T^{q_m}(x_s, y_*)$ if (x_s, y_*) is a point of the invariant ω. The algorithm to do this for the golden mean invariant circle consist in reorder a F_{n-1}/F_n-periodic orbit of large n so (x_0, y_0) is the point that pass through the symmetry line and the following points are an iterate of the previous, $(x_{n+1}, y_{n+1}) = F(x_n, y_n)$. This is,

$$\left\{ (x_0, y_0), \ldots, \underbrace{(x_{F_4}, y_{F_4})}_{5th \text{ iterate}}, \ldots, \underbrace{(x_{F_m}, y_{F_m})}_{F_m th \text{ iterate}}, \ldots, (x_{F_{n-1}}, y_{F_{n-1}}) \right\}_{\omega_n} . \tag{6.9}$$

  then the coefficients are computed by comparing the ratios of $x_{F_m} - x_0$ $(y_{F_m} - y_0)$ of successive (or "step-n") F_m's. For example,

$$\frac{x_5 - x_0}{x_{F_{21}} - x_0} \approx \frac{x_{F_m} - x_0}{x_{F_{m+3}} - x_0} \approx \cdots \to \alpha_3 \,, \tag{6.10}$$

$$\frac{y_5 - y_0}{y_{F_{21}} - y_0} \approx \frac{y_{F_m} - y_0}{y_{F_{m+3}} - y_0} \approx \cdots \to \beta_3 \,. \tag{6.11}$$

  Following this method may produce good estimates on the coefficients only for intermediate F_m's, as $F_m \to F_n$ the approximation of the dynamic on the invariant circle by the F_n-periodic orbit will diminish since the periodic orbit has to close: $x_{F_n} - x_0 = 0 \neq F^{F_n}(x_0) - x_0$, this is illustrated in Fig. 6.2.

- *Strategy #3: compute an approximate conjugation K for the critical invariant circle*
  Compute Kadanoff's α and β using directly the parameterization $K : \mathbb{S} \to \mathbb{S} \times \mathbb{R}$ using the Eqs. (6.1) and (6.2),

$$\frac{x_{F_m} - x_0}{x_{F_{m+1}} - x_0} = \frac{K_x(\theta_0 + F_m\omega) - K_x(\theta_0)}{K_x(\theta_0 + F_{m+1}\omega) - K_x(\theta_0)} \longrightarrow \alpha_0 \,, \tag{6.12}$$

$$\frac{y_{F_m} - y_0}{y_{F_{m+1}} - y_0} = \frac{K_y(\theta_0 + F_m\omega) - K_y(\theta_0)}{K_y(\theta_0 + F_{m+1}\omega) - K_y(\theta_0)} \longrightarrow \beta_0 \,, \tag{6.13}$$

  where $K_x(\theta_0)$ is in the symmetry line.

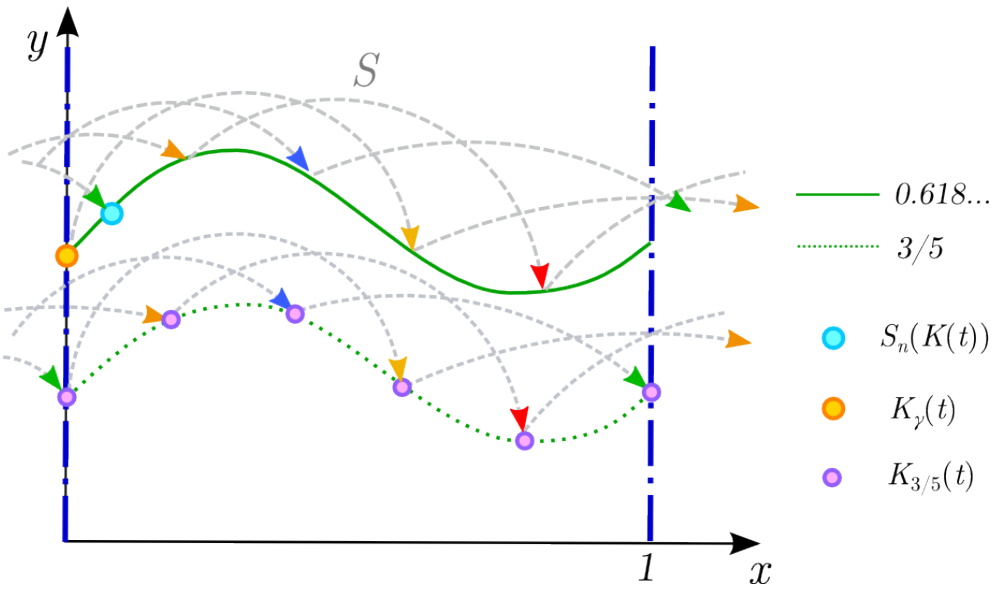

Figure 6.2: Illustration of the dynamic of q_n-iteration of a map S ($S_n \equiv S^{q_n}$) for the 3/5-periodic orbit and the golden mean torus.

6.3 Implementation on non-reversible maps

Kadanoff's geometrical coefficients can be computed from the periodic orbits obtained from the compound method for critical values of the parameters for the different maps. There are however two considerations to take first to be

able to compute them for non-reversible maps: criticality of the parameters values and symmetry lines substitutes.

6.3.1 Critical parameters

Greene's method (Sec. 2.6) conjecture implies that the parameters $(\kappa_1^*, \kappa_2^*, ...)$ are critical when the series of stable (elliptic) periodic orbits of rotation numbers ω_n that approximate an invariant circle of rotation number ω cease to exist for minor variation of the values. Directly prove that all the elliptic periodic orbits change their stability is an impossible task, instead what it is used is the observation made by Greene[18] that residue of all the computable periodic orbits as function of the perturbation parameter is monotonous and follow an scaling rule around a critical value of the perturbation parameter, so the behavior of high period periodic orbits can be determined. In the case of the the Chirikov-Taylor map, it is observed that for $\kappa_G = 0.971635406...$ the residue of all elliptic (hyperbolic) periodic orbits with rotation numbers F_{n-1}/F_n cross around $R \sim 0.2505$ ($R \sim -0.2505$) following an scaling rule of the form,

$$R \sim |\kappa - \kappa_G|^{F_n} . \tag{6.14}$$

This is one of the fundamental contributions made by Greene to base the existence of a renormalization process that determines the dynamic in the critical point. Using results from the renormalization theory, these bounds of the residue should be universal for all two dimensional twist maps, varying only as function of the rotation number of the invariant circle ω. Then, for periodic orbits with rotation numbers F_{n-1}/F_n, it should be reasonable to say that the parameter values of a given twist map are close to critical if the residue of the elliptic (hyperbolic) orbit is close to 0.25 (-0.25). And this critical residue value is expected to vary for any rotation number ω different from the golden mean γ; in principle it could be not a fixed value but a periodic set of values as it is the case in the standard non-twist map [92].

6.3.2 Symmetry lines substitutes

The election by Kadanoff and Shenker to use the dominant symmetry lines of the Chirikov-Taylor map $\{x = 0, 0.5\}$ as the reference point to compute of the scalings α and β was for practical reasons. Their computation was based on the use of periodic orbits and, as mentioned before, it is easier

to find them on reversible map and also there is always a convenient point of every periodic orbit in the symmetry line from which make comparisons. In later works like Ref. [67] it was established and then used [104, 29] that the universal scalings α and β of the critical invariant circle $\mathcal{C}_\gamma$ exist in neighborhoods of certain points of circle. The numerical evidence shows that these points are in the neighborhood with the most and least density of points in the x-axis, see Fig. 6.3. This behavior of the density of points is consistent with an anti-integrable theory argument used in Ref. [94] that involves the Frenkel-Kontorova potential (the integral of the perturbation function V' from (2.24)). However the potential argument can not be applied to all the maps considered since it is not possible to establish V for the two-period NASM even though it presents the same behavior, see Fig. 6.5.

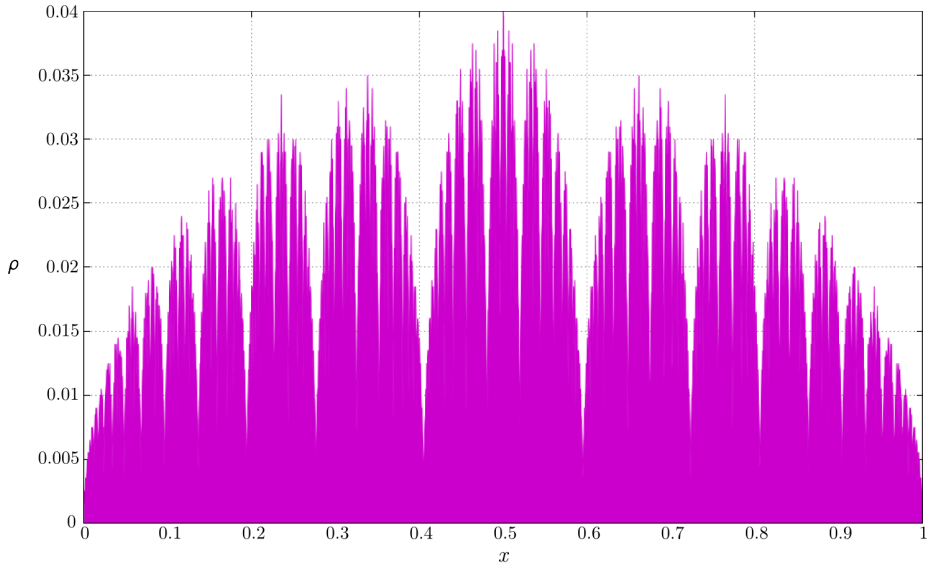

Figure 6.3: Density of points a long the x coordinate for cell of size 0.005 of the elliptic periodic orbit with rotation number 46368/75025 of the Chirikov-Taylor map (4.6) for the parameter values $\kappa = 0.97163$.

In principle, due the self-similarity of the critical invariant circle, the computation of the coefficients can be done with points of other regions of the circle but the values will vary since they are local estimates of the self-similarity.

For the particular election of sign for the Chirikov-Taylor map in (4.6), the

value around which the iterates of map $\mathcal{S}_{\kappa_{\mathcal{G}}}$ are the most rarefied is $x_{rar} = 0$, mean while the most dense is $x_{den} = 0.5$. The, invoking the renormalization theory, the best points of the periodic orbits over which the computation of Kadanoff's coefficient **should** recover the reported values of the universal scalings of the standard map are the points with the least (x_{rar}) and most (x_{den}) density of points in their neighborhood. Typical histograms of the density of points in a high order periodic orbit close to critical parameter values can be appreciated in Fig. 6.4 and 6.5, note that the fractal structure is present.

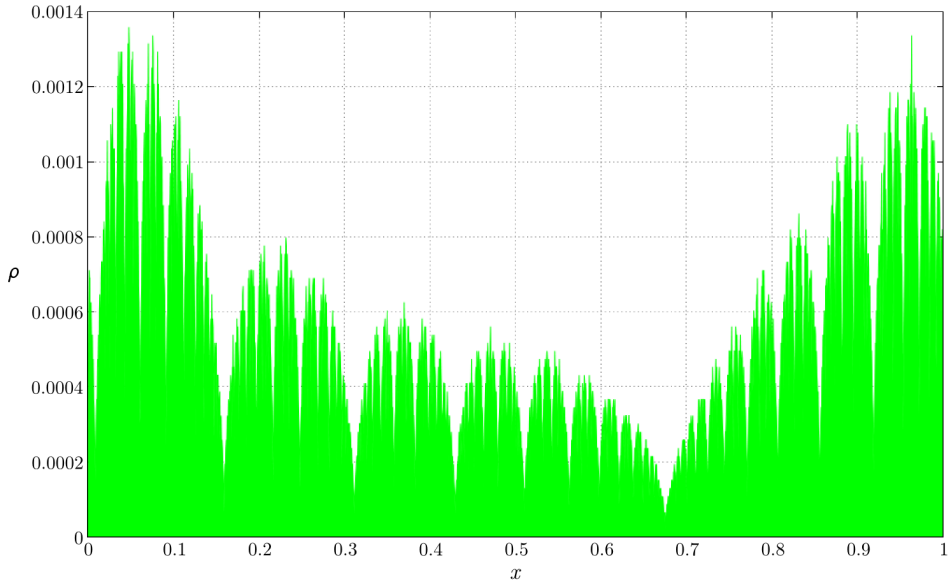

Figure 6.4: Density of points a long the x coordinate for cell of size 0.001 of the elliptic periodic orbit with rotation number 28657/46368, of the rational harmonic map (5.23)-(5.25) for the parameter values $(\kappa, p_a, p_m) = (1.73353335146, 3.0, 0.4)$.

It is worth mentioning that the similarities between Figs. 6.3 and 6.5 suggest the persistence of the dominant symmetry lines from the Chirikov-Tayor map (4.6) on the two-period NASM (4.4), even if at the present moment we are unable to find a decomposition into involutions for the later map.

Additionally preliminary numerical evidence found by the compound method shows that it may be possible to skip the statistical analysis of the points in a periodic orbit by plotting the inverse of the derivative of K_x (the radial

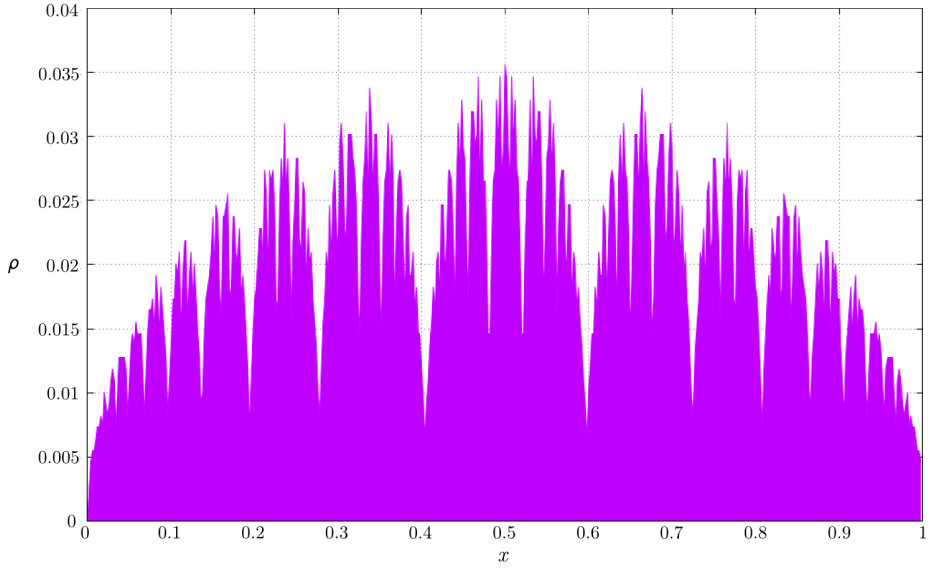

Figure 6.5: Density of points a long the x coordinate for cell of size 0.0005 of **an** elliptic periodic orbit with rotation number 6765/10946, of the two periodic NASM (4.4) for the parameter values $(\kappa_1, \kappa_2) = (0.542853638894466, 0.2)$.

component of the parameterization K), see Fig. 6.6.

6.4 Renormalization theory results on non-reversible maps

The renormalization theory applies to all twist maps around any critical invariant circle and makes no distinction if the map is reversible or not. Yet, there are no examples in the literature that verifies this. The original parameterization method described in Sec. 2.8 can be used (strategy #3, Sec.6.2) to compute properties of the critical invariant circle such as the Kadanoff's coefficients that can verify results from the renormalization theory, although considerations like the ones in the past section are required.

At the present moment, the compound method can compute reliably periodic orbits of periods equal or lower than 46368 for critical values of the parameters for the maps considered. This upper bound on the period causes

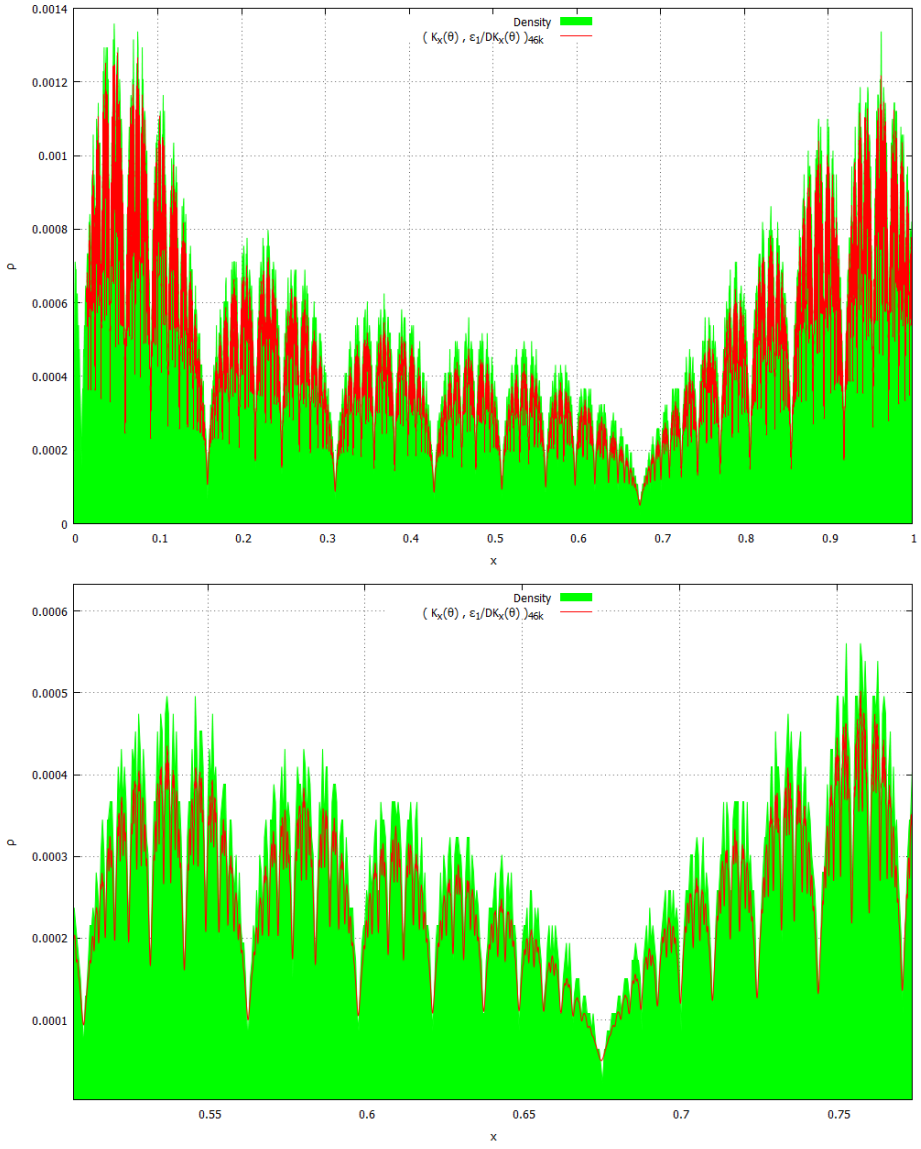

Figure 6.6: Comparison between the density of points from Fig. 6.4 and the inverse of derivative of the x-component of the parameterization DK_x for the elliptic periodic orbit with rotation number 28657/46368 of the rational harmonic map (5.23)-(5.25) for the parameter values $(\kappa, p_a, p_m) = (1.73353335146, 3.0, 0.4)$.

that the computation of Kadanoff's coefficients via the strategy #2 to not be as accurate as desirable due a short amount of data to do the statistic.

6.4.1 Results

The process to of estimating the values of α_0 and α_3 for the 28657/46368-periodic orbit of rational harmonic map (5.23)-(5.25) for the parameter values $(\kappa, p_a, p_m) = (1.73353335146, 3.0, 0.4)$ following the strategy #2 can be appreciated in Fig. 6.7. The figure shows the quotients obtained for each one of the F_m's computable for this orbit ($F_m < F_{23} = 46368$) over x_{rar} and x_{den}, respectively. The variables in $\hat{\alpha}(1,m)$ and $\hat{\alpha}(3,m)$ in the figure correspond to the quotients definitions[3],

$$\hat{\alpha}_(n,m) \equiv \frac{x_{F_m} - x_0}{x_{F_{m+n}} - x_0}\,, \qquad \hat{\beta}_(n,m) \equiv \frac{y_{F_m} - y_0}{y_{F_{m+n}} - y_0}\,. \tag{6.15}$$

The strategy #2 works optimally when it is computed over the actual quasi-periodic invariant circle. If a p/q-periodic orbit is used instead, the convergence of $\hat{\alpha}_(n,m)$ and $\hat{\beta}_(n,m)$ will happen as long the m is not close to the period q of the orbit, at that point the dynamic of the periodic orbit is a bad approximation of the quasi-periodic curve. Nevertheless it can be appreciated in Fig. 6.7 this phenomenon of *partial convergence* when m is less than 6765. To improve these bounds, higher order ($\gtrsim 10^6$) periodic orbits must be computed for critical values of the parameters.

It can be appreciated in the figure, that the series computed on the x_{den} found for this orbit does not yield yet the desired precision. This is explainable by due the "step-3" scaling, $\hat{\alpha}(3,m)$ depends in a bigger range of F_m. A higher order periodic orbit may be needed to compute better bounds for α_3 and β_3.

Following the previous considerations, Kadanoff's coefficients: α_0, β_0, α_3 and β_3, were computed for different maps using the corresponding periodic orbit 28657/46368 for critical values of the parameters. The results are displayed [4] in Table 6.2, although the data is insufficient to make the statistic of the reported values trustworthy. There is a need to find higher order periodic orbits for parameters closer to critical in all the cases reported.

[3]Note that with this notation, $\hat{\alpha}(1,m)$ ($\hat{\beta}(1,m)$) should converge as $m \to \infty$ to α_0 (β_0) if (x_0, y_0) is a point with most rarefaction.

[4]For display purposes the Chirikov-Taylor map (4.6) is labeled as "standard".

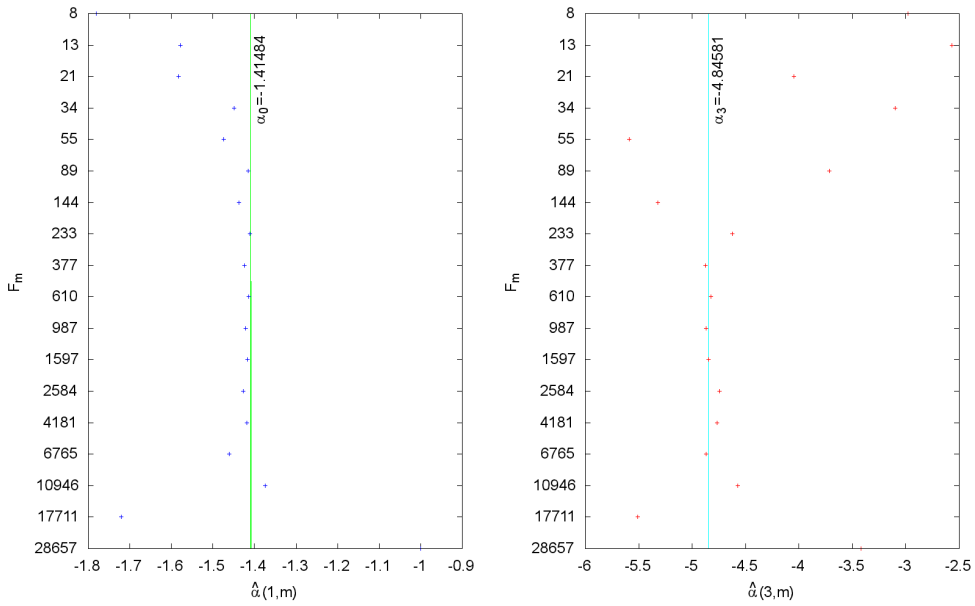

Figure 6.7: Values of $\hat{\alpha}_1(m)$ and $\hat{\alpha}_3(m)$ computed using the strategy #2 from Sec. 6.1 for the 28657/46368-periodic orbit of the *rational harmonic* map (5.23)-(5.25) with parameter values $(\kappa, p_a, p_m) = (1.73353335146, 3.0, 0.4)$.

It should be addressed that there is no a priori "most rarefied" or "most dense" point in a given orbit. Many points need to be tested around the "most dense" and "most rarefied" regions to find one that best reproduce the universal bounds. Since the structure of the periodic orbit tends to be fractal, it is common to find points in locally rarefied (or dense) regions that also reproduce the bounds but with the same number of digits.

6.5 Discussion and remarks

The computation of high order periodic orbits around critical values is a challenging problem even with the new *compound method*. It is almost guarantied that the parameterization curve K found by the *modified parameterization method* will be not optimal to contain in an approximate manner points with a self-similar distribution and the basins of attraction for the 2D pseudo-Newton are smaller (slimmer) as the order of the period increase. And on top of that there are free parameters like the numerical continuation

Map	Par.	x_{rar} / x_{den}	$\lvert R\rvert$	α_0 / α_3
Standard	κ 0.97160	$0.00000000000 \times 10^{-00}$	2.5×10^{-01}	-1.414
		$5.00000000000 \times 10^{-01}$		-4.846
NASM	κ_1 0.54299	$1.225371559785 \times 10^{-05}$	5.3×10^{-14}	-1.428
	κ_2 0.20000	$5.000011030386 \times 10^{-01}$		-4.845
Rational harmonic	κ 1.73353	$6.793464641760 \times 10^{-01}$	3.7×10^{-02}	-1.428
	p_a 3.0 p_m 0.4	$5.148782114378 \times 10^{-02}$		-4.855

Table 6.2: Kadanoff's geometrical coefficients α_0 and α_3 computed for the points x_{den} and x_{rar} found for a periodic orbit 28657/46368 with the $|R|$ close to 0.25 for the different maps via the compound method.

step size or the maximum number of harmonics, whose election may affect the success of the search.

However it was possible to corroborate for the rational harmonic map (5.23) and the period-two NASM (4.4), up to the order of the orbits that where computed, the universal self-similar behavior of predicted by the renormalization theory. Although the results are not optimal, this is the first evidence that renormalization theory results are valid for non-reversible maps.

Aside from computing higher order periodic orbits, it is still pending to compute the Kadanoff's coefficients for the period-two NASM using periodic orbits whose rotation numbers p_i/q_i approximate the double of the golden mean $2\gamma = \sqrt{5}-1 = [1;4,4,4,...] = 1.236067977....$ This can be unexpectedly challenging since the numbers in the sequence given by the continued fraction grows faster than the Fibonacci sequence,

$$\begin{aligned}
[1;4,0,0,0,0,0,\ldots] &= 1+\tfrac{1}{5} &&= 1.2000000\ldots\\
[1;4,4,0,0,0,0,\ldots] &= 1+\tfrac{5}{21} &&= 1.2380952\ldots\\
[1;4,4,4,0,0,0,\ldots] &= 1+\tfrac{21}{89} &&= 1.2359551\ldots\\
[1;4,4,4,4,0,0,\ldots] &= 1+\tfrac{89}{377} &&= 1.2360743\ldots\\
[1;4,4,4,4,4,0,\ldots] &= 1+\tfrac{377}{1597} &&= 1.2360676\ldots
\end{aligned}$$

Chapter 7

Conclusions and future work

This work presented a Hamiltonian mean-field dynamical system related to a plasma physics model of chaotic transport. Because of the similarities of the equations it can also be interpreted as a fluid dynamics model that describes the growth of a perturbation embedded in a plane Couette flow in a point-vortex representation. The results and simulations from Chapter 1, showed consistently with Ref. [1] that the model reproduces at least a qualitative level the behavior of the continuous model and allowed to consider the transport problem from the point of view of dynamical systems, particularly as a symplectic map. For this kind of maps, after considering the material reviewed in Chapter 2, it is natural to consider structures like the KAM tori natural topological barriers for the transport, understood as the unbound evolution in the momentum variable (y is most of cases) of a given set of initial conditions.

The reduced cases studied in Chapter 1 for low N-particle cases helped to picture in a discrete frame the behavior of "monopole" (or "macroparticle") and "dipole" states studied before in the continuous in Refs. [1] and [4], respectively. The reduced maps permitted to obtain parameter values and initial conditions that yielded coherent "macroparticle" states and evidence that the "dipole" states are not stable in the map model. Additionally it was possible to recreate the exact solution of a "Water-Bag mode" as coherent state in the map model. Although the existence of this last state is intrinsically tied to the velocity value of the Galilean frame of reference (U or Ω), just as in the continuous case, see Ref. [7].

The oscillatory state of the mean field variables was probed in Chapter 3, trying to relate it with periodic orbits of the model. General properties of the

periodic orbits were found and with the use of normal forms, an specific set of symmetric periodic orbits were computed. Although the results did not seem to directly relate with the observed oscillatory state, the fine tuning required added further evidence of the critical dynamical impact of the velocity value of the Galilean frame of reference and its relation with specific types of initial conditions.

After a not entirely successful search in the literature for results that could help to determine the persistence of invariant circles in similar models, a new simpler map was considered. Taking into account the obvious similarities between the original model and the Chirikov-Taylor map, the proposed new map was constructed to mimic the oscillatory state of the original map model and help to determine in a concrete case if an small and non-random "oscillation" of the perturbation parameter in the Chirikov-Taylor map could produce or not global transport. The literature offered a few entries to this problem, Refs. [59, 105, 60], but not a procedure to find numerical bounds to the parameters and from this work point of view, all these works were more focused in the general study quasi-periodic oscillation. The new further reduced map model proposed was named a "non-autonomous standard map" (NASM) and the two-periodic case was studied in Chapter 4 from different angles: symmetries, low order periodic orbits, global critical transport and KAM invariant circles. The last approach was done by the implementation of one the newest and state of art method in dynamical systems: the parameterization method. The sum of efforts on the two-periodic NASM gave quantitative values to determine the region in the parameter space for which there was no global transport. Comparing these results with the literature [59, 60], the bounds found are also surprisingly good bounds for the global critical transport for a quasi-periodic NASM case or, in context of these works, the existence of 2D-tori for a 3D-map.

To give answers to open questions about the behavior of the two-periodic NASM for parameter values close to critical, a new method to estimate periodic orbits for non reversible maps was proposed and implemented in Chapter 5. The main goal was to compute the self-similar coefficients find by Kadanoff and Shenker [64, 68] that appear in the Chirikov-Taylor map for perturbation parameter values close the critical. The new method consisted in a modified parameterization method (MPM) that attempted to find a parametric curve that passed over the points of an a priori fixed periodic orbit and 2D-pseudo-Newton algorithm to refine the results. An unexpected correspondence between a regularized error and Greene's residue helped to

optimize the approximation of the MPM, although the error in the computation of high order periodic orbits grows near critical values of the parameters. Three maps were considered to test the method: the Chirikov-Taylor map, the two-periodic NASM and three parameter rational harmonic map . The compound method allowed to compute periodic orbits for the three maps, although further study is required to use the method to find periodic orbits of higher order close to critical parameter values. The bounds of Kadanoff's coefficients are not yet optimal, but they are expected improve as higher order periodic orbits are computed. The results reproduced the known behavior of Chirikov-Taylor map and the apparent existence of symmetry lines on the two-periodic NASM, even though it has not been possible to rewrite it as a composition of involutions. For the rational harmonic map, this study allowed to give a better characterization of it, finding a 2D-manifold with folds in the parameter space for the critical values of the parameters. But possibly the most unexpected observation is that this new method may help to find seed data for the standard parameterization method for invariant circles that may resurge along a given trajectory on the parameter space, however further study is need to transform this observation to an algorithm.

Ideas for future work

Some unexplored **topics** that were not explicit mentioned in previous chapters and that could lead to to improve or generalize results of this work are presented in this last section.

▶ Critical rotation numbers and critical exponents

The work presented in Sec. 4.5.2, specifically Figs. 4.8 and 4.9 can be improved. A study over the rotation number of most "robust" invariant tori as function of the parameters (κ_1, κ_2) can lead to further understanding the symmetry break between the locally "robust" invariant tori $\gamma = [0; 1, 1, ...]$ and $2\gamma = [0; 4, 4, ...]$. Further study may help to improve or deny the hypothesis that the most robust invariant tori always are *usually* constant type numbers, *golden* numbers with a tail of 1's in their continuous fraction expansion[1].

[1]Note that the rotation number $2\gamma = [0; 4, 4, ...]$ is a counterexample of this hypothesis, hence the use of "usually".

Also the use of the hybrid method described in chapter 5 can lead to determining the critical geometrical scaling coefficients (α, β) (see Ref. [64]) of the map (4.1) for the critical parameter values (blue curve in Fig. 4.8).

▶ A more faithful non-autonomous standard map

A different map to study that could mimic better the oscillatory behavior of the map (1.1) as seen in Fig. 1.4 and 1.5 than the (4.1) map, would be a non-autonomous map of the form,

$$\hat{x}_{n+1} = \hat{x}_n + \hat{y}_{n+1} \qquad \text{mod } (1), \tag{7.1a}$$

$$\hat{y}_{n+1} = \hat{y}_n + \frac{\kappa_n}{2\pi}\sin(2\pi\hat{x}_n + n\delta)\,, \tag{7.1b}$$

a map that has a constant drag δ in the angle as the evolution observed for θ^n. Nevertheless, an immediate complication of this map is that the autonomous reduction analogous to the one done for (4.1) in Sec. 4.1, would be significantly harder to study even for the two periodic case. The two periodic reduction have the form,

$$x_{n+2} = x_n + 2y_n + \mathcal{G}_1(x_n, y_n, n; \kappa_1, \kappa_2, \delta) \qquad \text{mod } (1) \tag{7.2a}$$

$$y_{n+2} = y_n + \mathcal{G}_2(x_n, y_n, n; \kappa_1, \kappa_2, \delta) \tag{7.2b}$$

where $\mathcal{G}_1$ and $\mathcal{G}_2$ are defined as,

$$\mathcal{G}_1(x, y, n; \kappa_1, \kappa_2, \delta) = \frac{\kappa_1}{2\pi}\sin(2\pi x + \delta n) + \mathcal{G}_2\,, \tag{7.3a}$$

$$\begin{aligned}\mathcal{G}_2(x, y, n; \kappa_1, \kappa_2, \delta) = {} & \frac{\kappa_1}{2\pi}\sin(2\pi x + \delta n) \\ & + \frac{\kappa_2}{2\pi}\sin\left\{2\pi\left[x + y + \frac{\kappa_1}{2\pi}\sin(2\pi x + \delta n)\right] + \delta(n+1)\right\}\,.\end{aligned} \tag{7.3b}$$

The complication is not just the map (7.2) has more parameters than Eq. (4.4), but it also have an explicit dependence on the iterate number n. Because of this, there would be the need to modify the implementation of parameterization method among others.

Bibliography

[1] D. del-Castillo-Negrete. Self-consistent chaotic transport in fluids and plasmas. *Chaos*, 10(1):75–88, 2000.

[2] G. Bofetta, D. del-Castillo-Negrete, C. López, G. Pucacco, and A. Vulpiani. Diffusive transport and self-consistent dynamics in coupled maps. *Phys. Rev. E*, 67:026224, 2003.

[3] L. Carbajal, D. del-Castillo-Negrete, and J.J. Martinell. Dynamics and transport in mean-field coupled, many degrees-of-freedom, area-preserving nontwist maps. *Chaos*, 22(1):013137, 2012.

[4] D. del-Castillo-Negrete and M.-C. Firpo. Coherent structures and self-consistent transport in a mean field hamiltonian model. *Chaos*, 12(2):496–507, 2002.

[5] T.M. O'Neil, J.H. Winfrey, and J.H. Malmberg. Nonlinear interaction of a small cold beam and a plasma. *Physics of Fluids (1958-1988)*, 14(6):1204–1212, 1971.

[6] D. del-Castillo-Negrete. Nonlinear evolution of perturbations in marginally stable plasmas. *Physics Letters A*, 241(1):99–104, 1998.

[7] D. del-Castillo-Negrete. Weakly nonlinear dynamics of electrostatic perturbations in marginally stable plasmas. *Physics of Plasmas*, 5(11):3886–3900, 1998.

[8] D. Martínez-del-Río, D. del-Castillo-Negrete, A. Olvera, and R.C. Calleja. Self-consistent chaotic transport in a high dimensional mean-field hamiltonian map model. *QTDS*, 14(2):313–335, 2015.

[9] R. Calleja, D. del-Castillo-Negrete, D. Martínez-del-Río, and A. Olvera. Global transport in a nonautonomous periodic standard map. *Communications in Nonlinear Science and Numerical Simulation*, 51:198–215, 2017.

[10] B.V. Chirikov. A universal instability of many-dimensional oscillator systems. *Physics reports*, 52(5):263–379, 1979.

[11] R. Calleja, A. Celletti, and R. de la Llave. A KAM theory for conformally symplectic systems: efficient algorithms and their validation. *J. Differential Equations*, 255(5):978–1049, 2013.

[12] R. Calleja and R. de la Llave. Computation of the breakdown of analyticity in statistical mechanics models: numerical results and a renormalization group explanation. *J. Stat. Phys.*, 141(6):940–951, 2010.

[13] R. Calleja and R. de la Llave. A numerically accessible criterion for the breakdown of quasi-periodic solutions and its rigorous justification. *Nonlinearity*, 23(9):2029–2058, 2010.

[14] À. Haro, M. Canadell, J.-Ll. Figueras, A. Luque, and J.-M. Mondelo. *The parameterization method for invariant manifolds. From rigorous results to effective computations.* Springer, 2016.

[15] D. del-Castillo-Negrete. Coherent structures in the plasma wave–particle interaction. *Plasma physics and controlled fusion*, 47(5A):A53, 2005.

[16] A. Simon and M.N. Rosenbluth. Single-mode saturation of the bump-on-tail instability: Immobile ions. *Physics of Fluids (1958-1988)*, 19(10):1567–1580, 1976.

[17] S.I. Tsunoda, F. Doveil, and J.H. Malmberg. Experimental test of the quasilinear theory of the interaction between a weak warm electron beam and a spectrum of waves. *Physical review letters*, 58(11):1112, 1987.

[18] J. M. Greene. A method for determining a stochastic transition. *Journal of Mathematical Physics*, 20:1183–1201, June 1979.

[19] D. del-Castillo-Negrete. Dynamics and self-consistent chaos in a mean field hamiltonian model. In *Dynamics and Thermodynamics of Systems with Long-Range Interactions*, pages 407–436. Springer, 2002.

[20] I.B. Bernstein, J.M. Greene, and M.D. Kruskal. Exact nonlinear plasma oscillations. *Physical Review*, 108(3):546, 1957.

[21] P. Bertrand, J.P. Doremus, G. Baumann, and M.R. Feix. Stability of inhomogeneous two-stream plasma with a water-bag model. *The Physics of Fluids*, 15(7):1275–1281, 1972.

[22] J.D. Meiss. Symplectic maps, variational principles, and transport. *Rev. Modern Phys.*, 64(3):795–848, 1992.

[23] V.I. Arnold. Mathematical methods of classical mechanics. *Springer, New York, NY*, 10013, 1978.

[24] L. Reichl. *The transition to chaos: conservative classical systems and quantum manifestations*. Springer Science & Business Media, 2013.

[25] A.J. Lichtenberg and M.A. Lieberman. *Regular and stochastic motion*, volume 38. Springer Science & Business Media, 2013.

[26] C. Golé. *Symplectic twist maps: global variational techniques*, volume 18. World Scientific, 2001.

[27] Shaun Bullett. Invariant circles for the piecewise linear standard map. *Communications in Mathematical Physics*, 107(2):241–262, 1986.

[28] R.S. MacKay. Greene's residue criterion. *Nonlinearity*, 5(1):161, 1992.

[29] A. Olvera and N. P. Petrov. Regularity properties of critical invariant circles of twist maps, and their universality. *SIAM Journal on Applied Dynamical Systems*, 7(3):962–987, 2008.

[30] A. Olvera and C. Simó. An obstruction method for the destruction of invariant curves. *Physica D*, 26(2):181–192, 1987.

[31] J.N. Mather. Non-existence of invariant circles. *Ergodic Teory and Dyn. Syst.*, 2:301–309, 1984.

[32] R.S. MacKay and I.C. Percival. Converse kam: theory and practice. *Communications in mathematical physics*, 98(4):469–512, 1985.

[33] J. Stark. An exhaustive criterion for the non-existence of invariant circles for area-preserving twist maps. *Communications in mathematical physics*, 117(2):177–189, 1988.

[34] R. de la Llave. A tutorial on KAM theory. In *Smooth ergodic theory and its applications (Seattle, WA, 1999)*, volume 69 of *Proc. Sympos. Pure Math.*, pages 175–292. Amer. Math. Soc., Providence, RI, 2001.

[35] R. de la Llave, A. González, À. Jorba, and J. Villanueva. KAM theory without action-angle variables. *Nonlinearity*, 18(2):855–895, 2005.

[36] E. Zehnder. Generalized implicit function theorems with applications to some small divisor problems. I. *Comm. Pure Appl. Math.*, 28:91–140, 1975.

[37] R. Calleja and R. de la Llave. Fast numerical computation of quasi-periodic equilibrium states in 1D statistical mechanics, including twist maps. *Nonlinearity*, 22(6):1311–1336, 2009.

[38] G. Huguet, R. de la Llave, and Y. Sire. Computation of whiskered invariant tori and their associated manifolds: new fast algorithms. *Discrete Contin. Dyn. Syst.*, 32(4):1309–1353, 2012.

[39] J.-Ll. Figueras, A. Haro, and A. Luque. Rigorous computer assisted application of KAM theory: a modern approach. *ArXiv e-prints*, January 2016.

[40] À. Haro, M. Canadell, J.-Ll. Figueras, A. Luque, and J.-M. Mondelo. *The parameterization method for invariant manifolds. From rigorous results to effective computations.* Springer, 2016.

[41] R. Calleja and A. Celletti. Breakdown of invariant attractors for the dissipative standard map. *Chaos*, 20(1):013121, 9, 2010.

[42] R. Calleja and J.-Ll. Figueras. Collision of invariant bundles of quasi-periodic attractors in the dissipative standard map. *Chaos*, 22(3):033114, 10, 2012.

[43] A. M. Fox and J. D. Meiss. Greene's residue criterion for the breakup of invariant tori of volume-preserving maps. *Phys. D*, 243:45–63, 2013.

[44] M. Haragus and G. Iooss. *Local bifurcations, center manifolds, and normal forms in infinite-dimensional dynamical systems*. Springer Science & Business Media, 2010.

[45] A. Chenciner and R. Montgomery. A remarkable periodic solution of the three-body problem in the case of equal masses. *Annals of Mathematics-Second Series*, 152(3):881–902, 2000.

[46] H. Kook and J.D. Meiss. Periodic orbits for reversible, symplectic mappings. *Physica D: Nonlinear Phenomena*, 35(1-2):65–86, 1989.

[47] E.J. Doedel. Lecture notes on numerical analysis of nonlinear equations. In *Numerical Continuation Methods for dynamical systems*, pages 1–49. Springer, 2007.

[48] A. Delshams and R. De La Llave. KAM theory and a partial justification of greene's criterion for nontwist maps. *SIAM Journal on Mathematical Analysis*, 31(6):1235–1269, 2000.

[49] A. Olvera. Estimation of the amplitude of resonance in the general standard map. *Experimental Mathematics*, 10(3):401–418, 2001.

[50] J.M. Greene and J.M. Mao. Higher-order fixed points of the renormalisation operator for invariant circles. *Nonlinearity*, 3(1):69, 1990.

[51] C. Baesens and R.S. MacKay. The one to two-hole transition for cantori. *Physica D: Nonlinear Phenomena*, 71(4):372–389, 1994.

[52] R. Moeckel. Generic drift on cantor sets of annuli. In *Celestial Mechanics, Dedicated to Donald Saari for his 60th Birthday*, page 163, 2002.

[53] J. Moser. On invariant curves of area-preserving maps of an annulus. nach. *Akad. Wiss., Gottingen, Math. Phys. Kl. II*, 1(1), 1962.

[54] R. C. Calleja, A. Celletti, C. Falcolini, and R. de la Llave. An extension of Greene's criterion for conformally symplectic systems and a partial justification. *SIAM J. Math. Anal.*, 46(4):2350–2384, 2014.

[55] J.N. Mather. Variational construction of orbits of twist diffeomorphisms. *Journal of the American Mathematical Society*, 4(2):207–263, 1991.

[56] J.N. Mather. Existence of quasi-periodic orbits for twist homeomorphisms of the annulus. *Topology*, 21(4):457–467, 1982.

[57] G. Gómez, J.-M. Mondelo, and C. Simó. A collocation method for the numerical fourier analysis of quasi-periodic functions. i. numerical tests and examples. *Discrete Contin. Dyn. Syst. Ser. B*, 14(1):41–74, 2010.

[58] A. Luque and J. Villanueva. Quasi-periodic frequency analysis using averaging-extrapolation methods. *SIAM Journal on Applied Dynamical Systems*, 13(1):1–46, 2014.

[59] S. Tompaidis. Numerical study of invariant sets of a quasiperiodic perturbation of a symplectic map. *Exp. Math.*, 5(3):211–230, 1996.

[60] C. Simó. Experiments looking for theoretical predictions. *Indagationes Mathematicae*, 2015.

[61] A.C. Newell and J.A. Whitehead. Finite bandwidth, finite amplitude convection. *Journal of Fluid Mechanics*, 38(2):279–303, 1969.

[62] J. Ford and Gary H. Lunsford. Stochastic behavior of resonant nearly linear oscillator systems in the limit of zero nonlinear coupling. *Physical Review A*, 1(1):59, 1970.

[63] J. Ford. The transition from analytic dynamics to statistical mechanics. *Adv. Chem. Phys*, 24:155–185, 1973.

[64] L.P. Kadanoff. Scaling for a critical kolmogorov-arnold-moser trajectory. *Physical Review Letters*, 47(23):1641, 1981.

[65] R. de La Llave, A. Olvera, and N.P. Petrov. Universal scalings of universal scaling exponents. *Journal of Physics A: Mathematical and Theoretical*, 40(23):F427, 2007.

[66] A. Katok. Some remarks on birkhoff and mather twist map theorems. *Ergodic theory and dynamical systems*, 2(2):185–194, 1982.

[67] R.S. MacKay. *Renormalization in area-preserving Maps*. Disertation, Princeton University, 1982.

[68] S.J. Shenker and L.P. Kadanoff. Critical behavior of a KAM surface: I. empirical results. *Journal of Statistical Physics*, 27(4):631–656, 1982.

[69] R.S. MacKay. A renormalization approach to invariant circles in area-preserving maps. *Physica D: Nonlinear Phenomena*, 7(1-3):283–300, 1983.

[70] R.L. Devaney. Reversible diffeomorphisms and flows. *Transactions of the American Mathematical Society*, 218:89–113, 1976.

[71] M.B. Sevryuk. Reversible systems. volume 1211 of lecture notes in mathematics, 1986.

[72] John A.G. Roberts and M.l Baake. Trace maps as 3d reversible dynamical systems with an invariant. *Journal of Statistical Physics*, 74(3):829–888, 1994.

[73] E. Piña and L. Jiménez-Lara. On the symmetry lines of the standard mapping. *Physica D: Nonlinear Phenomena*, 26(1-3):369–378, 1987.

[74] J.A.G. Roberts and G.R.W. Quispel. Chaos and time-reversal symmetry. order and chaos in reversible dynamical systems. *Physics Reports*, 216(2-3):63–177, 1992.

[75] D. del-Castillo-Negrete, J.M. Greene, and P.J. Morrison. Area preserving nontwist maps: periodic orbits and transition to chaos. *Physica D: Nonlinear Phenomena*, 91(1):1–23, 1996.

[76] J.E. Dennis Jr and R.B. Schnabel. *Numerical methods for unconstrained optimization and nonlinear equations*, volume 16. SIAM, 1996.

[77] A. Apte, R. de la Llave, and N.P. Petrov. Regularity of critical invariant circles of the standard nontwist map. 2005.

[78] K. Fuchss, A. Wurm, A. Apte, and P.J. Morrison. Breakup of shearless meanders and "outer" tori in the standard nontwist map. *Chaos*, 16(3):033120, 2006.

[79] A. Olvera and C. Vargas. A continuation method to study periodic orbits of the Froeschlé map. *Physica D: Nonlinear Phenomena*, 72(4):351–371, 1994.

[80] H. Kook and J.D. Meiss. Application of newton's method to lagrangian mappings. *Physica D: Nonlinear Phenomena*, 36(3):317–326, 1989.

[81] R. DeVogelaere. Contributions to the theory of nonlinear oscillations, edited by S. Lefschetz (Princeton UP, Princeton, NJ, 1958), Vol. IV.

[82] A. Haro. Private communication. 2018.

[83] R. de la Llave and D. Rana. Accurate strategies for small divisor problems. *Bulletin of the American Mathematical Society*, 22(1):85–90, 1990.

[84] I.C. Percival. Chaos in hamiltonian systems. *Proc. R. Soc. Lond. A*, 413(1844):131–143, 1987.

[85] R.S. MacKay. Exact results for an approximate renormalisation scheme and some predictions for the breakup of invariant tori. *Physica D: Nonlinear Phenomena*, 33(1-3):240–265, 1988.

[86] D.G. Luenberger, Y. Ye, et al. *Linear and nonlinear programming*, volume 2. Springer, 1984.

[87] O.E. Lanford III. A computer-assisted proof of the feigenbaum conjectures. *Bulletin of the American Mathematical Society*, 6(3):427–434, 1982.

[88] R. Castelli, J.-P. Lessard, and J.D. Mireles-James. Parameterization of invariant manifolds for periodic orbits (ii): A posteriori analysis and computer assisted error bounds. *Journal of Dynamics and Differential Equations*, pages 1–57, 2017.

[89] A. Hungria, J.-P. Lessard, and J.D. Mireles-James. Rigorous numerics for analytic solutions of differential equations: the radii polynomial approach. *Mathematics of Computation*, 85(299):1427–1459, 2016.

[90] S. Day, J.-P. Lessard, and K. Mischaikow. Validated continuation for equilibria of pdes. *SIAM Journal on Numerical Analysis*, 45(4):1398–1424, 2007.

[91] J.-P. Lessard, J.D. Mireles James, and C. Reinhardt. Computer assisted proof of transverse saddle-to-saddle connecting orbits for first order vector fields. *Journal of Dynamics and Differential Equations*, 26(2):267–313, 2014.

[92] D. del Castillo-Negrete, J.M. Greene, and P.J. Morrison. Renormalization and transition to chaos in area preserving nontwist maps. *Physica D: Nonlinear Phenomena*, 100(3-4):311–329, 1997.

[93] A. Olvera and C. Simó. Private communication. 1987.

[94] A.M. Fox and J.D. Meiss. Critical invariant circles in asymmetric and multiharmonic generalized standard maps. *Commun Nonlinear Sci Numer Simulat*, 19(4):1004–1026, 2014.

[95] J.M. Ortega. The newton-kantorovich theorem. *The American Mathematical Monthly*, 75(6):658–660, 1968.

[96] H. Poincaré. Sur les courbes definies par les equations differentielles. *J. Math. Pures Appl.*, 3(8):251–286, 1882.

[97] A. Denjoy. Sur les courbes définies par les équations différentielles à la surface du tore. *Journal de mathématiques pures et appliquées*, 11:333–376, 1932.

[98] V.I. Arnold. Small divisors. i. on the mapping of a circle into itself. *Izv. Akad. Nauk., SSSR Mat*, 25(1):21–26, 1963.

[99] M.R. Herman. Sur la conjugaison différentiable des difféomorphismes du cercle à des rotations. *Publications Mathématiques de l'Institut des Hautes Études Scientifiques*, 49(1):5–233, 1979.

[100] J.N. Mather. Destruction of invariant circles. *Ergodic Theory and Dynamical Systems*, 8(8*):199–214, 1988.

[101] R.S. Mackay and C. Tresser. Transition to topological chaos for circle maps. *Physica D: Nonlinear Phenomena*, 19(2):206–237, 1986.

[102] I. Putnam, K. Schmidt, and C. Skau. C*-algebras associated with denjoy homeomorphisms of the circle. *Journal of Operator Theory*, pages 99–126, 1986.

[103] R. de la Llave and A. Olvera. The obstruction criterion for non-existence of invariant circles and renormalization. *Nonlinearity*, 19(8):1907, 2006.

[104] R. de la Llave and N.P. Petrov. Regularity of conjugacies between critical circle maps: an experimental study. *Experimental mathematics*, 11(2):219–241, 2002.

[105] M. Canadell and R. de la Llave. KAM tori and whiskered invariant tori for non-autonomous systems. *Physica D*, 310:104–113, 2015.